

**RAPID AFFINITY PURIFICATION BASED ON ION
CONCENTRATION SHOCK WAVES AND POROUS
POLYMER MONOLITHS**

A DISSERTATION
SUBMITTED TO THE DEPARTMENT
OF MECHANICAL ENGINEERING
AND THE COMMITTEE OF GRADUATE STUDIES
OF STANFORD UNIVERSITY
IN PARTIAL FULFILMENT OF THE REQUIREMENTS
FOR THE DEGREE OF
DOCTOR OF PHILOSOPHY

Viktor Shkolnikov

June 2015

© 2015 by Viktor Shkolnikov. All Rights Reserved.

Re-distributed by Stanford University under license with the author.



This work is licensed under a Creative Commons Attribution-Noncommercial 3.0 United States License.

<http://creativecommons.org/licenses/by-nc/3.0/us/>

This dissertation is online at: <http://purl.stanford.edu/yt510fd5490>

I certify that I have read this dissertation and that, in my opinion, it is fully adequate in scope and quality as a dissertation for the degree of Doctor of Philosophy.

Juan Santiago, Primary Adviser

I certify that I have read this dissertation and that, in my opinion, it is fully adequate in scope and quality as a dissertation for the degree of Doctor of Philosophy.

Kenneth Goodson

I certify that I have read this dissertation and that, in my opinion, it is fully adequate in scope and quality as a dissertation for the degree of Doctor of Philosophy.

Ali Mani

Approved for the Stanford University Committee on Graduate Studies.

Patricia J. Gumport, Vice Provost for Graduate Education

This signature page was generated electronically upon submission of this dissertation in electronic format. An original signed hard copy of the signature page is on file in University Archives.

© 2015 by Viktor Shkolnikov. All Rights Reserved.

Re-distributed by Stanford University under license with the author.



This work is licensed under a Creative Commons Attribution-Noncommercial 3.0 United States License.

<http://creativecommons.org/licenses/by-nc/3.0/us/>

This dissertation is online at: <http://purl.stanford.edu/yt510fd5490>

I certify that I have read this dissertation and that, in my opinion, it is fully adequate in scope and quality as a dissertation for the degree of Doctor of Philosophy.

Juan Santiago, Primary Adviser

I certify that I have read this dissertation and that, in my opinion, it is fully adequate in scope and quality as a dissertation for the degree of Doctor of Philosophy.

Kenneth Goodson

I certify that I have read this dissertation and that, in my opinion, it is fully adequate in scope and quality as a dissertation for the degree of Doctor of Philosophy.

Ali Mani

Approved for the Stanford University Committee on Graduate Studies.

Patricia J. Gumport, Vice Provost for Graduate Education

This signature page was generated electronically upon submission of this dissertation in electronic format. An original signed hard copy of the signature page is on file in University Archives.

Abstract

Micro total analysis systems have the potential to drastically improve the fields of healthcare, agriculture, and environmental monitoring by rapidly providing decision influencing answers directly in the field. Sample preparation represents on the remaining challenges in achieving in achieving such systems. This dissertation focuses on developing a rapid sample preparation method based affinity purification and preconcentration that is compatible with integration into a micro total analysis system. Our method couples ion-concentration shockwaves with porous polymer monolith based micro affinity columns to achieve rapid affinity purification, minimizing purification time and maximizing affinity substrate utilization.

We begin with describing methodology for synthesis of porous polymer monoliths and control of their porous properties. We leverage the flexibility of structure, chemical composition, and surface chemistry (including wettability) of porous polymer monoliths to design, fabricate, and characterize hydrophilic porous monoliths, with the aim of achieving high permeability wick materials. We show that variations in monomer concentration and porogen composition can affect mode pore diameters ranging from 6.3 to 10.1 μm and permeabilities ranging from 0.73×10^{-12} to $1.9 \times 10^{-12} \text{ m}^2$. In addition, we identify a rough dependence of monolith permeability on porosity times the square of mode pore diameter and discuss key figures of merit characterizing capillary transport. As an example application, we then detail a custom injection molding procedure, where we in situ polymerize $\sim 150 \text{ }\mu\text{m}$ thick wicks conformally onto the surface of metal channels of a polymer electrolyte fuel cell cathode.

We then present a novel technique where we couple ion-concentration shock waves (isotachophoresis) with affinity chromatography to achieve rapid, selective purification with high column utilization. We use isotachophoresis to simultaneously preconcentrate analytes and purify them based on differences in mobility of sample components, excluding species that may foul or compete with the target at the affinity substrate. Isotachophoretic preconcentration accelerates the affinity reaction, reducing assay time, improving column utilization and allowing for capture of targets with higher dissociation constants. Furthermore, our method separates the target and contaminants into non-diffusing zones, thus achieving high resolution in a short distance and time. We present an analytical model for spatiotemporal dynamics of our method. We identify and explore the effect of key process parameters including target distribution width and height, isotachophoresis zone velocity (shock velocity), forward and reverse reaction constants, and probe concentration on necessary affinity region length, assay time, and capture efficiency. Our analytical approach shows collapse of these variables to three non-dimensional parameters. The analysis yields simple analytical relations for capture length and capture time in relevant regimes, and demonstrates how isotachophoresis greatly reduces assay time and improves column utilization in affinity chromatography.

Lastly, we present an experimental study of coupling of isotachophoresis and affinity chromatography to effect rapid, selective purification with high column utilization and high resolution. We provide a detailed protocol for performing this method and describe the design of a buffer system to perform sequence specific separation of nucleic acids. We describe the synthesis and functionalization of our affinity substrate, poly(glycidyl methacrylate-co-ethylene dimethacrylate) porous polymer monolith. This

substrate allows easy immobilization of affinity probes, is non-sieving (even to macromolecules), and exhibits negligible non-specific binding. We demonstrate our method with 25 nt, Cy5 labeled DNA target and a DNA probe and study the spatiotemporal dynamics using epifluorescence imaging. We make qualitative and quantitative comparisons between these data and the analytical model we developed for our method. We vary the target concentration from 1 to 100 pg μl^{-1} and ITP velocity over the range of 10 to 50 $\mu\text{m s}^{-1}$, and thereby explore over 4 orders of magnitude of scaled target amount. We observe very good agreement between predictions and experimental data for the spatiotemporal behavior of the coupled isotachopheresis and affinity process, and for key figures of merit including scaled capture length and maximum capture efficiency. Finally, we demonstrate that the resolution of our method increases linearly with time and purify 25 nt target DNA from 10,000-fold higher abundance background (contaminating) genomic fish sperm DNA. We perform this capture from 200 μl of sample in under 1 mm column length and in less than 10 min.

Table of Contents

1	Introduction	1
1.1	Ion concentration shockwaves (isotachophoresis)	2
1.1.1	Peak-mode vs. plateau mode.....	3
1.1.2	Finite vs. semi-infinite injection	4
1.2	Synthesis of porous polymer monoliths (PPM)	6
1.2.1	Background and applications of PPM.....	6
1.2.2	PPM synthesis theory.....	9
1.2.3	Discussion	14
1.2.4	Summary of PPM synthesis	23
1.3	Functionalization of pore surfaces in GMA-co-EDMA PPM.....	24
1.3.1	Functionalization of GMA-co-EDMA PPM surface with small molecules	24
1.3.2	Functionalization of GMA-co-EDMA PPM surface with nucleic acids	27
1.3.3	Functionalization of GMA-co-EDMA PPM surface with proteins	30
1.4	Scope of thesis.....	32
1.5	Supplementary Information.....	34
2	Design and Fabrication of Porous Polymer Wicks	41
2.1	Introduction	41
2.2	Materials and Methods	43
2.2.1	Materials	43

2.2.2	Polymer chemistry	44
2.2.3	Fabrication of samples for ex-situ permeability and pore size measurements.....	45
2.2.4	Measurement of permeability	45
2.3	Results	46
2.3.1	Review of general mechanisms and trends in monolith polymerization	47
2.3.2	Control and optimization of wick porosity and pore structure	48
2.3.3	Designing high performance porous polymer wick material.....	52
2.3.4	Fabrication of resin negative mold	61
2.3.5	Injection molding of wicks	61
2.3.6	Removal and cleaning.....	63
2.4	Conclusions and Recommendations.....	64
2.5	Supplementary Information.....	65
2.5.1	Notes regarding permeability measurement setup.....	67
3	Coupling Isotachophoresis with Affinity Chromatography for Rapid and Selective Purification with High Column Utilization: Theory	68
3.1	Introduction	68
3.2	Concept and theory.....	72
3.2.1	Method concept.....	72
3.2.2	Transport and focusing of trace analytes in isotachophoresis	74

3.2.3	One dimensional transport reaction model	74
3.3	Results and Discussion.....	84
3.3.1	Analytical solution for bound and free target concentration	84
3.3.2	Spatiotemporal dynamics predicted by analytical solution	85
3.3.3	Limiting regimes of ITP-aided capture dynamics	93
3.4	Conclusions	95
3.5	Supplementary Information.....	96
3.5.1	Solution to the simplified advection-reaction equations.....	96
3.5.2	Separation resolution of ITP-AC	113
4	Coupling Isotachophoresis with Affinity Chromatography for Rapid and Selective Purification with High Column Utilization: Experimental Study.....	121
4.1	Introduction	121
4.2	Experimental Methods	124
4.2.1	Experimental setup.....	124
4.2.2	Materials	126
4.2.3	Porous polymer monolith synthesis and functionalization	127
4.2.4	ITP-aided affinity chromatography protocol	127
4.2.5	ITP-AC choice of buffer chemistry	129
4.3	Results and Discussion.....	130
4.3.1	Brief review of ITP-AC trends predicted by our model	130

4.3.2	Measurement of ITP-AC parameters	131
4.3.3	Spatiotemporal behavior of ITP-AC	132
4.3.4	Comparison between predicted and measured spatiotemporal behavior of ITP-AC	134
4.3.5	Effect of α and Da on scaled capture length	137
4.3.6	Effect of α and Da on capture efficiency	140
4.3.7	Sequence specific extraction of target from 10^4 x more abundant contaminant	141
4.4	Conclusions	143
4.5	Supplementary Information.....	144
4.5.1	Extraction of analyte from the TE reservoir in semi-infinite injection ITP	144
4.5.2	Calibration of Cy5 fluorescence to DNA concentration.....	150
4.5.3	Synthetic DNA oligo sequences used	152
4.5.4	Measurement of PPM void fraction.....	156
4.5.5	Image of custom built capillary setup	157
4.5.6	Choice of porous polymer monolith chemistry, synthesis, and functionalization	158
4.5.7	Choice of buffer chemistry for ITP-AC.....	161
4.5.8	Analyses of ITP-AC purified 25 nt target from 10,000x contaminant via electrophoresis	162

4.5.9	Recommended ITP-AC parameters	164
5	Contributions, conclusions, and recommendations	172
5.1	Major contributions	172
5.1.1	Design and fabrication of porous polymer wick structures	172
5.1.2	Coupling ITP with AC: Theory	173
5.1.3	Coupling ITP with AC: Experimental Study	173
5.2	Conclusions	174
5.2.1	Design and fabrication of porous polymer wick structures	174
5.2.2	Coupling ITP with AC: Theory	175
5.2.3	Coupling ITP with AC: Experimental Study	176
5.3	Recommendations for Future Work.....	176
A.	Fast, Specific, and Efficient Affinity Purification of Target DNA from Whole Human Blood by Coupling Isotachophoresis with Affinity Chromatography	180
A.1	Introduction	180
A.2	Theory	181
A.3	Experimental	182
A.4	Results and Discussion.....	183
A.5	Conclusion.....	185
B.	Rapid Sequential Affinity Probing of Multiple Regions of Nucleic Acids Without Amplification or Sample Spiting	186

B.1	Introduction	186
B.2	Concept.....	188
B.3	Materials and Methods	193
B.3.1	Column Fabrication	193
B.3.2	Imaging systems.....	194
B.4	Discussion	194
B.4.1	Demonstration of sequential capture and release of target	195
B.4.2	Control and measurement of target hybridization rate	199
B.5	Conclusion.....	199
B.6	Supplementary Information.....	200
B.6.1	Timescale of temperature transients during switching from capture to elution	200
B.6.2	Approximate radial temperature distribution in the capillary	209
B.6.3	Capillary surface temperature measurements	211
B.6.4	Optimal distance between affinity regions	213
B.6.5	Image of custom built capillary setup with two affinity regions	216
B.6.6	Synthetic DNA oligo sequences used	217
B.6.7	Spatiotemporal behavior of target during capture and elution.....	220
B.6.8	Performance metrics of serial-recycling and traditional parallel affinity assays	222

C.	Practical guidelines for PPM synthesis and functionalization	230
C.1	Materials	230
C.2	Preparation of polymerization solution	231
C.3	Vinylizing glass surfaces	233
C.4	Custom-built UV polymerization setup	234
C.5	UV polymerization of PPM in capillaries	236
C.6	Functionalization of GMA-co-EDMA PPM with DNA	237
C.7	Functionalization of GMA-co-EDMA PPM with Streptavidin	238

List of Figures

Figure 1.1 Schematics illustrating isotachophoretic focusing of a target using finite (a,c,e) and semi-infinite injection schemes (b,d,f). (a) In a finite injection scheme the sample containing the target is placed in a sample reservoir located between a trailing electrolyte (TE) reservoir and the separation channel filled with leading electrolyte (LE); this channel connects to an LE reservoir. (b) In semi-infinite injection scheme, the sample is mixed with the TE and placed into the TE reservoir. This reservoir connects to the separation channel (filled with LE), which connects to and LE reservoir filled with LE. (c and d) For peak mode ITP, the target is focused into a narrow peak at the interface of LE and TE. The peak width is roughly the width of the LE-TE interface (e and f) In contrast, in plateau mode ITP the target is focused into a wide zone, much wider than the LE-TE interface width. 6

Figure 1.2. Scanning electron micrographs of porous polymer monoliths synthesized by Viklund et al. [1]. These correspond to monoliths in Table 1.1a (see Supplementary Information, Chapter 1), lines 25-36. (a corresponds to line 25, b to line 26 and so forth). Porous polymer monoliths are composed of globules and the size of the globules controls the size of the void spaces between them (i.e., pore size). The size of the globules (hence pore size) can be varied with solvent composition, crosslinker and monomer concentrations, temperature, and initiator concentration. 11

Figure 1.3. The relationship between volume fraction of thermodynamically poor solvent and pore size for (a) poly(glycidyl methacrylate-*co*-ethylene dimethacrylate), (b) poly(2-hydroxyethyl methacrylate-*co*- ethylene dimethacrylate), (c) poly(butyl methacrylate-*co*-ethylene dimethacrylate-*co*-[2-(methacryloyloxy)ethyl] trimethyl amonium chloride) (d)

poly(butyl methacrylate-*co*-ethylene dimethacrylate-*co*-2-acrylamido-2-methyl-1-propanesulfonic acid) investigated by Yu et al. [2] and (e) poly(butyl methacrylate-*co*-ethylene dimethacrylate) studied by Eeltink et al. [6]. Data in (a), (d) and possibly (e) show a sigmoidal relationship between volume fraction of poor solvent and pore size. Data in (b) and (c) show a relationship with a peak in pore size, indicating that the sigmoidal relationship is not universal. 17

Figure 1.4. Functionalization reactions of GMA-*co*-EDMA PMM to obtain (a) strong anion exchange surface (b) weak anion exchange surface (c) strong cation exchange surface and (d) weak anion exchange surface. R represents the bulk of the porous polymer monolith. (a) GMA-*co*-EDMA reacts with 2-chloro-N,N-diethylethylamine hydrochloride to produce a quaternary amine surface. (b) GMA-*co*-EDMA reacts with diethylamine to produce a tertiary amine surface. (c) GMA-*co*-EDMA reacts with sodium sulfite to produce a sulfonate groups on the monolith surface. (d) GMA-*co*-EDMA reacts with ethylenediamine and then with chloroacetic acid to produce carboxylic groups on the surface of the monolith. 27

Figure 2.1. Mode pore diameter as a function of mass fractions w_{MeOH} ($= m_{MeOH}/m_{solvents}$) and $w_{solvent}$ ($= m_{solvents}/m_{total}$). Mode pore diameter roughly increases with both increasing solvent and MeOH fractions. Pore diameter dependence on solvent fraction is more pronounced. 50

Figure 2.2. Predicted versus measured permeability for polymer monoliths. Predicted permeability calculated using (2.2), with $d = d_{mode}$, and with $k' = 1.3$ as a fitting parameter for porous polymer monoliths. Grey symbols (■) represent monolith data from the current study as summarized in Table 2.1. Inset shows only the current study data for which $k' =$

2.4 provides a best fit. Open symbols represent data taken from literature: Viklund *et al.*[15] (●), [30] (◁), and Mehrar *et al.* [26](▷). Data show rough dependence of permeability on εd_{mode}^2 . Significant scatter suggests physics governing hydraulic resistance are not fully captured when using porosity and d_{mode} as a single measured length scale. 55

Figure 2.3. Monolith permeability as a function of w_{MeOH} and $w_{solvent}$. Permeability ranged from 0.73×10^{-12} to $1.9 \times 10^{-12} \text{ m}^2$. Results show permeability increased with increasing w_{MeOH} and $w_{solvent}$. Monolith permeability is consistent with trends in porosity and pore diameter (see Figure 2.1). 57

Figure 2.4. Schematics of procedure for *in situ* wick fabrication. *Fabrication of negative mold*: (1) We placed an aluminum positive template into an acrylic casting base designed to hold the casting resin. This template formed one surface of the resulting wicks by defining a negative image in the resin mold, and the part of interest here (the fuel cell cathode channels) defined the opposite surface. (2) We poured a solvent-resistant polyester resin over the aluminum positive template and allowed to cure for one week. Aluminum template was then removed. *Injection molding of wicks*: (3) We sandwiched the fuel cell cathode channels between the resin negative mold and a back support plate and compressed. (4) We then injected polymerization solution to fill remaining void space (injection ports not shown and wick layer thickness exaggerated for clarity), sealed the mold assembly, and then irradiated with UV for 1 h. *Removal and cleaning*: (5) Aluminum cathode channel plate, with attached wicks, was then removed and soaked in an MeOH bath for 24 h. Sample was then dried..... 60

Figure 2.5. Image of resulting *in situ* fabricated wick material integrated into fuel cell cathode channels. Polymerization resulted in high-quality, 150 μm thick monolithic wicks,

which conform and are attached to the surface of the fuel cell cathode channels. The top of the channel-defining “ribs” are purposely left uncoated with wick material to promote good electrical contact for electrical current collection. The blow up is a cut away illustration, showing wick geometry (white) on aluminum cathode channel (grey) surface.

..... 63

Figure 2.6. Pore size distributions of two separate fabrications of monolith chemistry, HE05. Shown are versions 1, HE05v1 (solid), and 2, HE05v2 (dashed). y-axis represents dlogP/dV , normalized by its maximum value. As is standard with porosimetry measurements, here P is capillary pressure and V is mercury intrusion volume. Results show moderately good agreement of pore-size distributions for the two realizations, with the first realization showing slightly larger pore sizes and wider distribution as compared to the second. 66

Figure 3.1. (a) Schematic of assay for ITP-aided affinity chromatography (ITP-AC). We consider an assay in a capillary with a semi-infinite affinity capture region as shown. Under the influence of electric field, target is extracted from a sample reservoir, separated from contaminants, and concentrated at the LE-TE interface. It is then transported to and through the affinity region. Within the affinity region, the target reacts with the immobilized capture probe via a second-order reversible reaction where k_1 and k_2 are the forward and reverse reaction rate constants, respectively. (b) Initial conditions for our model of ITP-AC. At $t = 0$, the target has a Gaussian distribution with standard deviation σ and peak concentration a ; its peak is located 3σ from the entrance of the affinity region. The target moves with velocity u through the affinity region. The affinity region is semi-infinite

beginning at $z = 0$ (where z is the axial coordinate of the capillary) and containing a uniformly distributed probe of volume-averaged concentration N 72

Figure 3.2. Model predictions of spatiotemporal dynamics of bound target scaled by initial probe concentration (n/N). The abscissa and ordinate can be interpreted as scaled axial distance and time, respectively. We show various values of non-dimensionalized equilibrium dissociation constant β and saturation parameter αDa . (a), (b), and (c) show dependence of the spatiotemporal capture dynamics on β for $\alpha Da = 4.3 \times 10^{-4}$ and $\alpha = 1.1 \times 10^{-3}$ (non-saturated regime, $\alpha Da < 1$). This set of αDa and α is similar to that in one of the experiments we will describe in Chapter 4. As β increases, the capture reaction becomes more reversible until about $\beta = 3$, where the target is no longer effectively captured and streaks through the affinity region. (d) shows spatiotemporal capture dynamics in a saturated regime ($\alpha Da > 1$). Here, the leading edge of the affinity region becomes saturated, shifting the spatiotemporal capture contours upward and to the right. 87

Figure 3.3. Model predictions for the (a) scaled capture length, (b) scaled capture time, and (c) maximum capture efficiency as a function of (a, c) scaled peak target concentration α and (b) scaled target distribution width Da for low β (plotted at $\beta = 10^{-4}$). Inset in (a) shows a linear plot of scaled capture length as a function of α from 0 to 40. In (a), when $\alpha Da < 1$ and so the affinity region is not locally saturated, capture length is only governed by the balance of reaction and advection, i.e., $u/(k_l N)$. Therefore in this regime p_z^* is invariant of α or Da . When $\alpha Da > 1$ the affinity region becomes locally saturated and the length of saturated region governs the capture length. Since the length of locally saturated region is proportional to αDa , p_z^* is proportional to both α and Da . In (b), scaled capture time p_t^*

is approximately 4.3 for $Da < 0.1$. For $Da > 1$, scaled capture time increases linearly with Da . Interestingly, the scaled capture time is independent of total scaled target amount, αDa (since the length scale of capture region is insensitive to capture amount provided ligand is not saturated, $\alpha Da \leq 1$). In (c) n/N increases linearly with α and Da for $\alpha Da < 1$ (i.e., when the affinity region is not saturated). For $\alpha Da > 1$ the affinity region becomes locally saturated and $n/N = 1$ 89

Figure 3.4. $\max(n/N)$ scaled by αDa for values of β between 10^{-6} and 1, Da between 0.01 and 1000, and α between 0.01 and 100. As β increases the reverse reaction (dissociation) becomes more prominent until no effective binding occurs and the target streaks through the affinity region. Capture efficiency n/N always decreases with increasing β , and this effect becomes more pronounced with increasing Da and α . Therefore, decreasing Da (e.g., by preconcentrating the target with ITP) allows one to achieve larger capture efficiencies for a given dissociation constant. 92

Figure 4.1. (a) Schematic of the experimental setup consisting of a custom-built capillary setup, a high voltage power supply, and an epifluorescence microscope with a CCD camera. The inset in the lower left is a bright field image of the GMA-EDMA PPM inside a 500 μm inner diameter borosilicate glass capillary. (b) SEM micrograph of our GMA-EDMA substrate for probe immobilization. The PPM morphology consisted of globules approximately 1 μm in diameter, and these formed roughly 2 μm diameter pores ensuring that the porous affinity region had small hydrodynamic resistance and easily permitted ITP focusing and transport without sieving effects. 126

Figure 4.2. (a) Schematic illustrating our assay for ITP-aided affinity chromatography in a porous polymer monolith column. We filled the LE reservoir and affinity column with LE

buffer (via vacuum at the TE reservoir), and then introduce the sample and TE mixture into the TE reservoir (Step 1). We apply an electric field (from LE to TE) and the target species are extracted and focus into a sharp ITP peak (Step 2). The target migrates into the affinity region and is captured by the immobilized probe (Step 3). After capture, we displace the LE and TE buffers with air to arrest the desorption reaction. We then introduce a small (roughly 5 μ l) slug of elution buffer to remove and collect the bound target from the column (Step 4).

(b) Spatiotemporal plot of experimentally measured target concentration showing dynamics of a typical ITP-AC binding experiment. The concentrated target (visualized with Cy5 fluorescence) entered the porous affinity region from the left and was captured by the immobilized probes. In this experiment $\alpha Da = 1.0 \times 10^{-4}$ and $\alpha = 1.3 \times 10^{-3}$ 129

Figure 4.3. Predicted (a, b, c) and measured (d, e, f) spatiotemporal behavior fluorescently labeled DNA target in ITP-AC inside the affinity region. The spatiotemporal plots show the logarithm of cross sectional area averaged fluorescence intensity of the target as a function of axial coordinate z and time. Location $z = 0$ is at the leading edge of the PPM affinity region (see Figure 4.2a). (a), (b) and (c) show theoretically predicted captured target distribution for $\alpha Da = 1.0 \times 10^{-1}$ and $\alpha = 1.3 \times 10^{-1}$, $\alpha Da = 4.3 \times 10^{-4}$ and $\alpha = 1.1 \times 10^{-3}$, $\alpha Da = 1.7 \times 10^{-4}$ and $\alpha = 9.2 \times 10^{-4}$ respectively. (d), (e) and (f) show experimentally observed captured target distribution for the same respective αDa and α . The predicted spatiotemporal distribution of target agreed well with that experimentally observed.... 137

Figure 4.4. Predicted and experimentally observed (a) scaled capture length, and (b) maximum capture efficiency as a function of total scaled target amount, αDa . C_s is the target concentration in the TE, and I_{cap} is the capture current in the ITP-AC experiment. Scaled capture length is invariant of αDa for $\alpha Da < 1$ and equals approximately 2.8. For

$\alpha Da > 1$, the affinity region is locally saturated and scaled capture length increases linearly with αDa . Maximum capture efficiency increases linearly with αDa for $\alpha Da < 1$. For $\alpha Da > 1$, the affinity region is locally saturated and $\max(n/N)$ approaches unity. 139

Figure 4.5. Spatiotemporal plots showing separation of rare target DNA from 10,000-fold more abundant contaminating DNA using ITP-AC. The plots show the target and contaminant migrating from free solution into the porous polymer. SYBR Green I mostly visualized the highly abundant background contaminant fish sperm DNA and Cy 5 visualized the 25 nt target. (a) Separation observed in the SYBR Green I optical channel showing the migration of fish sperm DNA. Fish sperm DNA was not captured by the immobilized probe on the PPM and continued to migrate in ITP. This indicates that there was little non-specific binding of DNA to PPM. (b) Separation observed in the Cy5 optical channel. The Cy5-labeled, low-abundance target DNA was quickly and selectively captured. (c) Separation observed in overlapped SYBR Green I and Cy5 channels shows separation between the trace target DNA and the 10,000-fold more abundant contaminating fish sperm DNA. 142

Figure 4.6. Schematic of a channel with LE and TE reservoirs in which ITP with semi-infinite injection is performed. Labeled numerically are three planes through which the flux of analyte is analyzed. We analyze this problem to study of the influence of the length between the TE reservoir and the affinity capture region (cross hatched) on the fraction of sample extracted. Planes (1) and (2) are fixed, while Plane (3) is located at and moves with the LE-TE interface. Plane (1) is located just inside the channel near the TE reservoir and experiences the same concentration of analyte as in the TE reservoir. 145

Figure 4.7. Plot of Cy5 fluorescence and DNA concentration from 10 nM to 10 μ M and proportional fit between Cy5 fluorescence and DNA concentration. The slope of the proportional fit is $2.19 \times 10^{-5} \mu\text{M}/(\text{arbitrary unit})$. The coefficient of determination for the proportional fit is $R^2 = 0.98$ 151

Figure 4.8. Cy5 fluorescence intensity near the interface of the open bore section of the capillary and the section with the porous polymer monolith (PPM). For this experiment we filled the capillary and the PPM inside the capillary with a solution of Cy5 labeled DNA using pressure driven flow. The mean fluorescence intensity in the free solution region was 707 (arbitrary units), while that in the PPM was 1230 (arbitrary units). The black rectangles indicate the areas that were averaged for these estimates. 152

Figure 4.9. Image of custom-built capillary setup consisting of LE reservoir, 500 μ m inner diameter borosilicate glass capillary with GMA-EDMA PPM, and a TE reservoir. Platinum electrodes were dipped into the LE and TE reservoirs to apply current through the capillary. 158

Figure 4.10. Electropherograms of nucleic acid mixtures before and after application of our purification process. Shown are electropherograms of (a) mixture of trailing electrolyte (25 mM HEPES, 50 mM Tris) and 25 nt target and 10,000x more abundant (by mass) fish sperm DNA before purification, (b) fish sperm DNA alone (c) 25 nt target alone, and (d)-(f) three replicates of ITP-AC purified samples which initially contained 25 nt target and 10,000x more abundant fish sperm DNA. All electropherograms were obtained via Agilent Bioanalyzer Small RNA chip (6-150 nt range). In all electropherograms the signal from the Bioanalyzer instrument was normalized by the maximum signal for the sample. ITP-

AC reproducibly enriches the amount of 25 nt target and removes the majority of the background contaminant. 164

Figure A.1. (a) Schematic of ITP-AC process. We fill the leading electrolyte (LE) reservoir and affinity column with LE buffer and place the sample in the sample reservoir and trailing electrolyte (TE) into the TE reservoir (Step 1). We applied an electric field (from LE to TE) and the target species are extracted and focus into a sharp ITP peak (Step 2). The target migrates into the affinity region and is captured by the immobilized probe (Step 3). We then remove the LE and TE buffers and introduce a small slug of elution buffer to elute the target (Step 4). (b) Spatiotemporal plot of experimentally measured target concentration showing dynamics of a typical ITP-AC binding experiment. The concentrated target (visualized with Cy5 fluorescence) enters the porous affinity region from the left and is captured by the immobilized probes. 183

Figure A.2. Experimentally measured spatiotemporal plots showing ITP-AC separation of rare target DNA from 13,000-fold more abundant endogenous blood DNA from 12.5 μ l whole blood sample. The plots show the target and endogenous DNA migrating from free solution into the porous polymer. (a) Endogenous DNA (from lysed blood cells, visualized via SYBR Green I) is not captured by the immobilized probe on the PPM and continues to migrate in ITP. (b) The Cy5-labeled, low-abundance target DNA of the correct sequence is quickly and selectively captured. (c) Overlapped signals from SYBR Green I and Cy5 optical channels show separation between trace target DNA and 13,000-fold more abundant contaminant in under 1 mm column length and in less than 5 min. 185

Figure B.1. Schematic illustrating our assay for sequential ITP-aided affinity chromatography with multiple porous polymer monolith affinity regions (ARs). We filled

the LE reservoir and the capillary containing porous ARs with LE buffer (by applying vacuum at the TE reservoir). Then we introduce the sample into the sample reservoir and TE into the TE reservoir (Step 1). We apply an electric current (from LE to TE) and the target species are extracted and focused into a sharp ITP peak (Step 2). We lower the current value and the target migrates into the first AR and is captured by the immobilized probe (Step 3). Once the target is separated from any other species not captured by the immobilized probe, we raise the current value to increase Joule heating the electrolyte solution in the AR and elute the target. The target then catches up with the migrating LE-TE interface. (Step 4). We then repeat steps 3 and 4 $n-1$ times for the subsequent $n-1$ ARs to probe the target n times..... 192

Figure B.2. Florescence intensity of Cy5 labeled DNA target (black dashed) and current (red solid) in ARs 1 and 2 as a function of time. The target, focused in ITP, entered the first AR under capture current of 200 μ A (generating optimal temperature for hybridization) and began to hybridize to immobilized cDNA capture probes. Once hybridization was over and non-complimentary target was removed focused in ITP (see SI Figure S-5) we eluted the captured target by increasing current to 800 μ A (capture current). This current generated optimal temperature for the reverse reaction (melting) and eluting the captured DNA. This DNA migrated rapidly through the TE to catch up with the LE-TE interface and refocus. Once the DNA was refocused, we lowered the current to 200 μ A and repeated the capture and elution process at the second AR containing a different probe than AR1. Thus we interrogated two regions of the same target with two different probes..... 195

Figure B.3. Solution to the transcendental equation (B.24) as a function of Biot number.

For $Bi < 1$, we approximate $\mu_1^2 \approx 1.8Bi$, which is accurate to within 10%; for $Bi > 50$ we approximate $\mu_1^2 \approx 5.8$ which is also accurate to within 10%. 207

Figure B.4. Mean $(T_{ss} * Bi) / \Omega$ (a) and $\Delta T_{ss} * \Omega$ (b) inside the capillary as a function of scaled internal thermal diffusivity, A_i (from 0.1 to 2), scaled inner capillary radius, R_i (from 0.05 to 0.95). Both $(T_{ss} * Bi) / \Omega$ and $\Delta T_{ss} * \Omega$ increase with increasing R_i (and so increasing portion of capillary generating heat) and decreasing A_i (electrolyte and PPM trapping heat inside the capillary more effectively). Mean $(T_{ss} * Bi) / \Omega$ (a) and $\Delta T_{ss} * \Omega$ (b) inside the capillary as a function of scaled internal thermal diffusivity, A_i (from 0.1 to 2), scaled inner capillary radius, R_i (from 0.05 to 0.95). Both $(T_{ss} * Bi) / \Omega$ and $\Delta T_{ss} * \Omega$ increase with increasing R_i (and so increasing portion of capillary generating heat) and decreasing A_i (electrolyte and PPM trapping heat inside the capillary more effectively). 211

Figure B.5. Spatiotemporal plots showing radially averaged temperature in the TE and LE and in free solution and inside the porous affinity region under capture (a) and elution (b) conditions. We show the affinity region (18.3 mm long) bounded inside the black dashed lines. The temperature of the TE is higher than that of the LE, due to lower conductivity of the TE resulting in higher heat generation inside the TE (see SI Section B.6.2). For example, during capture, mean temperature in the TE was approximately 27°C, while that in the LE was 24°C. For the elution condition, the temperature adjacent to the porous affinity region is observably higher than that in free solution. (TE, free solution 45°C vs. TE, PPM 50°C; LE, free solution 33°C vs. LE, PPM 34°C). We attribute this to the relatively poor thermal diffusivity of the PPM solid compared to the electrolyte, thus trapping heat inside the porous affinity region (see Table B.1), as well as higher heat

generation inside the PPM vs. free solution. This effect is more prominent at higher heat generation rates, hence a more noticeable temperature difference between free solution and PPM for the elution condition..... 213

Figure B.6. Image of custom-built capillary setup consisting of LE reservoir, 500 μm inner diameter borosilicate glass capillary with two GMA-EDMA PPM for the two ARs, and a block containing sample reservoir and TE reservoir. Platinum electrodes were dipped into the LE and TE reservoirs to apply current through the capillary..... 217

Figure B.7. Spatiotemporal plots showing Cy5 labeled target capture and elution inside affinity regions 1 and 2 (origin of axial coordinate is the leading edge of the affinity region). Intensity is proportional to the concentration of Cy5 labeled target. The target focused in ITP under capture current (200 μA) enters the AR, and a large portion of the target complementary to the immobilized affinity probe is captured and becomes immobile (~30% for AR1, 85% for AR2). The rest of the target continues to migrate focused in ITP. This cleanly separates the target components, with a resolution increasing linearly with time [3]. We then elute the captured portion of the target (at 270 s for AR1, 490 s AR2) by increasing the current to an elution current of 800 μA . Upon application of higher current the temperature inside the column increases (see SI Sections SI 3-5) beyond the melting temperature of the target-probe hybrid, melting off the target. The observed target fluorescence intensity near the leading edge quickly decreases (time constant: 15 s for AR1, 11 s for AR2, see Figure B.2, main text) and over 95% of the target is eluted. The target then quickly migrates through the TE and catches up with the LE-TE interface, ready to repeat the capture and elution processes. 221

Figure C.1. Schematic showing preparation of the inhibitor removal column and purification of monomers. Step 1: Pack a small piece of a cotton sponge into the neck of a 5.75 in Pasteur pipette. Step 2: Fill the three-fourths of the pipette body with inhibitor removal beads and place a small piece of a cotton sponge on top of the beads. Step 3: Apply monomer solution to the column. Step 4: Use a pipette bulb to apply gentle pressure and flow the monomer solution through the column..... 233

Figure C.2. Custom built UV polymerization setup. The setup consisted of a UV LED panel controlled by a timer (not shown), panel supports, an aluminum plate mirror, a polycarbonate stage for capillaries, and a cardboard enclosure (not shown). To perform UV polymerization, we placed capillaries on the stage, covered the UV LED panel with the enclosure, and turned on the timer to turn on the UV LED. The timer automatically turned off the UV LED once polymerization time was reached. 235

1 Introduction

Development of micro total analysis systems (μ TAS) has the potential to revolutionize the fields of healthcare, agriculture, and environmental monitoring by rapidly and inexpensively gathering a large amount of previously inaccessible information about respective samples [5, 6]. Integration of sample preparation into μ TAS represents one of the remaining challenges towards achieving portable and point-of-care total analysis devices [7]. Often, the analyte of interest is present in low amounts and is accompanied by a highly complex matrix within the sample. This often inhibits analyte quantitation directly from the raw sample. Thus, automated isolation, purification, and preconcentration of a particular analyte or a set of analytes is desirable for most samples.

The current work deals with developing a rapid affinity purification and preconcentration method compatible with μ TAS. Typical fundamental steps constituting analysis in a total analysis system include mixing, chemical reactions, analyte concentration, analyte separation and subsequent detection. A convenient way of integrating and controlling these fundamental steps in a μ TAS is by using electrokinetic transport, i.e., the transport of fluid, particles, and chemical species using electric fields. Employing electrokinetic transport in μ TAS often obviates the need for moving parts and additional (e.g., pneumatic) controllers between the fluidic system and the electronic control system of the device. The current work leverages an electrokinetic phenomenon of ion-concentration shock waves to accelerate and control an affinity reaction and subsequent separation in a porous polymer monolith (PPM) [3, 8].

This chapter first introduces fundamental concepts of ion concentration shockwaves (isotachopheresis, ITP). We follow this by a fundamental review of PPM synthesis, focusing on controlling monolith pore size. We then briefly review surface functionalization of poly(glycidyl methacrylate-co-ethylene dimethacrylate) (GMA-co-EDMA) PPM. Lastly, we present the scope and main contributions of the thesis at the end of the chapter.

1.1 Ion concentration shockwaves (isotachopheresis)

ITP is an electrophoretic technique that leverages multiple electrolytes to concentrate and separate ions of interest [9-11]. ITP has a wide range of applications and has been applied to extract and quantify analytes from various samples including soils, foods, and biological samples [12-16]. ITP has also been used to preconcentrate analytes prior to separation by CE (to increase CE resolution and sensitivity) [17]; and recently to accelerate and control chemical reactions [3, 8, 18-23]. Figure 1.1 shows a schematic of a typical ITP experiment. Initially the sample, containing ions of interest, is placed between a leading electrolyte (LE) and a trailing electrolyte (TE). The LE consists of a leading ion of the same charge but higher absolute electrophoretic mobility as the ion of interest in the sample and a counterion (an ion opposite charge to leading ion) [11]. Similarly, the TE consists of a trailing ion of the same charge but lower absolute electrophoretic mobility as the ion of interest in the sample and a counterion. Usually the counterion of the LE and the TE are the same. An electric field is applied such that the sample ion moves in the direction towards the LE. The conductivity of the LE is higher than that of the TE due to the mobility of the leading ion being higher than that of the trailing ion. Additionally, while during migration the concentration of the LE remains the same as was initially, the TE

concentration adjusts to a lower ionic strength value. The adjusted TE concentration is set by the LE, such that the velocity of the LE-TE interface is equal to the quotient of the difference of the flux of a particular ion (between LE and TE) and the difference of the concentration of that ion (between LE and TE). (This is a jump condition similar to Rankine–Hugoniot jump condition in compressible flow [24]; the ion-concentration shock occurs at the interface between the LE and the TE). Therefore, the electric field in the LE is lower than that in TE. (Note that LE and TE carry the same ionic current due to current continuity). This causes the velocity of the leading ion, trailing ion, and the sample ions to be the same everywhere in the system. Hence the name isotachophoresis, in which "isos" means "equal" and "takhos" means "speed" [9]. This also causes the interface between the LE and the TE (or between any zones, see Section 1.1.1) to be self-sharpening. For example, if the slower trailing ion diffuses into the LE, it finds itself in a low electric field and so falls back into the TE zone. On the other hand, if a faster leading ion diffuses into the TE, it finds itself in a high electric field, and so accelerates back into the LE zone. This sharpens the interface between the LE and TE and so the interface width depends on the balance between diffusion (or dispersion) and electromigration [22, 25, 26].

1.1.1 Peak-mode vs. plateau mode

Sample ions of interest focus between the LE and the TE since they have a mobility intermediate between that of the leading and trailing ions. If the total amount of sample ion of interest is less than the product of adjusted concentration for that ion (via the jump condition) and the volume of the LE-TE interface (the shock layer) then the ion focuses at the interface. The focused ion occupies a space roughly equal to the volume of the LE-TE interface (shock layer). When the target zone is visualized, it appears as a sharp peak, hence

this mode is termed “peak mode” [27] (see Figure 1.1c and d). Since the initial volume occupied by the ion (the sample volume) is likely to be several orders of magnitude larger than the LE-TE interface volume, ITP greatly concentrates the sample ion of interest. For example, Jung et al. demonstrated over million fold increase in analyte concentration with ITP [28]. Note again if this ion diffuses out of the LE-TE interface into the LE zone, it finds itself in a lower electric field, and so it falls back. Similarly, if this ion diffuses into the TE zone, it finds itself in a higher electric field and so accelerates back into the LE-TE interface.

On the other hand, if the total amount of sample ion of interest is greater than the product of adjusted concentration for that ion and the volume of the LE-TE interface, then the ion creates its own wide zone between the LE and the TE. The concentration of the ion in the zone is set by the jump condition. The width of the zone is determined by the concentration of the ion and the total amount of ion in the sample. When visualized, the target ion zone appears as a wide region, hence this mode is termed “plateau mode” [27] (see Figure 1.1e and f). When the total amount of sample ion in the sample is greater than what the LE-TE interface can accommodate and when the adjusted ion concentration is higher than the soluble concentration, the species of interest may precipitate. Such situations should be avoided.

1.1.2 Finite vs. semi-infinite injection

Samples can be introduced into ITP either via finite or semi-infinite injection. In finite injection, the sample is placed in a reservoir sandwiched between the LE and the TE (see Figure 1.1a). In this injection scheme, sometime after starting ITP, the TE electrophoretically fills the sample chamber, while all the sample ions of interest (with

intermediate mobilities between the leading and trailing ions) fill the space where LE used to be. This ensures that after some time these sample ions form steady spatial distributions and are therefore either separated from one another or can now be reacted all at once with, for example, immobilized reactants downstream. The two main advantages of finite injection are that all the ions of interest in the sample focus in ITP; and that the ITP system is highly insensitive to sample ionic strength or composition. One drawback of finite injection is the need for a special reservoir for the sample in the ITP system.

An alternative to finite injection is semi-infinite injection. In semi-infinite injection, the sample is usually mixed with the TE (although can be mixed with LE, or both TE and LE in special circumstances) (see Figure 1.1b). The sample ions of interest, having higher mobility than the trailing ions, overspeed the trailing ions and focus at the LE-TE interface. This focusing continues, and the sample ions are never fully depleted (and therefore recovered) from the TE reservoir. This method can be used only with samples of relatively low ionic strength. Once the sample is mixed with the TE, the trailing ion has to be the major component (approximately > 75%) of the mixture. High electrophoretic mobility background (matrix) ions in the sample (e.g. chloride) should also be in lower concentrations than the target ions. This presents a problem for biological samples, as many physiological fluids contain high concentration of chloride. Hence, this scheme may not be directly compatible with certain important samples. The main advantage of semi-infinite injection scheme is that it is easier to implement since the semi-infinite injection ITP system does not need a special sample reservoir.

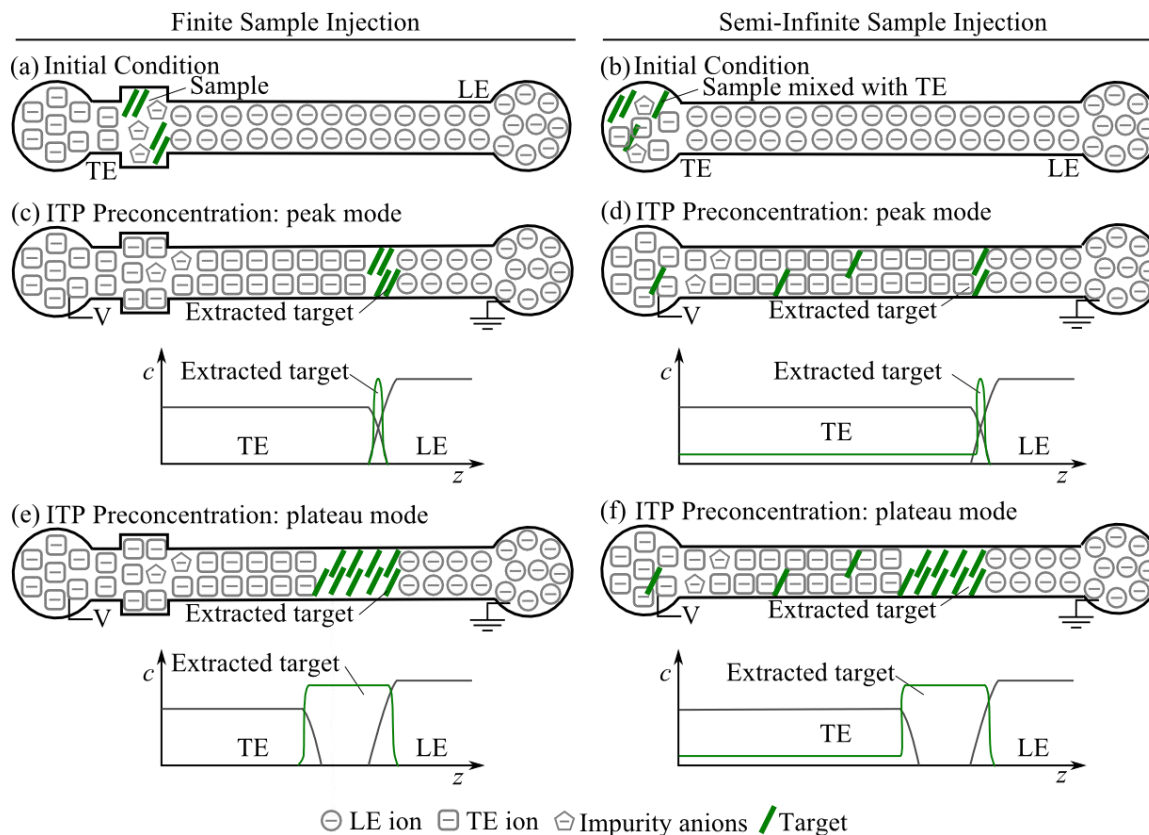


Figure 1.1 Schematics illustrating isotachophoretic focusing of a target using finite (a,c,e) and semi-infinite injection schemes (b,d,f). (a) In a finite injection scheme the sample containing the target is placed in a sample reservoir located between a trailing electrolyte (TE) reservoir and the separation channel filled with leading electrolyte (LE); this channel connects to an LE reservoir. (b) In semi-infinite injection scheme, the sample is mixed with the TE and placed into the TE reservoir. This reservoir connects to the separation channel (filled with LE), which connects to an LE reservoir filled with LE. (c and d) For peak mode ITP, the target is focused into a narrow peak at the interface of LE and TE. The peak width is roughly the width of the LE-TE interface. (e and f) In contrast, in plateau mode ITP the target is focused into a wide zone, much wider than the LE-TE interface width.

1.2 Synthesis of porous polymer monoliths (PPM)

1.2.1 Background and applications of PPM

Porous polymer monoliths were first demonstrated by Tennikova et al. in 1990 [29] and since then have found a wide range of applications in chromatography, solid phase

chemistry, catalysis [30, 31], hydrogen storage [32], electroosmotic pumps [33], and water management in fuel cells [34, 35]. While packed beds can be and have been traditionally used for some of these applications, porous polymer monoliths offer the advantage of a more controllable porous structure that varies less with device history and possess better mass transfer properties [31, 36, 37]. Porous polymer monoliths possess a mechanically stable matrix that persists both when the monolith is swollen and when the monolith is dry [38]. The mode pore size for these monoliths can range from 10 to 10,000 nm and they can have monomodal or multimodal pore distributions [39]. Additionally, PPM can be fabricated with hydrophobic, hydrophilic, ionizable, and zwitterionic pore surface chemistries [36]. Furthermore, grafting may be employed [36] to obtain a monolith with, for example, hydrophobic bulk core and hydrophilic pore surface (or the opposite) if desired. Porous polymer monoliths are generally synthesized via radical polymerization of monomers and crosslinkers (a crosslinking monomer); however, polycondensation and polyaddition preparation methods have also been demonstrated [40]. Preparation of porous polymer monoliths has been extensively reviewed in [40].

One of the most important properties of the monolith for many applications is pore size and pore size distribution. Pore size and pore size distribution affect the hydrodynamic resistance of the structure and control the monolith's specific surface area. The pore size of the monolith is typically controlled by controlling the phase separation between the solid polymer phase and the solvent. This in turn is controlled by the rate of polymer growth and polymer precipitation (and nuclei formation) in the solvent [31]. These rates are controlled by the choice of solvent mixture, monomer and crosslinker type, polymerization temperature, initiator concentration and decomposition rate [31]. Other factors that affect

pore size and distribution include polymerization time [39] and confinement of the polymerization [30, 41].

In this section, we will focus on the methods to control the mode pore size via choice of porogen solvent, monomer and crosslinker type and their ratio, the temperature of polymerization and the choice and concentration of the initiator. We will specifically review only polymer monoliths synthesized via free-radical polymerization in a closed non-stirred vessel with a single phase solvent (no surface tension). While this introductory section is not meant to be an exhaustive review of porous polymer monolith synthesis via radical polymerization, it means to give a set of rules along with a table that a researcher can use to select the correct system in order to obtain a porous monolith with the desired pore size. Therefore, we first describe the mechanism of polymer monolith formation. We then describe the effects of altering porogen and crosslinker concentrations, temperature, and initiator concentration on the polymer monolith, thus developing a set of rules for tailoring existing porous monolith chemistries to obtain desired properties. We aggregate over 100 different existing polymerization conditions that produce pore sizes from 10 nm to 10,000 nm. This allows us to compare monolith synthesis practices across many different synthesis efforts and conditions, rather than over only a few conditions as is done in the current literature. Finally, we compare the trends from these synthesis efforts to the predicted trends and attempt to qualify and quantify these trends based on data from reviewed literature.

1.2.2 PPM synthesis theory

1.2.2.1 Formation of porous polymer monoliths

We here consider only porous polymer monoliths synthesized via free radical polymerization in bulk with a system consisting of a monomer (monovinyl functional monomer), crosslinker (divinyl or other crosslinking monomer), radical initiator, and a porogenic solvent. We also only consider cases where the polymerization reaction reaches steady state. The mechanism of porous monolith formation is as follows: The free radical initiator decomposes at a particular temperature either spontaneously or due to UV, gamma radiation, or electron beam radiation [39, 40]. These radicals start the polymerization reaction. The decomposition step is usually one with the highest activation energy and thus is most affected by temperature [39]. The polymer chains then grow and precipitate out of solution once the chain reaches a certain size. This size is determined by the solubility of the polymer in the porogen solvent, and thus is determined by choice of porogen, monomer, and crosslinker. The precipitated polymer chains thus form nuclei. The monomers are generally thermodynamically better solvating agents for the polymer than the porogen. Thus, the monomers position themselves around the nuclei as much as possible. Therefore, while polymerization continues within both the solvent bulk and on the surface of the nuclei, since more monomer is present near the nuclei, polymerization predominates there. Polymer molecules that are formed in solution are captured by the growing nuclei. The growing nuclei thus form globules. However, the crosslinked nature of the nuclei (globules) prevents the globules, once they meet each other, from coalescing into one structure. The globules instead form clusters with spaces between the globules, which form "mesopores" (see Figure 1.2). These clusters associate further to form the monolith. Voids

between the clusters form "macropores." Sometimes the globules themselves may be also porous and these pores are termed "micropores". Some polymer chains may be captured by multiple globules and even multiple clusters, enhancing mechanical properties of the monolith. The voids in the structures of the monolith capture the porogen solvent. Once the porogen solvent is removed, this volume becomes the pore space. Thus percent pore volume is directly related to the porogen volume fraction [39]. The presence of voids on three scales often results in monoliths that have multimodal pore distributions. While this complicates the concept of "pore size," this often results in monoliths with both high surface area (due to small pores) and low hydrodynamic resistance (due to large pores), features that are usually desired in many applications. Here (and in majority of the literature reviewed in this section) we will be concerned with pores due to voids between the globules and assume that this is the dominant pore size (the mode measured pore size).

1.2.2.2 Controlling pore size with porogenic solvent system

One way to control the pore size is through manipulation of the thermodynamic quality of the porogenic solvent system in relation to the monomer - crosslinker system. The porogen solvent system generally consists of a thermodynamically good and thermodynamically poor solvent mixed as to create a miscible solvent system that would precipitate the growing polymer at a specific polymer size. The system may also consist of a single solvent [40]. The more thermodynamically poor the porogen is, the earlier (at

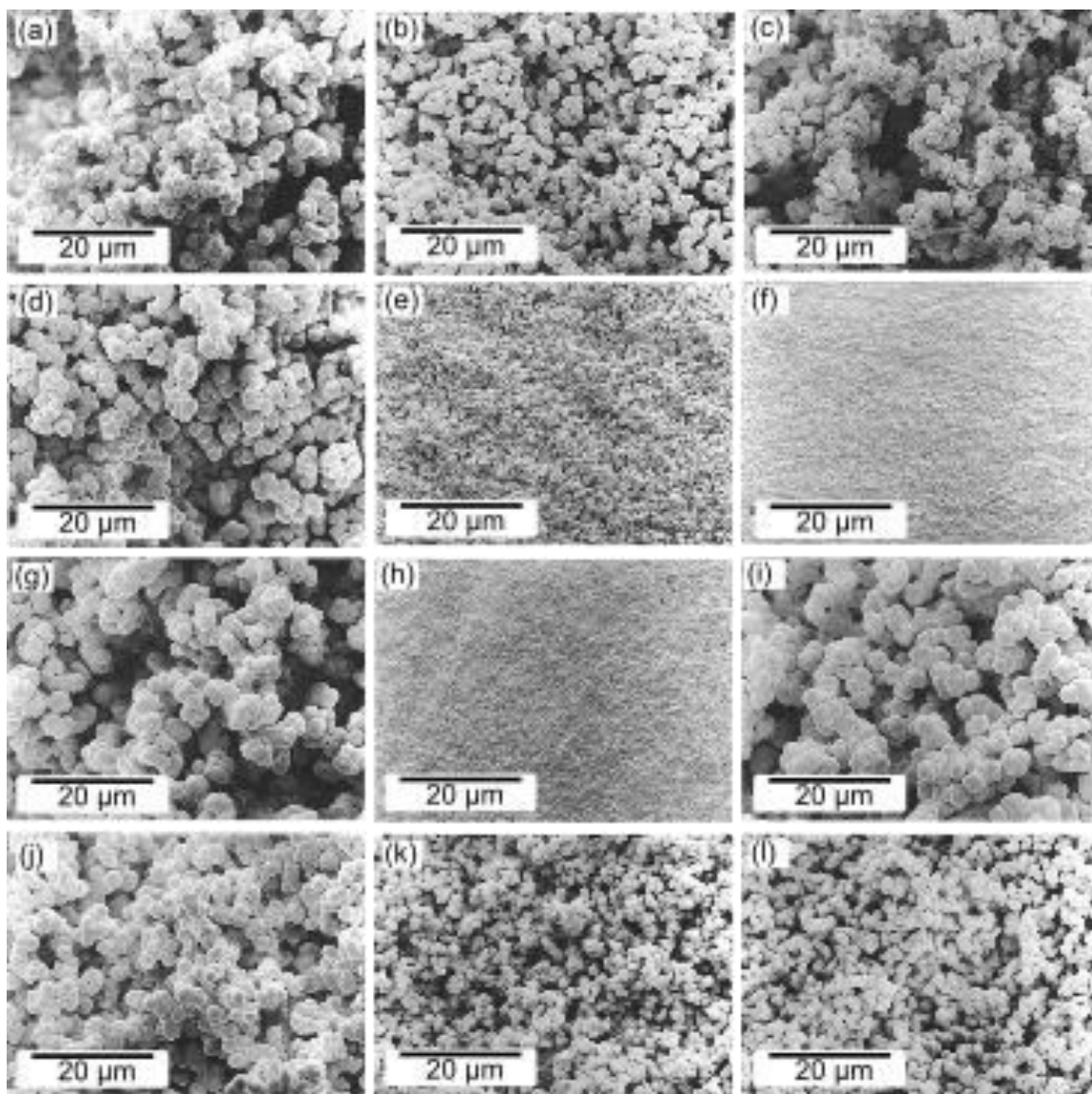


Figure 1.2. Scanning electron micrographs of porous polymer monoliths synthesized by Viklund et al. [1]. These correspond to monoliths in Table 1.1a (see Supplementary Information, Chapter 1), lines 25-36. (a corresponds to line 25, b to line 26 and so forth). Porous polymer monoliths are composed of globules and the size of the globules controls the size of the void spaces between them (i.e., pore size). The size of the globules (hence pore size) can be varied with solvent composition, crosslinker and monomer concentrations, temperature, and initiator concentration.

smaller nuclei size) the phase separation occurs [31]. At first glance, since there is a limited amount of monomer, this should result in a larger number of smaller globules, and thus smaller voids between the globules and smaller pore size. However, since the solvent is thermodynamically poor, instead of more nuclei forming in the solvent phase, the monomers, being better solvents for the polymer, concentrate around the already formed nuclei. Thus, these nuclei grow into globules and instead of obtaining many small globules, a small number of large globules results. Since the globules are larger, the voids between them are larger, and so the pore size is larger as well. Thus, the more thermodynamically poor the porogen system, the larger the pore size [31].

1.2.2.3 Controlling pore size with cross-linking monomer

Another way to control the pore size is through manipulation of the ratio of monomer to crosslinker. Increasing the amount of crosslinker leads to increased crosslinking of the polymer. This decreases the polymer solubility and leads to precipitation and nuclei formation at smaller chain size. However, unlike with the thermodynamically poorer porogen solvent, the monomers are more or less highly soluble in the solvent and are poorly soluble with the highly crosslinked polymer. Thus, there is a lower concentration of monomers around the nuclei, and so as a result of early precipitation and limited amount of monomer, many small nuclei form. These grow into a large number of small globules, which in turn have small voids between them. Thus increasing crosslinker concentration at the expense of monomer concentration decreases monolith pore size [31].

1.2.2.4 Controlling pore size with polymerization temperature

Temperature affects the polymerizing system and thus the pore distribution mainly in two competing ways. Temperature affects the rate of free radical initiator decomposition, while simultaneously changing the thermodynamic quality of the solvent. The higher the reaction temperature, the larger the number of free radicals produced [38]. Typically, it is the initiation step that has the highest activation energy and thus temperature affects the initiator decomposition the most [39]. Thus, at higher temperatures a larger number of nuclei and eventually globules are formed. Since a specific polymer mixture has a specific amount of monomer, if more globules are produced, the globules are smaller. Since packing of smaller globules leads to smaller voids, smaller pore sizes are expected from the increase of number of free radicals produced. Thus, through this mechanism, an increase in temperature should yield a smaller pore size [38].

On the other hand, the effect of temperature on solvent quality and polymer-solvent solubility relationship suggests the opposite effect on pore size. With the exception of polymers with a lower critical solution temperature, polymer solvent mixing is an endothermic process. Thus, increasing the temperature increases the amount of energy available for dissolution and so promotes the dissolution of polymers and delays precipitation. As a result, the nuclei grow to a much larger size before precipitation, and thus the resulting globules are larger. This in turn yields larger voids and larger pore size. Thus, through this mechanism, an increase in temperature should yield a larger pore size [38].

Both effects are experimentally observed [31] and the polymer-solvent solubility determines which effect dominates. For good solvents it appears that the radical initiator

concentration effect is more dominant, while for systems with a poor solvent, the polymer-solvent solubility effect is the dominant one [31]. The advantage of using temperature to control monolith pore size is that this control does not require any change in the composition of the reaction mixture. However, the disadvantage of using temperature to control pore size is that one usually does not initially know whether the radical initiator concentration effect or the polymer-solvent solubility effect will dominate at each temperature for a new polymer system.

1.2.2.5 Controlling pore size with initiator concentration and decomposition rate

The effect of initiator concentration and decomposition rate on monolith pore size is similar to the temperature radical initiator concentration effect. The larger the initiator concentration and/or the larger the decomposition rate of the initiator, the larger the number of free radicals produced. Thus there is a larger number of nuclei produced and larger number of globules produced. Since a specific polymer mixture has a specific amount of monomer, if more globules are produced, the globules must become smaller, and thus form smaller voids. Therefore, increasing initiator concentration or employing an initiator with a higher decomposition rate leads to smaller pore size [38].

1.2.3 Discussion

Here we describe the some efforts to synthesize porous polymer monoliths and compare the trends observed in these efforts to the rules predicted in Section 1.2.2. Qualitatively, as predicted, porous polymer monoliths are composed of globules and the size of the globules controls the size of the void spaces between them (i.e., pore size) (see Figure 1.1). The size of the globules (hence pore size) can be varied with solvent

composition, crosslinker and monomer concentrations, temperature, and initiator concentration. Hence pore size can be varied from 10 to 10,000 nm.

1.2.3.1 Effect of porogen solvent on pore size

In synthesis of porous polymer monoliths a variety of solvent systems and single porogen solvents have been used. Cyclohexanol - dodecanol system appears to be the most popular one and has been very widely used [4, 41-45] (however, only [4, 41, 42] report direct pore size information - others report other useful information such as capacity for electroosmotic flow). Another popular solvent is methanol, and it is used both alone and in combination with other solvents [2]. The effect of porogen solvent thermodynamic quality has been widely investigated [1, 2, 4, 31, 39]. Viklund et al. 1996, Viklund et al. 1997, Hilder et al., and Svec et al. demonstrated that increasing the fraction of the thermodynamically poor solvent generally leads to larger pore size [1, 31, 39, 46], which agrees with the prediction of Section 1.2.2.2. However, depending on the solvent and the monomer system solvent volume fractions of poor solvent as low as 3% to as high as 80% (of the total porogen volume) are used [31]. Yu et al. and Eeltink et al. determined the relationship between volume fraction of thermodynamically poor solvent and pore size [2, 4]. Both found that pore size rises sigmoidally with increasing volume fraction of thermodynamically poor solvent [2, 4] (see Figure 1.3). In other words, the increase in pore size at low volume fractions of poor solvent is small, then the increase in pore size becomes rapid, and then the pore size levels and the increase in pore size becomes small again. However, this relationship, is not always valid: Yu et al. also found for some systems, the pore size rises with increasing volume fraction of poor solvent, peaks, and then decreases again [2]. This may be explained by the fact that for these systems the

thermodynamic quality of the porogen system is not given by the linear combination of the volume fractions of the constituent solvents weighted by their thermodynamic quality. Thus, to alter the pore size in the correct direction, one has to first determine which region of the curve one is currently operating in. In addition, for sigmoidal shaped curves, one can take advantage of both the slowly changing pore size and the dramatically changing pore size regions. The dramatically changing regions can be used to easily control the pore size of the monolith when one has good control over volume fraction of solvents. However, many solvents used in porous polymer synthesis are somewhat prone to evaporation (and not at the same rate) at synthesis temperatures. Thus for situations where solvent evaporation and thus solvent fraction is difficult to control, one may wish to operate at the flat regions of the sigmoidal curve. For such cases, to change the thermodynamic quality of the solvent system, one can either chose a different the thermodynamically poor or thermodynamically good solvent. To this end, Yu et al. varied the solvents in the porogen system to control pore size [2] (lines 57-77 in Table 1.1). While Yu et al. do not include the solubility parameters for these solvents, we add these to Table 1.1. For the methanol - coporogen system, while one would expect that as the solubility parameter of the coporogen becomes closer to methanol (the thermodynamically poorer solvent) the pore size should increase. However, this is not the observed case. This is likely because while the volume fractions for the solvents are the same in each case, they did not correspond to the same regime (e.g., rapidly vs. slowly changing pore size) of the poor solvent volume fraction vs. pore size curve. In other words, for one solvent system this volume fraction corresponds to an initial plateau region, but corresponds to the rapidly rising region of the curve for another system.

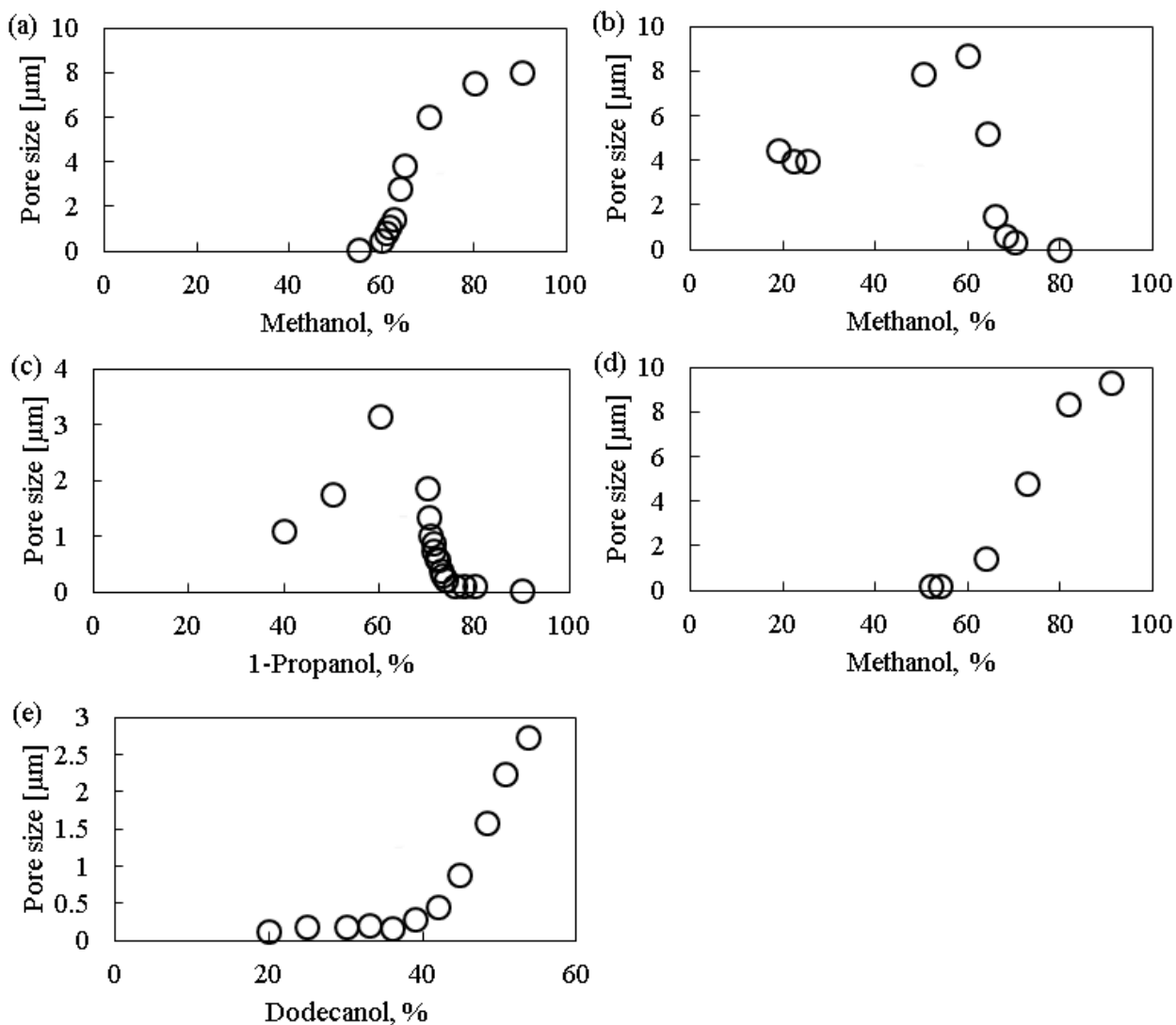


Figure 1.3. The relationship between volume fraction of thermodynamically poor solvent and pore size for (a) poly(glycidyl methacrylate-*co*-ethylene dimethacrylate), (b) poly(2-hydroxyethyl methacrylate-*co*-ethylene dimethacrylate), (c) poly(butyl methacrylate-*co*-ethylene dimethacrylate-*co*-[2-(methacryloyloxy)ethyl] trimethyl ammonium chloride) (d) poly(butyl methacrylate-*co*-ethylene dimethacrylate-*co*-2-acrylamido-2-methyl-1-propanesulfonic acid) investigated by Yu et al. [2] and (e) poly(butyl methacrylate-*co*-ethylene dimethacrylate) studied by Eeltink et al. [4]. Data in (a), (d) and possibly (e) show a sigmoidal relationship between volume fraction of poor solvent and pore size. Data in (b) and (c) show a relationship with a peak in pore size, indicating that the sigmoidal relationship is not universal.

1.2.3.2 Effect of porogen to monomer ratio on pore size

While the porogen to monomer ratio is intended to control the porosity (pore volume/total volume) of the monolith, which it does very effectively [1, 42, 47], it has the

unintended effect of also changing the pore size. Both Danquah et al. and Yu et al. found that increasing the porogen to monomer ratio increases the pore size [42, 47]. This can be explained by the fact that when there is more solvent and less monomer, larger globules are more soluble (as there is more solvent to solubilize them) and thus larger globules form [1]. Formation of larger globules leads to larger interglobular voids and thus larger pore sizes. Only a certain range of porogen to monomer ratio yields a porous monolith: very low ratios produce a non-porous structure, while at very high ratios no solid monomer can be formed [47]. For example, Yu et al. found that for poly(butyl methacrylate-*co*-ethylene dimethacrylate) polymer no monolith forms beyond when methanol (porogen solvent) is 75% of the total polymerization mixture [47].

1.2.3.3 Effect of porogen on initiator decomposition rate and thus pore size

In addition to temperature, solvent has a significant effect on the initiator decomposition rate. For example, for the very commonly used initiator azobisisobutyronitrile (discussed below), decomposition rate ranges from $7.2 \times 10^{-4} \text{ s}^{-1}$ in methyl methacrylate to $9.8 \times 10^{-6} \text{ s}^{-1}$ in toluene at 60°C - almost two orders of magnitude [48]. While the effect of porogen solvent on decomposition rate is not as strong as that of temperature, researchers should be aware of this effect when varying the porogen solvent in attempt to control pore size.

1.2.3.4 Effect of crosslinker concentration on pore size

In synthesis of porous polymer monoliths a wide variety of crosslinkers are used and concentration of crosslinker can be used to control monolith pore size. Ethylene dimethacrylate is by far the most commonly used crosslinker [2, 31, 37, 42, 43, 46, 47, 49-66], but trimethylolpropane [1], divinylbenzene [31] and others [40] have also been used.

Mair et al., Yu et al. Viklund et al. 2006, Viklund et al. 2007 and Danquah et al. all observed a monotonic decrease in monolith pore size with increasing crosslinker to monomer ratio for both ethylene dimethacrylate and trimethylolpropane. Plotting the data of Danquah et al. [42] one observes a roughly inverse relationship of pore size with crosslinker to monomer ratio. This is consistent with the prediction of Section 1.2.2.3 that increasing crosslinker concentration at the expense of monomer concentration decreases monolith pore size.

1.2.3.5 Effect of temperature on pore size

Temperature may also be used to control pore size, and consequently temperature must be carefully controlled to obtain monoliths with reproducible and uniform pore size. Under certain conditions, obtaining a uniform temperature is difficult or not feasible, since the polymerization reaction is exothermic. For example, Peters et al. found that preparation of porous polymer monoliths of 50 mm in diameter (and even at smaller diameters) produced significant temperature variations across the monolith cross section, and significant variations in pore size [67]. However, one may leverage this as an advantage and produce monoliths with a pore size gradient. Another difficulty with controlling pore size using temperature is that temperature controls two competing pore size controlling mechanisms, one or the other being more dominant dependent on polymerization system and temperature.

1.2.3.6 Free radical initiator concentration effect

Increase in temperature increases the initiator decomposition rate. This results in increase in free radical concentration and smaller pore size. The decomposition rate scales exponentially with temperature [48]. Danquah et al., Viklund et al., and Svec et al.

observed the effect that pore size decreases with temperature increase for the majority of the investigated temperature range [31, 38, 39, 42] suggesting that this effect is the more dominant of the two temperature effects. Plotting the data of Danquah et al. [42] one observes a roughly linear decrease of pore size with temperature, while plotting the data of Svec et al., [38] one observes a roughly exponential decay (an initial rapid decrease of pore size with temperature, followed by a leveling of). Thus there is no conclusive quantitative relationship between temperature and pore size.

1.2.3.7 Polymer-solvent solubility effect

Increase in temperature generally improves the thermodynamic quality of the porogen solvent, delaying precipitation and allowing globules to grow to a larger size. When this polymer-solvent solubility effect is dominant, an increase in temperature is expected to yield larger pore size. While this effect dominates far less often, it was still observed by Viklund et al., Svec et al., and Danquah et al. [31, 38, 42] in a poor solvent, or at the lower end of the investigated temperature range. It is expected that this effect may dominate especially at lower temperatures as thermodynamic quality of the solvent becomes poorer at lower temperature, and this effect is dominant in poorer solvents (as explained in Section 1.2.2.4). Unfortunately, this effect has been observed too infrequently to obtain a quantitative relationship between temperature and pore size when this effect dominates.

1.2.3.8 Effect of initiator concentration and decomposition rate on pore size

In synthesis of porous polymer monoliths two types of initiators are commonly used: thermal initiators and photo initiators [40]. Thermal initiators decompose spontaneously at a specific temperature, producing radicals that start the polymerization

reaction. The Polymers Handbook [48] lists a large number of organic free radical initiators and their decomposition rates as a function of temperature in different solvents. Photo initiators are free radical initiators that similarly decompose when exposed to UV (most common), gamma, or even electron beam radiation. All of these have been explored for synthesis of porous polymer monoliths [40].

Azobisisobutyronitrile appears to be the most common initiator for synthesis of porous polymer monoliths [2, 31, 37-39, 42, 50-52, 54-59, 61-63] and is used as both a photo UV initiator and a thermal initiator. The reason why it is so widely used is likely that it is one of the most well characterized radical initiators. The Polymers Handbook lists decomposition rates for this initiator for over one hundred solvent and temperature conditions (including temperature correlations)[48]. Other commonly used UV initiators for porous polymer monolith synthesis include 2,2-dimethoxy-2-phenylacetophenone [4, 43, 46, 47, 49, 53, 60, 64, 66] and benzoin methyl ether [1, 35].

Yu et al. employed 2,2-dimethoxy-2-phenylacetophenone in the study of the effect of increasing initiator concentration on monolith pore size [47] (lines 39-41 in Table 1.1). Yu et al. increased initiator concentration from 3 to 5 wt% (relative to monomers) and observed a decrease in pore size from 1600 to 160 nm as the initiator concentration increased. This is consistent with the prediction of Section 2.5 that increasing initiator concentration leads to smaller pore size.

Viklund et al. qualitatively observed the effect of benzoin methyl ether initiator on monolith pore size [1]. Viklund et al. varied benzoin methyl ether concentration from 0.5 to 3 wt%. For low initiator concentrations, they observed high coalescence of globules and sometimes a failure to form a monolith. This is likely because at low initiator

concentrations, a small number of nuclei are formed, and so the resulting globules are larger. If the globules are too large (and so the voids between them are too large), they may fail to form a solid monolith, possibly because the surface to volume ratio is too small. Viklund et al. also observed that at high initiator concentrations cracks would form in the monolith [1]. This may be explained by the fact that at a large initiator concentration, many nuclei are formed, and so the globules and the pores are small. If the initiator concentration is too high, the monoliths may become solid instead of porous, and would have a propensity to crack. This also suggests that there is only a narrow range of radical concentration that would successfully produce a porous monolith structure. Thus, typically initiator concentration around 1 wt% is used [2, 4, 31, 38, 39, 42, 53].

Svec et al. compared synthesis of porous beads using benzoyl peroxide and azobisisobutyronitrile at 70°C and 90°C [38]. While the mechanism for pore formation in bead polymerization and monolith polymerization differs slightly, the mechanism is similar enough to warrant a comparison [38]. Benzoyl peroxide decomposition rate is slower than that of azobisisobutyronitrile by a factor of 4, and larger pores are observed with benzoyl peroxide than with azobisisobutyronitrile. This is consistent with the prediction of Section 1.2.2.5 that employing an initiator with a higher decomposition rate (azobisisobutyronitrile) leads to smaller pore size.

Thus, the higher the free radical concentration (either due to larger initiator concentration, higher decomposition rate, higher UV flux or other conditions) the smaller the pore size. Therefore, to produce a successful monolith, at lower temperature (or lower UV flux) higher concentration of initiators should be used. On the other hand, at higher temperatures (or higher UV flux) lower concentration should be used.

1.2.4 Summary of PPM synthesis

Porous polymer monoliths can be synthesized with pore sizes ranging from 10 to 10,000 nm, with different pore size distributions and with a wide variety of surface and bulk properties to suit the needs of a particular application. Here we describe the mechanisms of how solvent composition, monomer and crosslinker concentrations, initiator concentration, decomposition rate, and temperature can be used to control pore size. Using each of these variables to control pore size has its own advantages and disadvantages. For example, polymerization temperature is generally easy to control, even dynamically during processing, however its effect on pore size (whether the pore size will increase or decrease) is determined by the composition of the polymerization mixture. Varying initiator concentration seems to be a very promising way to control pore size, as change in pore size is monotonic; however, this method has not been very widely investigated. Controlling the pore size by changing porogen solvent composition seems also promising, as again change in pore size is monotonic; however, one has to beware that solvent composition also affects initiator decomposition rate. Lastly, controlling the pore size by controlling crosslinker composition also appears promising; however, this also changes the monolith chemistry and likely surface properties. Additionally, one has to keep in mind that while changing these variables to affect pore size, other properties of the monolith such as porosity are often affected as well.

To help the reader synthesize a porous polymer monolith with a desired pore size, we provide a table of over 100 synthesis conditions, spanning monoliths with pore sizes from 10 to 10,000 nm (see Table 1.1 in Supplementary Information, Chapter 1). One example of use of this table for a "quick and dirty" synthesis of a polymer with desired

pore size and pore surface chemistry would be first use the table to look up conditions for fabricating GMA-co-EDMA PPM with a pore size close to the desired pore size. Then, one would use the rules provided to slightly alter the synthesis conditions to obtain a desired pore size. Lastly, to obtain desired pore surface chemistry one would graft species of interest onto the pore surface using the epoxy group from the glycidyl methacrylate.

1.3 Functionalization of pore surfaces in GMA-co-EDMA

PPM

Preparation of porous polymer monolith with a specific functional surface by copolymerization of a functional monovinyl or divinyl monomers requires re-optimization of polymerization conditions for each set of functional monomers [68]. This process is often difficult and laborious. Additionally, the functional monomer constitutes both the surface and the bulk of the monolith and so a large number of its functional groups of interest are inaccessible for interactions [68]. A better approach is to graft the pore surface of the monolith with the functional group of interest. GMA-co-EDMA porous polymer monoliths have a surface epoxy group and therefore offer convenient chemistry for altering the pore surface properties of the monolith. Here we briefly review strategies to functionalize the surface of GMA-co-EDMA PPM with small molecules, nucleic acids, and proteins.

1.3.1 Functionalization of GMA-co-EDMA PPM surface with small molecules

Pore surfaces of GMA-co-EDMA PPM can easily be functionalized to produce cation and anion exchange surfaces via reactions of small molecules. Here we give just a few

examples of synthesis of anion and cation exchange columns based on GMA-co-EDMA PPM.

Functionalizing GMA-co-EDMA PPM with 2-chloro-N,N-diethylethylamine hydrochloride (DEAE-Cl) creates a strong anion exchange surface in the PPM. [69, 70] (Figure 1.4a). This reaction introduces quaternary amines on to the surface of the PPM. For example, Danquah et al. performed this functionalization by first washing GMA-co-EDMA PPM with a solution of 0.5 M Na_2CO_3 , 1 M NaCl, pH 11.5 [69]. (The wash buffer should not contain primary amines, as amines may react with surface epoxy groups, and may form unwanted side products on the surface.) They then filled the PPM with a 290 mM DEAE-Cl and allowed the reaction to proceed for 15 hr at 60°C [69]. They then washed the resulting PPM with DI water for 30 min (recommend >100 column volumes) and dried at 70°C under laboratory vacuum. They obtained a ligand density of order 2 mmol/g of PPM (1 M assuming bulk PPM density of ~1 g/ml and 50% porosity) [69, 71].

Functionalizing GMA-co-EDMA PPM with diethylamine produces a weak anion exchange PPM surface [72] (Figure 1.4b). This introduces tertiary amines on the surface of the PPM. For example, Svec et al. obtained this weak anion exchange surface by first washing the PPM with tetrahydrofuran (THF) [72]. Then they pumped pure diethylamine through the monolith (to remove remaining trace THF) and allowed the monolith to react with diethylamine for 8 hr at 70°C [72]. They then washed the resulting monolith with water, and then 10 mM Tris-HCl buffer pH 7.6 [72]. They obtained a ligand density of order 3 mmol/g PPM [72]. Bruchet et al. gives an alternative, higher yield synthesis protocol using ethanol water solution of diethylamine in place of pure diethylamine [73].

Sulfonation of GMA-co-EDMA PPM with sodium sulfite produces a strong cation exchange surface [74-76] (Figure 1.4c). This introduces sulfonate groups on the monolith surface. For example, Ueki et al. performed this functionalization by washing the PPM with ethanol and then with water to remove remaining porogenic solvent and unreacted monomers [74]. Subsequently, they pumped 1 M sodium sulfite into the PPM and allowed the monolith to react at 75°C for 12 hr [74]. They then washed the monolith with 10 mM nitric acid and then water [74]. They obtained a ligand density of order 100 mM [74].

Functionalization of GMA-co-EDMA PPM first with ethylenediamine and then with chloroacetic acid creates a weak cation exchange surface [77-79] (Figure 1.4d). This introduces carboxylic groups onto the surface of the monolith. For example, Wei et al. obtained a weak cation exchange surface by first washing the PPM with THF to remove remaining porogenic solvent and unreacted monomers [78]. They then pumped ethylenediamine into the PPM and allowed the reaction to proceed at 80°C for 24 hr [78]. Subsequently they washed the monolith first with dioxane/20% NaOH (3:2, v/v), second with dioxane/water (3:2, v/v), third with pure dioxane, and lastly with pure ethanol [78]. Next they pumped 14% chloroacetic acid pH 11 into the monolith and allowed this reaction to proceed at 70°C for 24 hr [78]. They then washed the monolith with 5 mM acetate buffer [78]. They obtained a ligand density of order 0.4 mmol/g PPM [78].

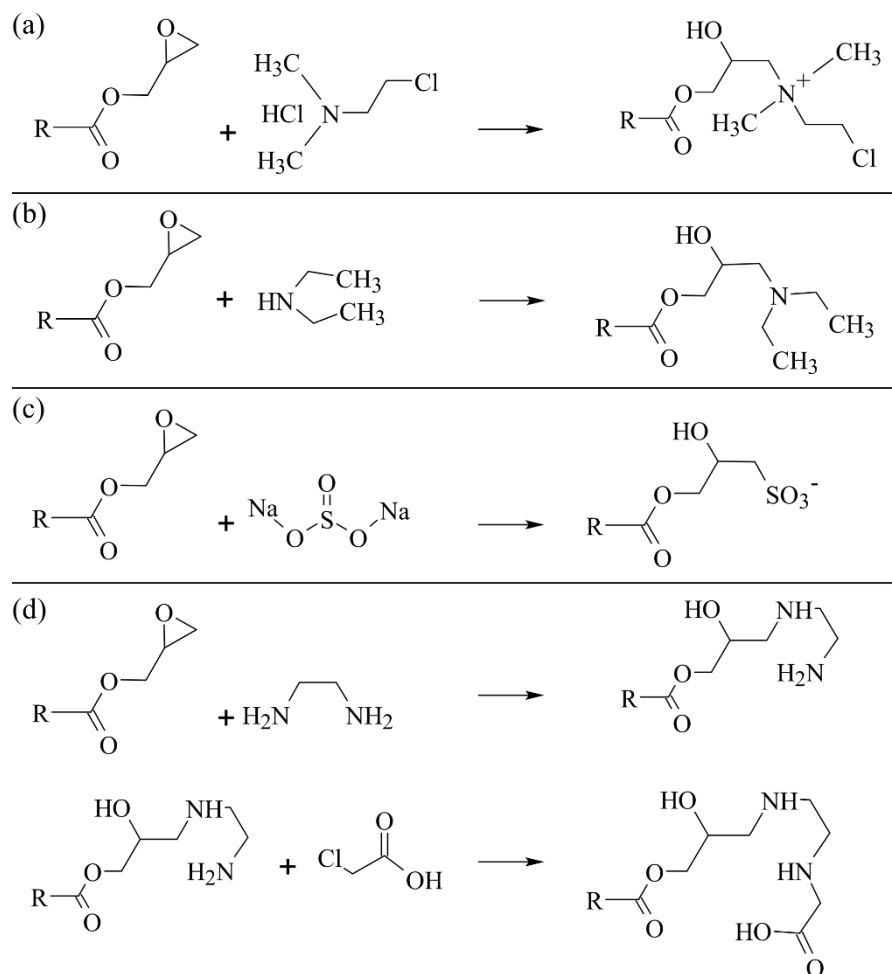


Figure 1.4. Functionalization reactions of GMA-co-EDMA PMM to obtain (a) strong anion exchange surface (b) weak anion exchange surface (c) strong cation exchange surface and (d) weak anion exchange surface. R represents the bulk of the porous polymer monolith. (a) GMA-co-EDMA reacts with 2-chloro-N,N-diethylethylamine hydrochloride to produce a quaternary amine surface. (b) GMA-co-EDMA reacts with diethylamine to produce a tertiary amine surface. (c) GMA-co-EDMA reacts with sodium sulfite to produce a sulfonate groups on the monolith surface. (d) GMA-co-EDMA reacts with ethylenediamine and then with chloroacetic acid to produce carboxylic groups on the surface of the monolith.

1.3.2 Functionalization of GMA-co-EDMA PPM surface with nucleic acids

Oligonucleotides can be immobilized on epoxide-bearing surfaces via nucleophilic and electrophilic groups covalently attached to the oligonucleotides. Such groups include

aminoalkyl, mercaptoalkyl, aminooxyalkyl, phosphoryl, and thiophosphoryl [80]. However, we here concentrate on immobilization of nucleic acids via the aminoalkyl group as it is the only functional group so far demonstrated to couple oligos to GMA-co-EDMA PPM [8, 81-83]. Specifically we will compare DNA immobilization protocols of Satterfield et al. [82], West and Satterfield [83], and Sinitsyna et al. [81].

Satterfield et al. immobilized 30 nt DNA oligos on GMA-co-EDMA PPM to perform affinity purification of RNA [82]. To start the immobilization, they first washed the PPM with diethylpyrocarbonate treated water [82]. Satterfield et al. then filled the monolith with an immobilization solution consisting of 500 μ M 5'NH₂-C₆ oligo solution in 10 mM phosphate buffer, 500 mM NaCl, and 0.05-0.1% sodium dodecyl sulfate (SDS) [82]. They then allowed the immobilization reaction to proceed for 1 hr at 90°C [82]. Finally, unreacted epoxide groups on the monoliths surface were blocked with 100 μ l of 10 mM Tris-HCl buffer with 180 mM NaCl and 0.1% SDS at 120°C for 30s [82]. Satterfield et al. found that reaction temperature had a dramatic effect on the concentration of immobilized DNA. For example, when they increased the reaction temperature from 60°C to 90°C, they observed a doubling of immobilized DNA concentration [82]. Additionally, they observed that the resulting functionalized monoliths could be stored for weeks without any decrease in immobilized DNA concentration [82]. This is also consistent with our observations.

West and Satterfield follow a similar protocol [83] but with a different immobilization buffer and higher immobilization temperature. West and Satterfield used an immobilization solution consisting of order 500 μ M 5'NH₂-C₆ DNA oligos in 3x saline-sodium citrate (SSC) buffer with 0.05% SDS [83]. They then denatured any oligo

secondary structure by heating the solution at 95°C for 5–10 min and then introduced the immobilization solution into the monolith [83]. They allowed the immobilization reaction to proceed at 120°C for 30 min [83]. Finally, they washed the resulting PPM with 30 column volumes of 3x SSC 0.05% SDS buffer [83]. Similar to Satterfield et al. they observed that the DNA functionalized PPM can be stored without noticeable DNA degradation for up to 6 months [83].

Sinitsyna et al. compared the effect of temperature, time, and buffer on DNA oligo immobilization onto the surface of GMA-co-EDMA PPM [81]. After washing the PPM, they filled the monolith with 10-50 μ M 48 nt DNA in either (a) 0.01 M sodium borate buffer, pH 9.4 or (b) 3x SSC, pH 7.0 [81]. They then allowed the reaction to proceed first at 80°C for 1 to 3 hr, followed by an incubation at room temperature for 0.5 to 14 hr [81]. Following the immobilization, they washed the monolith with 0.2% SDS and then with water and blocked the surface with either (a) 1% bovine serum albumin (BSA), 6x SSC, 0.1% SDS or (b) 50 mM ethanolamine 0.1 M Tris pH 9.0, 0.1% SDS or (c) fresh solution of 0.55 g of succinic anhydride (SA) in 34 mL of DMSO and 2 mL NaHCO₃, pH 9.4 [81]. They allowed the blocking reaction to proceed for 45 min at 42°C for the BSA blocking solution, and at room temperature for the other two [81]. Sinitsyna et al. observed over 2x higher immobilized DNA surface concentration using 3x SSC, pH 7.0 than using the 0.01 M sodium borate buffer as the immobilization buffer [81]. Furthermore, they saw an increase in immobilized DNA surface concentration with increasing initial concentration of DNA in the immobilization buffer [81]. They observed an increase in immobilized DNA surface concentration with increasing reaction time but saw no increase immobilized DNA surface concentration after 2 hr [81]. BSA and ethanolamine blocking

solutions consistently outperformed the succinic anhydride blocking solution, and BSA based blocking solution slightly outperformed the ethanolamine one [81]. Sinitsyna et al. work suggests using 50 μ M DNA in 3x SSC, pH 7.0 as the immobilization solution, allowing the immobilization reaction to proceed for 2 hr at 80°C for DNA immobilization [81]. This recommendation is consistent with the protocol recommended by West and Satterfield.

1.3.3 Functionalization of GMA-co-EDMA PPM surface with proteins

Functionalizing the pore surface of GMA-co-EDMA PPM with proteins is useful for preparation of affinity chromatography substrates [84] and enzymatic microreactors [85]. The protein attaches to the PPM surface either through a direct reaction with epoxide groups or via specialized functional groups grafted onto the monolith surface. Both classes of methods rely on the reaction of the protein's primary amine groups on amino acid side chains (e.g., that of lysine) or the terminal amine of the protein. Hence, the protein must have these amine groups accessible on its surface for a successful immobilization. We here will briefly review reaction conditions only for the direct monolith-protein coupling via epoxide group method.

1.3.3.1 Direct coupling of proteins to monolith surface via the epoxide group

Direct coupling of a protein with the monolith's epoxide groups is the simpler functionalization method, as it requires only a single reaction step and thus potentially resulting in higher concentration of protein on the surface. However, proteins with less accessible amine groups are likely to have a lower attachment yield due to steric hindrance from the monolith surface.

Direct protein immobilization typically begins with a wash of the synthesized PPM with first a porogenic solvent, then with a porogenic solvent-water mixture, and lastly with pure DI water and/or buffer. This first removes unreacted monomers and then removes the remaining porogenic solvent. For example, Vlakh et al. washed their synthesized PPM with ethanol, ethanol–water (1:1) mixture, pure water, and lastly with 0.1 M sodium carbonate buffer (pH 9.3) [86]. Next, a buffered solution with the protein of interest is introduced into the monolith. Typically, the buffer is either a sodium carbonate buffer with pH 9.3-10.5 [84-91] or sodium borate buffer with pH 8-10 [90, 92, 93]. The buffer should have as high a pH as the protein will tolerate without degradation to ensure the lysine's side chain primary amine ($pK_a = 10.7$ [94]) is not protonated. This ensures that this amine is able to mount a nucleophilic attack on the terminal carbon of the monolith's epoxy function and complete the attachment reaction [95]. Initial protein concentration in the buffer usually ranges from 1-10 mg/ml [84-93]. Typically, the protein immobilization reaction proceeds for 16-24 hr at 30-37°C [84, 86, 87, 92, 93] or for 24-48 hr at room temperature [88-90]. Third, the resulting monolith is washed to remove any unbound protein. Typically this buffer is the same as the protein immobilization buffer but without the protein [86, 96]. Lastly, the residual epoxide groups are blocked and the blocking solution is washed out of the monolith. Typical blocking solutions include 1 M ethanolamine [84, 87, 90, 91]. Ethanolamine blocking reaction typically proceeds for 1 hr at room temperature [84, 87]. Other blocking solutions include 1 mg/ml aspartic acid [85], 200 mM Tris-HCl buffer (pH 8.0) [85] and 5% milk solution [92]. The blocking solution is typically washed from the monolith using a storage buffer (10-200 mM phosphate buffered saline or Tris-HCl

buffers). The resulting monoliths are typically stored filled with the storage buffer at around 4°C [84, 86-88, 91, 93, 96].

1.4 Scope of thesis

The objective of this dissertation is to advance the state of the art of purification of macromolecules, synthesis and functionalization of PPM for separation processes, and control of chemical reactions with ion-concentration shock waves. The dissertation makes the following major contributions:

1. Development of guidelines and methodology for control of permeability and pore size in poly(2-hydroxyethyl methacrylate-co-ethylene dimethacrylate) (HEMA-co-EDMA) PPM.
2. Development of a semi-empirical model relating permeability and pore size in hydrophilic HEMA-co-EDMA PPM.
3. Development of a novel purification method by coupling ITP with AC; Development and experimental validation of an analytical model capturing the spatio-temporal dynamics of ITP-AC and identification of key dimensionless groups describing ITP-AC, reducing six dimensional variables to three dimensionless groups.
4. Derivation of simplified algebraic relations for key ITP-AC parameters such as length of affinity substrate needed to capture >95% of the target, and the time to capture >95% of the target for various ITP-AC regimes.
5. Development of synthesis and functionalization protocols for GMA-co-EDMA PPM for ITP-AC and experimental demonstration of ITP-AC in custom built experimental setup.

6. Demonstration of sequence specific purification of rare DNA target from over 10,000-fold more abundant background DNA via ITP-AC.
7. Demonstration of sequence specific purification of rare DNA target from over 13,000-fold more abundant endogenous DNA directly from whole human blood via ITP-AC.

This thesis is composed of three main chapters. In Chapter 2 we present an experimental study of synthesis and pore size and permeability control in HEMA-co-EDMA PPM. We also present an empirical model relating PPM permeability and pore size based on a modified Carman-Kozeny model. In Chapter 3 we describe a novel purification method based on coupling ITP and AC. We then develop an analytical model for spatiotemporal dynamics of ITP-AC. We identify and explore the effect of key ITP-AC process parameters, including target distribution width and height, ITP zone velocity, forward and reverse reaction constants, and probe concentration on necessary affinity region length, assay time, and capture efficiency. Our analysis yields simple analytical relations for capture length and capture time in relevant ITP-AC regimes, and demonstrates how ITP greatly reduces assay time and improves column utilization. In Chapter 4 we present experimental demonstration of ITP-AC and validation of the analytical model from Chapter 3. We describe the synthesis and DNA functionalization of GMA-co-EDMA PPM. We then provide protocols for performing of ITP-AC. Lastly, we demonstrate purification of a rare DNA target from over 10,000-fold more abundant background DNA in under 10 min, and under 1 mm column length using ITP-AC. In Chapter 5 we summarize our work, including concluding results and our contributions, and present recommendations for future research on macromolecule purification and control of chemical reactions via ion-

concentration shock waves. We also provide three appendices in which we describe two applications of ITP-AC (purification of DNA from blood, and sequential probing of the same nucleic acid) and provide more details regarding practical aspects of PPM synthesis.

1.5 Supplementary Information

Table 1.1. Polymerization Conditions

Table 1.1a. Synthesis conditions for porous polymer monoliths in order published

#	Ref.	Pore Size (nm)	Monomer		Crosslinker		Initiator		Good Solvent			Poor Solvent			T ⁴	Initiat or type
			Name	%	Name	%	Name	% ³	Name	%	δ	Name	%	δ		
1	[31]	1250	GMA	24	EDMA	16	AIBN	1	cyc	60	11.4	dod	0	9.8	55	Th
2	[31]	1930	GMA	24	EDMA	16	AIBN	1	cyc	57	11.4	dod	3	9.8	55	Th
3	[31]	1900	GMA	24	EDMA	16	AIBN	1	cyc	53	11.4	dod	6	9.8	55	Th
4	[31]	1840	GMA	24	EDMA	16	AIBN	1	cyc	45	11.4	dod	15	9.8	55	Th
5	[31]	150	GMA	24	EDMA	16	AIBN	1	cyc	60	11.4	dod	0	9.8	70	Th
6	[31]	260	GMA	24	EDMA	16	AIBN	1	cyc	57	11.4	dod	3	9.8	70	Th
7	[31]	480	GMA	24	EDMA	16	AIBN	1	cyc	53	11.4	dod	6	9.8	70	Th
8	[31]	2570	GMA	24	EDMA	16	AIBN	1	cyc	45	11.4	dod	15	9.8	70	Th
9	[31]	80	GMA	24	EDMA	16	AIBN	1	cyc	60	11.4	dod	0	9.8	80	Th
10	[31]	60	GMA	24	EDMA	16	AIBN	1	cyc	57	11.4	dod	3	9.8	80	Th
11	[31]	100	GMA	24	EDMA	16	AIBN	1	cyc	53	11.4	dod	6	9.8	80	Th
12	[31]	1330	GMA	24	EDMA	16	AIBN	1	cyc	45	11.4	dod	15	9.8	80	Th
13	[31]	5660	STY	20	DVB	20	AIBN	1	tol	60	8.9	dod	0	9.8	60	Th
14	[31]	4370	STY	20	DVB	20	AIBN	1	tol	50	8.9	dod	10	9.8	60	Th
15	[31]	1750	STY	20	DVB	20	AIBN	1	tol	45	8.9	dod	15	9.8	60	Th
16	[31]	680	STY	20	DVB	20	AIBN	1	tol	40	8.9	dod	20	9.8	60	Th
17	[31]	7090	STY	20	DVB	20	AIBN	1	tol	60	8.9	dod	0	9.8	70	Th
18	[31]	7355	STY	20	DVB	20	AIBN	1	tol	50	8.9	dod	10	9.8	70	Th
19	[31]	1250	STY	20	DVB	20	AIBN	1	tol	45	8.9	dod	15	9.8	70	Th
20	[31]	290	STY	20	DVB	20	AIBN	1	tol	40	8.9	dod	20	9.8	70	Th
21	[31]	9590	STY	20	DVB	20	AIBN	1	tol	60	8.9	dod	0	9.8	80	Th
22	[31]	1070	STY	20	DVB	20	AIBN	1	tol	50	8.9	dod	10	9.8	80	Th
23	[31]	180	STY	20	DVB	20	AIBN	1	tol	45	8.9	dod	15	9.8	80	Th
24	[31]	60	STY	20	DVB	20	AIBN	1	tol	40	8.9	dod	20	9.8	80	Th
25	[1]	3600	GMA	9	TMP	21	BME	1.5	tol	21	8.9	iso8	49	14.3	20	Ph 1
26	[1]	3230	GMA	15	TMP	35	BME	1.5	tol	15	8.9	iso8	35	14.3	20	Ph 1
27	[1]	3280	GMA	21	TMP	9	BME	1.5	tol	21	8.9	iso8	49	14.3	20	Ph 1

28	[1]	2590	GMA	35	TMP	15	BME	1.5	tol	15	8.9	iso8	35	14.3	20	Ph	1
29	[1]	225	GMA	9	TMP	21	BME	1.5	tol	49	8.9	iso8	21	14.3	20	Ph	1
30	[1]	33	GMA	15	TMP	35	BME	1.5	tol	35	8.9	iso8	15	14.3	20	Ph	1
31	[1]	4900	GMA	21	TMP	9	BME	1.5	tol	49	8.9	iso8	21	14.3	20	Ph	1
32	[1]	1800	GMA	35	TMP	15	BME	1.5	tol	35	8.9	iso8	15	14.3	20	Ph	1
33	[1]	4530	GMA	20	TMP	20	BME	1.5	tol	30	8.9	iso8	30	14.3	20	Ph	1
34	[1]	4520	GMA	20	TMP	20	BME	1.5	tol	30	8.9	iso8	30	14.3	20	Ph	1
35	[1]	4540	GMA	20	TMP	20	BME	1.5	tol	30	8.9	iso8	30	14.3	20	Ph	1
36	[1]	4480	GMA	20	TMP	20	BME	1.5	tol	30	8.9	iso8	30	14.3	20	Ph	1
37	[53]	2600	BMA	24	EDMA	16	DMPA	NR	-	-	-	ldec	60	9.8	20	Ph	1
38	[53]	1300	BMA	28	EDMA	12	DMPA	NR	-	-	-	ldec	60	9.8	20	Ph	1
39	[47]	1600	BMA	18	EDMA	27	DMPA	3	-	-	-	MeOH	55	14.5	20	Ph	1
40	[47]	670	BMA	18	EDMA	27	DMPA	4	-	-	-	MeOH	55	14.5	20	Ph	1
41	[47]	160	BMA	18	EDMA	27	DMPA	5	-	-	-	MeOH	55	14.5	20	Ph	1
42	[47]	2230	BMA	23	EDMA	22	DMPA	3	-	-	-	MeOH	55	14.5	20	Ph	1
43	[47]	1600	BMA	18	EDMA	27	DMPA	3	-	-	-	MeOH	55	14.5	20	Ph	1
44	[47]	1020	BMA	14	EDMA	31	DMPA	3	-	-	-	MeOH	55	14.5	20	Ph	1
45	[47]	270	BMA	38	EDMA	37	DMPA	3	-	-	-	MeOH	25	14.5	20	Ph	1
46	[47]	2230	BMA	23	EDMA	22	DMPA	3	-	-	-	MeOH	55	14.5	20	Ph	1
47	[47]	2970	BMA	18	EDMA	17	DMPA	3	-	-	-	MeOH	65	14.5	20	Ph	1
48	[39]	91	GMA	24	EDMA	16	AIBN	1	cyc	54	11.4	dod	6	9.8	70	Th	
49	[39]	93	GMA	24	EDMA	16	AIBN	1	cyc	54	11.4	dod	6	9.8	70	Th	
50	[39]	809	GMA	24	EDMA	16	AIBN	1	cyc	48	11.4	dod	6	9.8	55	Th	
51	[39]	935	GMA	24	EDMA	16	AIBN	1	cyc	48	11.4	dod	6	9.8	55	Th	
52	[39]	85	GMA	24	EDMA	16	AIBN	1	cyc	48	11.4	dod	12	9.8	70	Th	
53	[39]	283	GMA	24	EDMA	16	AIBN	1	cyc	48	11.4	dod	12	9.8	70	Th	
54	[39]	315	GMA	24	EDMA	16	AIBN	1	cyc	48	11.4	dod	12	9.8	70	Th	
55	[39]	1530	GMA	24	EDMA	16	AIBN	1	cyc	48	11.4	dod	12	9.8	55	Th	
56	[39]	1527	GMA	24	EDMA	16	AIBN	1	cyc	48	11.4	dod	12	9.8	55	Th	
57	[97]	4700	GMA	24	EDMA	16	AIBN	1	MeOH	30	14.5	EtOH	30	13	20	Ph	1,2
58	[97]	64	GMA	24	EDMA	16	AIBN	1	MeOH	30	14.5	THF	30	9.1	20	Ph	1,2
59	[97]	41	GMA	24	EDMA	16	AIBN	1	MeOH	30	14.5	MeCN	30	11.9	20	Ph	1,2
60	[97]	52	GMA	24	EDMA	16	AIBN	1	MeOH	30	14.5	TCM	30	9.3	20	Ph	1,2
61	[97]	53	GMA	24	EDMA	16	AIBN	1	MeOH	30	14.5	EA	30	9.1	20	Ph	1,2
62	[97]	5220	GMA	24	EDMA	16	AIBN	1	MeOH	30	14.5	hex	30	7.3	20	Ph	1,2
63	[97]	54	HEMA	24	EDMA	16	AIBN	1	MeOH	60	14.5	-	-		20	Ph	1,2
64	[97]	51	HEMA	24	EDMA	16	AIBN	1	MeOH	30	14.5	EtOH	30	13	20	Ph	1,2
65	[97]	7959	HEMA	24	EDMA	16	AIBN	1	MeOH	30	14.5	hex	30	7.3	20	Ph	1,2
66	[97]	54	HEMA	24	EDMA	16	AIBN	1	MeOH	60	14.5	-	-		20	Ph	1,2
67	[97]	34	HEMA	24	EDMA	16	AIBN	1	MeOH	48	14.5	H2O	12	23.4	20	Ph	1,2
68	[97]	64	HEMA	24	EDMA	16	AIBN	1	MeOH	36	14.5	H2O	24	23.4	20	Ph	1,2
69	[97]	43	HEMA	24	EDMA	16	AIBN	1	MeCN	60	11.9	-	-		20	Ph	1,2
70	[97]	7	HEMA	24	EDMA	16	AIBN	1	MeCN	48	11.9	H2O	12	23.4	20	Ph	1,2
71	[97]	9072	BMA	24	EDMA	16	AIBN	1	MeOH	60	14.5	-	-		20	Ph	1,2
72	[97]	1523	BMA	24	EDMA	16	AIBN	1	MeOH	30	14.5	EtOH	30	13	20	Ph	1,2

73	[97]	10	BMA	24	EDMA	16	AIBN	1	MeOH	30	14.5	THF	30	9.1	20	Ph	1,2
74	[97]	32	BMA	24	EDMA	16	AIBN	1	MeOH	30	14.5	MeCN	30	11.9	20	Ph	1,2
75	[97]	18	BMA	24	EDMA	16	AIBN	1	MeOH	30	14.5	TCM	30	9.3	20	Ph	1,2
76	[97]	20	BMA	24	EDMA	16	AIBN	1	MeOH	30	14.5	EA	30	9.1	20	Ph	1,2
77	[97]	58	BMA	24	EDMA	16	AIBN	1	MeOH	30	14.5	hex	30	7.3	20	Ph	1,2
78	[38]	1279	GMA	24	EDMA	16	AIBN	1	cyc	54	11.4	dod	6	9.8	55	Th	
79	[38]	2009	GMA	24	EDMA	16	AIBN	1	cyc	54	11.4	dod	6	9.8	60	Th	
80	[38]	1200	GMA	24	EDMA	16	AIBN	1	cyc	54	11.4	dod	6	9.8	65	Th	
81	[38]	583	GMA	24	EDMA	16	AIBN	1	cyc	54	11.4	dod	6	9.8	70	Th	
82	[38]	126	GMA	24	EDMA	16	AIBN	1	cyc	54	11.4	dod	6	9.8	80	Th	
83	[38]	34	GMA	24	EDMA	16	AIBN	1	cyc	54	11.4	dod	6	9.8	90	Th	
84	[4]	119	BMA	24	EDMA	16	DMPA	1	cyc	40	11.4	dod	20	9.8	30	Ph	
85	[4]	173	BMA	24	EDMA	16	DMPA	1	cyc	35	11.4	dod	25	9.8	30	Ph	
86	[4]	178	BMA	24	EDMA	16	DMPA	1	cyc	30	11.4	dod	30	9.8	30	Ph	
87	[4]	198	BMA	24	EDMA	16	DMPA	1	cyc	27	11.4	dod	33	9.8	30	Ph	
88	[4]	158	BMA	24	EDMA	16	DMPA	1	cyc	24	11.4	dod	36	9.8	30	Ph	
89	[4]	307	BMA	24	EDMA	16	DMPA	1	cyc	21	11.4	dod	39	9.8	30	Ph	
90	[4]	480	BMA	24	EDMA	16	DMPA	1	cyc	18	11.4	dod	42	9.8	30	Ph	
91	[4]	876	BMA	24	EDMA	16	DMPA	1	cyc	15	11.4	dod	45	9.8	30	Ph	
92	[4]	1579	BMA	24	EDMA	16	DMPA	1	cyc	12	11.4	dod	48	9.8	30	Ph	
93	[4]	2238	BMA	24	EDMA	16	DMPA	1	cyc	9	11.4	dod	51	9.8	30	Ph	
94	[4]	2733	BMA	24	EDMA	16	DMPA	1	cyc	6	11.4	dod	54	9.8	30	Ph	
95	[42]	116	GMA	36	EDMA	24	AIBN	1	cyc	40	11.4	-	-		60	Th	
96	[42]	236	GMA	30	EDMA	20	AIBN	1	cyc	50	11.4	-	-		60	Th	
97	[42]	347	GMA	24	EDMA	16	AIBN	1	cyc	60	11.4	-	-		60	Th	
98	[42]	532	GMA	18	EDMA	12	AIBN	1	cyc	70	11.4	-	-		60	Th	
99	[42]	876	GMA	12	EDMA	8	AIBN	1	cyc	80	11.4	-	-		60	Th	
100	[42]	1073	GMA	21	EDMA	9	AIBN	1	cyc	70	11.4	-	-		55	Th	
101	[42]	826	GMA	18	EDMA	12	AIBN	1	cyc	70	11.4	-	-		55	Th	
102	[42]	652	GMA	15	EDMA	15	AIBN	1	cyc	70	11.4	-	-		55	Th	
103	[42]	427	GMA	12	EDMA	18	AIBN	1	cyc	70	11.4	-	-		55	Th	
104	[42]	312	GMA	9	EDMA	21	AIBN	1	cyc	70	11.4	-	-		55	Th	
105	[42]	829	GMA	15	EDMA	10	AIBN	1	cyc	75	11.4	-	-		55	Th	
106	[42]	702	GMA	15	EDMA	10	AIBN	1	cyc	75	11.4	-	-		60	Th	
107	[42]	593	GMA	15	EDMA	10	AIBN	1	cyc	75	11.4	-	-		65	Th	
108	[42]	416	GMA	15	EDMA	10	AIBN	1	cyc	75	11.4	-	-		70	Th	

Table 1.1b. Synthesis conditions for porous polymer monoliths in pore size order.

#	Ref.	Pore	Monomer		Crosslinker		Initiator		Good Solvent			Poor Solvent			T ⁴	Initiat or type	
		Size (nm)	Name	%	Name	%	Name	% ³	Name	%	δ	Name	%	δ			
70		7	HEMA	24	EDMA	16	AIBN	1	MeCN	48	11.9	H ₂ O	12	23.4	20	Ph	1,2
73		10	BMA	24	EDMA	16	AIBN	1	MeOH	30	14.5	THF	30	9.1	20	Ph	1,2
75		18	BMA	24	EDMA	16	AIBN	1	MeOH	30	14.5	TCM	30	9.3	20	Ph	1,2
76		20	BMA	24	EDMA	16	AIBN	1	MeOH	30	14.5	EA	30	9.1	20	Ph	1,2
74		32	BMA	24	EDMA	16	AIBN	1	MeOH	30	14.5	MeCN	30	11.9	20	Ph	1,2
30		33	GMA	15	TMP	35	BME	1.5	tol	35	8.9	iso8	15	14.3	20	Ph	1
67		34	HEMA	24	EDMA	16	AIBN	1	MeOH	48	14.5	H ₂ O	12	23.4	20	Ph	1,2
83		34	GMA	24	EDMA	16	AIBN	1	cyc	54	11.4	dod	6	9.8	90	Th	
59		41	GMA	24	EDMA	16	AIBN	1	MeOH	30	14.5	MeCN	30	11.9	20	Ph	1,2
69		43	HEMA	24	EDMA	16	AIBN	1	MeCN	60	11.9	-	-		20	Ph	1,2
64		51	HEMA	24	EDMA	16	AIBN	1	MeOH	30	14.5	EtOH	30	13	20	Ph	1,2
60		52	GMA	24	EDMA	16	AIBN	1	MeOH	30	14.5	TCM	30	9.3	20	Ph	1,2
61		53	GMA	24	EDMA	16	AIBN	1	MeOH	30	14.5	EA	30	9.1	20	Ph	1,2
63		54	HEMA	24	EDMA	16	AIBN	1	MeOH	60	14.5	-	-		20	Ph	1,2
66		54	HEMA	24	EDMA	16	AIBN	1	MeOH	60	14.5	-	-		20	Ph	1,2
77		58	BMA	24	EDMA	16	AIBN	1	MeOH	30	14.5	hex	30	7.3	20	Ph	1,2
10		60	GMA	24	EDMA	16	AIBN	1	cyc	57	11.4	dod	3	9.8	80	Th	
24		60	STY	20	DVB	20	AIBN	1	tol	40	8.9	dod	20	9.8	80	Th	
58		64	GMA	24	EDMA	16	AIBN	1	MeOH	30	14.5	THF	30	9.1	20	Ph	1,2
68		64	HEMA	24	EDMA	16	AIBN	1	MeOH	36	14.5	H ₂ O	24	23.4	20	Ph	1,2
9		80	GMA	24	EDMA	16	AIBN	1	cyc	60	11.4	dod	0	9.8	80	Th	
52		85	GMA	24	EDMA	16	AIBN	1	cyc	48	11.4	dod	12	9.8	70	Th	
48		91	GMA	24	EDMA	16	AIBN	1	cyc	54	11.4	dod	6	9.8	70	Th	
49		93	GMA	24	EDMA	16	AIBN	1	cyc	54	11.4	dod	6	9.8	70	Th	
11		100	GMA	24	EDMA	16	AIBN	1	cyc	53	11.4	dod	6	9.8	80	Th	
95		116	GMA	36	EDMA	24	AIBN	1	cyc	40	11.4	-	-		60	Th	
84		119	BMA	24	EDMA	16	DMPA	1	cyc	40	11.4	dod	20	9.8	30	Ph	
82		126	GMA	24	EDMA	16	AIBN	1	cyc	54	11.4	dod	6	9.8	80	Th	
5		150	GMA	24	EDMA	16	AIBN	1	cyc	60	11.4	dod	0	9.8	70	Th	
88		158	BMA	24	EDMA	16	DMPA	1	cyc	24	11.4	dod	36	9.8	30	Ph	
41		160	BMA	18	EDMA	27	DMPA	5	-	-	-	MeOH	55	14.5	20	Ph	1
85		173	BMA	24	EDMA	16	DMPA	1	cyc	35	11.4	dod	25	9.8	30	Ph	
86		178	BMA	24	EDMA	16	DMPA	1	cyc	30	11.4	dod	30	9.8	30	Ph	
23		180	STY	20	DVB	20	AIBN	1	tol	45	8.9	dod	15	9.8	80	Th	
87		198	BMA	24	EDMA	16	DMPA	1	cyc	27	11.4	dod	33	9.8	30	Ph	
29		225	GMA	9	TMP	21	BME	1.5	tol	49	8.9	iso8	21	14.3	20	Ph	1
96		236	GMA	30	EDMA	20	AIBN	1	cyc	50	11.4	-	-		60	Th	
6		260	GMA	24	EDMA	16	AIBN	1	cyc	57	11.4	dod	3	9.8	70	Th	

45		270	BMA	38	EDMA	37	DMPA	3	-	-	-	MeOH	25	14.5	20	Ph	1
53		283	GMA	24	EDMA	16	AIBN	1	cyc	48	11.4	dod	12	9.8	70	Th	
20		290	STY	20	DVB	20	AIBN	1	tol	40	8.9	dod	20	9.8	70	Th	
89		307	BMA	24	EDMA	16	DMPA	1	cyc	21	11.4	dod	39	9.8	30	Ph	
104		312	GMA	9	EDMA	21	AIBN	1	cyc	70	11.4	-	-		55	Th	
54		315	GMA	24	EDMA	16	AIBN	1	cyc	48	11.4	dod	12	9.8	70	Th	
97		347	GMA	24	EDMA	16	AIBN	1	cyc	60	11.4	-	-		60	Th	
108		416	GMA	15	EDMA	10	AIBN	1	cyc	75	11.4	-	-		70	Th	
103		427	GMA	12	EDMA	18	AIBN	1	cyc	70	11.4	-	-		55	Th	
7		480	GMA	24	EDMA	16	AIBN	1	cyc	53	11.4	dod	6	9.8	70	Th	
90		480	BMA	24	EDMA	16	DMPA	1	cyc	18	11.4	dod	42	9.8	30	Ph	
98		532	GMA	18	EDMA	12	AIBN	1	cyc	70	11.4	-	-		60	Th	
81		583	GMA	24	EDMA	16	AIBN	1	cyc	54	11.4	dod	6	9.8	70	Th	
107		593	GMA	15	EDMA	10	AIBN	1	cyc	75	11.4	-	-		65	Th	
102		652	GMA	15	EDMA	15	AIBN	1	cyc	70	11.4	-	-		55	Th	
40		670	BMA	18	EDMA	27	DMPA	4	-	-	-	MeOH	55	14.5	20	Ph	1
16		680	STY	20	DVB	20	AIBN	1	tol	40	8.9	dod	20	9.8	60	Th	
106		702	GMA	15	EDMA	10	AIBN	1	cyc	75	11.4	-	-		60	Th	
50		809	GMA	24	EDMA	16	AIBN	1	cyc	48	11.4	dod	6	9.8	55	Th	
101		826	GMA	18	EDMA	12	AIBN	1	cyc	70	11.4	-	-		55	Th	
105		829	GMA	15	EDMA	10	AIBN	1	cyc	75	11.4	-	-		55	Th	
91		876	BMA	24	EDMA	16	DMPA	1	cyc	15	11.4	dod	45	9.8	30	Ph	
99		876	GMA	12	EDMA	8	AIBN	1	cyc	80	11.4	-	-		60	Th	
51		935	GMA	24	EDMA	16	AIBN	1	cyc	48	11.4	dod	6	9.8	55	Th	
44		1020	BMA	14	EDMA	31	DMPA	3	-	-	-	MeOH	55	14.5	20	Ph	1
22		1070	STY	20	DVB	20	AIBN	1	tol	50	8.9	dod	10	9.8	80	Th	
100		1073	GMA	21	EDMA	9	AIBN	1	cyc	70	11.4	-	-		55	Th	
80		1200	GMA	24	EDMA	16	AIBN	1	cyc	54	11.4	dod	6	9.8	65	Th	
1		1250	GMA	24	EDMA	16	AIBN	1	cyc	60	11.4	dod	0	9.8	55	Th	
19		1250	STY	20	DVB	20	AIBN	1	tol	45	8.9	dod	15	9.8	70	Th	
78		1279	GMA	24	EDMA	16	AIBN	1	cyc	54	11.4	dod	6	9.8	55	Th	
38		1300	BMA	28	EDMA	12	DMPA	NR	-	-	-	1-Dec	60	9.8	20	Ph	1
12		1330	GMA	24	EDMA	16	AIBN	1	cyc	45	11.4	dod	15	9.8	80	Th	
72		1523	BMA	24	EDMA	16	AIBN	1	MeOH	30	14.5	EtOH	30	13	20	Ph	1,2
56		1527	GMA	24	EDMA	16	AIBN	1	cyc	48	11.4	dod	12	9.8	55	Th	
55		1530	GMA	24	EDMA	16	AIBN	1	cyc	48	11.4	dod	12	9.8	55	Th	
92		1579	BMA	24	EDMA	16	DMPA	1	cyc	12	11.4	dod	48	9.8	30	Ph	
39		1600	BMA	18	EDMA	27	DMPA	3	-	-	-	MeOH	55	14.5	20	Ph	1
43		1600	BMA	18	EDMA	27	DMPA	3	-	-	-	MeOH	55	14.5	20	Ph	1
15		1750	STY	20	DVB	20	AIBN	1	tol	45	8.9	dod	15	9.8	60	Th	
32		1800	GMA	35	TMP	15	BME	1.5	tol	35	8.9	iso8	15	14.3	20	Ph	1
4		1840	GMA	24	EDMA	16	AIBN	1	cyc	45	11.4	dod	15	9.8	55	Th	
3		1900	GMA	24	EDMA	16	AIBN	1	cyc	53	11.4	dod	6	9.8	55	Th	
2		1930	GMA	24	EDMA	16	AIBN	1	cyc	57	11.4	dod	3	9.8	55	Th	
79		2009	GMA	24	EDMA	16	AIBN	1	cyc	54	11.4	dod	6	9.8	60	Th	

42		2230	BMA	23	EDMA	22	DMPA	3	-	-	-	MeOH	55	14.5	20	Ph	1
46		2230	BMA	23	EDMA	22	DMPA	3	-	-	-	MeOH	55	14.5	20	Ph	1
93		2238	BMA	24	EDMA	16	DMPA	1	cyc	9	11.4	dod	51	9.8	30	Ph	
8		2570	GMA	24	EDMA	16	AIBN	1	cyc	45	11.4	dod	15	9.8	70	Th	
28		2590	GMA	35	TMP	15	BME	1.5	tol	15	8.9	iso8	35	14.3	20	Ph	1
37		2600	BMA	24	EDMA	16	DMPA	NR	-	-	-	1-Dec	60	9.8	20	Ph	1
94		2733	BMA	24	EDMA	16	DMPA	1	cyc	6	11.4	dod	54	9.8	30	Ph	
47		2970	BMA	18	EDMA	17	DMPA	3	-	-	-	MeOH	65	14.5	20	Ph	1
26		3230	GMA	15	TMP	35	BME	1.5	tol	15	8.9	iso8	35	14.3	20	Ph	1
27		3280	GMA	21	TMP	9	BME	1.5	tol	21	8.9	iso8	49	14.3	20	Ph	1
25		3600	GMA	9	TMP	21	BME	1.5	tol	21	8.9	iso8	49	14.3	20	Ph	1
14		4370	STY	20	DVB	20	AIBN	1	tol	50	8.9	dod	10	9.8	60	Th	
36		4480	GMA	20	TMP	20	BME	1.5	tol	30	8.9	iso8	30	14.3	20	Ph	1
34		4520	GMA	20	TMP	20	BME	1.5	tol	30	8.9	iso8	30	14.3	20	Ph	1
33		4530	GMA	20	TMP	20	BME	1.5	tol	30	8.9	iso8	30	14.3	20	Ph	1
35		4540	GMA	20	TMP	20	BME	1.5	tol	30	8.9	iso8	30	14.3	20	Ph	1
57		4700	GMA	24	EDMA	16	AIBN	1	MeOH	30	14.5	EtOH	30	13	20	Ph	1,2
31		4900	GMA	21	TMP	9	BME	1.5	tol	49	8.9	iso8	21	14.3	20	Ph	1
62		5220	GMA	24	EDMA	16	AIBN	1	MeOH	30	14.5	hex	30	7.3	20	Ph	1,2
13		5660	STY	20	DVB	20	AIBN	1	tol	60	8.9	dod	0	9.8	60	Th	
17		7090	STY	20	DVB	20	AIBN	1	tol	60	8.9	dod	0	9.8	70	Th	
18		7355	STY	20	DVB	20	AIBN	1	tol	50	8.9	dod	10	9.8	70	Th	
65		7959	HEMA	24	EDMA	16	AIBN	1	MeOH	30	14.5	hex	30	7.3	20	Ph	1,2
71		9072	BMA	24	EDMA	16	AIBN	1	MeOH	60	14.5	-	-		20	Ph	1,2
21		9590	STY	20	DVB	20	AIBN	1	tol	60	8.9	dod	0	9.8	80	Th	

1. Reported as room temperature; actual temperature not reported, and so we assume 20 °C

2. Not reported which solvent is a thermodynamically good and which is thermodynamically poor solvent. Listed in arbitrary order.

3. Weight percent initiator to monomer.

4. Polymerization temperature (°C).

Abbreviations:

GMA - glycidyl methacrylate

STY – styrene

BMA - butyl methacrylate

HEMA - 2-hydroxyethyl methacrylate

EDMA - ethylene dimethacrylate

TMP – trimethylolpropane

DVB – divinylbenzene

AIBN – azobisisobutyronitrile

DMPA - 2,2-dimethoxy-2-phenylacetophenone

BME - benzoin methyl ether

cyc - cyclohexanol

MeOH - mEtOH

tol – toluene

dod – dodecanol

iso8 - isooctane

1dec - 1-decanol

hex – hexane

EtOH – ethanol

THF – tetrahydrofuran

MeCN – acetonitrile

TCM - chloroform

EA - ethyl acetate

Th – Thermal initiation

Ph – Photo initiation

Table 1.1c. Common monomers and crosslinkers for synthesis of porous polymer monoliths.

Monomer	δ	Hydrogen bonding	Hits	Crosslinker	δ	Hydrogen bonding	Hits
glycidyl methacrylate	9.5*		59	ethylene dimethacrylate	11.2	strong	84
butyl methacrylate	8.2	medium	28	trimethylolpropane	9.5*		12
styrene	9.3	poor	12	divinylbenzene	9.4*		12
2-hydroxyethyl methacrylate	9.5*		8				

* Estimated using group theory using parameters of Hoy in Introduction to Polymer Science and Chemistry: a problem solving approach (Manas Chanda)[98]. Hits are the number of occurrences in Table 1a.

Table 1.1d. Common initiators for synthesis of porous polymer monoliths.

Initiator	Decomposition rate	Thermal/Photo	Hits
Azobisisobutyronitrile*	10^{-7} - 10^{-3}	-thermal/ photo	74
2,2-dimethoxy-2-phenylacetophenone	Not given	photo	22
benzoin methyl ether	Not given	photo	12

* Over 100 conditions (various temp. and solvents), including temperature correlations for some solvents given in the Polymer Handbook[48].

Table 1.1e. Most common solvents for synthesis of porous polymer monoliths.

Solvent	δ	Hydrogen bonding	Hits
dodecanol	9.8	strong	52
cyclohexanol	11.4	strong	51
methanol	14.5	strong	28
toluene	8.9	poor	24

2 Design and Fabrication of Porous Polymer

Wicks

The contents of this chapter were previously published by V. Shkolnikov, D.G. Strickland, D.P. Fenning, and J.G. Santiago [1] in *Sensors and Actuators B: Chemical* journal and are reproduced here with minor modifications.

2.1 Introduction

In 1990, Tennikova *et al.* [1] first demonstrated highly crosslinked, rigid, microporous polymer monoliths as separation media for high performance membrane chromatography. This initial demonstration has since led to a wide variety of techniques for preparation of porous polymer monoliths, which allow control over pore morphology, mechanical stability, and surface chemistry [2]. Pore size distributions are often bimodal, with large and small pores resulting in materials with both high permeability and high specific surface area. These materials are therefore ideal for many separation applications including liquid chromatography [3], capillary separations [4], capillary electrochromatography [5-7], thin layer chromatography [8] and, more recently, gas chromatography [9]. In addition, polymer monoliths have been used as porous frits in electroosmotic pumps [10], in microfluidic devices for on-chip separations and low Reynolds number mixing [11, 12], as hydrogen storage media [13], and for water management in fuel cells [14]. To our knowledge, outside of the recent effort by Strickland and Santiago [14], there have been no dedicated efforts aimed at realizing high permeability, hydrophilic, porous polymer monoliths suitable for wicking and other liquid transport applications.

Porous polymer monoliths are synthesized by carrying out free-radical polymerization of crosslinking and monovinyl monomers, in the presence of solvents. Heat, ultraviolet (UV) irradiation, or gamma-rays generate free-radicals by destabilizing an initiating compound [2]. These free-radicals initiate rapid polymer chain growth at what become nucleation sites, which continue to grow as the reaction proceeds. As polymer molecular weight increases, solubility decreases, and a two-phase system of solid polymer and liquid solvent results. The resulting monolith microstructure consists of an agglomeration of globules, whose size directly impacts resulting pore-size distribution. Globule size is influenced by many factors, including the number of nucleation sites present, monomer concentration, solubility, and degree of cross-linking [15]. Thus, polymer microstructure can be controlled by rate of reaction, monomer/porogen ratio, type of porogenic solvents and fraction of cross-linking monomers. Detailed descriptions of various chemistries and characterization of resulting monoliths can be found in [2] and [15].

In the present work, we designed, fabricated, and characterized porous monoliths of 2-hydroxyethyl methacrylate-*co*-ethylene dimethacrylate (HEMA-*co*-EDMA) with the aim of achieving high permeability, hydrophilic, dimensionally and chemically stable materials for use as wicks. In general, wicks are porous, hydrophilic structures that are commonly used to absorb and transport liquids. Wicks are applied to heat pipes and vapor chambers [16], microfluidic systems [17], lateral flow chemical assays on cellulose paper [18], fuel cells [19, 20], and electrospray nozzles [21]. For most applications, an ideal wick has high permeability and can support significant capillary-pressure-induced liquid pressure gradients. Often these two properties are in competition: large pores are required

for high permeability, while small pores induce large capillary pressures. In the following sections, we identify key parameters affecting resulting monolith permeability and pore size, discuss competing microstructure properties in detail, and identify strategies to optimize performance for a given application. As an example application, we then discuss a custom injection molding procedure, where we integrated wicks with order 100 μm feature sizes in a polymer electrolyte fuel cell cathode flow field. The latter integration was described as part of a prototype fuel cell system we reported previously [14], however, that study centered on the performance of the wick as a component of the system. Here, we present new analysis, methods, and results which specifically focus on the chemistry, process optimization, molding, *in situ* polymerization, and capillary transport properties of the wick structure itself. Our aim is to enable wider applications of such *in situ* polymerized wicks.

2.2 Materials and Methods

We here describe materials, discuss choice of chemistry, and present *ex situ* fabrication methods of polymer monolith samples used for characterization. Characterization included permeability, pore size, and surface area measurements. We describe *in situ* polymerization of the monolith structures in Section 2.3.3.5.

2.2.1 Materials

Ethylene dimethacrylate (EDMA - CAS# 97-90-5), 2-hydroxyethyl methacrylate (HEMA - CAS# 868-77-9), inhibitor removal media (product number: 311332 - CAS 9003-70-7), benzoin methyl ether (CAS# 3524-62-7), and methanol (MeOH) 99.93% were purchased from Aldrich. n-Hexane HPLC grade 95+% was purchased from Alfa Aesar.

GE Type 214 quartz tubing (5 mm i.d., 7 mm o.d.) was purchased from National Scientific Company Inc. (Quakertown, PA). GE Type 214 quartz tubing was chosen for its high (>90%) UV 360 nm wavelength transmittance [22].

2.2.2 Polymer chemistry

Wicking structures require hydrophilic surface functionality to absorb water or aqueous solutions. We therefore chose a polymerization chemistry that incorporates the monovinyl monomer, HEMA, which has a polar hydroxyl functional group. Adapting a chemistry from Yu *et al.* [23], we crosslinked HEMA with EDMA via free radical, UV-initiated polymerization in the presence of MeOH and hexane as solvents. As Yu *et al.* showed, an MeOH/Hexane binary solvent system provides satisfactory solubility for polymerization and is ideal for large-pore formation (we discuss effect of polymer solubility on pore size in Section 2.3.1.3).

We photo-initiated polymerization via UV irradiation and destabilization of benzoin methyl ether. We chose photo, rather than thermal, initiation for the present polymerization. Thermal initiators often require long polymerization times and elevated temperatures, which can lead to significant evaporative loss of solvents in imperfectly sealed molds. In contrast, photo-initiation can be carried out at room temperature over shorter polymerization times, thus minimizing evaporative solvent loss.

To characterize the chemistry and resulting monoliths, we varied two separate ratios: (1) total monomer/solvent and (2) MeOH/hexane. We list recipes in Table 2.1. In all cases, 1.25% (by mass, with respect to monomers) benzoin methyl ether was used.

2.2.3 Fabrication of samples for ex-situ permeability and pore size measurements

Both EDMA and HEMA were received with polymerization inhibitors, which we removed by passing through columns packed with inhibitor removing media. We then mixed the photo-initiator (benzoin methyl ether), HEMA, EDMA, MeOH and hexane in the order listed, in glass vials and subsequently purged with nitrogen to minimize oxygen dissolved in solution. Purge was carried out by bubbling nitrogen at $3 \times 10^{-9} \text{ m}^3 \text{ s}^{-1}$ for ~2.5 min. In all cases, solution weight change before and after purge was less than 3%.

We transferred solutions into quartz tubes, which we sealed with custom-fabricated Teflon caps. We then irradiated samples using a 100 W, ~365 nm peak wavelength UV lamp, at 8 cm exposure distance, for 1 h. During polymerization, solution changed from transparent to white and visibly opaque in less than 10 min. After polymerization, we flushed samples with methanol to remove unreacted monomers and solvents, and dried at 120 °C for 1 h.

2.2.4 Measurement of permeability

Permeability, k , of a specific porous material can be interpreted as a material property. Specifically, it is the proportionality constant in Darcy's law relating pressure difference to superficial fluid velocity in porous media [24]. A form of Darcy's law is:

$$\bar{u} = \frac{k}{\mu} \nabla P_l \quad (2.1)$$

where μ is fluid viscosity, \bar{u} is the superficial liquid velocity, and ∇P_l is the pressure gradient in the liquid phase. \bar{u} can be integrated over the cross-sectional area normal to the

flow to obtain a linear relationship between pressure gradient and flow rate. Assuming a one dimensional linear pressure distribution and rearranging, this yields $k = \mu(Q/\Delta P)(L/A)$, where Q is the flow rate, A is the cross-sectional area normal to the superficial velocity vector, and L is the distance across which the pressure difference, ΔP , is applied. To measure permeability, we manually pushed the samples out of the quartz tubing and transferred them into 3/16" heat shrink tubing (SPC Technology, Chicago, IL). Heat shrink is thin-walled polymer tubing which, upon heating, permanently contracts and can conform to shapes inside it. Heat shrink sealed around and connected samples to silicone tubes on either end. We observed a good seal around polymer samples with minimal dimensional change due to compression.

We connected samples to a mass flow controller (MC-5SLPM-D, Alicat Scientific, Tucson, AZ) and upstream pressure transducer (PX139 – 030D4V Omega Engineering, Stamford, CT). Permeability was measured by flowing air (ultra zero grade compressed air cylinder, Praxair Inc., San Ramon, CA) through the sample at seven different flow rates in the range of 20 to 1000 sccm. We set flow rate and measured ΔP across the sample using a PC with LabView 8.5. To determine k , we performed a linear regression fit for each sample to determine the $Q/\Delta P$ slope. R^2 values for these fits were higher than 0.98, indicating relatively constant permeability over the range tested. Since ΔP depends linearly on Q , we determined permeability by directly substituting $Q/\Delta P$ into the above derived one dimensional expression for k . We report results in Table 2.1.

2.3 Results

The microstructure of a porous wick material strongly affects its capacity to transport fluids. In this section, we first discuss mechanisms and general trends in resulting

monolith microstructure. We then explore the corresponding impact on monolith permeability and capillary transport. Finally, we detail a method for integrating wick structures into a fuel cell as a sample application which requires fine geometric control.

2.3.1 Review of general mechanisms and trends in monolith polymerization

Mechanisms and trends for methacrylate monolith polymerization chemistries are discussed in detail by Vlakh *et al.* [25]. We summarize here major concepts from Vlakh *et al.* as we leveraged their study to guide our design and characterization experiments. As mentioned above, four main parameters control resulting monolith structure and properties: (1) rate of reaction, (2) monomer/porogen ratio, (3) solubility and (4) degree of cross-linking.

2.3.1.1 Rate of reaction

Typically, photo- or thermal-initiators are used to induce polymerization. Initiators form free radicals when exposed to UV radiation or heat, which then induce rapid polymer chain growth by opening and linking monomer vinyl groups. As such, initiator concentration, reaction temperature, and irradiation intensity all influence reaction rate. In general, characteristic pore size decreases with increasing reaction rate. This relationship is attributed to increased polymer nucleation site concentration, which affects polymer globules of increased number density and smaller characteristic dimension.

2.3.1.2 Monomer-to-porogen ratio

Porosity is roughly equal to the volumetric fraction of porogenic solvents present [26]. The volumetric ratio of total monomer to total porogenic solvent, therefore, gives

fairly direct control over resulting monolith porosity. Physical properties of resulting monoliths limit the range of porosities that can be achieved: non-porous samples typically result at high monomer concentration (roughly $> 0.6 \text{ mL mL}^{-1}$), while samples become friable for low monomer concentration ($< 0.2 \text{ mL mL}^{-1}$).

2.3.1.3 Solubility

A binary solvent system, comprised of a good and poor solvent, is typically used to control polymer solubility. In general, pore size increases with decreasing solubility of monomers. When a poor solvent is used, polymers become insoluble at lower molecular weights and therefore precipitate early in the reaction. Remaining monomers are a better solvent than the poor solvent selected, resulting in increased monomer concentration in their vicinity. Polymer growth near existing globules is therefore thermodynamically preferred, and leads to fewer polymer globules of larger characteristic dimension.

2.3.1.4 Degree of cross-linking

Degree of cross-linking is controlled by the ratio of multi-vinyl to mono-vinyl monomers. Changing this ratio affects both the pore size distribution and the chemical composition of the resulting polymer monolith. Pore size typically decreases as degree of cross-linking increases. During reaction, highly cross-linked polymers quickly become insoluble. This results in increased globule number density, and associated polymer globules of smaller characteristic dimension.

2.3.2 Control and optimization of wick porosity and pore structure

We limited the present study to exploring the effect of monomer/porogen ratio and solubility on resulting monolith pore structure when using HEMA and EDMA as

monomers. We refer the reader to work by Yu *et al.* [23] for characterization of a similar hydrophilic chemistry and comparison of resulting microstructure with additional EDMA crosslinked porous polymers (including those with hydrophobic surface chemistry). The data shown here represents example trends in synthesizing monoliths as part of a 3 x 3 parametric study, where we varied both monomer/solvent ratio and solubility (via the binary solvent mixture). We fabricated and characterized monoliths for monomer/solvent ratios of 30/70, 40/60, and 50/50, and MeOH/hexane ratios of 40/60, 50/50, and 60/40 (by mass). In all cases, HEMA/EDMA ratio was 50/50. Resulting monoliths were characterized using mercury intrusion porosimetry to determine pore size distribution and BET analysis to measure specific surface area (Porous Materials, Inc., Ithaca, NY). We measured monolith permeability in-house, as described in Section 2.2.4. Table 2.1 summarizes results. Chemistries for which resulting monoliths were non-porous are indicated with an “n/a” in the porous properties entries.

Table 2.1. Tested properties of porous polymer monolith.

Name	Chemical composition ^a				Properties:								
	HEMA	EDMA	MeOH	Hex	ϵ^b	d^c_{mode}	d^d_{median}	σ^e	V^f_{pore}	s^g_o	k^h	$d^i_{p,eq}$	k/d^j_{mode}
HE04	0.15	0.15	0.28	0.42	0.77	8.6	7.6	1.1	3.0	58.7	1.31	36.5	0.15
HE05	0.15	0.15	0.35	0.35	0.77	10.1	7.2	2.4	4.6	75.0	1.53	39.3	0.15
HE06	0.15	0.15	0.42	0.28	0.77	9.0	8.4	0.93	3.6	61.7	1.91	44.0	0.21
HE13	0.20	0.20	0.24	0.36	0.68	7.6	6.8	1.1	2.6	36.1	0.942	30.9	0.12
HE14	0.20	0.20	0.30	0.30	0.68	7.9	6.8	1.6	2.5	35.6	1.18	34.6	0.15
HE15	0.20	0.20	0.36	0.24	n/a	n/a	n/a	n/a	n/a	n/a	n/a	n/a	n/a
HE22	0.25	0.25	0.20	0.30	0.59	6.3	3.3	1.8	2.1	37.5	0.726	27.1	0.12
HE23	0.25	0.25	0.25	0.25	n/a	n/a	n/a	n/a	n/a	n/a	n/a	n/a	n/a
HE24	0.25	0.25	0.30	0.30	n/a	n/a	n/a	n/a	n/a	n/a	n/a	n/a	n/a

^aConcentration by mass fraction (g g^{-1}), ^bporosity, taken as volume fraction of monomers, ^cmost common pore diameter, taken as peak of pore size distribution (μm), ^dmedian pore diameter, taken as pore size at 50% of total pore volume during mercury intrusion (μm), ^echaracteristic pore size distribution width (μm), ^fpore volume (mL g^{-1}), ^gspecific surface area ($\text{m}^2 \text{g}^{-1}$), ^hpermeability ($\times 10^{-12} \text{m}^2$), ⁱequivalent particle diameter (μm), and ^jcapillary transport parameter (μm).

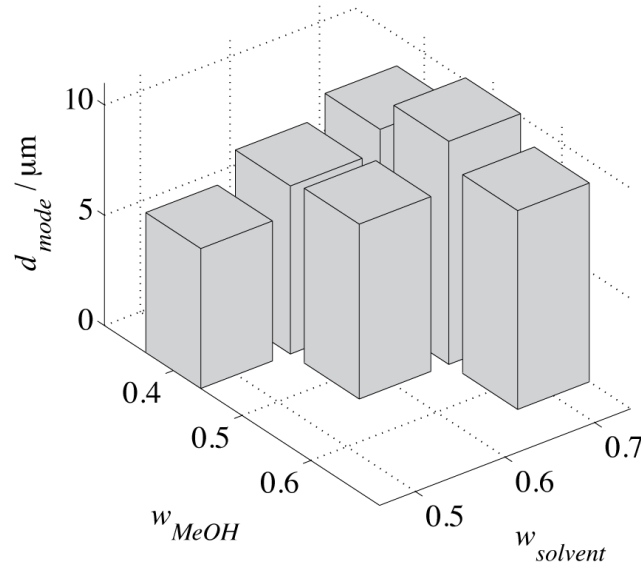


Figure 2.1. Mode pore diameter as a function of mass fractions w_{MeOH} ($= m_{MeOH}/m_{solvents}$) and $w_{solvent}$ ($= m_{solvents}/m_{total}$). Mode pore diameter roughly increases with both increasing solvent and MeOH fractions. Pore diameter dependence on solvent fraction is more pronounced.

In Figure 2.1, we plot mode pore diameter versus the gravimetric fractions w_{MeOH} $= m_{MeOH}/m_{solvents}$ and $w_{solvent} = m_{solvents}/m_{total}$. Note, we use here the term "mode pore diameter" to describe the characteristic scale of the pores of the monoliths, which we take

as the peak of the pore size distribution determined from mercury intrusion porosimetry measurements. We recognize that monolith morphology is complex and pores are not cylindrical (circular cross section) channels. This length scale therefore indicates the effective diameter of a circular capillary with equivalent capillary pressure.

For these example realizations, data showed an increase in pore diameter with increasing solvent fraction. This trend can be seen most clearly for $w_{MeOH} = 0.40$, where polymerizations were successful for all three solvent concentrations. As solvent fraction increases, so does total pore volume. For similar polymer globule formation characteristics (a reasonable assumption for these three cases, where porogen and monomer compositions are identical) porogenic solvents are expected to occupy volumes of larger characteristic dimension and increased pore size results.

In addition, the data of Figure 2.1 suggest a maximum in d_{mode} around $w_{MeOH} = 0.5$. This is seen most clearly for $w_{solvent} = 0.70$, where mode pore diameter increased from 8.6 to 10.1 and then decreased to 9.0 μm , for $w_{MeOH} = 0.4, 0.5$, and 0.6 , respectively. This result is consistent with trends observed by Yu *et al.* [23] who characterized the impact of porogenic solvent composition on median pore diameter. Yu reported a gradual increase in median pore diameter when increasing w_{MeOH} from 0.20 to 0.60. At $w_{MeOH} = 0.60$, pore diameter reached a maximum and then decreased suddenly upon further increase. We note that porogen composition is a particularly powerful tool for tailoring monolith pore structure for wick applications, as it has minimal impact on monolith chemical composition and porosity.

2.3.3 Designing high performance porous polymer wick material

We elucidate the effect of monolith microstructure on transport characteristics by again considering Darcy's Law. As equation (2.1) shows, holding all else constant, transport rate grows linearly with both permeability and liquid pressure gradient. In general, materials with large pores have high permeability, and therefore, high transport rates. At the same time, capillary transport requires small pores to maximize achievable liquid pressure gradients. In the next two sections, we will consider both permeability and capillary pressure dependency on microstructure in porous polymer monoliths. In addition, we will discuss opportunities to leverage key attributes of monolith microstructure to optimize transport for different applications.

2.3.3.1 Microstructure and permeability

Pore structure plays a critical role in determining resulting monolith permeability. We here discuss models for permeability, k , of equation(2.1), presented earlier. An often-used model for relating pore diameter to macroscopic permeability was developed by Carman and Kozeny [24]. Their model applies Hagen-Poiseuille type flow to an assumed pore structure comprised of many parallel, tortuous channels, of characteristic diameter, d . This results in the following relation for permeability:

$$k = \frac{\varepsilon d^2}{16k'}, \quad (2.2)$$

where ε is porosity, and k' is a geometric parameter describing pore shape and tortuosity. In real systems, there is no single pore dimension, and instead, the hydraulic diameter, d_H , is typically used for characteristic diameter. d_H is defined as four times the void volume to surface area ratio. For porous media, the resulting relation is:

$$d_H = \frac{4\varepsilon}{s_o(1-\varepsilon)}, \quad (2.3)$$

where s_o is specific area (pore surface area normalized by solid phase volume). Substituting into (2.2), we see that

$$k = \frac{\varepsilon^3}{k'(1-\varepsilon)^2 s_o^2}. \quad (2.4)$$

When applied to packed beds of spheres, specific surface area is related to particle diameter, d_p , as $s_o = 6/d_p$. Substituting and fitting to experimental data on packed beds, Carman found $k' = 5$, and obtained the result:

$$k = \frac{\varepsilon^3 D_p^2}{180(1-\varepsilon)^2} \quad (2.5)$$

Although (2.5) predicts permeability well for packed beds, its applicability across different types of porous media, including polymer monoliths, is limited [27]. Errors are associated with increased porosity (*i.e.*, porosity significantly greater than interstitial porosity of packed beds of spheres; typically ~0.4), wide distributions in pore diameters, and complex pore shapes and geometries. One approach is to determine an equivalent length scale describing monolith permeability, which can be used for comparison to more traditional porous media (*e.g.*, beds of packed spheres) [27]. For example, by employing (2.5), along with permeability measurements and an assumed packed-bed porosity of 0.4, we can determine an equivalent particle diameter, $d_{p,eq}$ [28, 29]. We give calculations of such a $d_{p,eq}$ of polymer monoliths in Table 2.1. Although this is a useful figure of merit for comparisons of hydrodynamic performance of diverse media, the physical significance of

$d_{p,eq}$ is difficult to discern, as it neither represents pore diameter nor correlates well with particle diameter, as calculated from specific surface area measurements.

Monolith pore structure complexity has limited the success of developing an analytical expression relating permeability to microscale properties. In particular, determining an appropriate length scale characterizing pore structure is difficult, as pore size distributions are often far from monodisperse. For example, Table 2.1 lists characteristic pore size distribution width, σ , for polymer monoliths. σ represents the standard deviation of a Gaussian, fit to the measured pore size distribution, and is an indicator of pore size variability within the monolith. As results indicate, in our polymer monoliths, distribution width is within an order of magnitude of d_{mode} .

As an approximation, Guiochon [28] suggests using a length scale related to average through-pore diameter, in conjunction with the Carman-Kozeny relation. Figure 2.2 shows measured versus predicted permeability, when using (2.2) with $d = d_{mode}$ and $k' = 1.3$ for our porous samples and samples of similar structures from the literature. The published data are from three manuscripts and cover a wide range of permeabilities [26, 15, 30]. In addition, the inset of Figure 2.2 shows measured versus predicted permeability using data from the present study only. In this inset and for these particular data, $k' = 2.4$ provided the best fit. Although results roughly show permeability dependence on εd_{mode}^2 , the significant scatter in data suggests that using a single measured length may not capture key physics which arise in polymer monoliths. Although beyond the scope of this work, further work is needed to explore specific flow effects associated with polymer monoliths,

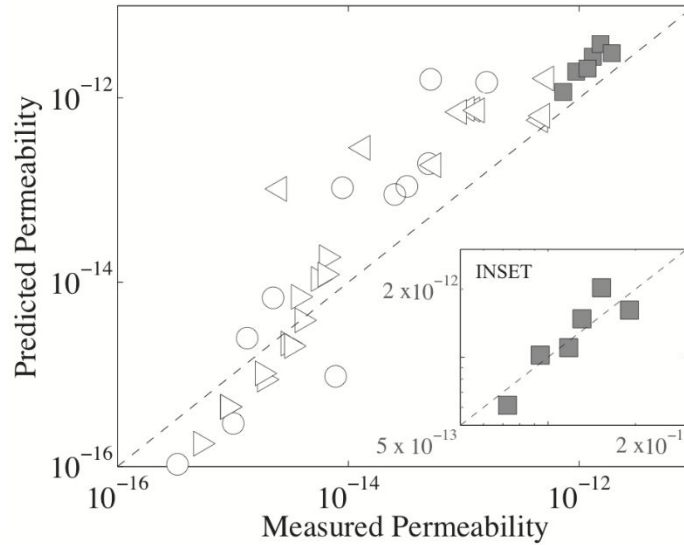


Figure 2.2. Predicted versus measured permeability for polymer monoliths. Predicted permeability calculated using (2.2), with $d = d_{mode}$, and with $k' = 1.3$ as a fitting parameter for porous polymer monoliths. Grey symbols (■) represent monolith data from the current study as summarized in Table 2.1. Inset shows only the current study data for which $k' = 2.4$ provides a best fit. Open symbols represent data taken from literature: Viklund *et al.* [15] (●), [30] (◁), and Mehrar *et al.* [26] (▷). Data show rough dependence of permeability on εd_{mode}^2 . Significant scatter suggests physics governing hydraulic resistance are not fully captured when using porosity and d_{mode} as a single measured length scale.

and reconcile these with porous flow data. Possible fruitful areas include accounting for bi-modal pore size distributions, the topography of these complex pore networks, and effects of broad pore size distributions.

2.3.3.2 Permeability dependence on polymerization chemistry

In Figure 2.3, we plot measured permeability of monoliths as a function of both w_{MeOH} and $w_{solvent}$. Measured permeabilities ranged from 0.73×10^{-12} to $1.9 \times 10^{-12} \text{ m}^2$. Data show permeability increased with increasing MeOH and total solvent fractions. In general, results are consistent with expected dependence on monolith pore diameter and porosity. For all samples, except for HE06, mode pore diameter increased with increasing w_{MeOH} and $w_{solvent}$. In addition, porosity is approximated by $w_{solvent}$. We therefore expect increases in w_{MeOH} and $w_{solvent}$ both to contribute toward high permeability. For the current chemistry, maximum permeability was achieved for the case of maximum w_{MeOH} and $w_{solvent}$ (*i.e.*, sample HE06). This result is not expected when using d_{mode} to characterize permeability, as d_{mode} for HE06 was slightly less than for HE05. We note that d_{median} , however, was indeed greatest for HE06. These results again highlight the difficulty associated with choosing a single measured length scale to characterize monolith microstructures and predict resulting permeability. In general, however, results confirm that when designing monoliths for high permeability, chemistries which result in high porosity and large pore diameters are desirable.

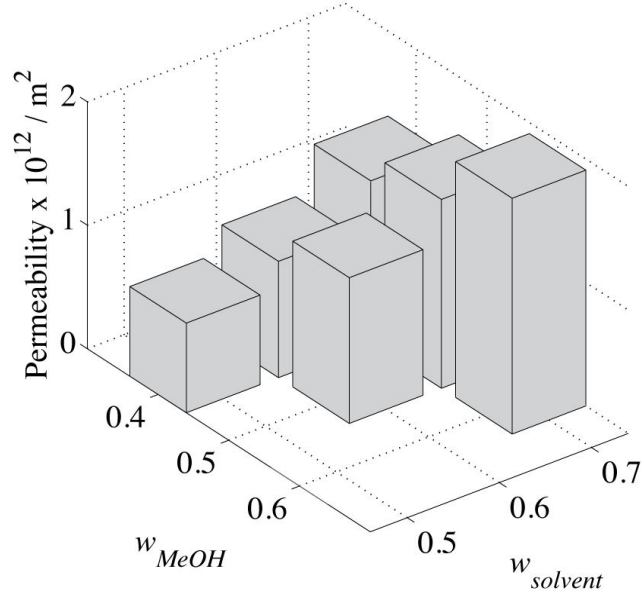


Figure 2.3. Monolith permeability as a function of w_{MeOH} and $w_{solvent}$. Permeability ranged from 0.73×10^{-12} to $1.9 \times 10^{-12} \text{ m}^2$. Results show permeability increased with increasing w_{MeOH} and $w_{solvent}$. Monolith permeability is consistent with trends in porosity and pore diameter (see Figure 2.1).

2.3.3.3 A note on wick geometry

We note that a wick's capacity to transport fluids is also highly dependent on macroscale wick geometry. Transport capacity increases with cross-sectional area normal to flow and is inversely proportional to characteristic wick length. For example, for the simple cylindrical shapes we fabricated for our permeability measurements (see Section 2.2.4), equation (2.1) can be integrated over wick cross-sectional area (normal to direction of flow), A , to obtain flow rate:

$$Q = \frac{k}{\mu} \left(\frac{A}{L} \right) \Delta P \quad (2.6)$$

where L is cylinder length (along flow direction), and ΔP is the total pressure drop across the wick. For more complex geometries, Litster *et al.* [31] defined a shape factor of the

form $(A/L)_{eff}$ which takes place of the area per length ratio in the equation above. For homogenous and isotropic wick materials (and wick dimensions significantly larger than pore dimensions) and similar flow distributions, this factor should be only a function of wick geometry and so is a key figure of merit in comparing wicks. Such formulations show how both wick microstructure (which determines k) and wick shape (which determine $(A/L)_{eff}$) are key to maximizing water transport rate.

2.3.3.4 Capillary transport

Capillary pressure arises due to surface tension and can be defined as the difference between gas and liquid pressures across a phase boundary. Capillary pressure is characterized by the Young-Laplace equation:

$$\Delta P_c = \frac{4\gamma \cos \theta}{d_{eff}}, \quad (2.7)$$

where γ is surface tension, θ is contact angle, and d_{eff} is the effective diameter of a hypothetical capillary.

An important figure of merit in wick systems is the product of the permeability of the material and the capillary pressure that it can sustain. For a given geometry (i.e., for fixed A/L in (2.6)), the maximum flow rate generated by surface tension effects is typically proportional to this product. For example, Ochterbeck [32] discusses the so-called capillary limit of heat pipes, which is defined as when the evaporation rate exceeds the maximum capillary transport rate in the heat pipe wick. Maximum capillary transport rate in these and similar wick systems is estimated using a capillary pressure of $\Delta P_c = 4\gamma/d_{eff}$ (Young-Laplace equation, with $\theta = 0$) and fully saturated wick permeability, k . Assuming

d_{eff} scales roughly with mode pore diameter,¹ we expect the maximum sustainable capillary transport rate to scale as k/d_{mode} . We therefore include this parameter on the right-hand side of Table 2.1.

For most applications, an ideal wick has pores small enough for sufficient capillary pressure and high permeability to minimize resistance to transport within the wick. As discussed in Section 2.3.3.1, permeability increases with characteristic pore diameter squared and, in most cases, capillary pressure must therefore be traded for permeability (and vice versa). Advanced wick materials, however, offer opportunity for enhanced capillary transport. For example, Huang *et al.* developed a micro-structured wick with a spatial gradient in pore size for use in a heat pipe. Pore size decreased from condenser to evaporator, thus simultaneously allowing for high capillary pressure in the evaporator and high permeability for transport in the adiabatic region [33]. Bimodal pore size distribution and spatial variations in microstructure that occur during polymerization [34] may possibly be leveraged for similar, high performance polymer wicks.

2.3.3.5 *In situ* fabrication of polymer wicks

We here describe an example application of the current porous polymer monoliths to the molding, synthesis, polymerization, and testing of *in situ* fabricated wicks for the parallel channel structure of a polymer electrolyte fuel cell cathode. We described the performance of this integrated wick and fuel cell system in a previous publication [14] but

¹ Note that the capillary pressure in a wick is a significant function of saturation, as described by Dullien [24]. Physically, this is associated with the fact that saturating liquid first fills the smallest pores associated with highest capillary pressure. Capillary pressure therefore decreases with increasing saturation. We here take the mode pore diameter simply as a scaling parameter.

here provide new and significant details regarding polymerization, fabrication, and preparation which should be useful to other applications of these porous monoliths. Figure 2.4 shows an overview of the fabrication procedure, which consists of three parts: (1-2) fabrication of a negative mold, (3-4) injection molding of polymer wicks, and (5) removal and cleaning.

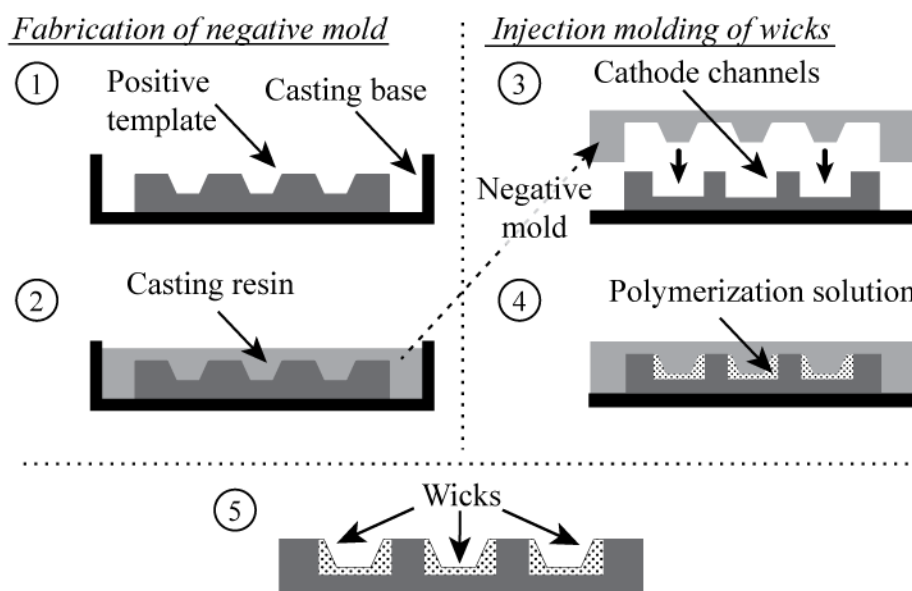


Figure 2.4. Schematics of procedure for *in situ* wick fabrication. *Fabrication of negative mold*: (1) We placed an aluminum positive template into an acrylic casting base designed to hold the casting resin. This template formed one surface of the resulting wicks by defining a negative image in the resin mold, and the part of interest here (the fuel cell cathode channels) defined the opposite surface. (2) We poured a solvent-resistant polyester resin over the aluminum positive template and allowed to cure for one week. Aluminum template was then removed. *Injection molding of wicks*: (3) We sandwiched the fuel cell cathode channels between the resin negative mold and a back support plate and compressed. (4) We then injected polymerization solution to fill remaining void space (injection ports not shown and wick layer thickness exaggerated for clarity), sealed the mold assembly, and then irradiated with UV for 1 h. *Removal and cleaning*: (5) Aluminum cathode channel plate, with attached wicks, was then removed and soaked in an MeOH bath for 24 h. Sample was then dried.

2.3.4 Fabrication of resin negative mold

We first fabricated a resin negative mold which would later define the top surface of the final wick geometry. Steps 1 and 2 of Figure 2.4 schematically show this fabrication procedure. We began with a positive template, whose geometry was precision end-milled from aluminum to match the desired top-surface geometry of the injection-molded wicks. We then transferred the positive template into a custom acrylic casting base, designed to hold the casting resin. A silicone rubber layer (not shown) between the aluminum positive template and casting base, prevented resin from seeping behind the positive template. We then coated the positive template and casting base with PVA mold-release (TAP plastics, Mountain View, CA) and allowed to dry for 1 h.

For UV initiated, *in situ* polymerization, the resin negative mold must be both UV transparent and solvent resistant. As such, we chose a polyester resin with moderate UV transparency and good solvent resistance (TAP Isophthalic High-Strength Resin, TAP Plastics, Mountain View, CA). We combined resin, catalyst (MEKP Liquid Catalyst, TAP Plastics, Mountain View, CA), and a surface curing agent (TAP Plastics, Mountain View, CA), mixed thoroughly and poured over the positive template. We allowed resin to cure at room temperature for one week. We then soaked the resin negative mold, with embedded positive template, in water to dissolve PVA mold release. We then removed the positive template, thereby leaving behind a negative image in the resin mold.

2.3.5 Injection molding of wicks

The fuel cell cathode channels (end milled from aluminum) were roughened to improve wick adhesion, and then sandwiched between the resin negative mold and a back support plate (Figure 2.4, step 3). A silicone layer between negative mold and support plate

helped to seal mold assembly. The present fuel cell application required high permeability wick material. We therefore chose solution HE06 for polymerization, which we injected into the mold assembly via two leuc-lock fittings (not shown), attached to the support plate. Mold assembly was then sealed and irradiated for 1 h, as described in Section 2.2.3 (Figure 2.4, step 4).

We note that we explored both thermal and UV initiation using AIBN and benzoin methyl ether as initiators, respectively. Thermal initiation required elevated polymerization temperature ($\sim 60^{\circ}\text{C}$) and long polymerization times (> 12 h). Over this period, evaporative porogenic solvent loss was significant and large voids formed in the resulting wick material. UV initiation required much shorter polymerization times (< 1 h) at room temperature, and evaporative losses of porogens were insignificant.

2.3.6 Removal and cleaning

Immediately following polymerization, we disassembled the mold assembly and carefully removed the aluminum cathode channels with polymer wicks attached (Figure 2.4, step 5). We placed the newly wick-integrated cathode channels in an MeOH bath for 24 h for diffusive removal of remaining monomers and porogens, refreshing with pure MeOH every 4 h. Figure 2.5 is an image of resulting cathode channels with integrated wicks. Polymerization resulted in high quality, monolithic, surface mounted wicks of $\sim 150\ \mu\text{m}$ thickness. This thickness is ~ 18 times the mean pore diameter. We note that wick thickness should be substantially greater than pore diameter to ensure good pore

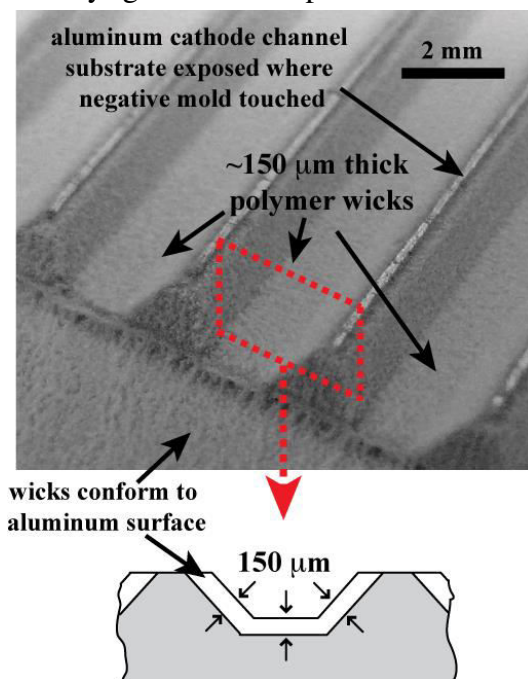


Figure 2.5. Image of resulting *in situ* fabricated wick material integrated into fuel cell cathode channels. Polymerization resulted in high-quality, $150\ \mu\text{m}$ thick monolithic wicks, which conform and are attached to the surface of the fuel cell cathode channels. The top of the channel-defining “ribs” are purposely left uncoated with wick material to promote good electrical contact for electrical current collection. The blow up is a cut away illustration, showing wick geometry (white) on aluminum cathode channel (grey) surface.

2.4 Conclusions and Recommendations

We fabricated and characterized porous monoliths of 2-hydroxyethyl methacrylate-*co*-ethylene dimethacrylate with the aim of achieving high permeability, hydrophilic materials for use as wicks and, once saturated, water transport layers. We characterized the effect of both monomer concentration and porogenic solvent composition on resulting monolith microstructure. Our example realizations indicated mode pore diameter increased with decreasing monomer concentration and increasing mass fraction of methanol (with respect to solvents). In addition, we found monolith permeability scaled roughly with porosity times the square of mode pore diameter, and reached a maximum of $1.91 \times 10^{-12} \text{ m}^2$. We recommend permeability normalized by mode pore diameter as an appropriate figure of merit which approximately captures the wick's capacity for capillary-pressure-driven flow. For a given wick geometry and flow orientation, maximum flow rate approximately scales with this figure in systems which leverage capillary pressure for liquid transport.

We then detailed a method to *in situ* polymerize wicks onto the surface of fuel cell cathode channels. Using a custom fabricated negative mold and UV polymerization, we achieved high quality, monolithic, polymer wicks of $\sim 150 \text{ }\mu\text{m}$ thickness which conformed to the surfaces of the fuel cell cathode channels. We hypothesize that this fabrication procedure can be adapted to other applications where precisely shaped and deposited wicks are advantageous for capillary liquid and/or multiphase transport.

Recommended future directions are numerous. Presently, analytical models do not accurately predict polymer monolith permeability. As such, exploring flow effects specific to polymer monoliths, including those associated with broad and bi-modal pore size

distributions, may be a fruitful future research direction. In addition, unique aspects of polymer monolith microstructure, including fabrication of monoliths with macroscopic gradients in pore-structure, could possibly be leveraged for high-performance capillary transport. Finally, the present work represents one of many possible methods for *in situ* fabrication of polymer wicking structures. Lithographically defined wicks represent a particularly exciting potential fabrication method that may offer fine geometric control, and also be amenable to batch fabrication processes.

2.5 Supplementary Information

Figure 2.6 shows measured pore size distributions for two separate realizations (synthesis runs) of monolith chemistry HE05. These distributions were determined from mercury porosimetry measurements performed by Porous Materials Inc. (Ithaca, NY). We also provide notes regarding permeability measurements.

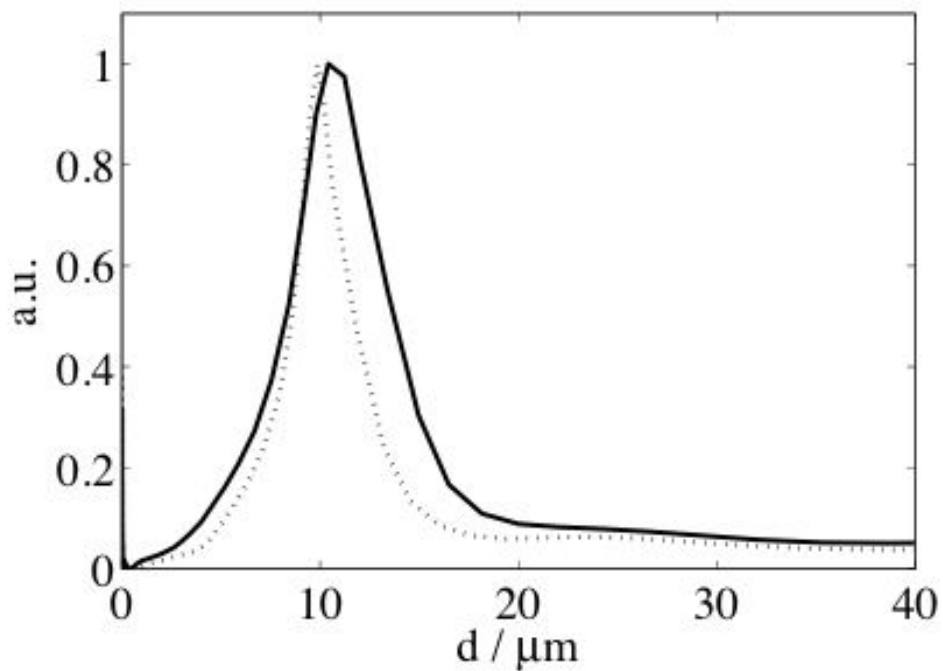


Figure 2.6. Pore size distributions of two separate fabrications of monolith chemistry, HE05. Shown are versions 1, HE05v1 (solid), and 2, HE05v2 (dashed). y-axis represents $d \log P / dV$, normalized by its maximum value. As is standard with porosimetry measurements, here P is capillary pressure and V is mercury intrusion volume. Results show moderately good agreement of pore-size distributions for the two realizations, with the first realization showing slightly larger pore sizes and wider distribution as compared to the second.

2.5.1 Notes regarding permeability measurement setup

After preparing samples via UV polymerization in quartz tubes, we flushed with methanol and then dried at 120 °C for 1 h. While drying, the monoliths shrunk slightly and partially delaminated from the quartz tubing walls. This allowed us to gently push samples out of the quartz tube. We then placed the samples into heat shrink tubing, along with silicone tubes (with slightly smaller diameter than our samples) on either end. Heat shrink tubing is thin-walled polymer tubing that becomes very pliable (plastically deforms easily) and shrinks when exposed to heat. Upon heating with hot air, the heat shrink permanently contracts and conformed to monolith samples and silicone tubes, creating a seal. We observed minimal compression of samples. In this way we achieved a good seal between silicone tubing and our sample. We then connected samples to a mass flow controller and pressurized air tank for permeability measurements, as described in the chapter.

3 Coupling Isotachophoresis with Affinity Chromatography for Rapid and Selective Purification with High Column Utilization: Theory

The contents of this chapter were previously published by V. Shkolnikov and J. G. Santiago [3] in *Analytical Chemistry* journal and are reproduced here with minor modifications.

3.1 Introduction

Affinity chromatography (AC) is a chromatographic technique that leverages a specific binding agent, the affinity ligand, for purification, separation, and/or analysis of sample components. The affinity ligand (probe) is used to selectively yet reversibly capture the sample component of interest (target). Numerous samples and sample components have been and continue to be analyzed or purified using AC, including enzymes, lectins, other proteins, and nucleic acids [99-102]. For many samples, including important biological samples (e.g., blood, cell lysate), the component of interest is present in very low concentration, while background, potentially fouling species are present in relatively high concentrations. This necessitates processing of a substantial sample volume through the affinity substrate. Additionally, low target concentrations imply low target-probe binding

rates [103]. These factors each increase the time of the affinity assay, can lead to poor substrate utilization, and/or poor purification yield, limiting applications of the method.

The aforementioned limitations of AC can be addressed by increasing the forward binding rate constant of reactions [103], but the binding rate constant is often difficult to improve upon [100]. A second method is to preconcentrate and purify the target prior to the affinity reaction. We here explore the use of increasing target purity and concentration using isotachopheresis (ITP). ITP uses a buffer with a high mobility co-ion (same charge as analyte) and a second buffer with a lower mobility co-ion. Analyte species of intermediate mobility focus between these co-ions and are thereby preconcentrated and separated [10, 11]. ITP has been demonstrated in a variety of applications related to the current work including extraction and purification of nucleic acids from complex biological samples[104], and 14,000-fold speed up of homogenous nucleic acid hybridization reactions in free solution [18].

ITP has been used in conjunction with affinity assays in several applications, and several models for these processes have been developed. For example, Garcia-Schwartz et al. presented an approach combining ITP and an affinity reaction to detect micro-RNA [105, 106]. They used ITP to accelerate hybridization between a mobile target species and a mobile fluorescent DNA probe in a microchannel. This ITP zone was then transported into a channel section containing cross-linked polyacrylamide gel functionalized with DNA complementary to the fluorescent DNA probe. This method was used to remove signal background (a negative enrichment strategy) and so enhance quantitation and specificity [105, 106]. Garcia-Schwartz et al. presented a volume averaged model for the reaction of the mobile species. However their analysis did not treat the spatiotemporal

dynamics of the surface (gel) affinity reaction. Their analysis focuses on reactions prior to and after the affinity column and assumes the affinity capture occurs instantaneously in negligible space. Recently (work published during preparation of this manuscript), Karsenty et al. used ITP to accelerate a reaction of a DNA target to an immobilized DNA probe on a short region of stationary magnetic beads and present a model for this process [107]. Their model captures the temporal, volume-averaged dynamics of a reaction between a target preconcentrated with ITP and a bead immobilized probe. However, their model only addresses the regime where the target concentration remains approximately constant during the reaction and is only applicable to short (order of ITP peak width) capture regions. Their model does not address the spatial dynamics of the reaction. Despite these related studies we know of no model or analysis of the coupled spatiotemporal dynamics of a reaction between a species focused in ITP and a surface, gel, or porous region.

We here investigate the theory behind physicochemical processes of integrating ITP and AC. We consider the case of an AC column composed of a porous polymer monolith (PPM) functionalized with a synthetic cDNA ligand. However, the current approach is easily extended to any integration of ITP and a stationary affinity column. The goal of this type of integration is to (a) drastically reduce assay time; (b) improve column utilization; (c) allow for capture of targets with higher dissociation constants; (d) obviate the need for high pressure specialized pumps; (e) directly integrate an automatic wash step into the process, eliminating a separate wash step; and (f) reduce affinity substrate fouling (and competing reactions) by partially separating sample compounds by their electrophoretic mobility.

We describe the principle of coupling ITP preconcentration and AC purification. We derive and present an analytically solvable one-dimensional transport model for coupling of ITP with a semi-infinite AC porous column and second order reversible reaction kinetics. Our model describes the spatiotemporal dynamics of target-probe binding in the affinity region, allowing for complete capture of target. This includes the coupled effects of target distribution width, distribution intensity, ITP zone velocity, forward and reverse reaction constants, and probe concentration on necessary affinity region length, assay time, and capture efficiency. Our new analytical approach allows us to collapse these six independent variables down to three non-dimensionalized parameters summarizing all regimes. In Chapter 4 [8], we experimentally validate our model and

demonstrate sequence specific purification of 25 nt target DNA from 10,000-fold more abundant fish sperm DNA.

3.2 Concept and theory

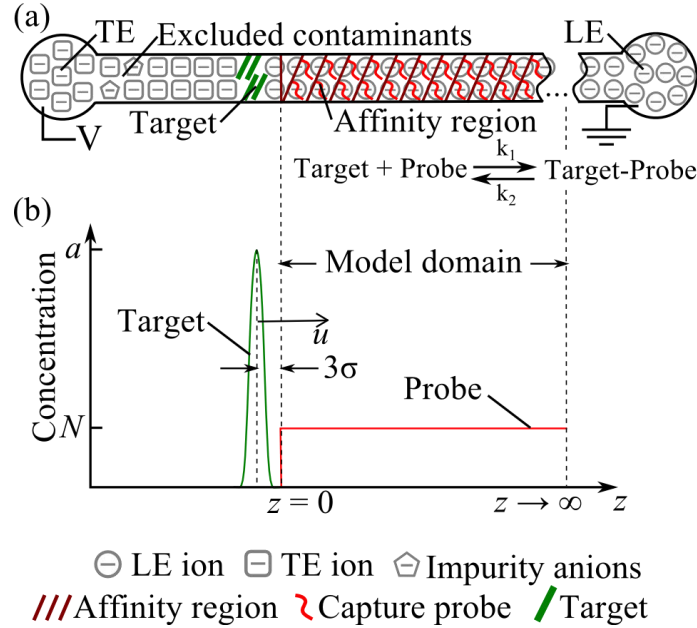


Figure 3.1. (a) Schematic of assay for ITP-aided affinity chromatography (ITP-AC). We consider an assay in a capillary with a semi-infinite affinity capture region as shown. Under the influence of electric field, target is extracted from a sample reservoir, separated from contaminants, and concentrated at the LE-TE interface. It is then transported to and through the affinity region. Within the affinity region, the target reacts with the immobilized capture probe via a second-order reversible reaction where k_1 and k_2 are the forward and reverse reaction rate constants, respectively. (b) Initial conditions for our model of ITP-AC. At $t = 0$, the target has a Gaussian distribution with standard deviation σ and peak concentration a ; its peak is located 3σ from the entrance of the affinity region. The target moves with velocity u through the affinity region. The affinity region is semi-infinite beginning at $z = 0$ (where z is the axial coordinate of the capillary) and containing a uniformly distributed probe of volume-averaged concentration N .

3.2.1 Method concept

We aim to decrease the assay time and improve affinity region utilization by purifying the target and increasing the affinity capture reaction rate. Figure 3.1 summarizes the key aspects of our approach and the initial conditions for our model. As in the

experiments we will show in the Chapter 4, we consider a free-standing capillary which contains a porous affinity region. The affinity region contains pores sufficiently large to allow easy pressure-driven pumping of liquid or air. First, we fill leading electrolyte (LE) in the LE reservoir and in the entire capillary (including the porous affinity region). We then fill the trailing electrolyte (TE) reservoir with a mixture of trailing electrolyte buffer and sample. Upon application of the electric field, the target is extracted from the TE reservoir, preconcentrated into the LE-TE interface, and transported toward and through the affinity region (Figure 3.1a). Possible contaminating species which are neutral, oppositely charged of the target, or co-ionic but with a lower electrophoretic mobility magnitude than the TE co-ion are excluded [104]. Upon reaching the affinity region, the target reacts with the immobilized capture probe and is captured. After capture, we pump air through the system to remove all liquid from the column and so arrest further reactions.

The initial focusing of ITP is selective [11, 104] and helps prevent fouling of the affinity region by unfocused background species. The increase of the target concentration via ITP promotes faster capture reaction and the target is captured in a smaller, upstream region of the column. Exposure of the ITP-focused analyte to reaction sites on the column is temporary and is followed by a wash associated with the TE zone entering the column. We limit the time between this electrokinetic wash step and the removal of liquids with air to control the stringency of the wash step. This approach limits the time for dissociation reaction to occur so the captured target concentration is effectively “frozen” by the introduction of air. This enables capture of targets with relatively high dissociation rate if necessary.

3.2.2 Transport and focusing of trace analytes in isotachophoresis

ITP is an electrokinetic technique used to preconcentrate and separate analytes [9-11]. We here leverage a mode of ITP known as “peak mode” ITP where trace analytes co-focus into a relatively narrow peak at the interface of LE and TE [9, 26, 27]. In peak mode ITP, trace analytes do not appreciably contribute to local conductivity. The peak width and analyte locations are determined by the mobilities of the ions of LE and TE and electric fields established by and at the interface between TE and LE buffers [26]. The analyte mobility in the TE zone is higher than that of the TE co-ion. The analyte mobility in the LE zone is also lower than that of the LE co-ion. This arrangement of mobilities enables purification of, for example, nucleic acids from complex mixtures and excludes possible fouling species from the ITP zone [9, 104]. If, as in our case, the analyte mobility is significantly different from that of the LE and TE ions, the target distribution is narrow and approximately Gaussian in shape [26].

3.2.3 One dimensional transport reaction model

We derive an unsteady, one-dimensional model for ITP which we will show captures the essential dynamics of the process. We chose a reduced order model to identify the key governing parameters of the process. We model focusing of an ionic target in peak mode ITP, and migrating towards a semi-infinite affinity capture region. In the affinity region, the target reacts with the surface bound probe according to a simple second-order reversible reaction of the following form: $\text{Target} + \text{Probe} \rightleftharpoons \text{Target-Probe}$. We set time $t = 0$ at the point where the target just starts to enter the affinity region (Figure 3.1b). We assume the target has a Gaussian concentration profile with a width given by the interface width between the LE and the TE. This is a common assumption for modeling the

distribution of trace analyte focused at the LE-TE interface [18, 27, 108]. As usual for peak mode ITP, we further assume that the change in concentration of the target has no effect on the electric field in ITP [18, 27, 108]. We start with the general advection-diffusion equation for the solution inside the porous affinity region with second order reversible reaction at the surface:

$$\frac{\partial c'}{\partial t} = \nabla \cdot (D \nabla c') - \nabla \cdot (\vec{u} c'), \quad (3.1)$$

where c' is the local target concentration, \vec{u} is the target velocity, D is the target diffusion coefficient, and t is time. The reaction with the target occurs at the boundary between the solvent and the surfaces of the porous solid. The solid is impermeable to the target and fluid. Hence at this boundary we have

$$-D \nabla c' \cdot \vec{q} = k_1' c' (N' - n') - k_2' n', \quad (3.2)$$

where \vec{q} is the unit normal to the surface of the monolith, n' is the surface density of the captured target (moles per area), N' is initial surface density of the probe, and k_1' and k_2' are the forward and reverse constants respectively. We also have an auxiliary relation for n'

$$\frac{\partial n'}{\partial t} = -k_1' c' (N' - n') + k_2' n'. \quad (3.3)$$

To simplify these three dimensional equations we note that the net flow occurs along the direction of the axis of the macroscopic porous affinity region and that this region is homogeneous and anisotropic. We model the region as a bundle of tortuous cylindrical pores [109] with a mean tortuosity τ . We define a coordinate s that follows the center

contour of these tortuous cylindrical pores, the coordinate r that is locally normal to s , and the azimuthal θ for cylindrical coordinates. We also note that we assume the target diffusion coefficient D to be constant everywhere. Therefore, we rewrite equations (3.1) and (3.2) as

$$\frac{\partial c'}{\partial t} = D \left[\frac{1}{r} \frac{\partial}{\partial r} \left(r \frac{\partial c'}{\partial r} \right) + \frac{1}{r^2} \frac{\partial^2 c'}{\partial \theta^2} + \frac{\partial^2 c'}{\partial s^2} \right] - \left[\frac{1}{r} \frac{\partial (ru_r c')}{\partial r} + \frac{1}{r} \frac{\partial (u_\theta c')}{\partial \theta} + \frac{\partial (u_s c')}{\partial s} \right] \quad (3.4)$$

$$-D \frac{\partial c'}{\partial r} \Big|_{r=r_0} = k'_1 c' (N' - n') - k'_2 n', \quad (3.5)$$

where r_0 is the radius of the pore. We assume that inside the tortuous pore the fluid flows only in the axial direction, and hence $u_r = u_\theta = 0$. This simplifies equation (3.4) to

$$\frac{\partial c'}{\partial t} = D \left[\frac{1}{r} \frac{\partial}{\partial r} \left(r \frac{\partial c'}{\partial r} \right) + \frac{1}{r^2} \frac{\partial^2 c'}{\partial \theta^2} + \frac{\partial^2 c'}{\partial s^2} \right] - \frac{\partial (u_s c')}{\partial s}. \quad (3.6)$$

Next we consider the rates of diffusion from the bulk of a pore to the pore surface where the reaction takes place, and the rate of reaction. The time for the target to diffuse from the center of the pore to the pore surface scales as [110]

$$t_{diff} \approx r_0^2 / D \quad (3.7)$$

and the time for the target to be captured scales as

$$t_{rxn} \approx 1 / (k_1 N). \quad (3.8)$$

We take the diffusion coefficient of our target DNA oligomer to be roughly $10^{-6} \text{ cm}^2 \text{ s}^{-1}$. This is a typical magnitude of the diffusion coefficient for 20 nt oligomers in aqueous solution [111]. Using this, and the forward rate constant, the probe density, and the pore size that we obtained in this work (see Chapter 4 [8]) we find $t_{diff} \approx 10^{-3} \text{ s}$ and $t_{rxn} \approx 20 \text{ s}$. We conclude that the pore stays locally well mixed via diffusion, despite the reaction, yielding an approximately uniform concentration through the micro-scale tortuous pore cross sectional area. Therefore, we simplify equation (3.6) and (3.5) further by defining a pore cross sectional area averaged concentration

$$c''(s) \equiv \frac{1}{\pi r_0^2} \int_0^{r_0} \int_0^{2\pi} c'(r, \theta, s) r dr d\theta. \quad (3.9)$$

We then integrate equation (3.6) subject to the boundary condition (3.5) over r from 0 to r_0 and over θ from 0 to 2π and obtain

$$\frac{\partial c''}{\partial t} + \frac{\partial(u_s c'')}{\partial s} = D \frac{\partial^2 c''}{\partial s^2} - k_1'' c'' (N'' - n'') + k_2'' n'' \quad (3.10)$$

$$\frac{\partial n''}{\partial t} = -k_1'' c'' (N'' - n'') + k_2'' n''. \quad (3.11)$$

Next, we transform equation (3.10) into the axial coordinate of the porous monolith, z (which is along the major axis of monolith and capillary, see Figure 3.1). As is usual, the coordinate z is related to the pore coordinate s through tortuosity τ such that $\tau = s/z$.

$$\frac{\partial c''}{\partial t} + \frac{1}{\tau} \frac{\partial(u_s c'')}{\partial z} = D \frac{1}{\tau^2} \frac{\partial^2 c''}{\partial z^2} - k_1'' c'' (N'' - n'') + k_2'' n''. \quad (3.12)$$

Next, we define an effective concentration averaged over the cross sectional area for the monolith as

$$c = \frac{1}{A_M} \int_{A_M} c_i'' dA = \frac{A_{cap}}{A_M} \frac{1}{M} \sum_{i=1}^M c_i'', \quad (3.13)$$

where A_M is the geometric cross sectional area of the monolith, A_{cap} is the total cross sectional area of the pores and M is the total number of the tortuous cylindrical pores making up the monolith. We define the void fraction ϕ to be $\phi = A_{cap}/A_M$. We apply this average to all tortuous cylindrical pore in the tortuous pore bundle concentration of which is described by equation (3.12) and (3.11) to obtain

$$\frac{\partial c}{\partial t} + \frac{\partial(vc)}{\partial z} = D \frac{1}{\tau^2} \frac{\partial^2 c}{\partial z^2} - k_1 c(N - n) + k_2 n \quad (3.14)$$

$$\frac{\partial n}{\partial t} = -k_1 c(N - n) + k_2 n, \quad (3.15)$$

where v is the advection velocity [109]. We henceforth work with this concentration as it directly defines the capacity of the affinity region (i.e., moles of target that can be captured per geometric volume of affinity region) and is directly, experimentally observable.

We simplify equation (3.14) by expanding the target velocity into a uniform velocity, u , (i.e., not a function of z) and a perturbation \tilde{u} which depends on z and t as follows:

$$v(z) = u + \tilde{u}(z, t). \quad (3.16)$$

The expansion of equation (3.14) follows:

$$\frac{\partial c}{\partial t} + u \frac{\partial c}{\partial z} + \frac{\partial(\tilde{u}c)}{\partial z} = D \frac{1}{\tau^2} \frac{\partial^2 c}{\partial z^2} - k_1 c(N - n) + k_2 n. \quad (3.17)$$

For our process, we assume our target remains focused by ITP, so that its velocity v is governed by the electric field of the ITP near the LE-TE interface [11]. Our experimental observations confirm that this assumption is accurate for the cases we considered (e.g., where target has strong affinity for the immobilized probe). Experimentally, we observe zones of unbound analytes remain focused in ITP and traveling at ITP-controlled velocities despite potential reactions with the affinity column (see the second part of this two-part series[8]). We note that, for situations where pressure driven and electroosmotic flow are important, we hypothesize that we can assume the advection velocity of the LE-TE interface will be the arithmetic sum of the macroscopic ITP and bulk flow velocities through the column. Next, we use this empirical observation concerning analyte velocity to construct an approximate (heuristic) description of the analyte velocity distribution near the ITP zone interface.

The target is a trace analyte, so it does not contribute significantly to the conductivities of the zones and hence the local electric field [18, 27, 108]. Hence, for a trace analyte focused at the LE-TE interface, its velocity is governed by the electric field distribution near the TE-to-LE interface. This shape of the electric field distribution can be approximated as sigmoidal curve, being highest in the TE and lowest in the LE [11, 25]. We here approximate the electric field as an error function. Further, the LE-TE interface electromigrates at the ITP zone velocity, so we assume the inflection of the sigmoid also migrates with the LE-TE interface. We let the deviation of the target velocity from the ITP LE-TE interface velocity u be some small fraction of the LE-TE velocity, εu . We set the characteristic width of the LE-TE interface as σ . Hence, we express the target velocity as

$$v = u + \varepsilon u \operatorname{erf} \left[-(z - ut + 3\sigma)/\sigma \right], \quad (3.18)$$

which has the form of a uniform velocity plus a perturbation as in equation (3.16). We approximate the quantity εu , the amplitude of the error function, as the difference between the analyte velocity in the adjusted TE (equal to $\mu_{a,TE}E_{TE}$, where E_{TE} is the electric field in the TE) and that the ITP LE-TE interface (equal to $\mu_{TEion,TE}E_{TE}$ [11]). Therefore, we write the smallness parameter as simply

$$\varepsilon = (\mu_{a,TE} - \mu_{TEion,TE}) / \mu_{TEion,TE}, \quad (3.19)$$

$\mu_{a,TE}$ is the mobility of the analyte in the TE, and $\mu_{TEion,TE}$ is the mobility of the TE ion in the TE. To exclude many contaminating species from focusing with the analyte, we choose the TE ion mobility to be near to that of the analyte (say within 10-20%), which makes ε small.

Next we cast (3.17) and (3.15) in dimensionless form as follows: c^* and n^* are free target and bound target concentrations normalized by initial probe concentration N , t^* is time normalized by the reaction time scale $1/(k_1N)$ and z^* is axial coordinate normalized by the advection-reaction length scale $u/(k_1N)$, and $\beta = k_2/(k_1N)$ is the non-dimensionalized equilibrium dissociation constant. We scale \tilde{u} by εu for \tilde{u}^* . We obtain

$$\frac{\partial c^*}{\partial t^*} + \frac{\partial c^*}{\partial z^*} + \varepsilon \frac{\partial(\tilde{u}^* c^*)}{\partial z^*} = \frac{Dk_1N}{\tau^2 u^2} \frac{\partial^2 c^*}{\partial z^{*2}} - c^*(1 - n^*) + \beta n^* \quad (3.20)$$

$$\frac{\partial n^*}{\partial t^*} - c^*(1 - n^*) + \beta n^* = 0. \quad (3.21)$$

As we shall show in Chapter 4 [8], our process is well characterized by the following parameters: $D \approx 10^{-6} \text{ cm}^2 \text{ s}^{-1}$ [111], $k_1 \approx 10^3 \text{ M}^{-1} \text{ s}^{-1}$, $N \approx 30 \text{ } \mu\text{M}$, $u \approx 0.05 \text{ mm s}^{-1}$, and τ between 1 and 2. We therefore estimate $Dk_1N/\tau^2 u^2$ to be between 0.0003 and 0.001,

significantly smaller than unity. We thus drop the first term on the right hand side and simplify (3.20) to

$$\frac{\partial c^*}{\partial t^*} + \frac{\partial c^*}{\partial z^*} + \varepsilon \frac{\partial(\tilde{u}^* c^*)}{\partial z^*} + c^*(1 - n^*) - \beta n^* = 0. \quad (3.22)$$

We combine (3.22) and (3.21) as

$$\frac{\partial c^*}{\partial t^*} + \frac{\partial c^*}{\partial z^*} + \varepsilon \frac{\partial(\tilde{u}^* c^*)}{\partial z^*} + \frac{\partial n^*}{\partial t^*} = 0 \quad (3.23)$$

$$\frac{\partial n^*}{\partial t^*} - c^*(1 - n^*) + \beta n^* = 0. \quad (3.24)$$

We seek a straightforward expansion for the solution of (3.23) and (3.24) in the form

$c = c_0 + \varepsilon c_1 + \varepsilon^2 c_2 + \dots$, $n = n_0 + \varepsilon n_1 + \varepsilon^2 n_2 + \dots$ and substitute these into (3.23) and (3.24).

Collecting the coefficients of each power of ε and equating:

$$\begin{aligned} \varepsilon^0 : \quad & \frac{\partial c_0^*}{\partial t^*} + \frac{\partial c_0^*}{\partial z^*} + \frac{\partial n_0^*}{\partial t^*} = 0 \\ & \frac{\partial n_0^*}{\partial t^*} - c_0^*(1 - n_0^*) + \beta n_0^* = 0 \end{aligned} \quad (3.25)$$

$$\begin{aligned} \varepsilon^1 : \quad & \frac{\partial c_1^*}{\partial t^*} + \frac{\partial c_1^*}{\partial z^*} + \frac{\partial n_1^*}{\partial t^*} + \frac{\partial(\tilde{u}^* c_0^*)}{\partial z^*} = 0 \\ & \frac{\partial n_1^*}{\partial t^*} - c_1^* + \beta n_1^* = 0 \end{aligned} \quad (3.26)$$

$$\begin{aligned} \varepsilon^2 : \quad & \frac{\partial c_2^*}{\partial t^*} + \frac{\partial c_2^*}{\partial z^*} + \frac{\partial n_2^*}{\partial t^*} + \frac{\partial(\tilde{u}^* c_1^*)}{\partial z^*} = 0 \\ & \frac{\partial n_2^*}{\partial t^*} - c_2^* + \beta n_2^* + c_1^* n_1^* = 0. \end{aligned} \quad (3.27)$$

For simplicity and emphasis, we here concentrate on the first order accurate (zeroth order) equations as we feel these represent the simplest engineering approximation which captures the essence of the problem. We will later show in Chapter 4 that predictions from these equations agree well with measurements of key ITP-AC parameters at our experimental conditions [8]. For interested readers, we discuss in the Supplementary Information (SI) (Section 3.5.1) the more accurate second and third order accurate formulations of our problem.

Initially the affinity region is free from target, which supplies the initial condition $c(z,0) = 0, n(z,0) = 0$ (Figure 3.1b). We model the Gaussian profile of the ITP focused target entering the affinity region as a time varying boundary condition on the affinity region,

$$c(0,t) = a \exp \left[- \left((ut - 3\sigma) / (\sqrt{2}\sigma) \right)^2 \right] \quad (3.28)$$

representing a Gaussian distribution with maximum concentration a and standard deviation σ traveling at ITP velocity u (Figure 3.1b). We chose arbitrarily that at $t = 0$ the Gaussian's maximum is 3σ to the left of the start of affinity region and therefore just beginning to interact with the affinity region (Figure 3.1b). We then cast the initial and boundary conditions in the following non-dimensionalized form:

$$c^*(z^*,0) = n^*(z^*,0) = 0 \quad (3.29)$$

$$c^*(0,t^*) = \frac{a}{N} \exp \left[- \left(\frac{ut^*}{k_1 N \sqrt{2}\sigma} - \frac{3}{\sqrt{2}} \right)^2 \right]. \quad (3.30)$$

We further introduce the following non-dimensional parameters

$$\begin{aligned}\alpha &= a\sqrt{2\pi}/N \\ Da &= \sigma k_1 N / u,\end{aligned}\tag{3.31}$$

and rewrite the boundary condition as

$$c^*(0, t^*) = \left(\alpha/\sqrt{2\pi}\right) \exp\left[-(t^*/Da - 3)^2/2\right].\tag{3.32}$$

Here, α represents the peak concentration of the target in the Gaussian distribution scaled by the initial probe concentration N . The Damkohler number, Da , as usual describes the characteristic ratio between an electrophoretic (advection) time scale σ/u and the time scale of reaction $1/(k_1 N)$. Da is also usefully interpreted as a characteristic width of the Gaussian distribution scaled by advection-reaction length scale $u/(k_1 N)$. The product αDa is the total amount of target in the Gaussian distribution scaled by u/k_1 and, as we will show later, determines whether the affinity region locally saturates. We perform a straightforward expansion of the boundary and initial conditions (3.29) and (3.32), similarly as for (3.23) and (3.24), and obtain

$$\begin{aligned}\varepsilon^0 : \quad & c_0^*(z^*, 0) = n_0^*(z^*, 0) = 0 \\ & c_0^*(0, t^*) = \frac{\alpha}{\sqrt{2\pi}} \exp\left[-\frac{(t^*/Da - 3)^2}{2}\right] \\ \varepsilon^1 : \quad & c_1^*(z^*, 0) = n_1^*(z^*, 0) = c_1^*(0, t^*) = 0 \\ \varepsilon^2 : \quad & c_2^*(z^*, 0) = n_2^*(z^*, 0) = c_2^*(0, t^*) = 0.\end{aligned}\tag{3.33}$$

Equations (3.25) through (3.27) and initial and boundary conditions (3.33) therefore constitute a well-posed, simplified description of our problem. Below we present solutions to these equations, identify key figures of merit, and discuss a series of limiting regimes of practical interest to the experimentalist.

3.3 Results and Discussion

3.3.1 Analytical solution for bound and free target concentration

We analytically solved equations (3.25) and demonstrate a solution method for equations (3.26) and (3.27). Our approach is similar to that of Thomas [112], but here subject to our boundary and initial conditions (3.33) including our heuristic description of ITP zone shape and propagation. Briefly, we transformed (3.25), (3.26) and (3.27) into a coordinate system moving with the ITP velocity. Then we converted the result into a potential function form which collapses the two equations into a single equation. We then solved the resulting equation using Laplace transforms. We provide the full solution in the SI, Section 3.5.1. We obtained first order accurate equations for non-dimensionalized bound target concentration as follows:

$$n^* = 1 - \frac{1}{\phi} \frac{\partial \phi}{\partial z^*} + O(\varepsilon) \quad (3.34)$$

and for free target concentration

$$c^* = \frac{1}{\phi} \frac{\partial \phi}{\partial y} - \beta + O(\varepsilon) \quad (3.35)$$

where

$$\phi(z^*, y) = I_0(2\sqrt{\beta y z^*}) + \int_0^y \Lambda(y - y') I_0(2\sqrt{\beta y' z^*}) dy' + \int_0^{z^*} \exp(z^* - z') I_0(2\sqrt{\beta y z'}) dz', \quad (3.36)$$

$$\Lambda(y) = \left(\frac{\alpha}{\sqrt{2\pi}} \exp \left[-\frac{(y/Da - 3)^2}{2} \right] + \beta \right) \exp \left[y\beta + \frac{\alpha Da}{2} \left(\operatorname{erf} \left(\frac{y/Da - 3}{\sqrt{2}} \right) - \operatorname{erf} \left(\frac{-3}{\sqrt{2}} \right) \right) \right], \quad (3.37)$$

$$y = t^* - z^*. \quad (3.38)$$

Here I_0 is the modified Bessel function of the first kind of zeroth order. For convenience, we evaluated numerical values of the solution using custom MATLAB scripts. We use these solutions to consider the effects of non-dimensionalized target-probe dissociation constant, non-dimensionalized target distribution width, and non-dimensionalized peak distribution concentration on key affinity capture figures of merit: capture efficiency n/N , capture length p_z , and capture time p_t . We then examine three important regimes of the solution: (a) $\alpha Da < 1$ (b) $Da \gg 1$ and (c) $\beta_{cn} \gg \beta_{target}$ (where subscript “cn” refers to contaminant).

3.3.2 Spatiotemporal dynamics predicted by analytical solution

3.3.2.1 Effect of non-dimensionalized equilibrium dissociation constant β

In Figure 3.2, we plot representative solutions for the scaled bound target concentration n/N versus scaled distance along the axis of the channel, and scaled times associated with a range of β from 10^{-6} to 3. These plots can be interpreted intuitively as spatiotemporal plots of bound target concentration (scalar) as a function of scaled distance and time in the abscissa and ordinate, respectively. In Figure 3.2a, b, and c, $\alpha Da = 4.3 \times 10^{-4}$ and $\alpha = 1.1 \times 10^{-3}$. In the regime of $\alpha Da < 1$, the affinity region is not locally saturated ($n/N < 1$). For relatively low β (e.g., 10^{-6}), the forward (affinity) reaction dominates and captured target remains bound. Here, as the target Gaussian peak enters the affinity region, the target

binds and the concentration of bound target n at the leading edge increases gradually with time (Figure 3.2a). At the same time, some of the target does not bind at the leading edge and is able to penetrate deeper into the affinity region and bind there. Even as this penetration proceeds, target continues to bind near the leading edge. This creates the J-shaped bound target concentration contours shown in Figure 3.2a. Under these conditions (as we will show in Section 3.3.2.2 below), 95% of the target is captured in approximately 2.8 advection-reaction length scales, providing an inherent non-dimensional capture length. As β increases to about 10^{-1} , some of the target can desorb and readsorb during the effective capture time, and so the target can penetrate deeper into the affinity region (Figure 3.2b). For β of order unity and higher, the concept of a capture length becomes invalid, as the target migrates through the affinity region, continuously adsorbing and desorbing as it travels. For our characteristic values of Da and α , this continuous transport becomes very prominent at $\beta = 3$ (Figure 3.2c). We hope to further study high β , chromatographic-separation-type regimes in the future.

In the regime of $\alpha Da > 1$, the leading edge of the affinity region becomes saturated ($n/N = 1$). This forces target to bypass the leading edge and penetrate deeper. In Figure 3.2d, we show the case where $\alpha Da = 8$, while α is still only 1.1×10^{-3} . We see that the effect of leading edge saturation is to establish a new effective leading edge for new captures. This new effective leading edge shifts up in time and rightward in the axial coordinate as free target penetrates and explores new regions of available sites (Figure 3.2d). The J-shaped profiles shift up and right accordingly. Under these conditions (as we will show in Section 3.3.2.2 below), the length of affinity region needed to capture 95% of

the target depends mostly on the absolute amount of target and the capacity of the affinity region, N (and less sensitive to balances between reaction and advection times).

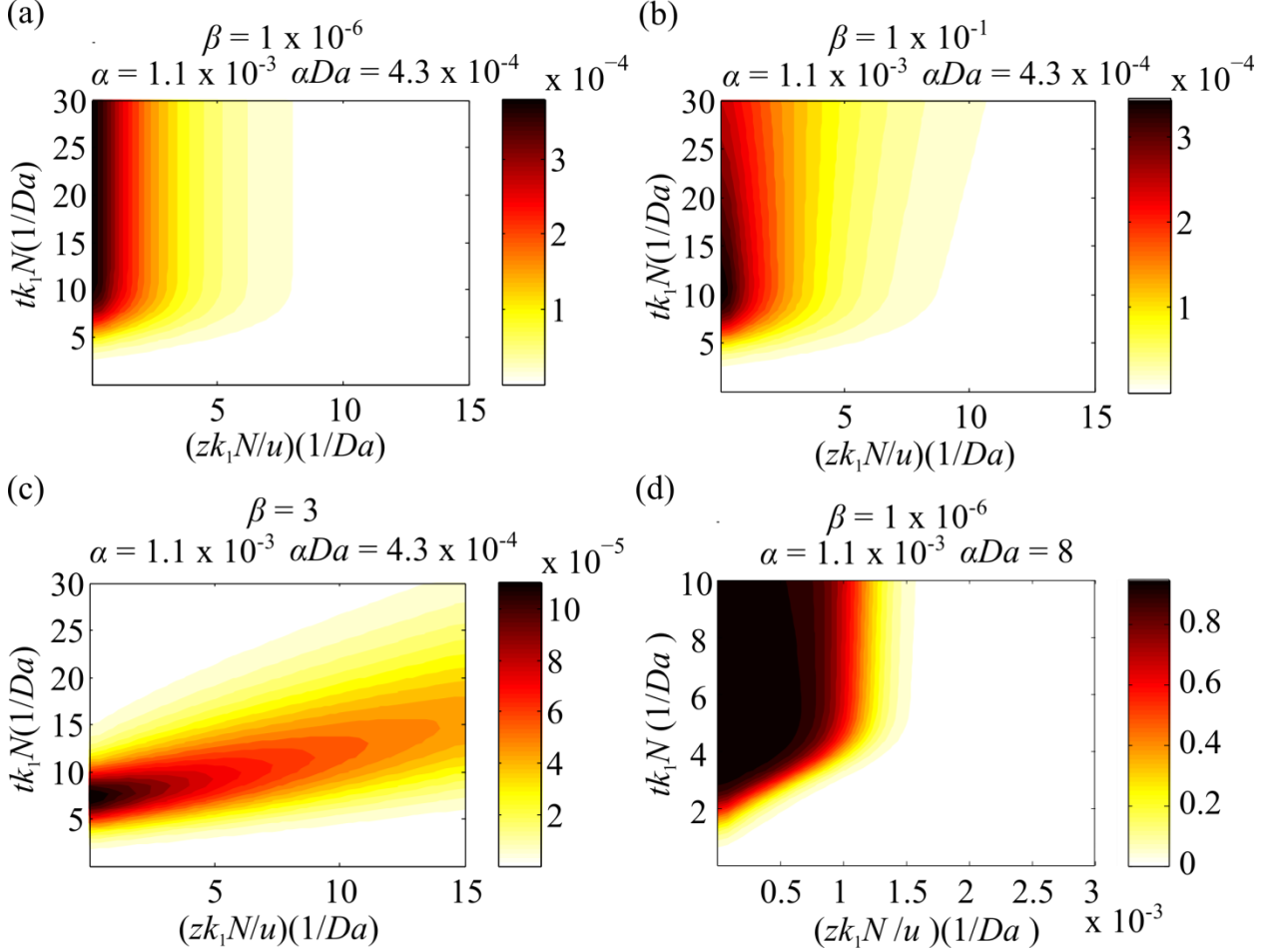


Figure 3.2. Model predictions of spatiotemporal dynamics of bound target scaled by initial probe concentration (n/N). The abscissa and ordinate can be interpreted as scaled axial distance and time, respectively. We show various values of non-dimensionalized equilibrium dissociation constant β and saturation parameter αDa . (a), (b), and (c) show dependence of the spatiotemporal capture dynamics on β for $\alpha Da = 4.3 \times 10^{-4}$ and $\alpha = 1.1 \times 10^{-3}$ (non-saturated regime, $\alpha Da < 1$). This set of αDa and α is similar to that in one of the experiments we will describe in Chapter 4. As β increases, the capture reaction becomes more reversible until about $\beta = 3$, where the target is no longer effectively captured and streaks through the affinity region. (d) shows spatiotemporal capture dynamics in a saturated regime ($\alpha Da > 1$). Here, the leading edge of the affinity region becomes saturated, shifting the spatiotemporal capture contours upward and to the right.

3.3.2.2 Control of capture length p_z

Figure 3.3 summarizes the major trends between advection, reaction, and capture length and time scales. We here formally define the dimensional capture length, p_z , as the physical length of affinity column necessary to capture 95% of target. Inverse capture length is therefore a measure of efficiency of column utilization for columns of constant cross sectional area. p_z is defined and useful only for small values of β , where the target is captured (versus transported through the region). We non-dimensionalize this length by the advection-reaction length scale $u/(k_1N)$ and call this p_z^* .

Figure 3.3a shows major trends of p_z^* . Most importantly, we see that p_z^* solutions collapse to a constant value of 2.8 for $\alpha Da < 1$ (Figure 3.3a). α and Da represent the scaled target distribution height and width, respectively, so the product αDa represents the scaled total target amount. Only when $\alpha Da > 1$ does the target zone contain sufficient target to locally saturate the affinity region near the leading edge (Figure 3.2d). For $\alpha Da < 1$, the target amount is insufficient to locally saturate the affinity region. For $\alpha Da < 1$, therefore, the capture length only depends on the balance of advection and reaction, i.e., $u/(k_1N)$. Hence, in this regime, p_z is proportional to $u/(k_1N)$. Thus also p_z^* is independent of α or Da as long as the product $\alpha Da < 1$ (Figure 3.3a). For $\alpha Da > 1$, the affinity region becomes locally saturated and the length of the locally saturated region dominates the capture length. Also in this regime, the saturated length increases in direct proportion to the total amount of target and therefore p_z^* increases linearly with the product αDa (Figure 3.3a).

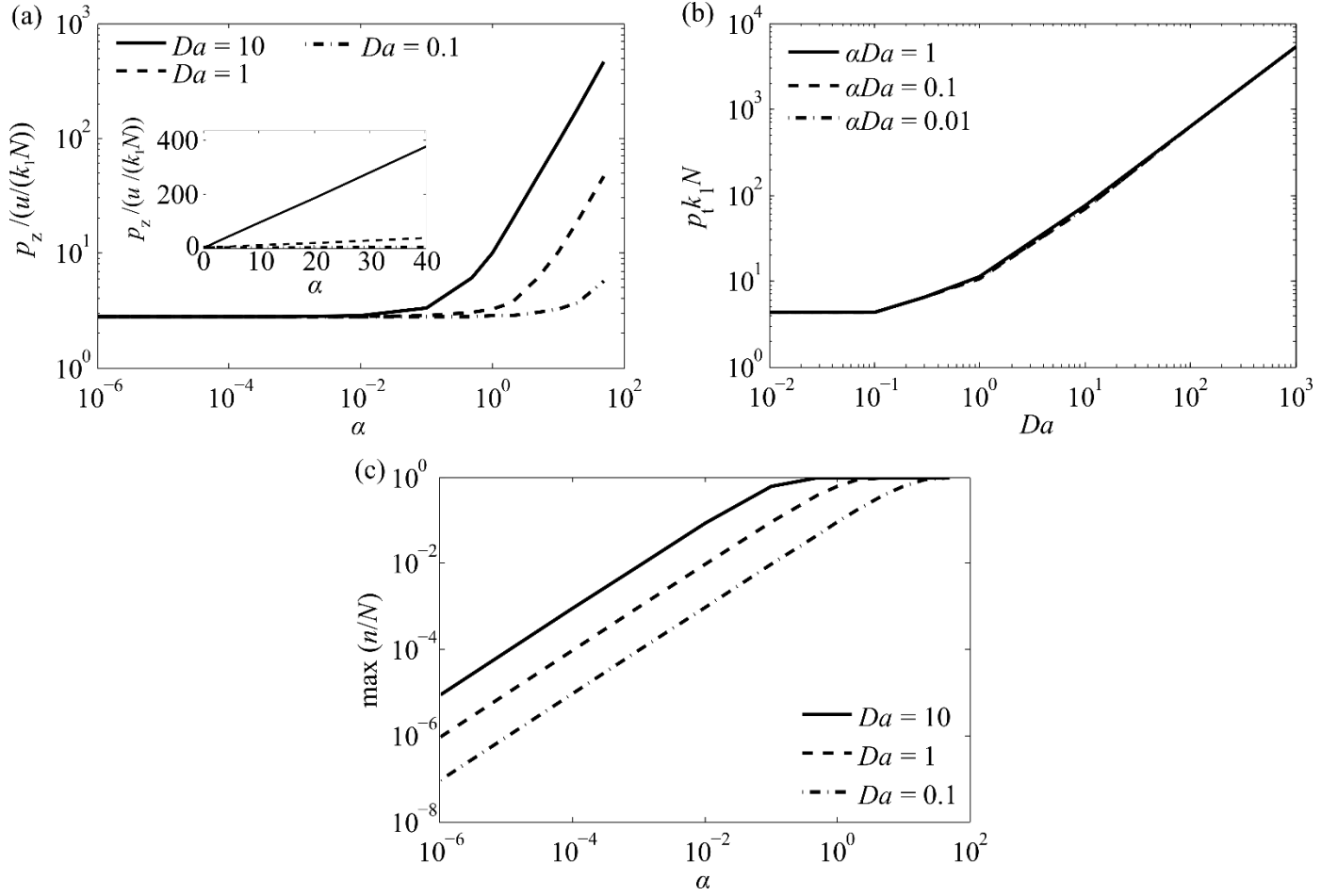


Figure 3.3. Model predictions for the (a) scaled capture length, (b) scaled capture time, and (c) maximum capture efficiency as a function of (a, c) scaled peak target concentration α and (b) scaled target distribution width Da for low β (plotted at $\beta = 10^{-4}$). Inset in (a) shows a linear plot of scaled capture length as a function of α from 0 to 40. In (a), when $\alpha Da < 1$ and so the affinity region is not locally saturated, capture length is only governed by the balance of reaction and advection, i.e., $u/(k_l N)$. Therefore in this regime p_z^* is invariant of α or Da . When $\alpha Da > 1$ the affinity region becomes locally saturated and the length of saturated region governs the capture length. Since the length of locally saturated region is proportional to αDa , p_z^* is proportional to both α and Da . In (b), scaled capture time p_t^* is approximately 4.3 for $Da < 0.1$. For $Da > 1$, scaled capture time increases linearly with Da . Interestingly, the scaled capture time is independent of total scaled target amount, αDa (since the length scale of capture region is insensitive to capture amount provided ligand is not saturated, $\alpha Da \leq 1$). In (c) n/N increases linearly with α and Da for $\alpha Da < 1$ (i.e., when the affinity region is not saturated). For $\alpha Da > 1$ the affinity region becomes locally saturated and $n/N = 1$.

3.3.2.3 Control of capture time p_t

We define a capture time, p_t , as the time necessary to capture 95% of target. Similar to capture length, this time is defined only for small values of β , where the target is captured

and does not appreciably desorb during the capture process. The capture time is proportional to the ITP-AC assay time for assays designed to capture nearly all of the target. We non-dimensionalize this time by the reaction time scale $1/(k_I N)$ and call this p_t^* . For the unsaturated regime of $aDa \leq 1$, scaled capture time p_t^* depends only on scaled target distribution width Da and is insensitive to the total amount of target aDa . Thus, we see that scaled capture times all collapse to a value of 4.3 for Da less than about 0.1 and for $aDa \leq 1$ (Figure 3.3b). In this regime, the target distribution standard deviation is significantly less than the advection-reaction length scale and the target distribution effectively acts as a Dirac delta distribution. Consequently, the time scale for capture is governed solely by the reaction time scale, $1/(k_I N)$. In this regime, the absolute capture length p_z is still approximately $2.8u/(k_I N)$, and the target's travel lasts $4.3/(k_I N)$. For $Da > 1$ (i.e., sufficiently wide scaled distributions), p_t^* increases linearly with Da (Figure 3.3b). The latter is simply because it takes proportionally more time for a wider distribution to completely enter the affinity region and be captured.

These observations lead us to the conclusion that there is little need to decrease the target distribution width below about $0.1u/(k_I N)$. That is, the regime of $Da < 1$ is sufficient to remove dependence on initial target distribution. As we shall show in Chapter 4, such target distribution widths are readily achievable using ITP focusing.

In traditional AC, the target is introduced to an affinity column with spatial distributions which are much wider and lower concentration than ITP achieves. ITP has been demonstrated to increase target concentration (and proportionately decrease target distribution width) up to 10^6 -fold under ideal conditions [28], and to order 10^4 -fold for the case of nucleic acids from complex biological samples [104]. The trends discussed above

therefore suggest that increases in concentration via ITP can translate to proportionally lower capture times and lower capture lengths. For example, consider that reaction times for wide distributions ($Da \gg 1$) benefit directly from any decrease in target zone width (c.f. Figure 3.3b). Further consider that, for fixed assay time, ITP preconcentration enables much lower advection velocity u and so proportionally lower capture lengths; thus maximizing column utilization.

3.3.2.4 Control of capture efficiency n/N

We define the capture efficiency as the concentration of target captured over the initial concentration of probe, n/N (a maximum of unity). The trends of capture efficiency are summarized in Figure 3.3c. For small β (i.e., approximately irreversible reactions), the highest value of n/N occurs at the leading edge of the affinity region where the affinity sites see the largest amount of target. For small β and $\alpha Da < 1$ (locally not saturated), the highest n/N (at the leading edge) is proportional to the total amount of target which enters the affinity region. Hence the highest value of n/N increases linearly with αDa until αDa reaches unity. For $\alpha Da \geq 1$, the capture zone saturates near the leading edge yielding n/N near unity.

In Figure 3.4, we summarize the effect of β on capture efficiency as a function of the scaled target distribution width Da , and scaled distribution peak concentration α . We here plot the maximum value of n/N , $\max(n/N)$, normalized by the scaled total target amount αDa . Overall, as β increases, the capture efficiency decreases (Figure 3.4), due to increasing reversibility of the capture. This increased adsorption/desorption of the target “smears” the target over a larger area of the affinity region (see Figure 3.2c). As the affinity

region becomes more locally overloaded (i.e., as α approaches and becomes greater than unity), the affinity region locally cannot capture the entire target distribution, necessitating the target distribution to migrate some distance. This widens the target distribution. When β is relatively large (e.g. 10^{-3}) desorption is prominent and so the wide bound target distribution is smeared over longer distances. Therefore, increasing α decreases capture efficiency in this regime. Similarly, when desorption is prominent, the wider the target distribution entering the affinity region (i.e., the larger the Da), the more smeared the distribution becomes. Hence, capture efficiency decreases with increasing Da . Thus decreasing Da (such as with strong ITP preconcentration) enables efficient capture of targets with larger dissociation constants.

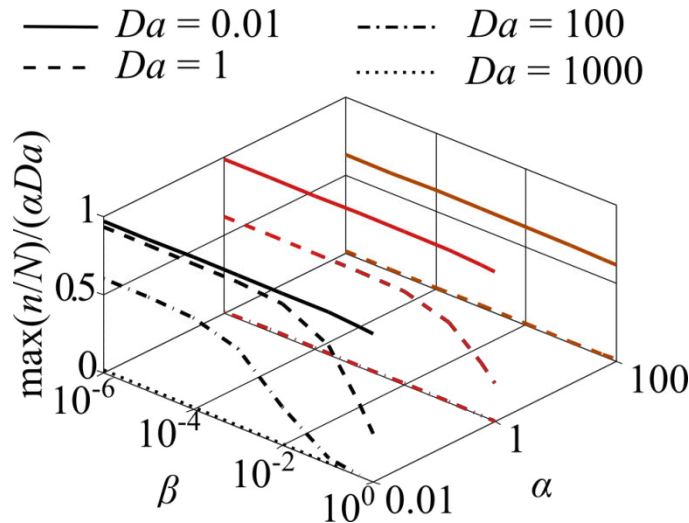


Figure 3.4. $\max(n/N)$ scaled by αDa for values of β between 10^{-6} and 1, Da between 0.01 and 1000, and α between 0.01 and 100. As β increases the reverse reaction (dissociation) becomes more prominent until no effective binding occurs and the target streaks through the affinity region. Capture efficiency n/N always decreases with increasing β , and this effect becomes more pronounced with increasing Da and α . Therefore, decreasing Da (e.g., by preconcentrating the target with ITP) allows one to achieve larger capture efficiencies for a given dissociation constant.

3.3.3 Limiting regimes of ITP-aided capture dynamics

We summarize several limiting regimes of immediate interest to the experimentalist, and associated closed-form (algebraic) solutions for the associated figures of merit.

3.3.3.1 Capture length in the low αDa regime

The low αDa regime is associated with an affinity region which is not locally saturated and so the concentration of bound target remains proportional to the total target amount (see Section 3.3.2.4). This is therefore an important regime for analytical quantification of target using ITP-AC. In this regime $p_z^* \approx 2.8$, and this value is invariant of αDa as shown in Figure 3.3a. We can therefore express the dimensional capture length as simply

$$p_z \approx 2.8u/(k_1 N). \quad (3.39)$$

This relation predicts the capture length to within 1% for $\alpha Da < 0.1$ and to within 20% for $\alpha Da < 1$. This relation also allows a simple way to measure the forward rate constant k_1 from a measurement of p_z , as u is set by setting running current for ITP (and measured by simple observations), and N is easily measured (see Section 4.3.2 in Chapter 4 [8]).

3.3.3.2 Capture time in the high Da regime

In the high Da regime the scaled target distribution width becomes much larger than the advection-reaction length scale, and therefore much larger than the capture length (albeit for non-saturated conditions so that $\alpha Da < 1$). In this regime, the capture time is solely determined by the time for the ITP zone to enter the affinity region and we can write (c.f. Figure 3.2b)

$$p_t \approx 5.4\sigma/u, \quad (3.40)$$

This relation predicts the capture time to within 13% for $Da > 100$ and $\alpha Da \leq 1$, and to within 24% for $Da > 10$ and $\alpha Da \leq 1$.

3.3.3.3 Separation resolution of ITP-AC

In ideal ITP-aided capture, $\beta_{cn} \gg \beta_{target}$ (where subscript “cn” refers to contaminant). This creates the opportunity to capture target (in time p_t) while allowing contaminants to migrate through the column. We consider here a regime where the target is completely captured (e.g., $\beta < 10^{-6}$) while the contaminant species remains focused in ITP and migrating at the ITP velocity. Following the common definition of resolution given by Giddings [113], and setting the width of captured target distribution as p_z and approximating the width of the ITP peak as per the classic theory of MacInnes and Longworth [22, 25], we can obtain the scaling for resolution for ITP-AC as

$$R_{ITP-AC} \approx \frac{ut}{\frac{u}{k_1 N} p_z + \frac{1}{u} \left(\frac{\mu_{L \text{ in LE}} \mu_{T \text{ in TE}}}{\mu_{L \text{ in LE}} - \mu_{T \text{ in TE}}} \right) \frac{k_B T}{e}}. \quad (3.41)$$

Here k_B is the Boltzmann's constant, T is the absolute temperature, e is the electron charge, and $\mu_{L \text{ in LE}}$ and $\mu_{T \text{ in LE}}$ are the mobilities of the LE ion in the LE and the TE ion in the TE respectively. We observe that the resolution for ITP-AC scales as proportional with time t . This is in sharp contrast to the resolution of traditional electrophoresis or of AC which scale as \sqrt{t} [114]. We provide more details regarding the derivation and analysis of resolution of ITP-AC processes in the SI (Section 3.5.2).

3.4 Conclusions

We have developed an analytical model for the spatiotemporal dynamics of isotachopheresis coupling with affinity chromatography. We investigated the coupled effects of target distribution width, distribution intensity, application velocity, forward and reverse reaction constants, and probe concentration on necessary affinity capture length, assay time, and capture efficiency. We collapsed these six independent variables to three non-dimensionalized parameters (α , β , and Da) and identified key limiting regimes in the problem.

We showed that scaled capture length (length necessary to capture 95% of the target scaled by the advection-reaction length scale) approaches a constant value of about 2.8 for the regime where the scaled total target amount, αDa , is less than about unity. (α and Da represent the scaled target distribution height and width respectively). In this regime the affinity region is not locally saturated and the maximum concentration of bound target is proportional to the total amount of target in the distribution. Therefore this regime provides a simple way to quantify total amount of target. For αDa values greater than unity, the affinity region is locally saturated and scaled capture length increases linearly with αDa . The saturation effectively shifts the leading edge of the capture zone progressively downstream until new capture sites are available. We also showed how increasing the non-dimensionalized equilibrium dissociation constant β decreases the capture efficiency n/N . The strength of this effect increases as both α and Da increase.

We showed that scaled capture time (time necessary to capture 95% of the target scaled by the reaction time scale) asymptotes to about 4.3 for $Da < 0.1$ and $\alpha Da \leq 1$. In this relevant regime, the target distribution acts a Dirac delta function. For Da greater than

about unity, scaled capture time increases linearly with Da , indicating that the capture of wide target distributions in this regime is simply limited by the time for them to enter the affinity column. By focusing the target into a narrow distribution, as is achieved with ITP, we decrease Da and therefore decrease the overall assay time. Furthermore, assay time is set by the time required to advect the target into the affinity region, which scales as target distribution width divided by target velocity, σ/u . For fixed assay time, preconcentration therefore yields proportionally lower capture length p_z , and improved column utilization.

Lastly, we showed the resolution of the most common mode ITP-AC purification should scale proportionally with time. Experimental validations of our model and a demonstration of ITP-AC purification of a target from 10,000-fold more abundant contaminant will be presented in Chapter 4.

3.5 Supplementary Information

In this supplementary information section, we present additional information on the following topics: (1) Solution to the simplified advection-reaction equations; (2) Separation resolution of ITP-AC; (3) Dispersion for ITP inside porous media; and (4) ITP-AC with accelerating shock wave.

3.5.1 Solution to the simplified advection-reaction equations

We solve the simplified advection-reaction equations derived in Section 3.2.2 of the main text. We start by finding the zeroth order solution for c and n following Thomas [112] but using the boundary and initial conditions pertinent to our problem. We then follow a similar procedure to find first and second order solutions. Similar procedure can be applied to obtain higher order solutions. However, in the main text we discuss and

explain the trends given only by the zeroth order solution (accurate to $O(\varepsilon)$), as it is the simplest engineering approximation to this problem. Fortunately, the results of the zeroth order solution agree well with experimental measurements of key ITP-AC parameters at our experimental conditions (presented in Chapter 4). At the end of this section we present the solution accurate to $O(\varepsilon^3)$ for situations where knowledge of spatiotemporal behavior of ITP-AC is needed to greater accuracy. While we continue to work with the non-dimensionalized equations (as we have in Section 3.2.2 of the main text), we here drop the asterisks above the variables for clarity of presentation.

3.5.1.1 Solution of zeroth order equations

We begin by transforming the two zeroth order equations into a coordinate moving with the LE-TE interface velocity (for the non-dimensionalized equations this velocity equals to unity). We then convert the result into a potential function form, thereby collapsing the two equations into a single equation. We then solve the resulting equation using Laplace transforms.

We write the zeroth order non-dimensionalized equations and their respective boundary and initial conditions here again for convenience:

$$\frac{\partial c_0}{\partial t} + \frac{\partial c_0}{\partial z} + \frac{\partial n_0}{\partial t} = 0, \quad (3.42)$$

$$\frac{\partial n_0}{\partial t} - c_0(1 - n_0) + \beta n_0 = 0, \quad (3.43)$$

$$\begin{aligned} c_0(z, 0) &= 0, \\ n_0(z, 0) &= 0, \end{aligned} \quad (3.44)$$

$$c_0(0,t) = \left(\alpha/\sqrt{2\pi}\right) \exp\left[-(t/Da-3)^2/2\right]. \quad (3.45)$$

We begin by transforming (3.42) through (3.32) into new independent variables, $x = z$ and

$y = (t-z)$:

$$\frac{\partial c_0}{\partial x} + \frac{\partial n_0}{\partial y} = 0, \quad (3.46)$$

$$\frac{\partial n_0}{\partial y} - c_0(1-n_0) + \beta n_0 = 0, \quad (3.47)$$

$$\begin{aligned} c_0(x,0) &= 0, \\ n_0(x,0) &= 0, \end{aligned} \quad (3.48)$$

$$c_0(0,y) = \left(\alpha/\sqrt{2\pi}\right) \exp\left[-(y/Da-3)^2/2\right]. \quad (3.49)$$

Next we introduce a potential function f such that

$$\begin{aligned} n_0 &= \frac{\partial f}{\partial x}, \\ c_0 &= -\frac{\partial f}{\partial y}. \end{aligned} \quad (3.50)$$

The potential function f automatically satisfies equation (3.46). Therefore, we substitute (3.50) into (3.47) and obtain

$$\frac{\partial^2 f}{\partial y \partial x} + \frac{\partial f}{\partial y} + \beta \frac{\partial f}{\partial x} - \frac{\partial f}{\partial y} \frac{\partial f}{\partial x} = 0. \quad (3.51)$$

Equation (3.51) is non-linear and we linearize it by substituting in

$$f(x,y) = x + y\beta - \ln \phi(x,y), \quad (3.52)$$

after which we obtain

$$\frac{\partial^2 \phi}{\partial y \partial x} = \beta \phi. \quad (3.53)$$

In this way, we have condensed equations (3.46) and (3.47) into a single equation (3.53). Next we transform the initial and the boundary conditions. We note that we use the only initial condition for c_0 . The initial condition on n_0 was applied much earlier, when we tacitly assumed that there is no bound target initially in the affinity region. See the main text when we first introduce the reaction equation in terms of N (eq. (2) of main text). The transformed initial and boundary conditions are

$$\frac{1}{\phi(x, 0)} \frac{\partial \phi}{\partial x}(x, 0) = 1 - \frac{\partial f}{\partial x} = 1 - c(x, 0), \quad (3.54)$$

$$\frac{1}{\phi(0, y)} \frac{\partial \phi}{\partial y}(0, y) = \beta - \frac{\partial f}{\partial y} = \beta + c(0, y). \quad (3.55)$$

We solve the differential equations (3.54) and (3.55) and obtain

$$\phi(x, 0) = \exp \left[x - \int_0^x c(x', 0) dx' \right] = H(x), \quad (3.56)$$

$$\phi(0, y) = \exp \left[y\beta + \int_0^y c(0, y') dy' \right] = G(y). \quad (3.57)$$

Next we apply the Laplace transform to equation (3.53) and use the result (3.57) to obtain

$$p \frac{d\bar{\phi}}{dx} = \beta \bar{\phi} + \frac{dH(x)}{dx}, \quad (3.58)$$

where the overbar denotes the Laplace transform of a function with respect to y (e.g., $\bar{\phi}(x, p)$ is the Laplace transform of ϕ and p is the Laplace transform variable). Also,

$$\bar{\phi}(0, p) = \bar{G}(p). \quad (3.59)$$

We solve the differential equation (3.58) by variation of parameters to obtain

$$\bar{\phi}(x, p) = \bar{G}(p) \exp\left[\frac{\beta x}{p}\right] + \frac{1}{p} \int_0^x \frac{dH(x')}{dx} \exp\left[\frac{\beta(x-x')}{p}\right] dx'. \quad (3.60)$$

We then take the inverse transform of (3.60) to obtain

$$\phi(x, y) = \int_0^y G(y-y') F_1(x, y') dy' + \int_0^x \frac{dH(x-x')}{dx} F_2(x', y) dx', \quad (3.61)$$

where

$$\begin{aligned} L[F_1(x, y)] &= \exp\left[\frac{\beta x}{p}\right], \\ L[F_2(x, y)] &= \frac{1}{p} \exp\left[\frac{\beta x}{p}\right]. \end{aligned} \quad (3.62)$$

$L[F(x, y)]$ designates the Laplace transform of $F(x, y)$. Taking the inverse Laplace transform of (3.62)[115] we obtain

$$\begin{aligned} F_1(x, y) &= \sqrt{\frac{\beta x}{y}} I_1(2\sqrt{\beta y x}) + \delta(y), \\ F_2(x, y) &= I_0(2\sqrt{\beta y x}). \end{aligned} \quad (3.63)$$

Here I_0 and I_1 are modified Bessel functions of the first kind of zeroth and first order respectively. We substitute (3.63) into (3.61) and obtain

$$\phi(x, y) = G(y) + \int_0^y G(y - y') \sqrt{\frac{\beta x}{y'}} I_1(2\sqrt{\beta y' x}) dy' + \int_0^x \frac{dH(x - x')}{dx} I_0(2\sqrt{\beta y x'}) dx'. \quad (3.64)$$

We then simplify (3.64) by evaluating the right hand side term via integration by parts and noticing that $G(0) = 1$

$$\phi(x, y) = I_0(2\sqrt{\beta y x}) + \int_0^y \frac{dG(y - y')}{dy} I_0(2\sqrt{\beta y' x}) dy' + \int_0^x \frac{dH(x - x')}{dx} I_0(2\sqrt{\beta y x'}) dx'. \quad (3.65)$$

This is the general solution to the zeroth order equations in terms of the potential function ϕ . Next we apply the initial and boundary conditions specific to ITP-AC. We begin by substituting (3.48) into (3.56) and obtain

$$H(x) = \exp(x), \quad (3.66)$$

and

$$\frac{dH(x)}{dx} = \exp(x). \quad (3.67)$$

Substituting, this simplifies (3.65) to

$$\phi(x, y) = I_0(2\sqrt{\beta y x}) + \int_0^y \frac{dG(y - y')}{dy} I_0(2\sqrt{\beta y' x}) dy' + \int_0^x \exp[(x - x')] I_0(2\sqrt{\beta y x'}) dx'. \quad (3.68)$$

We next apply the boundary condition by substituting (3.49) into (3.57) and obtain

$$G(y) = \exp \left[y\beta + \frac{\alpha Da}{2} \left(\operatorname{erf} \left(\frac{y/Da - 3}{\sqrt{2}} \right) - \operatorname{erf} \left(\frac{-3}{\sqrt{2}} \right) \right) \right], \quad (3.69)$$

and

$$\frac{dG(y)}{dy} = \left(\frac{\alpha}{\sqrt{2\pi}} \exp \left[-\frac{(y/Da - 3)^2}{2} \right] + \beta \right) \exp \left[y\beta + \frac{\alpha Da}{2} \left(\operatorname{erf} \left(\frac{y/Da - 3}{\sqrt{2}} \right) - \operatorname{erf} \left(\frac{-3}{\sqrt{2}} \right) \right) \right]. \quad (3.70)$$

Therefore

$$\phi(x, y) = I_0 \left(2\sqrt{\beta yx} \right) + \int_0^y \frac{dG(y - y')}{dy} I_0 \left(2\sqrt{\beta y'x} \right) dy' + \int_0^x \exp[(x - x')] I_0 \left(2\sqrt{\beta yx'} \right) dx', \quad (3.71)$$

where dG/dy is given by (3.70). Now c_0 and n_0 can be easily obtained by substituting (3.71) into (3.52) and substituting the result into (3.50). For convenience, we evaluated solutions numerically using custom MATLAB scripts as we analyzed the spatiotemporal behavior of the target in ITP-AC.

3.5.1.2 Solution of first order equations

We solve the first order equations following a procedure similar to the zeroth order equations. We again begin by transforming the two first order equations into a coordinate moving with the LE-TE interface velocity. We then convert the result into a potential function form, thereby again collapsing the two equations into a single equation. We again solve the resulting equation using Laplace transforms.

We write the first order non-dimensionalized equations and their respective boundary and initial conditions here again for convenience:

$$\frac{\partial c_1}{\partial t} + \frac{\partial c_1}{\partial z} + \frac{\partial n_1}{\partial t} + \frac{\partial(\tilde{u}c_0)}{\partial z} = 0, \quad (3.72)$$

$$\frac{\partial n_1}{\partial t} - c_1 + \beta n_1 = 0, \quad (3.73)$$

$$\begin{aligned} c_1(z, 0) &= 0, \\ n_1(z, 0) &= 0, \end{aligned} \quad (3.74)$$

$$c_1(0, t) = 0. \quad (3.75)$$

We then transform (3.72) through (3.75) into new independent variables, $x = z$ and $y = (t - z)$:

$$\frac{\partial c_1}{\partial x} + \frac{\partial n_1}{\partial y} + \frac{\partial(\tilde{u}c_0)}{\partial x} - \frac{\partial(\tilde{u}c_0)}{\partial y} = 0, \quad (3.76)$$

$$\frac{\partial n_1}{\partial y} - c_1 + \beta n_1 = 0. \quad (3.77)$$

Next we define new variables

$$\begin{aligned} C_1 &= c_1 + \tilde{u}c_0, \\ M_1 &= n_1 - \tilde{u}c_0, \end{aligned} \quad (3.78)$$

and recast (3.76) and (3.77) in these variables:

$$\frac{\partial C_1}{\partial x} + \frac{\partial M_1}{\partial y} = 0, \quad (3.79)$$

$$\frac{\partial M_1}{\partial y} + \frac{\partial(\tilde{u}c_0)}{\partial y} - (C_1 - \tilde{u}c_0) + \beta(M_1 + \tilde{u}c_0) = 0. \quad (3.80)$$

We also recast the initial and boundary condition in these variables

$$\begin{aligned} C_1(z, 0) - \tilde{u}(z, 0)c_0(z, 0) &= 0, \\ M_1(z, 0) + \tilde{u}(z, 0)c_0(z, 0) &= 0, \end{aligned} \quad (3.81)$$

$$C_1(0, t) - \tilde{u}(0, t)c_0(0, t) = 0. \quad (3.82)$$

Next we introduce a potential function f such that

$$\begin{aligned} M_1 &= \frac{\partial f}{\partial x} \\ C_1 &= -\frac{\partial f}{\partial y} \end{aligned} \quad (3.83)$$

and substitute this into (3.79) and (3.80). The potential function f automatically satisfies equation (3.79), and (3.80) becomes

$$\frac{\partial^2 f}{\partial y \partial x} + \frac{\partial f}{\partial y} + \beta \frac{\partial f}{\partial x} + \frac{\partial(\tilde{u}c_0)}{\partial y} + (1 + \beta)\tilde{u}c_0 = 0. \quad (3.84)$$

Now we apply f to the initial and boundary conditions

$$\frac{\partial f}{\partial x}(x, 0) = M_1(x, 0) = n_1(x, 0) - \tilde{u}(x, 0)c_0(x, 0), \quad (3.85)$$

$$\frac{\partial f}{\partial y}(0, y) = -C_1(0, y) = -c_1(0, y) - \tilde{u}(0, y)c_0(0, y). \quad (3.86)$$

We integrate (3.85) and (3.86)

$$f(x, 0) = \int_0^x n_1(x', 0) - \tilde{u}(x', 0)c_0(x', 0)dx', \quad (3.87)$$

$$f(0, y) = \int_0^y -c_1(0, y') - \tilde{u}(0, y')c_0(0, y')dy'. \quad (3.88)$$

Noticing that $n_1(x', 0) = 0$ and $c_1(0, y') = 0$ we simplify the above equations to

$$f(x, 0) = -\int_0^x \tilde{u}(x', 0)c_0(x', 0)dx' = H_1(x), \quad (3.89)$$

$$f(0, y) = -\int_0^y \tilde{u}(0, y')c_0(0, y')dy' = G_1(y). \quad (3.90)$$

Equations for initial and boundary conditions (3.89) and (3.90) are to be evaluated using the result from the zeroth order equations. \tilde{u} is of the form of an error function (see main text), i.e., $\tilde{u} = \text{erf}[(t - z - 3Da)/Da]$.

Next, we take the Laplace transform of (3.84) to yield

$$\frac{\partial \bar{f}}{\partial x} + \frac{p}{p + \beta} \bar{f} = \frac{1}{p + \beta} \left[\frac{\partial H_1(x)}{\partial x} + H_1(x) - (1 + \beta + p)\bar{w} + w(x, 0) \right], \quad (3.91)$$

where $w = \tilde{u}c_0$. We solve differential equation (3.91) using variation of parameters and obtain

$$\begin{aligned}
\bar{f} &= \bar{G}_1(p) \exp\left[\frac{-xp}{p+\beta}\right] \\
&+ \exp\left[\frac{-xp}{p+\beta}\right] \int_0^x \exp\left[\frac{x'p}{p+\beta}\right] \frac{1}{p+\beta} \left[\frac{\partial H_1(x')}{\partial x} + H_1(x') - (1+\beta+p)\bar{w} + w(x',0) \right] dx'.
\end{aligned}
\tag{3.92}$$

We expand this to

$$\bar{f} = \bar{G}_1(p) \bar{F}_1 + \int_0^x \left[\frac{\partial H_1(x'-x)}{\partial x} + H_1(x'-x) + w(x'-x,0) \right] \bar{F}_2 dx' - \int_0^x \bar{F}_3 \bar{w} dx',
\tag{3.93}$$

where

$$\begin{aligned}
\bar{F}_1 &= \exp\left[\frac{-xp}{p+\beta}\right], \\
\bar{F}_2 &= \frac{1}{p+\beta} \exp\left[\frac{px'}{p+\beta}\right], \\
\bar{F}_3 &= \frac{(1+\beta+p)}{p+\beta} \exp\left[\frac{p(x'-x)}{p+\beta}\right].
\end{aligned}
\tag{3.94}$$

We recommend finding the inverse Laplace transforms of equations in (3.94) numerically.

We then take the inverse Laplace transform of (3.93) to obtain

$$\begin{aligned}
f &= \int_0^y G_1(y-y') F_1(x, y') dy' \\
&+ \int_0^x \left[\frac{\partial H_1(x-x')}{\partial x} + H_1(x-x') + w(x-x',0) \right] F_2(x', y) dx' \\
&- \int_0^x \int_0^y w(x', y-y') F_3(x, y') dy' dx'.
\end{aligned}
\tag{3.95}$$

Now the functions c_1 and n_1 can be obtained fairly easily by substituting (3.95) into (3.83), and using the appropriate inverse Laplace transforms for (3.94) and the result from the zeroth order equations (as inputs for G_1 , H_1 , and w). We recommend evaluating this numerically using MATLAB.

3.5.1.3 Solution of second order equations

We solve the second order equations following a similar procedure to the zeroth and first order equations. We once again begin by transforming the two first order equations into a coordinate moving with the LE-TE interface velocity. We then convert the result into a potential function form, again collapsing the two equations into a single equation. We then solve the resulting equation using Laplace transforms.

We write the second order non-dimensionalized equations and their respective boundary and initial conditions here again for convenience:

$$\frac{\partial c_2}{\partial t} + \frac{\partial c_2}{\partial z} + \frac{\partial n_2}{\partial t} + \frac{\partial(\tilde{u}c_1)}{\partial z} = 0, \quad (3.96)$$

$$\frac{\partial n_2}{\partial t} - c_2 + \beta n_2 + c_1 n_1 = 0, \quad (3.97)$$

$$\begin{aligned} c_2(z, 0) &= 0, \\ n_2(z, 0) &= 0, \end{aligned} \quad (3.98)$$

$$c_2(0, t) = 0. \quad (3.99)$$

We transform (3.96) through (3.99) into new independent variables, $x = z$ and $y = (t-z)$:

$$\frac{\partial c_2}{\partial x} + \frac{\partial n_2}{\partial y} + \frac{\partial(\tilde{u}c_1)}{\partial x} - \frac{\partial(\tilde{u}c_1)}{\partial y} = 0, \quad (3.100)$$

$$\frac{\partial n_2}{\partial y} - c_2 + \beta n_2 + c_1 n_1 = 0. \quad (3.101)$$

Next, we define new variables

$$\begin{aligned} C_2 &= c_2 + \tilde{u}c_1, \\ M_2 &= n_2 - \tilde{u}c_1, \end{aligned} \quad (3.102)$$

and recast (3.100) and (3.101) in these variables

$$\frac{\partial C_2}{\partial x} + \frac{\partial M_2}{\partial y} = 0, \quad (3.103)$$

$$\frac{\partial M_2}{\partial y} + \frac{\partial(\tilde{u}c_1)}{\partial y} - (C_2 - \tilde{u}c_1) + \beta(M_2 + \tilde{u}c_1) + c_1 n_1 = 0. \quad (3.104)$$

We also recast the initial and boundary condition in these variables

$$\begin{aligned} C_2(z, 0) - \tilde{u}(z, 0)c_1(z, 0) &= 0, \\ M_2(z, 0) + \tilde{u}(z, 0)c_1(z, 0) &= 0, \end{aligned} \quad (3.105)$$

$$C_2(0, t) - \tilde{u}(0, t)c_1(0, t) = 0. \quad (3.106)$$

Next we introduce a potential function f such that

$$\begin{aligned} M_2 &= \frac{\partial f}{\partial x}, \\ C_2 &= -\frac{\partial f}{\partial y}, \end{aligned} \quad (3.107)$$

and substitute this into (3.103) and (3.104). The potential function f automatically satisfies equation (3.103), and (3.104) becomes

$$\frac{\partial^2 f}{\partial y \partial x} + \frac{\partial f}{\partial y} + \beta \frac{\partial f}{\partial x} + \frac{\partial(\tilde{u}c_1)}{\partial y} + (1 + \beta)\tilde{u}c_1 + c_1n_1 = 0. \quad (3.108)$$

Now we apply f to the initial and boundary conditions and obtain

$$\frac{\partial f}{\partial x}(x, 0) = M_2(x, 0) = n_2(x, 0) - \tilde{u}(x, 0)c_1(x, 0), \quad (3.109)$$

$$\frac{\partial f}{\partial y}(0, y) = -C_2(0, y) = -c_2(0, y) - \tilde{u}(0, y)c_1(0, y). \quad (3.110)$$

We integrate (3.109) and (3.110) and obtain

$$f(x, 0) = \int_0^x n_2(x', 0) - \tilde{u}(x', 0)c_1(x', 0) dx', \quad (3.111)$$

$$f(0, y) = \int_0^y -c_2(0, y') - \tilde{u}(0, y')c_1(0, y') dy'. \quad (3.112)$$

Noticing that $n_2(x', 0) = 0$ and $c_2(0, y') = 0$, we simplify the equations above to

$$f(x, 0) = -\int_0^x \tilde{u}(x', 0)c_1(x', 0) dx' = H_2(x), \quad (3.113)$$

$$f(0, y) = -\int_0^y \tilde{u}(0, y')c_1(0, y') dy' = G_2(y). \quad (3.114)$$

Equations for initial and boundary conditions (3.113) and (3.114) are to be evaluated using the result from the first order equations.

Next, we take the Laplace transform of (3.108) to obtain

$$\frac{\partial \bar{f}}{\partial x} + \frac{p}{p+\beta} \bar{f} = \frac{1}{p+\beta} \left[\frac{\partial H_2(x)}{\partial x} + H_2(x) - (1+\beta+p) \bar{w}_1 + w(x,0) - \bar{w}_2 \right], \quad (3.115)$$

where $w_1 = \tilde{u}c_1$, $w_2 = n_1c_1$. We solve differential equation (3.115) using variation of parameters and obtain

$$\bar{f} = (\bar{G}_2(p) + \Theta) \exp \left[\frac{-xp}{p+\beta} \right], \quad (3.116)$$

where

$$\Theta = \int_0^x \exp \left[\frac{x'p}{p+\beta} \right] \frac{1}{p+\beta} \left[\frac{\partial H_2(x')}{\partial x} + H_2(x') - (1+\beta+p) \bar{w}_1 + w_1(x',0) + \bar{w}_2 \right] dx'. \quad (3.117)$$

We expand (3.116) to

$$\bar{f} = \bar{G}_2(p) \bar{F}_1 + \int_0^x \left[\frac{\partial H_2(x'-x)}{\partial x} + H_2(x'-x) + w_1(x'-x,0) \right] \bar{F}_2 dx' - \int_0^x \bar{F}_3 \bar{w}_1 dx' + \int_0^x \bar{F}_4 \bar{w}_2 dx', \quad (3.118)$$

where

$$\begin{aligned}
\bar{F}_1 &= \exp\left[\frac{-xp}{p+\beta}\right], \\
\bar{F}_2 &= \frac{1}{p+\beta} \exp\left[\frac{px'}{p+\beta}\right], \\
\bar{F}_3 &= \frac{(1+\beta+p)}{p+\beta} \exp\left[\frac{p(x'-x)}{p+\beta}\right], \\
\bar{F}_4 &= \frac{1}{p+\beta} \exp\left[\frac{p(x'-x)}{p+\beta}\right].
\end{aligned} \tag{3.119}$$

We then take the inverse Laplace transform of (3.119) to obtain

$$\begin{aligned}
f &= \int_0^y G_2(y-y') F_1(x, y') dy' \\
&+ \int_0^x \left[\frac{\partial H_2(x-x')}{\partial x} + H_2(x-x') + w_1(x-x', 0) \right] F_2(x', y) dx' \\
&- \int_0^x \int_0^y w_1(x', y-y') F_3(x, y') dy' dx' \\
&+ \int_0^x \int_0^y w_2(x', y-y') F_4(x, y') dy' dx'.
\end{aligned} \tag{3.120}$$

Now functions c_2 and n_2 can be obtained by substituting (3.120) into (3.107) using the appropriate inverse Laplace transforms for (3.119) and the result from the first order equations (as inputs for G_2 , H_2 , w_1 , and w_2). Again, we recommend evaluating this numerically using MATLAB.

3.5.1.4 Third order accurate solutions

Finally, a third order accurate solution is obtained by combining results obtained from (3.71), (3.95), and (3.120) into

$$\begin{aligned} c &= c_0 + \varepsilon c_1 + \varepsilon^2 c_2^2 + O(\varepsilon^3), \\ n &= n_0 + \varepsilon n_1 + \varepsilon^2 n_2^2 + O(\varepsilon^3), \end{aligned} \tag{3.121}$$

where once again, ε is defined as

$$\varepsilon = \frac{\mu_{a,TE} - \mu_{TEion,TE}}{\mu_{TEion,TE}}. \tag{3.122}$$

Higher order equations can be obtained in a manner similar to that for first and second order equations and hence even higher order of accuracy solutions can be obtained.

3.5.1.5 Applicability of the perturbation method

In our perturbation solution we focus on a regime where the difference between the target velocity in the TE and that in the LE is small. We employ the ratio between the target velocity in the TE and that at the LE-TE interface as our perturbation parameter. This may appear as non-intuitive at first glance as it is this difference in the target velocity that is responsible for the entire focusing of the target in ITP, which is crucial to our ITP-AC method. However, the focusing of the target into the LE-TE interface (shock layer) has already occurred long before the shock layer reaches the porous affinity region (the domain in which we perform the perturbation). We account for this focusing via the width of the initial target distribution, which we specify as the time-varying boundary condition on the porous affinity domain. Inside the porous affinity region the difference between the target's velocity between that in the TE and that in the LE has only a small effect on the distribution of the bound target. Consider that in time the target reacts with the probes, the reaction time scale, the difference in the distance that the target traveled if it was traveling at its velocity in the TE versus that in the LE is approximately $2\varepsilon u/(k_I N)$. This distance is much

less than the advection reaction length scale, $u/(k_I N)$, since $\varepsilon < 1$. Thus, this distance is also small compared to the capture length, since capture length scales with advection reaction length scale in the non-saturated probes regime and is greater than the advection reaction length scale in the saturated probes regime. Therefore, while the difference in the target velocity in LE and TE is crucial for ITP-AC, by accounting for this via the boundary condition on the target, we are able to use the ratio of between the target velocity in the TE and that at the LE-TE interface as our perturbation parameter inside the porous affinity region.

3.5.2 Separation resolution of ITP-AC

As described in the main text, the ideal case for ITP-AC separation is that $\beta_{cn} \gg \beta_{target}$ (where subscript “cn” refers to contaminant). That is, target should be captured approximately irreversibly while contaminant is removed and transported downstream. For this regime, the target is captured in time p_t while contaminants migrate through the column. We present an experimental demonstration of such separation in the main text of Chapter 4. We consider here a regime where the target is completely captured (e.g., $\beta < 10^{-6}$) while the contaminant species remains focused in ITP and migrating at the ITP velocity. For this regime, we define a simple criterion for the time required to achieve sufficient separation between captured target and contaminant. We apply a common definition of resolution, R , given by Giddings [113] as follows:

$$R = \frac{\Delta L}{2\sigma_1 + 2\sigma_2}, \quad (3.123)$$

where ΔL is the distance between the two peaks and, σ_1 and σ_2 are the corresponding standard deviations of the two peaks. We let σ_1 be the standard deviation width of the captured (immobile) target peak and σ_2 the standard deviation of the contaminant peak. In ITP-AC the target attains zero velocity at time approximately p_z , and thereafter the width of the target distribution scales as p_z . After the target attains zero velocity, the distance between the target and the analyte simply scales as ut . Using the scaling for the ITP peak width from MacInnes and Longworth [22, 25], we obtain the scaling for resolution for ITP-AC, as we did in equation (42) of the main text. We write it here again for convenience:

$$R_{\text{ITP-AC}} \approx \frac{ut}{\frac{u}{k_1 N} p_z^* + \frac{1}{u} \left(\frac{\mu_{\text{L in LE}} \mu_{\text{T in TE}}}{\mu_{\text{L in LE}} - \mu_{\text{T in TE}}} \right) \frac{k_B T}{e}}, \quad (3.124)$$

where again, k_B is the Boltzmann's constant, T is the absolute temperature, e is the electron charge, and $\mu_{\text{L in LE}}$ and $\mu_{\text{T in TE}}$ are the mobilities of the LE ion in the LE and the TE ion in the TE respectively. We note that the resolution for ITP-AC scales as t . This is in contrast to the resolution of traditional electrophoresis or of AC which scale as \sqrt{t} [114]. The resolution of ITP-AC increases with increasing ITP velocity u and it asymptotes to a value of $tk_1 N / p_z^*$ for large u . We can achieve 95% of this resolution with

$$u_{95} \approx \sqrt{\frac{0.95}{0.05} \left(\frac{\mu_{\text{L in LE}} \mu_{\text{T in TE}}}{\mu_{\text{L in LE}} - \mu_{\text{T in TE}}} \right) \frac{k_B T}{e} \frac{k_1 N}{p_z^*}}. \quad (3.125)$$

Operating at ITP velocity lower than u_{95} results in loss of resolution. Operating at a velocity much higher than u_{95} leads to larger capture lengths with little gain in resolution and therefore loss in column utilization (see Section 3.3.2.2 of the main text). For a good compromise between resolution and column utilization, we therefore recommend operating at around u_{95} . For an ITP velocity of u_{95} and a convenient resolution, $R_{\text{ITP-AC}}$, value of, say, 10 (for well separated capture target and contaminant zone), the time to capture and purify, $t_{c,p}$ is approximately $10p_z^*/(k_1N)$. If αDa is also less than unity, then $t_{c,p}$ is approximately $28/(k_1N)$. For typical ITP-AC conditions such as those we employed in Chapter 4 ($\mu_{L \text{ in } LE} \approx -60 \times 10^{-9} \text{ m}^2\text{V}^{-1}\text{s}^{-1}$, $\mu_{T \text{ in } LE} \approx -13 \times 10^{-9} \text{ m}^2\text{V}^{-1}\text{s}^{-1}$, $k_I = 10^3 \text{ M}^{-1} \text{ s}^{-1}$, $N \approx 30 \text{ }\mu\text{M}$, and $p_z^* \approx 2.8$), u_{95} is on the order of 0.01 mm/s and $t_{c,p}$ is approximately 15 min [8].

3.5.3 Dispersion for ITP inside porous media

Dispersion of a target focused at the LE-TE interface in ITP has been thoroughly studied starting by Konstantinov and Oshurkova in 1966 [116], and more recently by Khurana and Santiago [27] and Garcia-Schwarz et al.[26]. These works considered the dispersion of the target for ITP in an open bore microfluidic channel or capillary. Here we briefly discuss the dispersion of the target focused at the LE-TE interface for ITP in porous media. We only consider here the dispersion due to flow and only consider the case where there is no externally applied pressure difference. In this case, the dispersion at the LE-TE interface is caused by a local pressure driven flow set up the imbalance of the

electroosmotic flow in the LE versus the TE. Inside a porous media, the combined flow rate, Q , due to pressure driven and electroosmotic flow (for thin double layers) is [117]

$$Q = \frac{\varphi}{\tau\mu_f} \left(-\frac{dP}{dz} \frac{\pi r_c^2 r_p^2}{8} - \varepsilon_f \zeta \pi r_c^2 \frac{j}{\sigma_{el}} \right), \quad (3.126)$$

where φ is porosity of the porous media, τ is the tortuosity, μ_f and ε_f are the dynamic viscosity and permittivity of the fluid respectively; r_c and r_p are the radii of the capillary and of the porous media pore respectively; ζ is the zeta potential of the pore surface; and dP/dz is the streamwise pressure gradient, j is the local electric current density, and σ_{el} is the local conductivity (where $j/\sigma_{el} = E$, the streamwise electric field within the pores). Here we have assumed that the thickness of the double layer is much smaller than the radius of the pore. In our experiments, our electrolyte ionic strength was order 0.1 M, therefore our Debye length was order 1 nm, while our pore radii were order 1 μm . Hence, our double layers were thin compared to our pore size.

Next, we observe that the flow rate in the LE and the TE must be equal due to continuity of the incompressible solvent (water). Furthermore, we assume that the flow is steady and fully developed, which suggests that the pressure distribution must be continuous and piecewise linear [118]. We also assume that the zeta potential in LE and TE is the same. Zeta potential strongly depends on the pH of the electrolyte in contact with the surface, but also weakly depends on the chemical composition of that electrolyte. For our experiments, the pH of the LE and TE were 8.2 and 8.5 respectively, hence we expect zeta potential to vary little from LE to TE. These constraints yield a readily solvable set of algebraic equations for the flow rate in the porous media,

$$Q = -\varepsilon_f \zeta \pi r_c^2 \frac{\varphi}{\tau \mu_f} j \left(\frac{L-z}{L} \left(\frac{1}{\sigma_{LE}} - \frac{1}{\sigma_{TE}} \right) + \frac{1}{\sigma_{TE}} \right), \quad (3.127)$$

where L is the length of the porous media, z is the position of the LE-TE interface relative to the leading edge of the porous media, and σ_{LE} and σ_{TE} are the conductivity of LE and TE respectively. The flow rate is maximum when the position of the LE-TE interface is at the end of the porous media ($z = L$), since the conductivity of the TE is lower than that of the LE and the electric field in the TE is higher than that in the LE.

$$Q_{\max} = -\varepsilon_f \zeta \pi r_c^2 \frac{\varphi}{\tau \mu_f} \frac{j}{\sigma_{TE}}. \quad (3.128)$$

The mean maximum velocity inside the pores, defined as $Q_{\max} / \pi r_c^2$ is then

$$\bar{U}_{\max} = -\varepsilon_f \zeta \frac{\varphi}{\tau \mu_f} \frac{j}{\sigma_{TE}}. \quad (3.129)$$

We note that inside the pores, the velocity profile is not parabolic, and the shape of the profile varies along axis of the capillary. However, for the purposes of using existing models for dispersion in porous media we assume that the velocity profile is in fact parabolic. For our experimental conditions $\varepsilon_f = 7.1 \times 10^{-12}$ F/m, $\mu_f = 1.0$ mPa s, $\tau = 1.1$, $\varphi = 0.8$, $j = 1270$ A/m², $\sigma_{TE} = 0.43$ S/m; we assume that approximately $\zeta = 25$ mV. Thus, we calculate that in our experiments maximum mean solvent velocity was typically 38 μ m/s. In our experiments, pore radius is order 0.5 μ m and the molecular diffusion coefficient of DNA is order 10^{-10} m²/s [111]. Hence, pore scale Peclet number, $Pe_p = \bar{U}_{\max} r_p / D$ for our experiments is 0.2. To estimate the effective dispersion coefficient, D_e , we employ a simple empirical correlation from Hiby [119, 120]

$$\frac{D_e}{D} = 0.67Pe_p + \frac{0.65Pe_p}{1 + 6.7\sqrt{1/Pe_p}}. \quad (3.130)$$

For our experiments, we obtain $D_e/D = 0.68$. This implies that the presence of porous media actually reduces dispersion. This somewhat counterintuitive result is predicted for low pore scale Peclet numbers by many geometric flow dispersion models and has been experimentally observed in a wide variety of porous media [120]. We refer the reader to a review by Perfect and Sukop for a detailed review of dispersion in porous media [120].

3.5.4 ITP-AC with accelerating shock wave

In the main text we considered a case of ITP-AC where the LE-TE interface moves at a constant velocity and obtained an analytical solution for the spatiotemporal behavior of ITP-AC. Here we briefly investigate formulation of an analytical solution for ITP-AC when the LE-TE interface velocity varies in time. For this case, we can write the velocity of the target as

$$v(z) = u + \varepsilon u \operatorname{erf} \left[-(z - ut + 3\sigma)/\sigma \right] + u_{acc}(t), \quad (3.131)$$

where u_{acc} is a known function of time describing the acceleration of the shock wave. We believe that the general case of ITP-AC with an accelerating shock wave would benefit from a direct numerical solution. However, here we consider a special case, where the change in shock velocity is small, and for this case, we outline a formulation for an analytical solution. For this case

$$u_{acc}(t) = \varepsilon_{acc} u \hat{u}_{acc}(t), \quad (3.132)$$

where

$$0 \leq \hat{u}_{acc}(t) \leq 1. \quad (3.133)$$

If ε_{acc} , a smallness parameter describing the acceleration is of the same order as ε , the smallness parameter describing the difference between target velocity in the LE and the TE, then we can approximately equate the two and write

$$v(z) = u + \varepsilon u \left(\operatorname{erf} \left[-(z - ut + 3\sigma)/\sigma \right] + \hat{u}_{acc}(t) \right). \quad (3.134)$$

Since the velocity profile is now again of the form (just like for the constant shock velocity case discussed in the main text)

$$v(z) = u + \tilde{u}(z, t) \quad (3.135)$$

the solution for the slowly accelerating shock ITP-AC follows the same procedure. Here

$$\tilde{u}(z, t) = \varepsilon u \left(\operatorname{erf} \left[-(z - ut + 3\sigma)/\sigma \right] + \hat{u}_{acc}(t) \right). \quad (3.136)$$

Thus, we similarly non-dimensionalize the equations, and then seek a straightforward expansion for their solution in the form $c = c_0 + \varepsilon c_1 + \varepsilon^2 c_2 + \dots$, $n = n_0 + \varepsilon n_1 + \varepsilon^2 n_2 + \dots$. We obtain the same system of perturbed equations and boundary conditions. The solution to the zeroth order equations remains unchanged. The solution to the first and second order equations is also similar to the similar solutions for a constant velocity shock, with the exception that the \tilde{u} in equations (3.72) onward and (3.96) onward in Sections 3.5.1.2 and 3.5.1.3 is that described by equation (3.136).

4 Coupling Isotachophoresis with Affinity Chromatography for Rapid and Selective Purification with High Column Utilization: Experimental Study

The contents of this chapter were previously published by V. Shkolnikov and J. G. Santiago [8] in *Analytical Chemistry* journal and are reproduced here with minor modifications.

4.1 Introduction

Affinity chromatography (AC) is a popular chromatographic technique for specific purification and/or analysis of enzymes, lectins, other proteins, and nucleic acids from various samples [99-102]. However, when sample components of interest are present in very low concentrations, a substantial volume of sample must be processed through the affinity substrate. Low target concentrations and high concentrations of fouling or competing species also imply low target-probe binding rates [103]. These factors increase the time of the affinity assay, can lead to poor substrate utilization, and/or poor purification yield, limiting applications of AC. As we presented in Part I, we propose to address these limitations of AC by preconcentrating and purifying the target immediately prior to and during affinity reaction using isotachophoresis (ITP) [3].

ITP has been used experimentally in conjunction with affinity-type assays in several applications. For example, Abelev et al. used ITP with counterflow to transport sample compounds onto regions of immobilized proteins on cellulose acetate and nitrocellulose membranes [121-127]. Abelev et al. used the binding to detect the presence of and analyze properties of antibodies [121-127], lectins [123, 124, 126], other proteins [121, 122], and nucleic acids [125]. However, in their work ITP was used only as a pump-free, reproducible transport mechanism, and not to substantially preconcentrate the analytes with ITP and demonstrably speed up reactions [127]. Garcia-Schwartz et al. presented an approach combining ITP and an affinity reaction to detect micro-RNA [105, 106]. They used ITP to accelerate hybridization between a target species and a mobile fluorescent DNA probe in a microchannel. This ITP zone was then transported into a channel section containing cross-linked polyacrylamide gel functionalized with DNA complementary to the fluorescent DNA probe. This method was used to remove signal background (a negative enrichment strategy) and so enhance sequence specific quantitation and specificity [105, 106]. Recently (in work published during preparation of this manuscript), Karsenty et al. used ITP to accelerate a reaction of a DNA target to an immobilized DNA probe on a short region of stationary magnetic beads [107]. In this relatively simple demonstration, only a small portion (<1%) of the target is captured uniformly by the short (order of ITP peak width) bead region and detected. Despite these related studies, we know of no use of ITP with affinity reactions to capture and recover (i.e., purify) target molecules. We also know of no demonstrations where most of ITP-focused target is captured and detected on an AC column.

In Chapter 3, we described the principle of coupling ITP preconcentration and AC purification to purify and/or analyze all of the target focused in ITP [3]. Relevant to the current experiments, we derived and discussed an analytically solvable one-dimensional transport model for coupling of ITP with a semi-infinite AC porous column with second order reversible reaction kinetics. Our model captured the spatiotemporal dynamics of target-probe binding including the coupled effects of target distribution width, distribution intensity, application velocity, forward and reverse reaction constants, and probe concentration on necessary affinity region length, assay time, and capture efficiency. Our formulation collapses these six independent variables to three non-dimensionalized parameters: α , β , and Da . α and Da represent the scaled target distribution height and width respectively and β represents scaled dissociation constant. We will discuss trends predicted by our model below, as these are relevant to the current comparisons between experimental results and our model.

We here demonstrate experimentally ITP-enhanced affinity capture in 500 μm inner diameter glass capillary with a poly(glycidyl methacrylate-co-ethylene dimethacrylate) (GMA-EDMA) porous polymer monolith (PPM) with order 2 μm pores, functionalized with cDNA probes. We employed GMA-EDMA as GMA epoxy group allowed for easy immobilization of DNA probes. These 2 μm diameter pores allowed us to migrate target macromolecules (here DNA) without target sieving, or exclusion effects from concentration polarization, or Donnan exclusion. Lastly, we used GMA-EDMA as it is translucent (enabling fluorescent detection of bound DNA), can be UV photopolymerized, and is easily incorporated into microfluidic devices.

In this chapter, we first explain our choice of the affinity substrate, GMA-EDMA PPM for ITP-AC. We then describe synthesis of GMA-EDMA, and its functionalization with DNA probes. Next, we describe our protocol for our ITP-enhanced affinity study, as well as the choice of buffer chemistry for ITP-AC of DNA. We chose a DNA target for this demonstration of ITP-AC as nucleic acids are important clinical markers and therapeutic agents [128-130] which often require rapid purification prior to analysis or use [131-135]. Next, we present an experimental validation of our model from Part I with experiments using Cy5 labeled 25 nt synthetic DNA target and synthetic DNA PPM immobilized probe. Lastly, using our technique, we demonstrate high resolution sequence specific purification of 25 nt target DNA from genomic fish sperm DNA, as an example of extraction from a high abundance background (with 10,000-fold greater mass than the target).

4.2 Experimental Methods

Here we describe our experimental setup and materials, our choice of affinity substrate, GMA-EDMA PPM, the synthesis of this PPM, and functionalization of this PPM with cDNA. We also discuss ITP-AC protocol and our choice of ITP-AC buffer chemistry.

4.2.1 Experimental setup

Figure 4.1 summarizes the major features of our experimental setup including the power supply, optical detection hardware, and the PPM affinity structure integrated into a capillary and forming the affinity column. We performed ITP-aided affinity chromatography experiments in VWR 53432-728 micropipette capillaries (inner diameter 501 μm , borosilicate glass) (Visalia, CA) secured in a custom built capillary set up, which

interfaced LE and TE reservoirs to the capillary (see Figure 4.1a and Supplementary Information (SI) Section 4.5.5). Using these capillaries allowed us to easily and cost-effectively iterate through PPM synthesis chemistries and DNA functionalization chemistries. To apply current for ITP, we used platinum wire electrodes (Sigma Aldrich, St. Louis, MO) and a Keithley 2410 high voltage sourcemeter (Keithley Instruments, Cleveland, OH) in galvanostatic mode.

We monitored our experiments and performed fluorescence measurements of the PPM with an Olympus IX70 inverted fluorescence microscope equipped with 4x (NA of 0.16) and 2x (NA of 0.08) objectives (Olympus, Hauppauge, NY), a model XF110-2 and XF115-2 filter cubes (Omega Optical, Brattleboro, VT), and 627 nm red and 470 nm blue LEDs (ThorLabs Newton, NJ) for illumination. We captured images with a 12-bit, 2048 x 2048 pixel charge coupled device (CCD) camera with 7.4 x 7.4 μm pixels (Photometrics CoolSNAP K4) controlled with WinView software, (Roper Scientific, Trenton, NJ). We post-processed the images with custom in-house scripts written in MATLAB (Mathworks, Natick, MA).

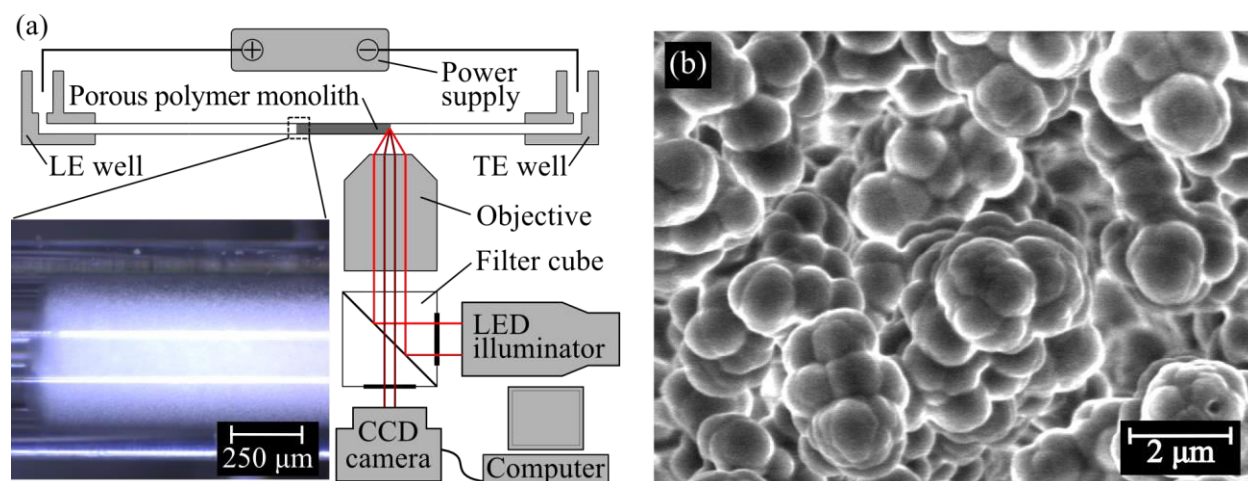


Figure 4.1. (a) Schematic of the experimental setup consisting of a custom-built capillary setup, a high voltage power supply, and an epifluorescence microscope with a CCD camera. The inset in the lower left is a bright field image of the GMA-EDMA PPM inside a 500 μm inner diameter borosilicate glass capillary. (b) SEM micrograph of our GMA-EDMA substrate for probe immobilization. The PPM morphology consisted of globules approximately 1 μm in diameter, and these formed roughly 2 μm diameter pores ensuring that the porous affinity region had small hydrodynamic resistance and easily permitted ITP focusing and transport without sieving effects.

4.2.2 Materials

Ethylene dimethacrylate (EDMA; CAS# 97-90-5), glycidyl methacrylate (GMA; CAS# 106-91-2), inhibitor removal media (product number: 311332; CAS# 9003-70-7), azobisisobutyronitrile (CAS# 78-67-1), 3-(trimethoxysilyl)propyl methacrylate (TSPM; CAS# 2530-85-0), sodium dodecyl sulfate (SDS), acetone, and methanol (MeOH) 99.93% were purchased from Sigma Aldrich. n-Hexane HPLC grade 95+% was purchased from Alfa Aesar. Saline-sodium citrate (SSC) buffer 20X was from Invitrogen (Carlsbad, CA). Fish sperm DNA (CAS# 100403-24-5) was from Amresco (Solon, OH). Synthetic oligos were purchased from Integrated DNA Technologies (Coralville, IA) and Stanford protein and nucleic acid (PAN) facility (Stanford, CA).

4.2.3 Porous polymer monolith synthesis and functionalization

For our affinity substrate we chose GMA-EDMA PPM since the epoxide group on GMA is known to be highly reactive to primary amines on biopolymers such as nucleic acids [83, 131] and proteins [81, 85, 136] and other well-known affinity ligands [101]. We cross-linked GMA with EDMA via a free-radical, UV-initiated polymerization in the presence of MeOH and hexane as solvents, with AIBN as photoinitiator [137]. We then functionalized the PPM with DNA, via epoxy-amine reaction between the GMA epoxy group and a primary amine on the synthetic DNA probe. See SI Section 4.5.6 for details regarding the choice of PPM chemistry, and protocols for PPM synthesis and functionalization.

4.2.4 ITP-aided affinity chromatography protocol

The protocol for our experiments is summarized in Figure 4.2, along with example experimental data. We began by filling the LE reservoir and the capillary with integrated affinity column with the LE buffer by applying 68 kPa vacuum to the TE reservoir. We then mixed the sample containing the target with the TE buffer and placed this in the TE reservoir (Figure 4.2a, Step 1). We then applied a constant current, inducing ITP extraction, purification, and focusing. We refer to this current as "run current". Under ITP transport, the LE ions in the capillary migrated toward the LE reservoir followed by the TE ions. The target ions (DNA) have an electrophoretic mobility intermediate to our LE and TE ions, and so overspeed neighboring TE ions and focus at the interface. The DNA is quickly (within 15 min) concentrated to at least 100-fold at the LE-TE interface, resulting in a sharp, Gaussian-like peak (Figure 4.2a, Step 2). The target DNA was labeled and visualized with fluorescent Cy5 dye. To purify unlabeled DNA, the LE-TE interface can be tracked

non-invasively, for example, with species altered fluorescence imaging [138] or via current monitoring [139]. Any matrix and/or interference ions with electrophoretic mobilities lower than that of the TE were separated from the target (Figure 4.2a, Step 2). Prior to the target migrating into the porous affinity region, we lowered the current to a value we refer to as "capture current". We thus employed two magnitudes of current for our experiments, allowing us to independently control the time to focus target and the rate of transport through the affinity region. The concentrated target then migrated into the porous affinity region where it was captured by the immobilized probe (Figure 4.2a, Step 2; Figure 4.2b). The LE-TE interface continued to migrate through the affinity region and beyond. We ended the experiment once the LE-TE interface migrated far enough from the capture region. To quickly terminate the reverse (dissociation) reaction, we displaced the LE and TE buffers entirely from the column with air (applying vacuum to the LE reservoir). This column dry out quickly disrupts any dissociation reactions, enabling capture levels close to those of the focused ITP concentration. To elute and harvest captured target, we then introduced into the capillary a finite liquid slug (approximately 5 μ l) of elution buffer. We used a syringe to drive this slug through the column and so elute the target (Figure 4.2a, Step 4). We removed this eluted volume from the column, and quickly quenched the alkaline elution buffer (50 mM NaOH) with 200 mM HEPES to achieve near neutral pH. In the SI (Section 4.5.1), we provide more details of our injection protocol, including an estimate of the efficiency of target extraction from the TE reservoir.

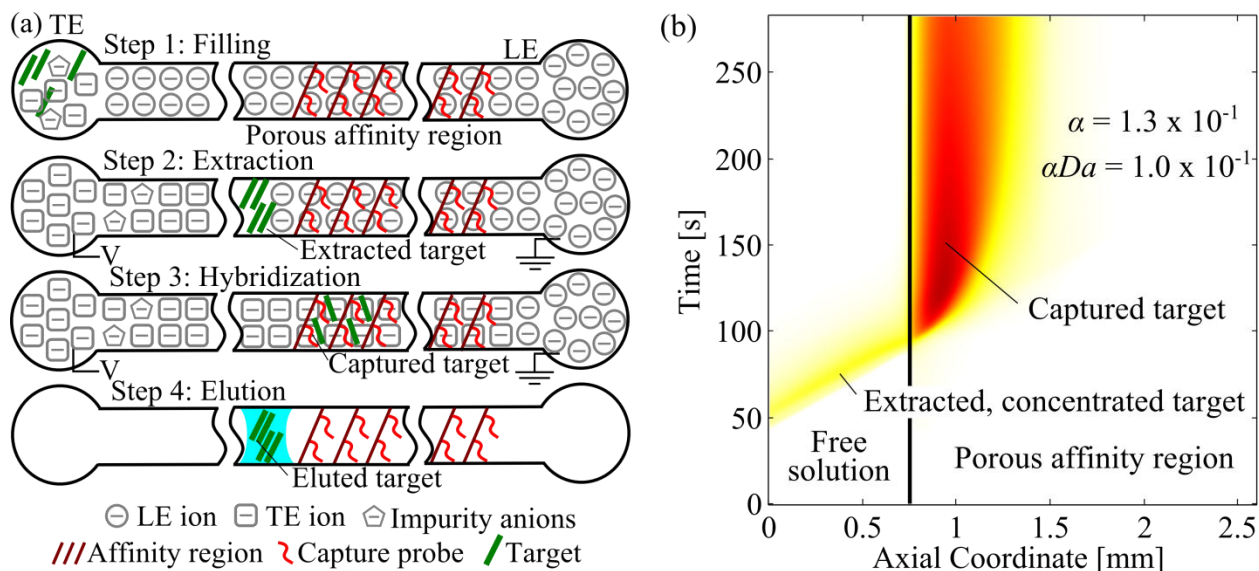


Figure 4.2. (a) Schematic illustrating our assay for ITP-aided affinity chromatography in a porous polymer monolith column. We filled the LE reservoir and affinity column with LE buffer (via vacuum at the TE reservoir), and then introduce the sample and TE mixture into the TE reservoir (Step 1). We apply an electric field (from LE to TE) and the target species are extracted and focus into a sharp ITP peak (Step 2). The target migrates into the affinity region and is captured by the immobilized probe (Step 3). After capture, we displace the LE and TE buffers with air to arrest the desorption reaction. We then introduce a small (roughly 5 μ l) slug of elution buffer to remove and collect the bound target from the column (Step 4). (b) Spatiotemporal plot of experimentally measured target concentration showing dynamics of a typical ITP-AC binding experiment. The concentrated target (visualized with Cy5 fluorescence) entered the porous affinity region from the left and was captured by the immobilized probes. In this experiment $\alpha Da = 1.0 \times 10^{-4}$ and $\alpha = 1.3 \times 10^{-3}$.

4.2.5 ITP-AC choice of buffer chemistry

We explored a significant number of variations of our chemistry and here summarize our final choice. The LE buffer consisted of 250 mM HCl and 500 mM Tris. The TE buffer as placed in the TE well consisted 25 mM HEPES, 50 mM Tris, and varying amounts of target and/or contaminating species. We chose chloride and HEPES as LE and TE ions respectively to provide a good tradeoff between focusing the target DNA and excluding contaminants. We chose Tris as a counterion to provide a pH of 8.2 for the

hybridization reaction, as the hybridization of DNA occurs readily around this pH [140, 141]. See SI Section 4.5.7 for more details regarding our choices of buffer chemistry for ITP-AC.

4.3 Results and Discussion

First, we briefly review results of our model from Chapter 3 and then present a series of experiments we used to study ITP-AC and validate our model. In these experiments, we measured the target migration in ITP and its subsequent hybridization reaction with the immobilized probe. We varied the scaled total target amount, αDa , over 4 orders of magnitude by varying target amount and ITP velocity. We compared the spatiotemporal behavior of ITP-AC, capture length, and capture efficiency to that predicted by our model described Part I of this two-part series. Lastly, we demonstrated purification of 25 nt DNA target from 10,000-fold more abundant fish sperm DNA.

4.3.1 Brief review of ITP-AC trends predicted by our model

We here summarize some insights from the model presented in Chapter 3. These insights guided our experimental efforts and are relevant to the experiment versus prediction comparisons presented below. Briefly, our analysis showed that the product αDa represents scaled total target amount, and acts as a saturation parameter. For $\alpha Da < 1$ there is insufficient target to locally saturate the affinity region. In this regime, the dimensional capture length, p_z , the physical distance to capture 95% of target, is governed only by the balance of advection and reaction. In this regime, $p_z = 2.8u/(k_1N)$. For $\alpha Da > 1$, the affinity region becomes locally saturated starting at the leading edge. In this regime, capture length is proportional to the total target amount. For $\alpha Da \leq 1$ and $Da < 0.1$, the target

distribution acts as a Dirac delta distribution relative to the affinity region. In this regime, capture time, p_t , the physical time to capture 95% of target, is determined solely by the kinetics of the reaction, and equals $4.3/(k_1 N)$. For $\alpha Da \leq 1$ and $Da > 1$, the target distribution is relatively wide and capture time is governed by the time to advect the target into the affinity region. In the latter regime, $p_t \approx 5.4\sigma/u$. We showed that by decreasing Da (e.g., as with ITP preconcentration) we can reduce AC assay time, and/or improve column utilization. Lastly we showed that the integration of ITP and AC separates the target and contaminants into non-diffusing zones, so the resolution of ITP-AC scales proportionally with time.

4.3.2 Measurement of ITP-AC parameters

In model versus experiments comparison, we strove to minimize the number of assumed parameters, and find global parameters which represented the entire data set (not just individual conditions). Our model requires three parameters α , β , and Da . To evaluate these, we directly measured values of u , p_z , a , n , and N , so we make no assumptions regarding these parameters. We measured u directly from spatiotemporal data of target migration in free solution in front of the PPM. We measured p_z by integrating the width-averaged measured fluorescence intensity with respect to the axial coordinate to find the bounds containing 95% of the total integrated intensity. We measured a and n by measuring fluorescence intensity in the spatiotemporal fluorescence data and by interpolating within calibration curve for Cy5 fluorescence vs. DNA concentration (SI, Section 4.5.2). Similarly, in separate experiments, we measured N by measuring fluorescence intensity of Cy5 modified probe bound to the PPM and interpolating on a Cy5 fluorescence vs. DNA concentration curve.

After measuring values of u , p_z , a , n , and N , we had several choices of obtaining the values of K_d , and k_1 . We chose to demonstrate our assay using DNA target and capture probes with high hybrid melting temperature, so the reactions in our experiments are strongly irreversible. This made the model predictions very weak functions of K_d . We chose to estimate and fix the value of K_d and then vary k_1 as the sole “free” parameter. We estimated K_d based on published experimental measurements of K_d for similar oligonucleotide lengths and similar ionic strengths (see SI, Section 4.5.3). For all our experiments, K_d was roughly 10^{-11} M and β was 3×10^{-7} . This β is far lower than a β for which any decrease of capture efficiency or streaking could be expected from target-affinity probe dissociation (see Chapter 3, Section 3.3.2.4). From our model versus experimental comparisons, we obtained a value for k_1 of $1.5 \times 10^3 \text{ M}^{-1} \text{ s}^{-1}$, and this provided the best global fit to all 18 experiments in our data set (spanning 6 experimental conditions). This value for on-rate constant is consistent with that observed by, for example, Gao et al. for surface hybridization of DNA with some secondary structure [142]. For example, Gao et al. obtained forward rate constants ranging from $3 \times 10^3 \text{ M}^{-1} \text{ s}^{-1}$ for probes and targets with some secondary structure to $5 \times 10^4 \text{ M}^{-1} \text{ s}^{-1}$ for probes and targets with little secondary structure for 25 nt probes and targets [142]. See SI Section 4.5.3 for the predicted secondary structure of our target and probe. See SI Section 4.5.9 for additional discussion and recommendations for practical ITP-AC parameters.

4.3.3 Spatiotemporal behavior of ITP-AC

We observed and quantified the spatiotemporal behavior of ITP-AC by tracking the target while it was migrating in ITP in free solution and while it was reacting with the immobilized probe in PPM. In Figure 4.2b we show a spatiotemporal plot of the target

entering the PPM from free solution and reacting with the immobilized probe in the PPM. We plot the channel cross sectional area averaged Cy5 fluorescence intensity as a function of distance along the axial coordinate and time.

In this experiment, we spiked 10 nM target DNA into the TE and performed ITP in galvanostatic mode with a run current of 800 μA and capture current of 200 μA . Both the ITP velocity and the electroosmotic flow velocity are proportional to current. For this system, the electroosmotic flow is in the direction opposite of the LE-TE interface migration, and therefore decreases the ITP velocity. The electric field in the LE-TE interface is also proportional the current in the system. This electric field counteracts target dispersion and therefore target distribution width is in this regime inversely proportional to the current in the system.[22, 25, 26, 143] Therefore, as in typical ITP dynamics, the capture current simultaneously controlled the net target velocity and the target distribution width. This combination of target concentration and capture current resulted in $\alpha = 1.3 \times 10^{-1}$ and $\alpha Da = 1.0 \times 10^{-1}$.

The target focused in ITP migrated at constant velocity in a Gaussian like distribution toward the PPM (Figure 4.2b). As we described in Section 4.2.4, we performed ITP-AC experiments with semi-infinite injection, meaning that small amount of target continuously streamed through the TE into the Gaussian peak. As we observe in Figure 4.2b, the concentration of target in the TE is negligibly small. Hence, we approximate the initial target distribution (the distribution just before the target enters the PPM) as a perfectly Gaussian distribution, as occurs with finite injection ITP (and as assumed by our model).

Upon reaching the monolith, target immediately began to bind with the affinity probe, penetrating about 2.8 advection-reaction length scales into the affinity region (Figure 4.2b). As shown in Figure 2b, there is an increase in fluorescence intensity (approximately 1.7x) when the target enters the PPM. This effect was observed both with ITP and without ITP in our PPMs. It was also observed with and without immobilized probes (see SI, Section 4.5.2). Such observations lead us to attribute this to the refractive optical properties of the PPM and we corrected for this when measuring a , n , and N .

4.3.4 Comparison between predicted and measured spatiotemporal behavior of ITP-AC

In Figure 4.3 we compare the spatiotemporal behavior of three ITP-AC experiments (bottom row) with that predicted by theory (top row) from Part I of this two-part series. We plot the logarithm of the channel cross sectional area averaged fluorescence intensity as a function of distance along the axial coordinate inside the PPM and time. To predict the spatiotemporal plots, we neglected the effects of photobleaching and assumed a proportional relationship between the fluorescence intensity of Cy5 and target concentration. For experiments shown in Figure 4.3d, 3e, and 3f we spiked 10000, 100, and 100 pM target DNA into the TE respectively. We performed ITP in galvanostatic mode with run current of 800 μ A and capture currents of 200, 200, and 600 μ A, respectively. These combinations of target concentrations and capture currents resulted in values of $\alpha Da = 1.0 \times 10^{-1}$ and $\alpha = 1.3 \times 10^{-1}$; $\alpha Da = 4.3 \times 10^{-4}$ and $\alpha = 1.1 \times 10^{-3}$; $\alpha Da = 1.7 \times 10^{-4}$ and $\alpha = 9.2 \times 10^{-4}$, respectively. We chose to operate at $\alpha Da < 1$ as to not locally saturate the affinity region (see Section 4.3.1). For experiments shown in Figure 4.3d, e, and f, as well as those in Figure 4.5, Da was of order 1, and ITP preconcentration was order 100

fold. We chose not to preconcentrate further as doing so would not significantly decrease p_i^* and therefore would not improve assay time or column utilization (see Chapter 3, Section 3.3.2.3).

Overall, our model showed very good qualitative agreement with experiments for over 3 orders of magnitude of target concentration. Both the predicted shape and the relative magnitude of J-shaped contours for bound target concentration agreed well with experimentally observed. For example, in the experiment shown in Figure 4.3d, the target concentration was larger than that shown in e, and f, and so the captured target fluorescence intensity (proportional to n/N) was markedly larger than that shown in e, and f. In the experiment shown in Figure 4.3f, capture current was larger than that shown in 3d, and 3e, and this resulted in a larger target velocity and so deeper penetration into the PPM than in experiments shown in Figure 4.3d and e. For all three experiments, upon penetrating approximately 2.8 advection-reaction length scales into the affinity region a steady state was reached and the target persisted on the PPM, as expected.

Our model also showed good quantitative agreement with our experiments. For example, for the experiment of Figure 4.3d, $p_z = 0.93$ mm, and $\max(n/N) = 7.2 \times 10^{-2}$. For the corresponding theoretical prediction shown in Figure 3a, $p_z = 1.03$ mm, and $\max(n/N) = 8.3 \times 10^{-2}$, which is within 11%, and 15% respectively of experimentally measured values. For the experiment of Figure 4.3e, $p_z = 0.91$ mm, and $\max(n/N) = 5.8 \times 10^{-4}$; while the corresponding prediction shown in Figure 4.3b, was $p_z = 0.97$ mm, and $\max(n/N) = 3.9 \times 10^{-4}$, (respectively within 7%, and 33% of the measured values). Lastly, for the experiment of Figure 4.3f, $p_z = 2.8$ mm and $\max(n/N) = 2.7 \times 10^{-4}$; and the corresponding theoretical prediction shown in Figure 3c is $p_z = 2.5$ mm, and

$\max(n/N) = 1.6 \times 10^{-4}$, which are within 11%, and 41%, respectively, of experimentally measured values.

We attribute slight distortions in the J-shaped profiles in Figure 4.3d and e to small amounts impurity present with the target that were not captured by the affinity probes. We attribute the difference in early-time slopes of the contours of Figure 4.3c and f to a difference in target velocity between our model and experiment. Our model assumes constant velocity of the target, resulting in linear low angle contours at early times of t in Figure 4.3c. In our experiments we observed that the target slowed down, which is reflected in the fluorescence slope of Figure 4.3f. One possible cause for this is the interactions of the target with the immobilized probes.

We attribute the small discrepancies in p_z and $\max(n/N)$ between theoretical predictions (Figure 4.3a, b, and c) and experimental observations (Figure 4.3d, e, and f) to small inhomogeneities in the PPM resulting in slightly non-homogeneous immobilized probe distribution. We hypothesize that this inhomogeneity was caused by air trapped in some of the pores. This air was likely trapped with a slightly different, random, distribution for each experiment. This trapped air blocked access to the immobilized probes causing effective inhomogeneity in probe distribution. This hypothesis is supported by our observations that the PPM material was somewhat hydrophilic, and thus trapped the less wetting phase (air) inside the pores.

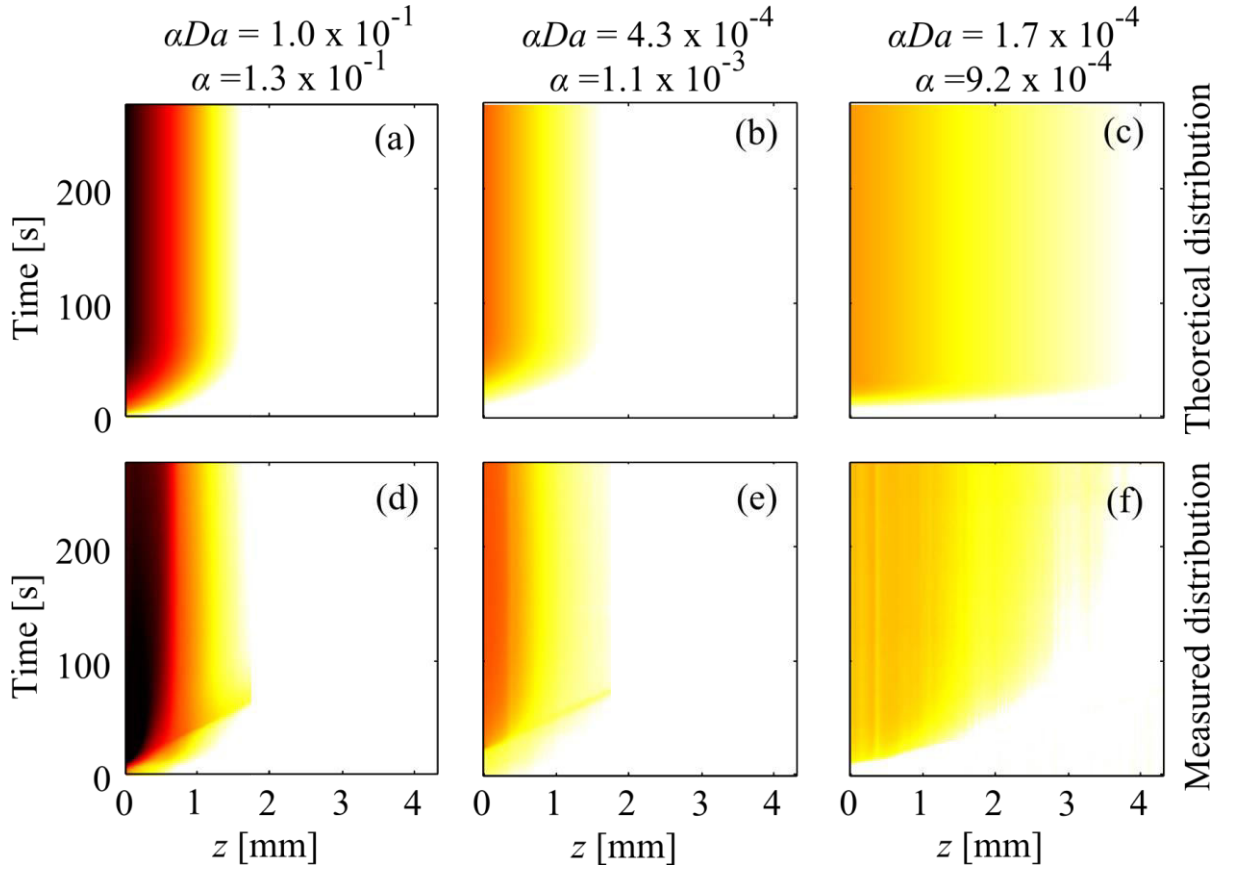


Figure 4.3. Predicted (a, b, c) and measured (d, e, f) spatiotemporal behavior fluorescently labeled DNA target in ITP-AC inside the affinity region. The spatiotemporal plots show the logarithm of cross sectional area averaged fluorescence intensity of the target as a function of axial coordinate z and time. Location $z = 0$ is at the leading edge of the PPM affinity region (see Figure 4.2a). (a), (b) and (c) show theoretically predicted captured target distribution for $\alpha Da = 1.0 \times 10^{-1}$ and $\alpha = 1.3 \times 10^{-1}$, $\alpha Da = 4.3 \times 10^{-4}$ and $\alpha = 1.1 \times 10^{-3}$, $\alpha Da = 1.7 \times 10^{-4}$ and $\alpha = 9.2 \times 10^{-4}$ respectively. (d), (e) and (f) show experimentally observed captured target distribution for the same respective αDa and α . The predicted spatiotemporal distribution of target agreed well with that experimentally observed.

4.3.5 Effect of α and Da on scaled capture length

To validate our predictions for scaled capture length p_z^* we measured p_z for 18 ITP-AC experiments (6 experimental conditions) varying αDa from 10^{-4} to 10^{-1} . We varied αDa by varying both the target concentration in the TE well (100 pM to 10 nM) and capture current (200 μA to 600 μA). We stayed within a regime of $\alpha Da < 1$ in our experiments so

as to not locally saturate the affinity capture region. To calculate p_z^* , we obtained u , p_z , N and k_1 as described in Section 4.3.2. We plot the measured p_z^* and the theoretically predicted p_z^* curves as a function of αDa in Figure 4.4a.

Figure 4.4a shows a successful collapse of our p_z^* data over 4 orders of magnitude of αDa (from 10^{-4} to 10^{-1}). This confirms our prediction that p_z^* is approximately constant for this most relevant range of αDa . We attribute small column-to-column variations in p_z^* to small, irreproducible inhomogeneities in the PPM.

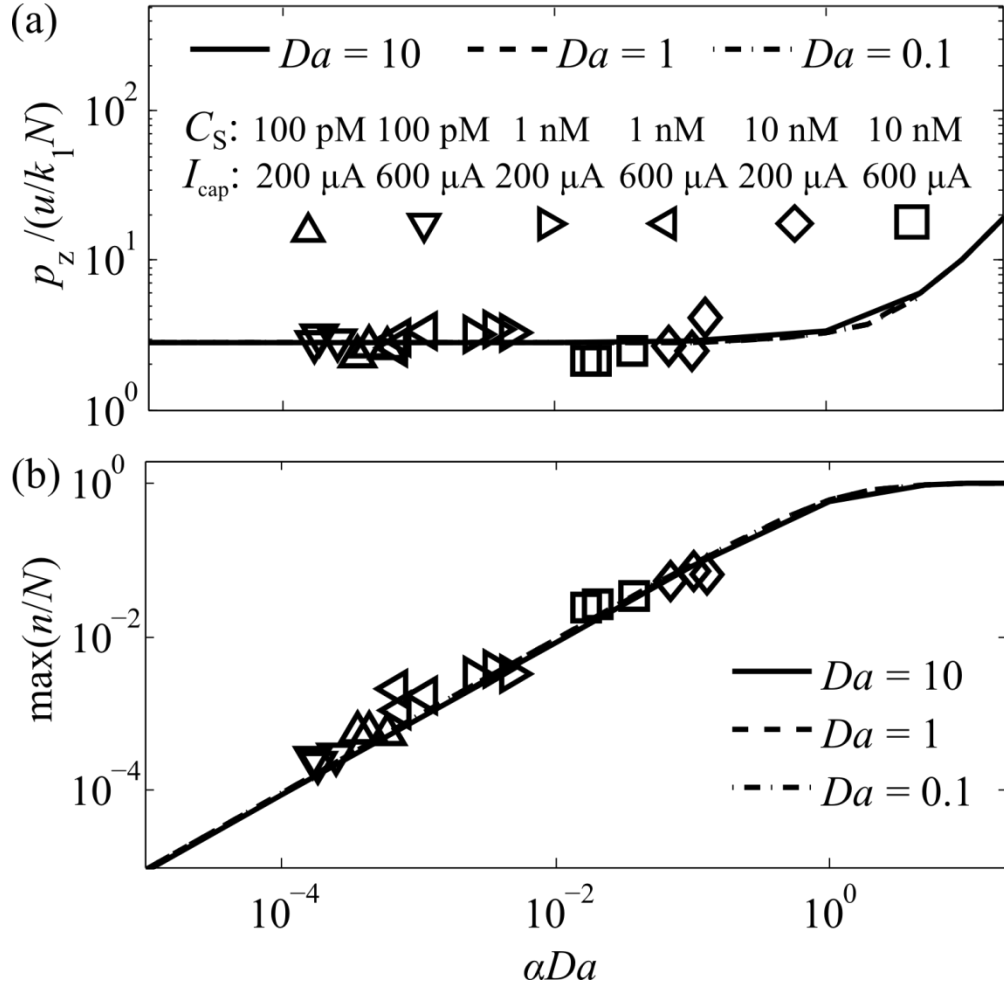


Figure 4.4. Predicted and experimentally observed (a) scaled capture length, and (b) maximum capture efficiency as a function of total scaled target amount, αDa . C_S is the target concentration in the TE, and I_{cap} is the capture current in the ITP-AC experiment. Scaled capture length is invariant of αDa for $\alpha Da < 1$ and equals approximately 2.8. For $\alpha Da > 1$, the affinity region is locally saturated and scaled capture length increases linearly with αDa . Maximum capture efficiency increases linearly with αDa for $\alpha Da < 1$. For $\alpha Da > 1$, the affinity region is locally saturated and $\max(n/N)$ approaches unity.

4.3.6 Effect of α and Da on capture efficiency

We validated our theoretical predictions for maximum capture efficiency $\max(n/N)$ with measurements of $\max(n/N)$ for 18 ITP-AC experiments varying αDa from 10^{-4} to 10^{-1} , as with Section 4.3.5. We again maintained $\alpha Da < 1$ so as to not saturate the affinity capture region. As Peterson et al. showed, local saturation of an affinity region with high DNA probe density is not always experimentally possible due to electrostatic repulsion of DNA [144].

To obtain $\max(n/N)$, we measured $\max(n)$ from the spatiotemporal data and N from separate calibration experiments (see Section 4.3.2). First, we measured the maximum fluorescence intensity of a bound target after a steady state was reached (i.e. the distribution of target was not changing). We then obtained $\max(n)$ by interpolating the fluorescence intensity on a Cy5 fluorescence intensity vs. DNA concentration calibration curve (SI, Section 4.5.2). We plot the measured $\max(n/N)$ and the theoretically predicted $\max(n/N)$ as a function of αDa in Figure 4b.

We observed that the measured values of $\max(n/N)$ over 4 orders of magnitude change in αDa and across all our conditions successfully collapses the data to a single linear relationship. This agrees very well with the theoretically predicted trend. We attribute the random variations in $\max(n/N)$ to experiment-to-experiment variations in inhomogeneity of N due to trapping of air in the PPM.

4.3.7 Sequence specific extraction of target from 10^4 x more abundant contaminant

Finally, as a demonstration of ITP-AC, we performed separations of Cy5 labeled 25 nt oligo DNA from 10,000-fold more abundant genomic fish sperm DNA. For these experiments, we placed into the TE reservoir $0.1 \mu\text{g ml}^{-1}$ of Cy5 labeled target DNA (total $0.02 \mu\text{g}$) and $1000 \mu\text{g ml}^{-1}$ fish sperm DNA (total $200 \mu\text{g}$). We included in the mixture 0.1x SYBR Green I to aid visualization of total nucleic acids. We performed ITP in galvanostatic mode with run current of $800 \mu\text{A}$ and capture current of $200 \mu\text{A}$. We visualized this experiment independently in the SYBR Green I optical channel (visualizing the very high abundance fish sperm DNA) and in the Cy5 optical channel (visualizing only the target) Lastly, we performed electrophoresis analysis of the eluate, providing an independent verification of the purification (see SI Section 4.5.8).

Figure 4.5 summarizes our demonstration of selective capture. Figure 4.5a shows the spatiotemporal plot of observed fluorescence from the experiment in the SYBR Green I channel. The fish sperm DNA migrated in ITP from free solution into the PPM and continued to migrate in ITP. This shows background DNA was not captured by the immobilized probe of the PPM, showing little non-specific binding of DNA to the GMA-EDMA PPM. We attribute the slight decrease in ITP velocity of fish sperm DNA to the effects of EOF on ITP.

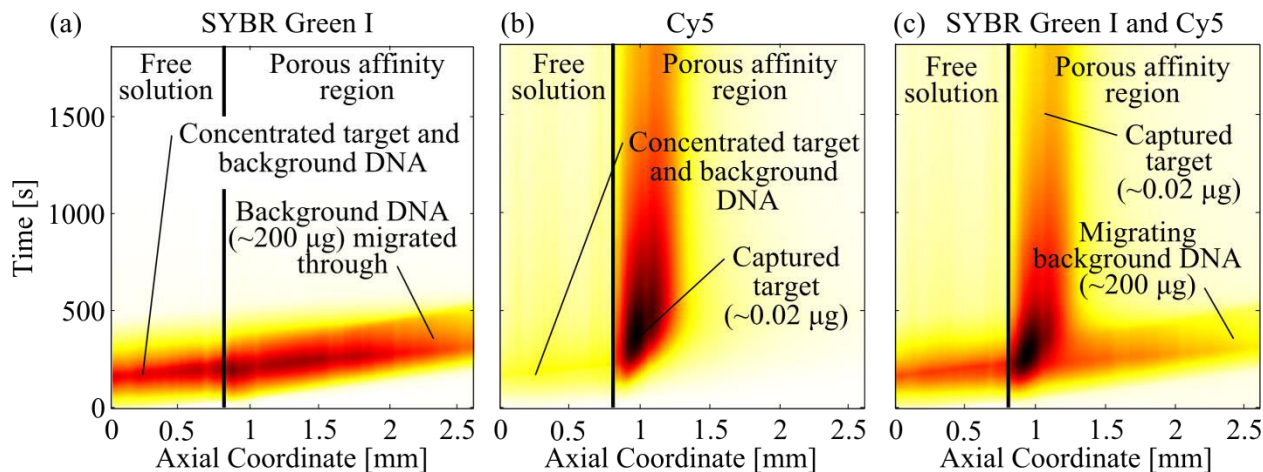


Figure 4.5. Spatiotemporal plots showing separation of rare target DNA from 10,000-fold more abundant contaminating DNA using ITP-AC. The plots show the target and contaminant migrating from free solution into the porous polymer. SYBR Green I mostly visualized the highly abundant background contaminant fish sperm DNA and Cy 5 visualized the 25 nt target. (a) Separation observed in the SYBR Green I optical channel showing the migration of fish sperm DNA. Fish sperm DNA was not captured by the immobilized probe on the PPM and continued to migrate in ITP. This indicates that there was little non-specific binding of DNA to PPM. (b) Separation observed in the Cy5 optical channel. The Cy5-labeled, low-abundance target DNA was quickly and selectively captured. (c) Separation observed in overlapped SYBR Green I and Cy5 channels shows separation between the trace target DNA and the 10,000-fold more abundant contaminating fish sperm DNA.

In Figure 4.5b we show the spatiotemporal plot of observed fluorescence from the experiment in the Cy5 channel. The Cy5-labeled target migrated in ITP from free solution into the PPM and was quickly captured by the immobilized probe on the PPM. The presence of 10,000-fold more abundant contaminating DNA did not interfere with capture of the target. We attribute the decrease in Cy5 fluorescence over time (which becomes prominent in Figure 4.5b after 1000 s) to photobleaching of Cy5.

In Figure 4.5c we show the spatiotemporal plot of observed fluorescence from the experiment in both the SYBR Green I and Cy5 channels. Figure 5c shows clearly how target species attain zero velocity in a time of p_t , while the contaminant species (fish sperm

DNA) continues to migrate at ITP velocity. This allows for superior separation as the target and contaminant are spatially confined to two distinct, non-diffusing regions [3]. The resolution of ITP-AC increases proportionally to time. For this experiment $\mu_{L \text{ in } LE} \approx -60 \times 10^{-9} \text{ m}^2\text{V}^{-1}\text{s}^{-1}$, $\mu_{T \text{ in } LE} \approx -20 \times 10^{-9} \text{ m}^2\text{V}^{-1}\text{s}^{-1}$, $k_1 = 10^3 \text{ M}^{-1} \text{ s}^{-1}$, $N \approx 30 \text{ }\mu\text{M}$, and $p_z^* \approx 2.8$. Hence, u_{95} , the target velocity to achieve 95% of maximum resolution with ITP-AC, was approximately 0.01 mm s^{-1} (see the SI of Chapter 3 [3] for a discussion of u_{95}). In this experiment, the target velocity was approximately 0.05 mm/s , and so we achieved higher than 95% of the maximum resolution. In this experiment we separated the target from fish sperm DNA in under 1 mm length of PPM and in under 10 min .

4.4 Conclusions

We presented an experimental demonstration of ITP-AC with Cy5 labeled synthetic DNA target and synthetic DNA probe immobilized onto an approximately $2 \text{ }\mu\text{m}$ pore diameter porous polymer monolith inside a $500 \text{ }\mu\text{m}$ glass capillary. We provided a detailed protocol for ITP-AC and discussed the choice of buffers to perform sequence specific separation of nucleic acids. We described our choice of the porous polymer monolith affinity substrate, poly(glycidyl methacrylate-co-ethylene dimethacrylate). This substrate was non-sieving and exhibited no non-specific binding. It therefore allowed for specific separation of large macromolecules. We described the synthesis of GMA-EDMA PPM and the functionalization of the PPM with DNA probes.

We performed ITP-AC experiments with 25 nt DNA target and compared these with our model presented in Chapter 3. For these experiments, we used epifluorescence imaging to track the Cy5 labeled target as it traveled and reacted within the affinity region. The predicted spatiotemporal dynamics of ITP-AC agreed very well with that measured

experimentally. By varying target concentration and ITP velocity, we explored capture length and capture efficiency for over 4 orders of magnitude of scaled target amount αDa (from 10^{-4} to 10^{-1}). The predicted scaled capture length and maximum capture efficiency agreed very well with experimentally measured values for the entire range explored. Lastly, using our technique, we demonstrated sequence specific purification of 25 nt target DNA from 200 μ l of sample and demonstrated that the resolution in ITP-AC increases linearly with time. In this experiment we successfully purified 25 nt target DNA from 10,000-fold more abundant background (contaminating) genomic fish sperm DNA in under 1 mm column length and in less than 500 s.

4.5 Supplementary Information

We here present additional information on the following topics: (1) Extraction of analyte from the TE reservoir in semi-infinite injection ITP; (2) Calibration of Cy5 fluorescence to DNA concentration; (3) Synthetic DNA oligo sequences used; (4) Measurement of PPM void fraction; (5) Image of custom built capillary setup; (6) Choice of porous polymer monolith chemistry, synthesis, and functionalization; (7) Choice of buffer chemistry for ITP-AC; (8) Analyses of ITP-AC purified 25 nt target from 10,000x contaminant via electrophoresis; (9) Recommended ITP-AC parameters; (10) Choice of pore size in ITP-AC.

4.5.1 Extraction of analyte from the TE reservoir in semi-infinite injection ITP

In the main text of Chapter 3, we focused our analysis on the case of finite sample injection [104], wherein sample is introduced into a finite section of the channel and

bounded by LE on the right side and pure TE on the left side (e.g., pure TE in the reservoir). Finite sample injection enables a designer to fairly easily collect all of the target analyte into the ITP zone prior to reaching the affinity region. See for example Bocek et al. [145] and Marshall [146] for analyses around requirements to focus all sample in ITP for finite injection. The arrangement of finite injection (i.e., requirement to "sandwich" the sample between pure LE and TE [138]) makes it less convenient experimentally, but the method is simpler to analyze and describe, so we used it in our model in Chapter 3.

We here briefly analyze the case of a so-called semi-infinite injection [104]. In semi-infinite injection, the sample is mixed with TE and this mixture is placed into a large reservoir, while the channel and affinity column are filled with pure LE. We present an estimate of the required length to extract most of the sample from the reservoir using semi-infinite injection.

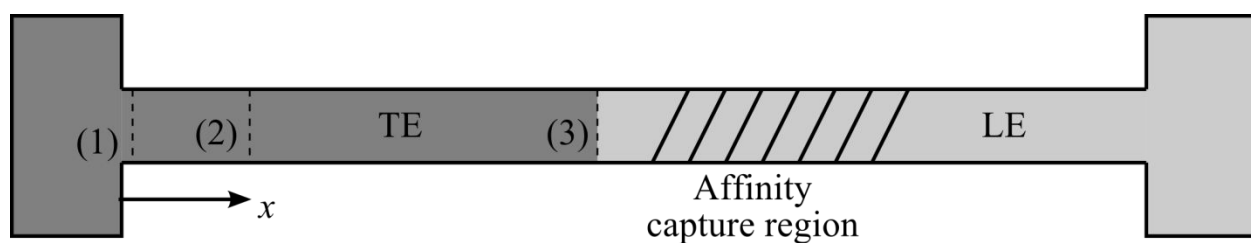


Figure 4.6. Schematic of a channel with LE and TE reservoirs in which ITP with semi-infinite injection is performed. Labeled numerically are three planes through which the flux of analyte is analyzed. We analyze this problem to study of the influence of the length between the TE reservoir and the affinity capture region (cross hatched) on the fraction of sample extracted. Planes (1) and (2) are fixed, while Plane (3) is located at and moves with the LE-TE interface. Plane (1) is located just inside the channel near the TE reservoir and experiences the same concentration of analyte as in the TE reservoir.

We derive an estimate for the length of channel from the TE reservoir to the affinity region that is necessary to nearly completely extract an analyte from the sample and TE

mixture in the TE reservoir. The analysis is an aid to designers as it determines how far downstream from the input reservoir an experimentalist should place the affinity column. Our analysis follows a similar form of that presented by Persat et al. for species exiting a reservoir [147] but is specific to our situation where the species are focusing in ITP.

We begin by noting that in the semi-infinite injection scheme the amount of analyte leaving the TE reservoir, ϕ_{P1} (i.e., passing through Plane 1 located a small distance into the channel as shown in Figure 4.6) is given by

$$\phi_{P1} = A_C \mu_{a,R} E_R c_{a,R}, \quad (4.1)$$

where A_C is the cross sectional area of the channel, $\mu_{a,R}$ is the mobility of the analyte in the reservoir, E_R is the effective electric field near the entrance of the channel, and $c_{a,R}$ is the concentration of analyte in the reservoir. We assume that the reservoir is well mixed (analyte always uniformly distributed in the reservoir) including near the entrance of the channel. Equation (4.1) can be rewritten using Ohm's law as

$$\phi_{P1} = A_C \mu_{a,R} \frac{I}{A_C \sigma_R} c_{a,R}, \quad (4.2)$$

where I is the current through the system, and σ_R is the conductivity of the TE reservoir. We assume that the reservoir is well buffered and that the conductivity of the TE reservoir does not change during the ITP process. In this convention and for anionic ITP, I is negative. The amount of analyte leaving the TE reservoir is proportional to the decrease in concentration of analyte in the reservoir,

$$\frac{dc_{a,R}}{dt} V_R = -\phi_{P1} = -\frac{\mu_{a,R} I}{\sigma_R} c_{a,R}, \quad (4.3)$$

where V_R is the volume of the reservoir. We solve the differential equation (4.3) subject to the initial condition of $c_{a,R} = c_{a0,R}$ at $t = 0$, which yields

$$c_{a,R} = c_{a0,R} \exp\left(-\frac{\mu_{a,R} I}{V_R \sigma_R} t\right). \quad (4.4)$$

The rate of accumulation of analyte at the LE-TE interface [145] is given by

$$\frac{dn_{a,LE-TE}}{dt} = A_C c_{a,TE} (\mu_{a,TE} E_{TE} - u_{ITP}), \quad (4.5)$$

where $n_{a,LE-TE}$ is the amount (e.g., number of moles) of analyte in the LE-TE interface, $c_{a,TE}$ is the concentration of analyte in the adjusted TE, $\mu_{a,TE}$ is the mobility of the analyte in the adjusted TE, E_{TE} is the electric field in the adjusted TE (assumed to be uniform), and u_{ITP} is the velocity of the LE-TE interface. Further, we note that amount of analyte traveling through Plane 1 in Figure 4.6 is equal to that traveling through Plane 2 as no accumulation occurs between these two planes. The amount of analyte traveling through Plane 2 is given by

$$\phi_{P2} = A_C \mu_{a,TE} E_{TE} c_{a,TE}. \quad (4.6)$$

Combining (4.5) with (4.6) and noting that $\phi_{P1} = \phi_{P2}$ we obtain

$$\frac{dn_{a,LE-TE}}{dt} = A_C \frac{\phi_{P1}}{A_C \mu_{a,TE} E_{TE}} (\mu_{a,TE} E_{TE} - u_{ITP}). \quad (4.7)$$

Combining (4.7) with (4.3) we obtain

$$\frac{dn_{a,LE-TE}}{dt} = c_{a,R} \frac{\mu_{a,R} I}{\sigma_R \mu_{a,TE} E_{TE}} (\mu_{a,TE} E_{TE} - u_{ITP}). \quad (4.8)$$

We then simplify (4.8), recalling that $u_{ITP} = \mu_{TEion,TE} E_{TE}$ (where $\mu_{TEion,TE}$ is the mobility of the TE ion in the adjusted TE) [11]

$$\frac{dn_{a,LE-TE}}{dt} = c_{a,R} \frac{\mu_{a,R}}{\mu_{a,TE}} \frac{I}{\sigma_R} (\mu_{a,TE} - \mu_{TEion,TE}). \quad (4.9)$$

Next, we combine (4.9) with the solution for the analyte concentration in the TE reservoir (4.4) to obtain

$$\frac{dn_{a,LE-TE}}{dt} = c_{a0,R} \exp\left(-\frac{\mu_{a,R} I}{V_R \sigma_R} t\right) \frac{\mu_{a,R}}{\mu_{a,TE}} \frac{I}{\sigma_R} (\mu_{a,TE} - \mu_{TEion,TE}). \quad (4.10)$$

We solve the differential equation (4.10) subject to the initial condition $n_{a,LE-TE} = 0$ at $t = 0$ giving

$$n_{a,LE-TE} = c_{a0,R} \frac{V_R \sigma_R}{\mu_{a,R} I} \left(\frac{\mu_{a,R}}{\mu_{a,TE}} \frac{I}{\sigma_R} (\mu_{a,TE} - \mu_{TEion,TE}) \right) \left(1 - \exp\left[-\frac{\mu_{a,R} I}{V_R \sigma_R} t\right] \right). \quad (4.11)$$

We simplify (4.11), recalling $c_{a0,R} V_R = n_{a0,R}$ and obtain

$$\frac{n_{a,LE-TE}}{n_{a0,R}} = \left(\frac{\mu_{a,TE} - \mu_{TEion,TE}}{\mu_{a,TE}} \right) \left(1 - \exp\left[-\frac{\mu_{a,R} I}{V_R \sigma_R} t\right] \right). \quad (4.12)$$

We note that ITP velocity can be written as

$$u_{ITP} = \frac{I \mu_{LEion,LE}}{A_C \sigma_{LE}}, \quad (4.13)$$

and we recast equation (4.12) in terms of the distance from the TE reservoir, x , that the LE-TE interface has traveled. We obtain

$$\frac{n_{a,LE-TE}}{n_{a0,R}} = \left(\frac{\mu_{a,TE} - \mu_{TEion,TE}}{\mu_{a,TE}} \right) (1 - \exp[\zeta]), \quad (4.14)$$

where

$$\zeta = x \frac{\mu_{a,R}}{\mu_{LEion,LE}} \frac{\sigma_{LE}}{\sigma_R} \frac{A_C}{V_R}. \quad (4.15)$$

We see that the fraction of extracted analyte focused into the LE zone, $n_{a,LE-TE}/n_{a0,R}$ is limited by species mobilities, ratio of LE buffer to TE reservoir conductivity, the volume of TE reservoir, the cross sectional area of the channel, and the distance from the TE well to the point of interest (i.e., the affinity region).

The mobilities term in the first brackets in equation (4.14) limits the maximum amount of analyte which can be extracted from the TE well. We see that there is a tradeoff between the amount which can be extracted from the TE well and the degree to which we can separate the extracted substance from a contaminant, co-ionic species not focused in ITP. For a high degree of separation between focused target and unfocused contaminant, the TE ion mobility should be close to that of the target (making the TE ion significantly faster than a contaminant). As per equation (4.14), however, this limits the fraction of target that we can extract from the reservoir.

For our experiments we chose HEPES for the TE ion as an acceptable tradeoff between separation from contaminants and fraction of sample removed from the reservoir. HEPES has been demonstrated to exclude PCR inhibitors from blood and the HEPES ion itself seems to not inhibit PCR [104, 139]. Blood is, of course, a highly clinically relevant biological sample and PCR an important downstream assay. For our buffer conditions, we

calculate (using SPRESSO[148]) that the HEPES anion mobility in the adjusted TE was $-13 \times 10^{-9} \text{ m}^2\text{V}^{-1}\text{s}^{-1}$, while the DNA mobility[149] was approximately $-25 \times 10^{-9} \text{ m}^2\text{V}^{-1}\text{s}^{-1}$. Based on term in the first brackets in equation (4.14) this gives us a maximum extraction efficiency of about 44%.

We next consider the term in the second brackets in equation (4.14). This term dictates at what distance along the channel a certain fraction of analyte is extracted. Hence it dictates the location in the channel where we should place the affinity region. We estimate that for our experimental setup, the term in the second brackets of (4.14) was about 0.25, giving an overall ITP extraction efficiency, $n_{a,LE-TE}/n_{a0,R}$, of about 10%.

We note that the semi-infinite injection model can, given sufficient length between sample reservoir and AC column, well approximate the finite injection ITP configuration. For trace analytes (as we consider) and open bore column lengths sufficient to focus by 50x or more, the concentration of target focused in the ITP zone is much larger than the concentration of analyte migrating through the adjusted TE zone. Therefore, most of the reaction product is determined by ITP-focused analyte and not the low concentration inlet flux. Further, ITP-aided AC capture drastically speeds up the capture process. Therefore, the amount of analyte accumulated in the ITP zone prior to its arrival at the AC column is much larger than the amount of analyte which accumulates at the ITP zone during capture.

4.5.2 Calibration of Cy5 fluorescence to DNA concentration

We performed a calibration relating DNA concentration in our system and measured fluorescence intensity. We performed this calibration without ITP and by simply filling the entire capillary with a known, uniform concentration of DNA. The calibration

relates Cy5 fluorescence in our optical system and Cy5-labeled DNA concentrations of 10 nM to 10 μ M. We quantified the fluorescence with the epifluorescence microscope setup described in Section 4.2.1 of the main text. We then performed a proportional fit between observed fluorescence and DNA concentration.

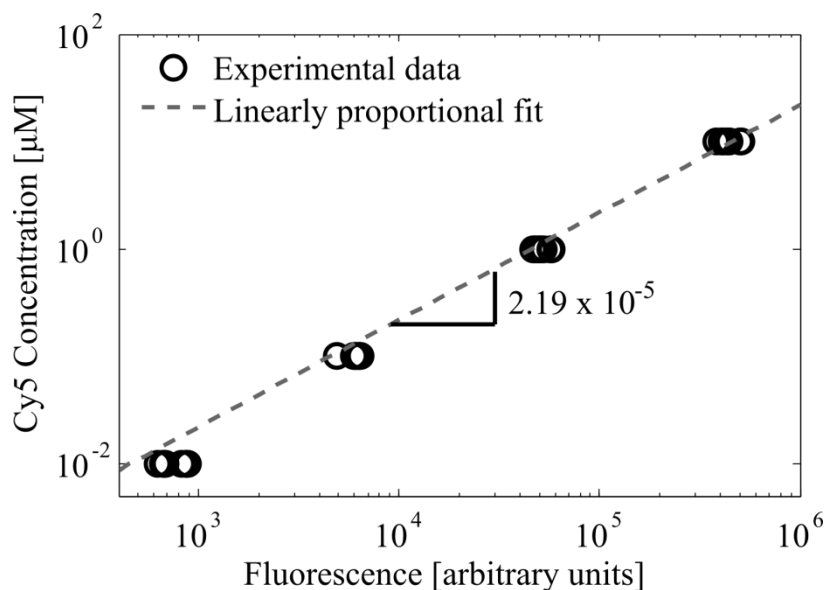


Figure 4.7. Plot of Cy5 fluorescence and DNA concentration from 10 nM to 10 μ M and proportional fit between Cy5 fluorescence and DNA concentration. The slope of the proportional fit is $2.19 \times 10^{-5} \mu\text{M}/(\text{arbitrary unit})$. The coefficient of determination for the proportional fit is $R^2 = 0.98$.

We observed that our GMA-EDMA PPM enhances significantly the fluorescence of Cy5 labeled DNA. For example, see Figure 4.8 where we used pressure driven flow to fill a solution of Cy5 into the capillary and image the region near the boundary of the PPM zone. There is a considerable difference in Cy5 fluorescence between the free solution and the PPM. We hypothesize that this may be due to higher index of refraction of the PPM compared to the surrounding media (water). The refractive index of GMA-EDMA monolith may be close to that of poly(methyl methacrylate) plastics, which have a reported value of 1.487 at 670 nm [150]. We hypothesize the increase in fluorescence could also

be caused in part by electronic interaction between the double bonds in the Cy5 dye and those on the PPM surface [151, 152]. In any case, the ratio of fluorescence intensity between the PPM and the free solution was 1.74. We accounted for this increase in fluorescence in the PPM in the calculations of probe density N and bound target concentration, n .

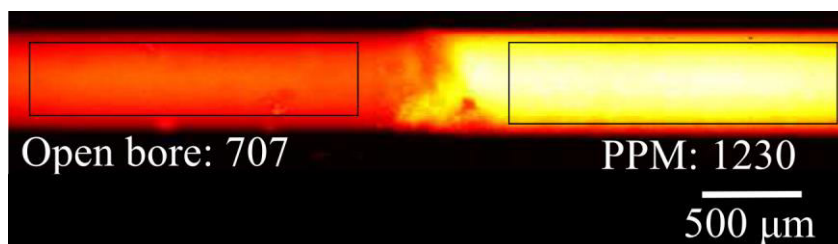


Figure 4.8. Cy5 fluorescence intensity near the interface of the open bore section of the capillary and the section with the porous polymer monolith (PPM). For this experiment we filled the capillary and the PPM inside the capillary with a solution of Cy5 labeled DNA using pressure driven flow. The mean fluorescence intensity in the free solution region was 707 (arbitrary units), while that in the PPM was 1230 (arbitrary units). The black rectangles indicate the areas that were averaged for these estimates.

4.5.3 Synthetic DNA oligo sequences used

Target sequence:

Sequence: 5'-CTCTGAACGGTAGCATCTTGACAAC-3'

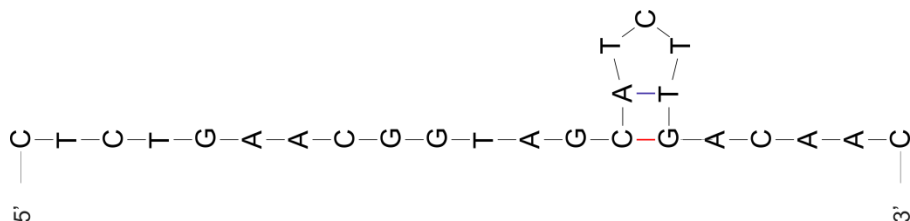
Modification: 5' Cy5

ΔG_{self} 0.0

(kcal/mol)

$T_{m self}$ (°C) 19.1

Secondary structure



Calculation conditions

Temperature (°C)

20

Na⁺ concentration (M)

0.2

Mg²⁺ concentration (M)

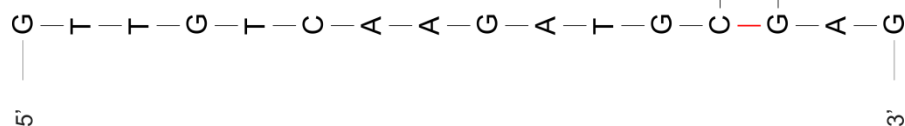
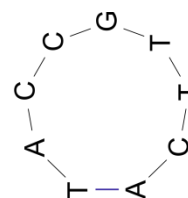
0

Probe sequence:

Sequence: 5'-GTTGTCAAGATGCTACCGTTCAGAG-3'

Modification: 5' C12-amine

ΔG_{self}
 (kcal/mol) 0.3
 $T_{m\ self}$ (°C) 15.0
 Secondary
 structure



Calculation
conditions

Temperature (°C)

20

Na⁺ concentration (M)

0.2

Mg²⁺
(M)

0

concentration

Hybrid:

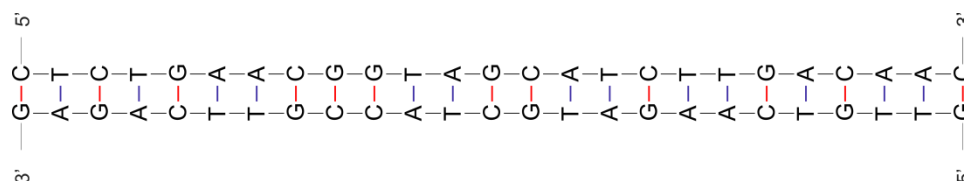
ΔG_{hybrid}
(kcal/mol)

-35.6

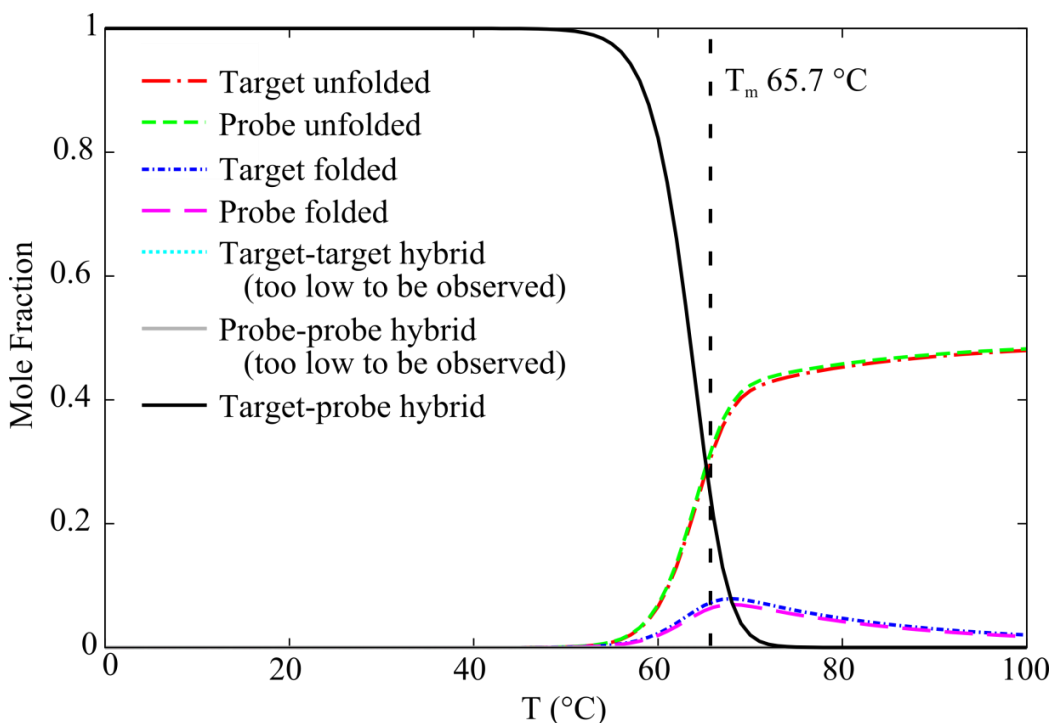
T_m hybrid (°C)

63.2

Structure



Hybridization
temperature
dependence



Calculation
conditions

Temperature (°C)

20

Strand

concentration (nM)

100

Na^+

concentration (M)

0.2

Mg^{2+}

concentration (M)

0

We calculated ΔG , T_m , and sequence secondary structure and hybrid structure using mFold (State University of New York at Albany) [153] at the conditions indicated. While the solution composition is not the same as that used in our ITP-AC experiments, the solution ionic strength is matched as closely as possible. Additionally, mFold calculations assume that the hybridization occurs in solution, not on a surface. We performed an initial calculation of the dissociation constant K_d using the Van't Hoff equation [154],

$$K_d = \exp\left(\frac{\Delta G_{\text{hybrid}}}{RT}\right) \quad (4.16)$$

to be 3×10^{-27} M. From this and the measurement of the probe density N , we estimated β to be 1×10^{-22} . We believe that this is an extremely low value for a dissociation constant, and is likely due to the overestimation of the absolute value of ΔG of hybridization by mFold for our conditions. Levicky and Horgan also report similarly large values for dissociation constants of DNA oligonucleotides of similar sizes and for similar ionic strengths for bulk solution hybridization [155]. However, Levicky and Horgan also report surface hybridization dissociation constants that are significantly higher than those for bulk solution hybridization for similar oligonucleotides [155].

Due to these difficulties in predicting K_d values, we here chose to estimate the expected order of magnitude of the surface hybridization K_d using published experimental values for oligonucleotides under similar hybridization conditions on a surface. For example, Stevens et al. found $K_d < 10^{-11}$ M for a 21 nt oligonucleotide hybridized on $0.75 \mu\text{m}$ paramagnetic latex particles in 100 mM ionic strength solution at 20°C [156]. Similarly, Okahata et al. found K_d to be 2.5×10^{-11} M for a 30 nt oligonucleotide hybridized on a gold plated quartz crystal microbalance surface in 10 mM ionic strength solution at 20°C [157]. Since the value of K_d strongly decreases with ionic strength [157], we conservatively expect a K_d of at most 10^{-11} M for our experimental conditions (order 100 mM ionic strength). From this and the measurement of the probe density N , we estimated β to be 3×10^{-7} . We note that for our ITP-AC conditions, the model predictions are very weak functions of β for $\beta < 10^{-5}$ (see Chapter 3, Figure 3.4). For example, a factor of 10 change in K_d results in less than 1 % change in capture efficiency in this range of β .

4.5.4 Measurement of PPM void fraction

We measured the void fraction of the PPM by obtaining the geometric volume of the PPM (i.e., volume of the cylindrical PPM as determined by the capillary inner diameter) and the true volume of the polymer structure. The void fraction, φ , is then given by

$$\varphi = \frac{V_{geom} - V_{solid}}{V_{geom}}, \quad (4.17)$$

where V_{geom} and V_{solid} are the geometric and true volumes respectively. We measured the volume of the polymer structure by measuring the volume of water it displaced.

During these experiments, we first measured the axial length of the PPM inside the micropipette capillary using a vernier caliper. We calculated the geometric volume of the PPM using this length and the inside diameter of the capillary (provided by the manufacturer). We then slowly filled the PPM with a slug of water of known volume and measured the length of the slug. Using this length and inside diameter of the capillary, we calculated the volume of water after it was displaced by the PPM. We obtained the volume of the solid by subtracting this volume from the initial volume of water. Using this method we obtained a PPM void fraction of 0.8.

4.5.5 Image of custom built capillary setup

We performed ITP-AC experiments in a custom built capillary setup (shown in Figure 4.9), which interfaced LE and TE reservoirs to the capillary with the PPM. The TE reservoir was fabricated via stereolithography (FineLine Prototyping, Raleigh, NC) from WaterShed XC 11122 and fitted with 1/4-28 female threads to mate to 1/4-28 nut and ferrule from IDEX Health & Science (Oak Harbor, WA). The LE reservoir consisted of an IDEX Health & Science 90 degree bend fitting (female to female threads). The capillary outer diameter was 1 mm. Custom machined acrylic brackets served to secure reservoirs and electrodes in place during experiments.

The 500 μm inner diameter capillary had 1 to 3 cm long GMA-EDMA PPM structures polymerized inside of it. The PPM was covalently attached to the capillary wall. We functionalized the surface of the PPM with 25 nt DNA probe complementary to the target. To initiate ITP-AC, we applied current to the capillary using platinum electrodes dipped into LE and TE reservoirs.

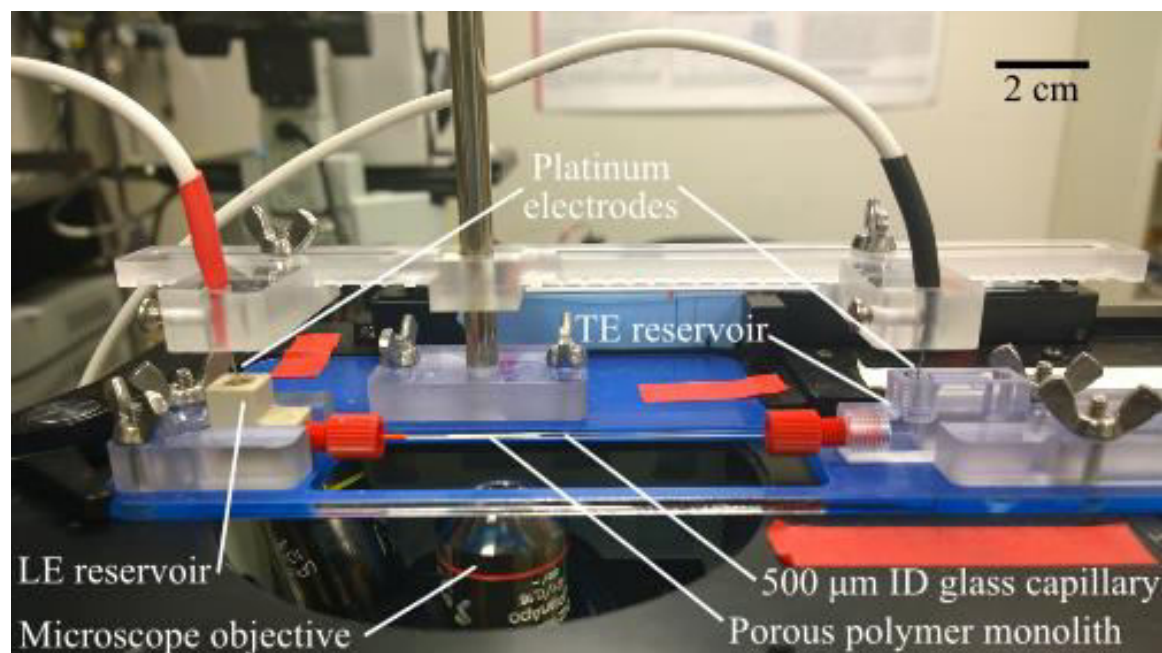


Figure 4.9. Image of custom-built capillary setup consisting of LE reservoir, 500 μm inner diameter borosilicate glass capillary with GMA-EDMA PPM, and a TE reservoir. Platinum electrodes were dipped into the LE and TE reservoirs to apply current through the capillary.

4.5.6 Choice of porous polymer monolith chemistry, synthesis, and functionalization

4.5.6.1 Choice of porous polymer chemistry

Affinity chromatography columns require surfaces to which affinity ligands can be readily bound, but which provide minimal non-specific binding of contaminants. Reproducible and robust affinity chromatography experiments with aqueous solutions also benefit from sufficiently hydrophilic surfaces. We chose a polymerization chemistry which incorporates the monovinyl monomer, GMA, which has an epoxide functional group. The epoxide group on GMA is known to be highly reactive to primary amines on biopolymers such as nucleic acids [83, 131], and proteins [81, 85, 136], and other well-known affinity ligands [101]. Furthermore, GMA-EDMA polymers exhibit little non-specific binding with

nucleic acids. GMA-EDMA PPMs also are sufficiently hydrophilic and are easy to use with aqueous solutions. Lastly, methacrylate PPM structures are highly scalable and have been synthesized in both microfluidic [2, 63, 158, 159] and 8 L scale formats [160].

We cross-linked GMA with EDMA via a free radical, UV-initiated polymerization in the presence of MeOH and hexane as solvents, with AIBN as photoinitiator.[137] We chose photo-, rather than thermal-initiation to be able to lithographically define regions of PPM. Ability to lithographically define PPM regions helps incorporate PPMs in prescribed, finite sections of capillaries or within microfluidic chips [2, 63, 158, 159].

4.5.6.2 Polymethacrylate porous polymer monolith (PPM) synthesis

Both EDMA and GMA were received with polymerization inhibitors, which we removed by passing through columns packed with inhibitor removing media. We then mixed the photo initiator AIBN (126 mM), GMA (12% v/v), EDMA (8% v/v), MeOH (64% v/v) and hexane (16% v/v) in a polypropylene vial. We injected a slug of this polymerization solution into already prepared, dry, micropipette capillaries with vinylized walls.

We vinylized the walls of the capillaries by placing the capillaries in a solution of 30% (v/v) TSPM, 70% (v/v) acetone solution overnight and then flushing the remaining solution with air.[159] The capillary walls were vinylized to ensure covalent attachment of the polymer to the capillary wall, and thus avoid channeling.[159] We then irradiated samples using a 12 W, ~405 nm peak wavelength UV lamp (Chauvet, Sunrise, FL) at 12 cm exposure distance for 2 h. After polymerization, we flushed the samples with air to remove unreacted monomers and solvents, and dried at 20°C under approximately 93 kPa vacuum for 30 min. This resulted in 1 to 3 cm long GMA-EDMA PPM structures bound

to the capillary wall with approximately 80% (measured) void fraction and order 2 μm pores (see Figure 4.1b in the main text and Section 4.5.4). This ensured that the porous affinity region had small hydrodynamic resistance, facilitating filling the system with LE buffer, and later the elution buffer without the need for high pressure pumps.

4.5.6.3 Probe DNA immobilization on PPM

We prepared DNA immobilization solution consisting of 3X SSC buffer (450 mM sodium chloride, 45 mM trisodium citrate), 2 mM SDS and 250 μM 5' amine modified synthetic oligo DNA [83]. We slowly injected a slug of this immobilization solution into the micropipette capillaries with the PPM inside. We then placed micropipette capillaries in a water bath at 70°C for 2 h. We then flushed each capillary with 2 ml of DI water (roughly 500 column volumes) and dried at 70°C under about 93 kPa gauge vacuum for 1 h.

We estimated the resulting volumetric density of immobilized DNA by immobilizing 5' amine, 3' Cy5 modified synthetic oligo DNA, measuring the resulting fluorescence intensity, comparing the result to a Cy5 labeled DNA fluorescence signal calibration (see Section 4.5.2). We estimate the volumetric density of immobilized DNA to be about 30 μM . This resulted in total column capacity of 6 to 24 $\times 10^{-11}$ moles of target or for 100 nt target 2 to 6 μg and for 1000 nt target 20 to 60 μg of target capacity.

For a rough estimate of surface density of immobilized DNA, we roughly approximate the PPM (see Figure 4.1b) as consisting of a cubic closed pack crystal of spheres with 1 μm diameter. This provides an estimate of immobilized DNA surface density of 1.2×10^{-12} molecules cm^{-2} . DNA probe surface densities of around 2×10^{-12} molecules cm^{-2} have been shown to provide high (>60%) hybridization efficiencies,

while higher probe surface densities decrease hybridization efficiency [144]. Peterson et al. attribute this to repulsive electrostatic and steric interactions that increase with increased probe density [144].

4.5.7 Choice of buffer chemistry for ITP-AC

In our final experiments the LE buffer consisted of 250 mM HCl and 500 mM Tris. The TE buffer as placed in the TE well consisted 25 mM HEPES, 50 mM Tris, and varying amounts of target and/or contaminating species. The LE ion (here chloride) maintains its concentration throughout the experiment. The LE buffer governs the concentration of the adjusted HEPES anion concentration (i.e., the TE ion concentration behind the LE-TE interface) [10, 11, 161]. The adjusted TE ion concentration is generally roughly 0.5-0.8 that of the LE ion [161]. In our experiments the adjusted TE concentration was calculated to be 150 mM using an electrokinetic simulation software SPRESSO [148].

We chose a relatively high LE concentration to ensure that the focused DNA target was in a buffer of high ionic strength. This suppresses the characteristic lengths of electric double layers associated with the surface of the PPM and the immobilized nucleic acids [162]. Increasing ionic strength mitigates the effects of electrostatic repulsion between the target DNA and probe DNA, thus also promoting the likelihood DNA hybridization [144, 163]. We also chose buffers of high ionic strength and a PPM with relatively large (2 μm) pores to create a low ratio of surface-to-bulk charge in the PPM. The latter minimizes the effects of concentration polarization [164, 165] and Donnan exclusion [166, 167] which can otherwise exclude the target from the affinity capture region. Our high ionic strength LE and TE also suppresses electroosmotic flow (EOF) [162, 168].

We chose chloride as the LE ion because it is commonly found in significant amounts in many relevant biological samples (e.g., blood, urine, intra and extracellular fluids) [169] and has a high absolute electrophoretic mobility [170] (higher than nucleic acids [149]). As discussed by Rogacs et al., chloride is a particularly convenient LE ion for samples containing significant concentrations of chloride itself [104]. We chose HEPES as the TE ion since its absolute mobility is sufficiently low (in the presence of Tris as the counterion) [170] to focus DNA [149], and yet is sufficiently high to exclude many matrix ions (e.g. PCR inhibitors found in blood) [104, 132, 139]. Choosing a TE ion with absolute mobility closer to that of DNA would exclude more contaminants and would be associated with a lower smallness parameter ε (as per the analysis of Chapter 3). However, this would also decrease the amount of analyte that can be extracted via semi-infinite injection ITP (see Section SI 1). Finally, Tris as a counterion provided a pH of approximately 8.2 for the hybridization reaction, and hybridization of DNA occurs readily around this pH [140, 141].

4.5.8 Analyses of ITP-AC purified 25 nt target from 10,000x contaminant via electrophoresis

We performed a series of experiments using electrophoresis to analyze our nucleic acid mixtures before and after purification. Figure 4.10 shows electropherograms of (a) a trailing electrolyte containing 25 nt target and 10,000x more abundant (by mass) fish sperm DNA, (b) fish sperm DNA alone, (c) 25 nt target alone, and (d)-(f) eluted fractions from three separate ITP-AC experiments where 25 nt target was purified from 10,000x more abundant fish sperm DNA. All electropherograms were obtained using Agilent 2100 Bioanalyzer Instrument (Santa Clara, CA) using the Small RNA chip. The Bioanalyzer

Small RNA chip can resolve nucleic acids in 6 to 150 nt range. In all electropherograms signal from the Agilent Bioanalyzer was normalized by the maximum signal of the sample. For experiments shown in (d)-(f) ITP-AC was performed as described in SI 7 and in Sections 4.2.4 and 4.3.7 of the main text. Specifically, after the target was captured (Step 3, Figure 4.2b of main text) the LE and TE buffers were removed by vacuum. We then eluted the captured target by introducing (with a syringe) 5 μ l elution buffer consisting of 50 mM sodium hydroxide. We used a syringe to drive this slug through the column and so elute the target. We quickly mixed the eluate with 5 μ l of 200 mM HEPES to achieve a solution with near neutral pH. We then stored the purified sample at -20°C until analysis via the Bioanalyzer electrophoresis instrument. The electrophoresis on the Bioanalyzer instrument was performed by Stanford Protein and Nucleic Acid Facility. The resulting electropherograms corroborate our assertion that we purify target DNA. This evidence is presented in addition to the strong spectral evidence shown in Figure 4.5 of the main text. Together, these data show that ITP-AC reproducibly enriches the amount of 25 nt target and removes the majority of the background contaminant.

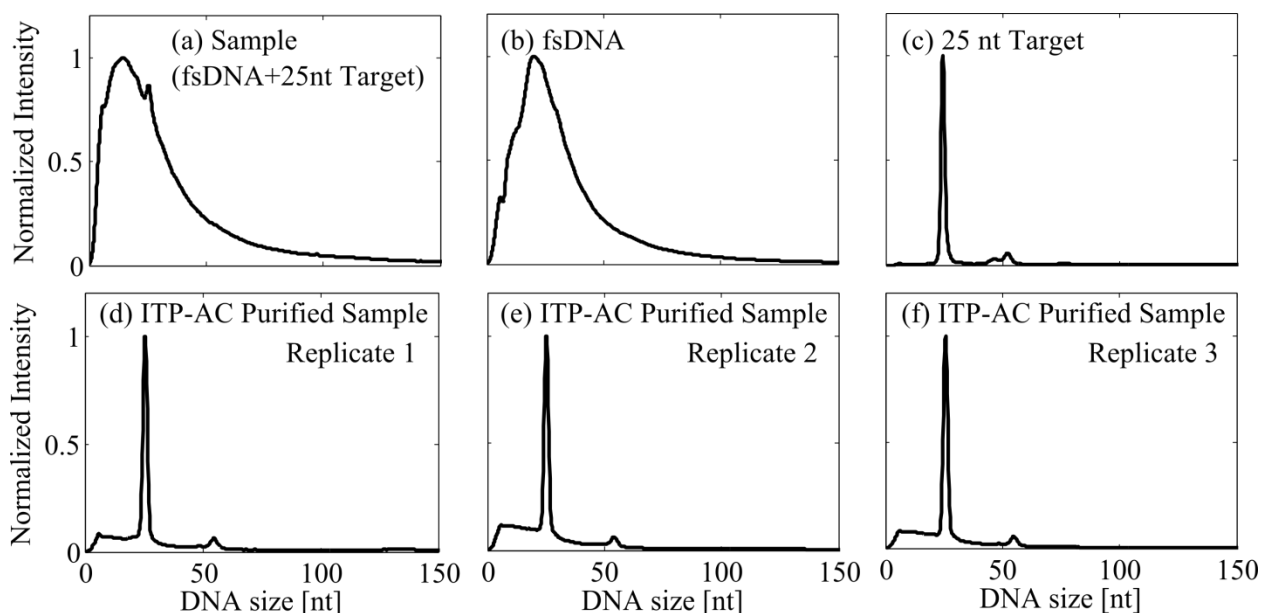


Figure 4.10. Electropherograms of nucleic acid mixtures before and after application of our purification process. Shown are electropherograms of (a) mixture of trailing electrolyte (25 mM HEPES, 50 mM Tris) and 25 nt target and 10,000x more abundant (by mass) fish sperm DNA before purification, (b) fish sperm DNA alone (c) 25 nt target alone, and (d)-(f) three replicates of ITP-AC purified samples which initially contained 25 nt target and 10,000x more abundant fish sperm DNA. All electropherograms were obtained via Agilent Bioanalyzer Small RNA chip (6-150 nt range). In all electropherograms the signal from the Bioanalyzer instrument was normalized by the maximum signal for the sample. ITP-AC reproducibly enriches the amount of 25 nt target and removes the majority of the background contaminant.

4.5.9 Recommended ITP-AC parameters

Here we provide a table of dimensional values of important ITP-AC parameters, which we recommend for performing ITP-AC experiments. We also include brief rationale for each choice.

Table 4.1. Recommended ITP-AC parameters

Parameter	Value	Rationale
Affinity region pore size	0.1 - 2 μm	(a)
Affinity probe concentration, N	0.3-300 μM	(b)
Target-probe dissociation constant, K_d	$< 10^{-9} \text{ M}$	(c)
ITP channel diameter	100-5000 μm	(d)
Affinity region length	0.1-100 mm	(e)
ITP velocity, u	0.5-0.005 mm s^{-1}	(f)
Affinity region porosity, ϕ	0.5-0.8	(g)
Target diffusion coefficient, D	$< 10^{-9} \text{ m}^2 \text{ s}^{-1}$	(h)

(a) We recommend that the PPM affinity region pore size be 10-100 times greater than the radius of gyration of the target macromolecule so that the target is not mechanically sieved by the affinity region [171]. For example, the radius of gyration of linearized λ phage DNA ranges from 0.18 μm for 4 kb strand to 2.5 μm for 309 kb strand [172]. For proteins, the radius of gyration typically ranges from 1.4 nm for 14 kDa protein (e.g., lysozyme from chicken egg white) to 6.4 nm for 820 kDa protein ($\alpha 2$ -Myoglobin) [173]. See Tyn and Gusek for a large table of radii of gyration for proteins [173]. However, we do not recommend using excessively large pores as this will lead to decreased affinity probe concentration (for a given probe surface density) and therefore decreased affinity column performance. Therefore, an affinity region with a pore size of less than about 2 μm should successfully perform affinity capture on a wide range of biomolecules and bioparticles without sieving effects.

(b) As we mention in SI Section 4.5.6.3 we recommend DNA probe surface densities of around $2 \times 10^{-12} \text{ molecules cm}^{-2}$ as these give roughly the highest hybridization efficiencies per probe [144]. We recommend using the highest possible volumetric density of the probe

(N) and therefore using the smallest affinity region pore size that will not cause sieving, concentration polarization or Donnan exclusion (see SI 4.5.7).

(c) We recommend that the non-dimensionalized target-probe dissociation constant β be less than about 10^{-5} as then the affinity reaction would appear irreversible, which is desired for effective capture of target (see Chapter 3, Figure 3.4). While ITP-AC can purify targets with higher β , this is not desirable as capture of the target is not effective and may be non-specific (see Chapter 3, Section 3.3.2.4). Therefore, if N is at least 10^{-4} M, we recommend that K_d , be less than about 10^{-9} M. Note that this condition is satisfied by surface hybridization of oligonucleotides [156, 157], a large number of antibodies [174], and a large number of aptamers [175].

(d) The lower range of ITP channel diameters is limited by the integration of the porous affinity region. We recommend that ITP channel diameter be 10 to 100 times the affinity region pore diameter for adequate structural stability of the porous region. The upper range of ITP channel diameters is limited by the Joule heating in ITP and the stability of the ITP interface [146, 176].

(e) We recommend choosing an affinity region length based on the anticipated capture length. If saturation of the affinity region is not anticipated, this can be calculated using equation (3.39) from Chapter 3. If saturation of the affinity region is anticipated, then the capture length is approximately equal to the target amount in the sample divided by the product of affinity region cross sectional area and affinity probe concentration. We recommend choosing affinity region length to be roughly twice the capture length as to capture the majority of the target while conserving space in the purification system.

(f) We recommend choosing ITP velocity during the hybridization phase based on the desired capture length, the forward rate constant of the target, and the probe density of the affinity region (see equation (3.39), Chapter 3). We note that the ITP velocity during the extraction phase can be (and likely should be) much higher than the velocity applied during the hybridization phase (see Figure 4.2) to minimize the overall assay time. The upper range of ITP velocities is limited by excessive heating due to the proportionally higher current density needed to maintain higher ITP velocity. Excessive heating can lead to outgassing of the solvent for the LE and TE buffers, possibly solvent boiling, and even thermal damage to the target itself [146]. The lower range of ITP velocities is limited by the desired maximum width of the target distribution (and/or maximum assay time). The lower the ITP velocity, the larger the target distribution width [22, 25] and therefore the gains of ITP preconcentration are diminished (see Figure 3.3, Chapter 3).

(g) We recommend choosing an affinity region porosity in the range of 0.5-0.8. Porous materials with larger porosities require less pressure to fill the affinity region with the leading electrolyte and later the elution buffer [137]. Porous materials with larger porosities can also present more surface area per volume of material to the flow, potentially allowing for larger probe concentration. However, excessively large porosities cause the porous region to be structurally weak, and therefore difficult to work with.

(h) We recommend that, when using the model in Chapter 3, and operating in the range of recommended parameters that the target diffusion constant be less than $10^{-9} \text{ m}^2 \text{ s}^{-1}$ so that the target diffusion will be negligible compared to target migration (see Chapter 3, equation(3.20)). This is easily satisfied for a majority of biomolecules and even viruses. For example, for DNA oligonucleotides diffusion constant is order $10^{-10} \text{ m}^2 \text{ s}^{-1}$ [111]. For

larger DNA, for example, for linearized λ phage DNA, the diffusion constant ranges from $2 \times 10^{-12} \text{ m}^2 \text{ s}^{-1}$ for 4 kb strand to $2 \times 10^{-13} \text{ m}^2 \text{ s}^{-1}$ for 309 kb strand [172]. For proteins, the diffusion constant typically ranges from $1.1 \times 10^{-10} \text{ m}^2 \text{ s}^{-1}$ for 14 kDa protein (e.g., lysozyme from chicken egg white) to $2.4 \times 10^{-11} \text{ m}^2 \text{ s}^{-1}$ for 820 kDa protein ($\alpha 2$ -Myoglobin) [173]. For viruses the diffusion constant ranges from $1.5 \times 10^{-11} \text{ m}^2 \text{ s}^{-1}$ for 5,000 kDa Bromegrass mosaic virus to $5 \times 10^{-12} \text{ m}^2 \text{ s}^{-1}$ for 50,000 kDa Tobacco mosaic virus. See Tyn and Gusek for an extensive and useful table of diffusion constants for proteins and viruses [173].

4.5.10 Choice of pore size in ITP-AC

Here we discuss the choice of pore size in designing a porous substrate for ITP-AC. The lower extreme limit for pore size for an ITP-AC substrate is set by the size at which the targets are excluded from the porous media, while the upper extreme limit is determined by the mechanical stability of the porous media. Thus, we recommend the substrate pore size be at least 10 times greater than the radius of gyration of the target molecule but be at least 10 less than the radius of channel that contains the porous media. However, there are both advantages and disadvantages in operating near the lower and upper limit and a designer may choose to design an ITP-AC substrate to operate closer to one or the other limit depending on the application. For example, an ITP-AC substrate with smaller pores allows for: (a) better mixing inside the pores, (b) larger initial probe concentrations, and (c) decreased axial dispersion. On the other hand, an ITP-AC substrate with larger pores creates less hydrodynamic resistance and is less likely to exclude the target from the porous media via sieving, Donnan exclusion or concentration polarization effects.

For optimal ITP-AC operation (and so that our mathematical model of ITP-AC correctly describes the operation), the concentration of target inside the pores should be fairly uniform - the target should be well mixed inside the pore. In other words, there should be no depletion boundary layer of the target near the wall of the pore. We can determine if the pore is well mixed by comparing the time scale for the target in solution to react with the probe on the pore wall ($t_{rxn} \approx 1/(k_1 N)$) and the time scale for the target to diffuse from the center of the pore to the wall ($t_{diff} \approx r_0^2/D$, see main text of Chapter 3). For the pore to be well mixed $t_{diff} < t_{rxn}$. The pore size at which diffusion and reaction time scales are equal is another upper bound on the pore size, which we recommend not to exceed. However, there is no additional benefit to mixing in making the pore size smaller than $r_0 = \sqrt{D/(10k_1 N)}$, the size at which the reaction time scale is 10 times greater than the diffusion time scale.

Smaller pores allow for larger probe concentrations as surface area per volume of the porous media roughly scales inversely with the first power of the pore radius and probe surface densities are usually fixed. Larger probe concentrations in turn lead to lower reaction time scales and so a faster affinity purification. We recommend setting surface probe densities to an optimal density of around 2×10^{12} molecules cm^{-2} for DNA as these give the highest hybridization efficiencies per probe, while larger probe surface densities interfere with hybridization [144]. However, increasing the probe concentration increases the magnitude of the diffusion parameter in equation (3.20) in Chapter 3 and may put ITP-AC in a regime where neglecting the diffusion term is no longer appropriate. In this regime, our analytical solution will no longer be applicable and a numerical solution to the

advection-reaction-diffusion equations will be necessary. Nevertheless, we recommend designing an ITP-AC porous substrate with as small pores as feasible.

Smaller pores also lead to decreased axial dispersion of the target (see Section 3.5.3). Briefly, for pore length scale Peclet numbers less than unity the ratio of effective dispersion to molecular diffusion asymptotes to roughly 0.67, i.e., the porous media impedes the axial diffusion of the target [120]. This allows us to operate ITP-AC at higher electric fields (since pore scale mean EOF velocity can be higher for smaller pore size to give the same Peclet number) and so higher target velocities. This in turn allows for more rapid purifications. Furthermore, if the initial pore length scale Peclet number for initial ITP-AC design was greater than unity, decreasing the pore size will decrease dispersion [120] and so decrease the magnitude of the diffusion parameter in equation (3.20) in Chapter 3. In this case, decreasing the pore size will both increase probe concentration and decrease dispersion, and so in net not alter the diffusion parameter equation (3.20) in Chapter 3, allowing us to neglect it and so apply our analytical solution to describe ITP-AC.

Smaller pores also lead to larger hydrodynamic resistance as hydrodynamic resistance (defined as the solvent flux rate per unit pressure gradient) scales as the square of the pore size. Thus having smaller pore size may necessitate having specialized pumps to deliver leading electrolyte and the elution buffer into the porous substrate. Thus, pump specifications in the device employing ITP-AC place another lower bound on the substrate pore size.

Finally, smaller pore size may lead to exclusion of the target from the porous media via sieving, Donnan exclusion or concentration polarization effects. To avoid sieving, we recommend that the substrate pore size be at least 10 times greater than the radius of gyration of the target molecule. To avoid Donnan exclusion or concentration polarization effects we recommend that the pore size be such that the Dukhin number is less than 0.1. We define Dukhin as per Delgado et al. [177] as

$$Du = \frac{2}{\sigma_{el}r_0} \left(1 + \frac{2\varepsilon_f R^2 T^2}{\mu_f F^2 z^2 D} \right) \left(\cosh \left(\frac{zF\xi}{2RT} \right) - 1 \right), \quad (4.18)$$

where μ_f and ε_f are the dynamic viscosity and permittivity of the fluid respectively; ξ is the zeta potential of the pore surface, σ_{el} is the electrical conductivity of the electrolyte, z is the valance of the electrolyte; and F is Faraday's constant, R is the gas constant, and T is the absolute temperature of the solution. This places another lower bound on the substrate pore size for ITP-AC.

5 Contributions, conclusions, and recommendations

In this chapter we summarize our contributions and conclusions of the work presented in this dissertation. We follow this by recommendations for future research directions based on this work.

5.1 Major contributions

Here we summarize major contributions of the current work in improving state-of-the-art of PPM synthesis, of purification of macromolecules, and of controlling chemical reactions via ion-concentration shockwaves.

5.1.1 Design and fabrication of porous polymer wick structures

1. Fabricated and characterized HEMA-co-EDMA PPM with the aim of achieving a hydrophilic material with high ratio of permeability to mode pore diameter. The ratio of permeability to mode pore diameter captures wick's capacity for capillary driven flow. When this ratio is high, both the capillary pressure (scales as inverse of pore size) is large and resistance to flow (scales as inverse of permeability) is small.
2. We characterized the effect of both monomer concentration and porogenic solvent composition on resulting monolith microstructure (pore diameter distribution, surface area) and permeability.
3. We developed an empirical model based on the Carman-Kozeny model relating PPM permeability and PPM mode pore diameter. The model correctly predicted

PPM permeability as a function of pore diameter for five orders of magnitude of permeability.

5.1.2 Coupling ITP with AC: Theory

1. We developed affinity purification method for macromolecules via coupling of ITP with AC in porous media and developed an analytical transport and reaction model that captures spatiotemporal dynamics of ITP-AC.
2. We non-dimensionalized transport equations describing the dynamics of ITP-AC, which enabled a description of ITP-AC in terms of 3 dimensionless groups instead of 6 original dimensional variables. We found an analytical solution to the transport and reaction equations describing ITP-AC using perturbation methods.
3. We identified limiting regimes of ITP-AC and developed simple algebraic relations for key figures of merit of ITP-AC such as capture length and capture time.
4. We derived a scaling for resolution of ITP-AC based on the Giddings criteria of resolution for chemical separation methods.

5.1.3 Coupling ITP with AC: Experimental Study

1. We developed a GMA-EDMA synthesis protocol, synthesized GMA-EDMA PPM with high permeability and large pore size, and functionalized the monolith surface with DNA. High permeability is desirable for ITP-AC so that the porous media can be easily filled (without specialized pumps) with leading electrolyte. Large pore size is desirable for ITP-AC so that macromolecules are not excluded from the porous media via mechanical sieving, concentration polarization, or Donnan exclusion.

2. We characterized functionalized PPM properties such as immobilized DNA concentration, monolith microstructure, and monolith void fraction.
3. We developed protocols for performing ITP-AC, including relevant electrolyte chemistry, and operating current. We also created guidelines for altering our ITP-AC protocol and selecting other electrolyte chemistries for alternate analytes.
4. We performed detailed experiments to validate our analytical model for ITP-AC, measuring target capture efficiency and capture length.
5. We demonstrated ITP-AC purification of a rare DNA target from 10,000-fold more abundant background DNA in under 500 s and under 1 mm column length.

5.2 Conclusions

5.2.1 Design and fabrication of porous polymer wick structures

1. We found that for HEMA-co-EDMA PPM mode pore diameter increased with decreasing monomer fraction. We attributed this to the earlier (at smaller chain size) precipitation of the growing polymer chain from solution due to the decreased amount of monomer to solvate the polymer chains. This in-turn causes larger globules as the monomers concentrate around the polymer chains, and so larger void spaces between the globules, leading to larger pore size.
2. We found that increasing mass fraction of methanol (relative to the second porogenic solvent, hexane) resulted in larger mode pore diameter of the monolith. We attribute this the change of quality of the solvent mixture as a result of higher methanol fraction, again causing earlier precipitation of solid polymer globules from solution. We found that changing porogen composition is a better tool for

tailoring monolith pore structure than changing monomer-to-crosslinker ratio as it has minimal impact on monolith chemical composition and porosity.

3. We found that monolith permeability scaled roughly with porosity times the square of mode pore diameter. Additionally we found that the geometric factor (accounting for pore shape and tortuosity) for PPM in Carman-Kozeny model for permeability was around 1.3, significantly differing from that for a bed of packed spheres (which is around 5).

5.2.2 Coupling ITP with AC: Theory

1. We found that coupling ITP with AC reduces purification time (~100x) and improves affinity column utilization (~10x).
2. Coupling ITP with AC allows for capture of targets with 2-3 orders of magnitude higher dissociation constants than traditional AC.
3. ITP-AC directly integrates an automatic wash step into the process post capture, eliminating the need for a separate wash step, which is required in traditional AC.
4. ITP-AC can reduce affinity substrate fouling by separating the target from fouling contaminants in the sample and not transporting the fouling species into the affinity substrate.
5. We found that capture length scaled by the advection-reaction length scale approaches a constant value of 2.8 for the ITP-AC regime where probes are not saturated. For the regime where the affinity probes are locally saturated, scaled capture length increases linearly with total target amount.
6. We found that increasing the target dissociation constant scaled by the probe concentration decreases the target capture efficiency.

7. We found that capture time scaled by the reaction time scale approaches a constant value of 4.3 for the regime where the probes are not saturated and the target distribution is small compared to the advection reaction length scale. When the target distribution is large compared to the advection-reaction length scale, capture time is proportional to the time necessary to advect the target distribution into the affinity substrate.

5.2.3 Coupling ITP with AC: Experimental Study

1. We found that GMA-co-EDMA PPMs with 2 μm diameter pores are nonsieving and exhibited no nonspecific binding and therefore are well suited for ITP-AC.
2. Electrokinetic transport of the target in ITP-AC obviates the need for specialized high-pressure pumps to needed to advect the target in traditional AC.
3. We observed that GMA-co-EDMA PPMs amplify the fluorescence signal of Cy5 roughly 1.7-fold.
4. We found that the capture length scaled by the advection-reaction length scale is independent of total target amount advected in the affinity substrate when the affinity probes are not locally saturated.
5. We found that capture efficiency increases linearly with total target amount advected in the affinity substrate when the affinity probes are not locally saturated.
6. We found that the resolution of ITP-AC scales proportionally with time.

5.3 Recommendations for Future Work

1. Performing ITP-AC to purify proteins, using either antibodies or aptamers as probes immobilized on the PPM.

2. Performing reaction in ITP upstream of ITP-AC and use ITP-AC to separate reaction products. For example, use ITP to hybridize DNA targets with RNA biotin labeled probes and then migrate this in ITP into a streptavidin labeled substrate. The free RNA and hybridized DNA-RNA will react and attach to the column, while free DNA will continue to migrate in ITP. Thus, targets complementary to probes will be separated from non-complementary ones.
3. Extending the model for ITP-AC described in this work to accurately capture ITP-AC regimes where the diffusion of the target is as important as reaction and advection.
4. We recommend extending ITP-AC to capture multiple (>1000) targets simultaneously. The simplest way to do this is to immobilize a mixture of probes in the same region of the PPM. However, this dilutes the concentration of probe, thus drastically increasing capture time. Thus increasing probe density is essential for the success of multiple capture ITP-AC.
5. Development of GMA-co-EDMA PPM with significantly larger (>100x) surface area by synthesis of the PPM with smaller monolith forming globules or porous globules. This would increase volumetric probe density and thus greatly decrease capture time and capture length.
6. Developing a model for multiplexed ITP-AC (multiple probes and multiple targets) where the targets may react with each other and react with probes other than their own (i.e. have cross reactions). This would more realistically model multiplexed ITP-AC than a model that assumes only correct target-probe reactions are possible and may be necessary for optimizing multiplexed ITP-AC.

7. We recommend exploring a method to lithographically immobilize probes onto the PPM surface (e.g., via a light activated functionalization reaction). This would create lithographically defined probe regions, turning the affinity column into a spatially multiplexed microarray. Fluorescent signal readout of the target binding can be improved by index matching between the solution and the PPM bulk, for example using high concentration sucrose solutions.
8. We recommend exploring fluorescent dye signal amplification by GMA-co-EDMA PPM. We attributed the 1.7-fold signal amplification we observed to mismatches of index of refraction or to electronic interaction between the dye and the conjugated backbone of the PPM. We believe this signal amplification effect can be increased further, thus providing a simple signal amplification strategy for analytical affinity assays and improving analyte limit of detection.
9. We recommend creating a network of channels with different PPM affinity regions to create affinity logic gates. For example, such network would test if a macromolecule has affinity sites a AND b (an AND gate) and a OR b (an OR gate, inclusive or exclusive OR). A sequencing by hybridization scheme can be designed around such a network, and might be useful for sequencing difficult to amplify macromolecules such as proteins.
10. Extending the model for ITP-AC described in this work to a target (e.g. a small molecule) focused in plateau mode ITP rather than peak mode ITP, with the entire amount of target captured by the PPM.
11. Create a 3D model of ITP-AC and include the effects of joule heating and convective cooling at the boundaries (and the resulting temperature gradients) on

the dynamics of ITP-AC with temperature sensitive reaction rates, species mobilities, and electrolyte conductivity. Such a model will be very useful for macrofluidic versions of ITP-AC where temperature gradients due to Joule heating become significant.

12. Development of a more detailed model for permeability in PPM with bimodal, multimodal, or highly skewed pore distributions that take into account higher moments of the pore size distribution.
13. Development of numerical simulations of phase separation during PPM synthesis including globule formation, and subsequent monolith formation. The simulation should include as inputs solvent quality, monomer and cross linker hydrophobicity, initiator concentration, UV flux and/or applied and resulting temperature field. This simulation would calculate the growth of polymer chains and their eventual precipitation from solution to form the monolith bulk. Such simulation would allow iterating PPM synthesis *in silico*, and so greatly reducing the labor necessary to obtain optimized PPM monoliths with desired transport properties.
14. We recommend developing a tool to predict forward rate constant of DNA hybridization based on the sequences of the two reacting strands. The predictions of this tool can then be verified by accurately measuring the forward rate constant via ITP-AC by measuring the capture length, ITP velocity and probe concentration.

A. Fast, Specific, and Efficient Affinity

Purification of Target DNA from Whole

Human Blood by Coupling Isotachophoresis

with Affinity Chromatography

The contents of this appendix were previously published by V. Shkolnikov and J. G. Santiago [178] in proceedings of 18th International Conference on Miniaturized Systems for Chemistry and Life Sciences (μ TAS) and are reproduced here with minor modifications.

A.1 Introduction

AC is a popular chromatographic technique for specific purification and/or analysis of proteins, lectins, and nucleic acids from various samples [99]. However, when sample components of interest are present in low concentrations, a substantial volume of sample must be processed through the affinity substrate, which can lead to long processing times and substrate fouling. Low target and high concentrations of fouling species also imply low target-probe binding rates [103]. These factors increase time of the AC, can lead to poor substrate utilization, and/or poor purification yield. We overcome these limitations of AC by preconcentrating and pre-purifying target immediately prior to and during affinity reaction using ITP. We then demonstrate this method by performing a sequence specific purification of a 25 nt target DNA from 13,000-fold more abundant endogenous blood DNA by processing a 12.5 μ l whole blood sample.

A.2 Theory

We aim to decrease assay time and improve affinity region utilization by purifying the target and increasing the affinity capture reaction rate. Figure A.1 summarizes our protocol for ITP-AC and presents example experimental data. First, we fill leading electrolyte (LE) in the LE reservoir and in the entire capillary (including the porous affinity region). We then place the sample in the sample reservoir, and fill the trailing electrolyte (TE) reservoir with TE. In an alternate setup there is no sample reservoir and we fill the TE reservoir with a mixture of trailing electrolyte buffer and sample. Upon application of the electric field, the target is extracted from the sample (or TE) reservoir and is preconcentrated at the LE-TE interface, and transported toward and through the affinity region (Figure A.1a, Step 2). Contaminating species which are neutral, oppositely charged of the target, or co-ionic but with a lower electrophoretic mobility magnitude than the TE co-ion are excluded [11]. Upon reaching the affinity region, the target reacts with the immobilized complimentary DNA capture probe and is captured (Figure A.1a, Step 3). The increase of the target concentration accelerates the affinity reaction and the target is captured in a smaller, upstream region of the column. Exposure of the ITP-focused analyte to reaction sites on the column is temporary and is followed by an automatic wash associated with the TE zone entering the affinity region. After capture, we pump air through the system to remove all liquid from the column and so arrest further reactions. This limits the time for dissociation and so enables capture of targets with relatively high dissociation rates if necessary.

A.3 Experimental

To demonstrate ITP-AC we first performed an experiment with a controlled sample, in which we extracted a 25 nt Cy5 labeled target from TE (Figure A.1b). We then demonstrated ITP-AC purification on a clinically relevant sample of whole human blood. In this demonstration we separated a spiked in 25 nt Cy5 labeled DNA target from 13,000-fold more abundant endogenous blood DNA in 12.5 μ l whole blood sample (Figure A.2). We describe in detail the experimental setup, as well as the preparation of the porous affinity region in recently published work by Shkolnikov et al. [8].

In the experiment shown in Figure A.1b, we mixed 17 ng of 25 nt Cy5 labeled DNA target into 25 mM HEPES and 50 mM Tris (TE). We then filled the channel with 250 mM HCl and 500 mM Tris as LE and placed the TE with 25 nt target into the TE reservoir. We applied a current of 800 μ A to extract the target and bring it to the affinity region and 200 μ A to migrate the target through the affinity region.

In the experiment shown in Figure A.2, we mixed 12.5 μ l of whole human blood (collected in 3.2% buffered sodium citrate vacuum tubes) with a lysis solution to a final concentration of 1% Triton-X100, 0.2 mg/ μ l of Proteinase K [139], 0.1x SYBR Green I and 1 ng of 25 nt Cy5 labeled DNA target and a final volume of 25 μ l. Whole human blood from healthy subjects aged 20-50 contains roughly 1 μ g/ μ l of endogenous DNA [179], hence we estimate our sample contained roughly 13 μ g of endogenous DNA. We filled the channel with 250 mM HCl and 500 mM Tris as LE, placed the lysed blood sample into the sample reservoir, and filled the TE reservoir with 25 mM HEPES and 50 mM Tris as TE. We again applied a current of 800 μ A for the extraction step and 200 μ A for the hybridization step.

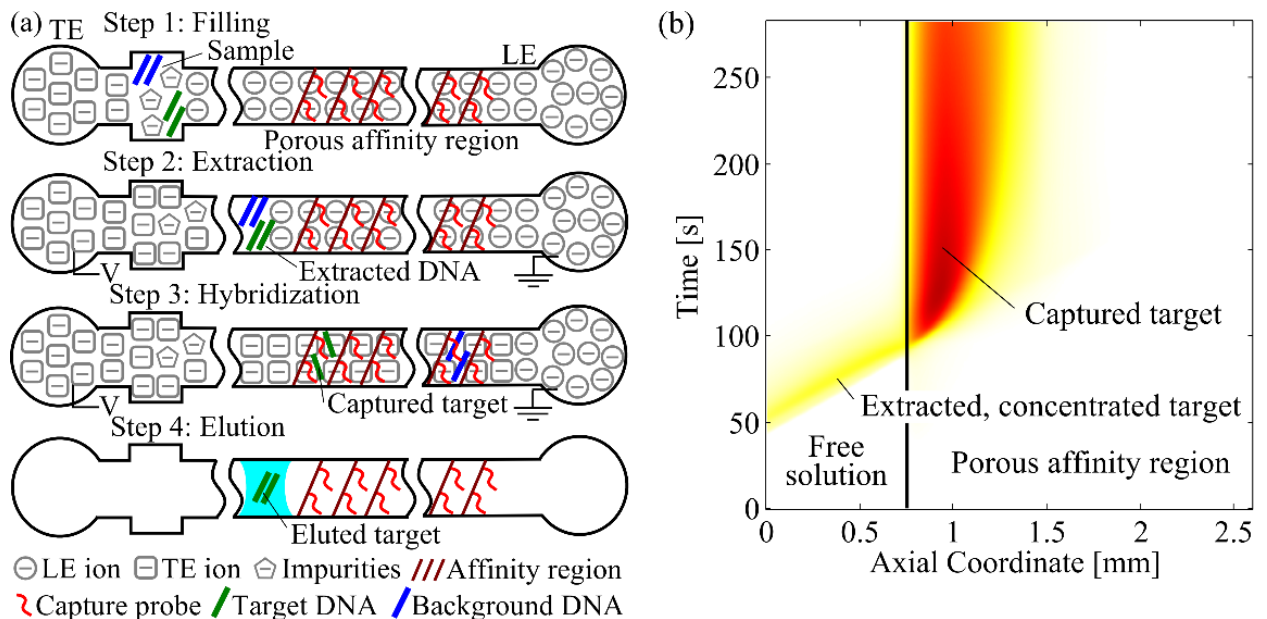


Figure A.1. (a) Schematic of ITP-AC process. We fill the leading electrolyte (LE) reservoir and affinity column with LE buffer and place the sample in the sample reservoir and trailing electrolyte (TE) into the TE reservoir (Step 1). We applied an electric field (from LE to TE) and the target species are extracted and focus into a sharp ITP peak (Step 2). The target migrates into the affinity region and is captured by the immobilized probe (Step 3). We then remove the LE and TE buffers and introduce a small slug of elution buffer to elute the target (Step 4). (b) Spatiotemporal plot of experimentally measured target concentration showing dynamics of a typical ITP-AC binding experiment. The concentrated target (visualized with Cy5 fluorescence) enters the porous affinity region from the left and is captured by the immobilized probes.

A.4 Results and Discussion

For the experiment with a controlled sample shown in Figure A.1b, the target focused in ITP migrated at constant velocity in a Gaussian like distribution toward the porous affinity region, as expected. Upon reaching the region it reacted with the immobilized DNA probes and was captured. As shown in Figure A.1b, there is an increase in fluorescence intensity (approximately 1.7x) when the target enters the PPM. We attribute this to the refractive optical properties of the PPM (see [8] for a more detailed discussion). As expected, the target persisted on the PPM as it was washed by the TE buffer. We eluted

the target with 50 mM NaOH and quickly quenched this with 200 mM HEPES to achieve near neutral pH.

Next, we extracted the 25 nt Cy5 labeled DNA target from 12.5 μ l whole blood sample with endogenous DNA (from lysed blood cells) as 13,000-fold background contaminant. Figure A.2a shows the spatiotemporal plot of observed fluorescence from the experiment in the SYBR Green I channel. The endogenous DNA extracted from lysed blood migrated in ITP from free solution into the PPM and continued to migrate in ITP. This shows background DNA was not captured by the immobilized probe of the PPM, showing little non-specific binding of DNA to the GMA-EDMA PPM.

In Figure A.2b we show the spatiotemporal plot of observed fluorescence from the experiment in the Cy5 channel. The Cy5-labeled 25 nt target migrated in ITP from free solution into the PPM and was quickly captured by the immobilized probe on the PPM. The presence of 13,000-fold more abundant contaminating endogenous blood DNA did not interfere with capture of the target. In Figure A.2c we show the spatiotemporal plot of observed fluorescence from the experiment in both the SYBR Green I and Cy5 channels. Figure A.2c shows clearly that the target species attain zero velocity in under 200s, while the contaminant species (endogenous blood DNA) continues to migrate at ITP velocity. This allows for superior separation as the target and contaminant are spatially confined to two distinct, non-diffusing regions. Hence, the resolution of ITP-AC increases proportionally with time.

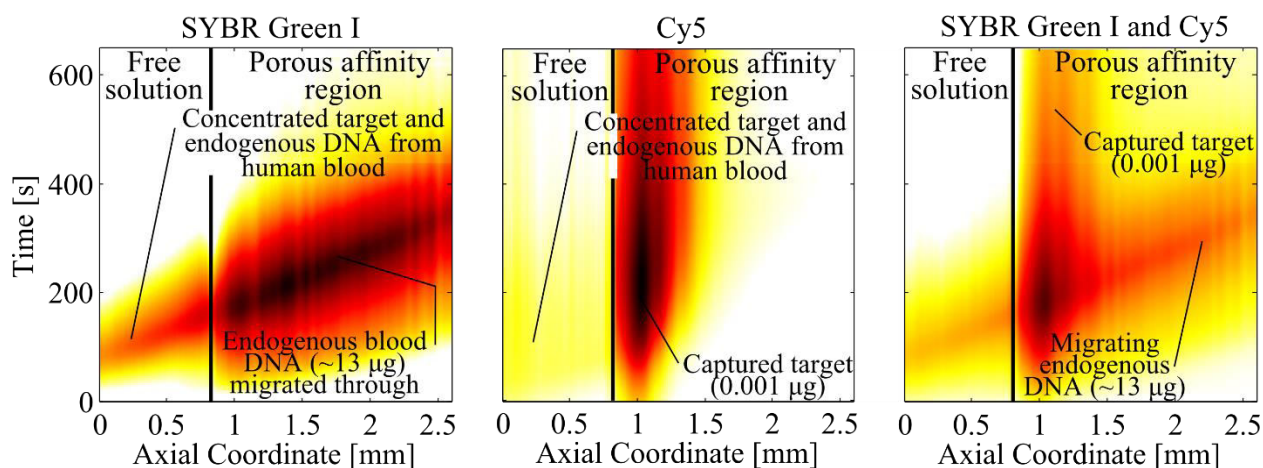


Figure A.2. Experimentally measured spatiotemporal plots showing ITP-AC separation of rare target DNA from 13,000-fold more abundant endogenous blood DNA from 12.5 μ l whole blood sample. The plots show the target and endogenous DNA migrating from free solution into the porous polymer. (a) Endogenous DNA (from lysed blood cells, visualized via SYBR Green I) is not captured by the immobilized probe on the PPM and continues to migrate in ITP. (b) The Cy5-labeled, low-abundance target DNA of the correct sequence is quickly and selectively captured. (c) Overlapped signals from SYBR Green I and Cy5 optical channels show separation between trace target DNA and 13,000-fold more abundant contaminant in under 1 mm column length and in less than 5 min.

A.5 Conclusion

Coupling ITP with AC significantly reduces assay time, improves column utilization and allows for capture of targets with higher dissociation constants. This approach obviates the need for high pressure specialized pumps; integrates an automatic wash step into the process, eliminating a separate wash step; and reduces affinity substrate fouling by partially separating sample compounds by their electrophoretic mobility prior to the affinity reaction. We here demonstrated ITP-AC by performing a sequence specific purification of a 25 nt target DNA from 13,000-fold more abundant endogenous blood DNA by processing a 12.5 μ l whole human blood sample.

B. Rapid Sequential Affinity Probing of Multiple Regions of Nucleic Acids Without Amplification or Sample Spitting

B.1 Introduction

A common and simple way to determine useful information about a specific nucleic acid target is to probe it in several regions by hybridizing complementary probes to these regions. Applications of this include genotyping microarrays for pathogen detection and analysis [180-185], tumor classification [186], detection and diagnosis of genetic diseases [187, 188], and sequencing-by-synthesis [180]. These methods typically involve breaking the target nucleic acid sequence into a large number of short fragments and hybridizing these to a large array of short complementary sequences. The array is then read and bioinformatics algorithms are used to reconstruct the sequence [189, 190]. The hybridization step is usually the most time consuming step of the genotyping process, as hybridization typically requires tens of hours [191-194] and still often does not reach equilibrium [194]. This implies that much of the target nucleic acid is typically not hybridized to its respective probe. Therefore, the sensitivity of these assays is much lower than what can be potentially achieved. One reason for this low rate of hybridization is the need to split the already low target concentration in the sample between a large number of simultaneously occurring reactions. Furthermore, the need to randomly fragment the target, cuts the target in the middle of many sequences of interest, therefore wasting a considerable amount of target.

We here propose one method of avoiding sample splitting and target loss due to fragmentation in genotyping assays: Perform a series of hybridization (capture) and melting (release) reactions involving a different probe sequences on the same set of target nucleic acid molecules. These hybridization reactions, separations (of hybridized vs. unhybridized species), and release events can form the basis of a sequence of logical operations on the target molecule, thereby determining useful information about multiple regions of the same target [189]. We achieve this by combining isotachophoresis (ITP), affinity chromatography (AC), and Joule-heating-based elution. ITP is an electrophoretic technique that uses a heterogeneous buffer system comprising of a leading electrolyte (LE) with a high mobility co-ion (same charge as the analyte) and a trailing electrolyte (TE) with a low mobility co-ion. Analyte species of intermediate mobility focus between these co-ions and are preconcentrated by a strong TE-to-LE electric field gradient [9]. ITP has been used in a variety of applications related to the current work, including extraction and purification of nucleic acids from complex biological samples [104], and acceleration of homogeneous hybridization reactions by 14,000-fold [18], and up to 100-fold acceleration of reactions between molecules in solution and surface immobilized probes [3, 8, 21, 107, 195]. Most relevant to the current work, Shkolnikov and Santiago developed a model for ITP assisted affinity reactions in a porous medium [3] and demonstrated sequence specific purification of a target from 10,000-fold more abundant background [8]. Despite these related studies, we know of no use of ITP with affinity reactions to sequentially interrogate the same target molecules multiple times.

Here we demonstrate sequential interrogation of a 112 nt Cy5 labeled DNA target by two short (29 nt and 26 nt) DNA probes complementary to two different regions of the

target with 8 nt overlap between the regions. We immobilized each probe onto the surface of a separate poly(glycidyl methacrylate-co-ethylene dimethacrylate) (GMA-EDMA) porous polymer monolith (PPM), which we polymerized inside a single 500 μm inner diameter glass capillary. We term these PPM regions containing a single probe "affinity regions" (ARs). To sequentially interrogate the target, we introduced the target into the capillary with two affinity regions. We first captured the target with the first AR, eluted the target, and then captured the same target with the second AR and eluted the target once again. With this method, valuable information about the target can be obtained by observing which affinity regions were able to capture the target. We term our method "sequential ITP-AC".

Here we first explain the concept of sequential ITP-AC including the use of multiple ARs and sequential capture/elution using ITP. We compare our assay's sensitivity, specificity, precision, and diagnostic odds ratio to traditional parallel affinity assays (e.g., genotyping microarrays). We analyze important design parameters such as channel material, geometry, and heat transfer rates on assay performance. We provide recommendations for these parameters as well as AR spacing and choice of capture, and elution conditions. We evaluate these recommendations with thermographic measurements of our system. Lastly, we discuss our experiments where we use epifluorescence microscopy to study sequential interrogation of 112 nt DNA target with two different probe sequences.

B.2 Concept

We aimed to interrogate the nucleic acid target rapidly and in an automated fashion. As depicted in Figure B.1, we use ITP to extract and preconcentrate target from a sample

volume; move the concentrated target into the first AR with ITP and allow it to hybridize with complimentary probes there; use ITP to remove unhybridized species; record the fluorescence signal of the hybridized species; elute the hybridized target by raising the temperature in the entire column; refocus the target with ITP and repeat the process with the next AR. We performed this process inside a 500 μm inner diameter capillary with two PPM each containing a single AR with immobilized cDNA probes. Each of these probes are complementary to two different regions on the target. (See Supplementary Information (SI) Section B.6.6 for probe and target sequences). The capillary is connected to leading electrolyte (LE) reservoir at one end, and a sample reservoir joined to a TE reservoir at the other end. (See SI Section B.6.5 for an image of this custom built setup). To begin our sequential ITP-AC process, we first fill LE in the LE reservoir and in the entire capillary (including the PPM ARs). We then fill the sample reservoir with the 112 nt Cy5 labeled DNA target in a sample buffer and then fill the TE reservoir with TE (Figure B.1, Step 1). We then apply a constant current from LE to TE, starting ITP. The target is extracted from the sample reservoir and focuses into a narrow, Gaussian distribution (i.e., ITP "peak", Figure B.1, Step 2) [18, 26, 27, 108]. We refer to this current as "run current". During this step species that may potentially foul the PPM ARs that are neutral, oppositely charged of the target, or co-ionic but with a lower electrophoretic mobility magnitude than the TE co-ion are not focused and are separated from the focused target. Furthermore, the increase of the target concentration via ITP accelerates the capture reaction and concentrates the target into a smaller region of the column [3]. When the target nears the first AR, we switch the current to a lower current value, which we refer to as "capture current". We migrate the concentrated target into the AR at this reduced current. This reduces Joule heating

throughout the column (and more importantly, the ARs) and reduces the target velocity. Reducing Joule heating creates a more favorable temperature for target-probe hybridization. Reducing target velocity reduces the length of column necessary to capture the target, as we have shown previously [3]. This in turn allows more ARs to be placed per length of column, and so allows implementing a higher degree of multiplexing. Upon reaching the AR, the target reacts with the immobilized capture probe and is captured, while analytes focused with the target with an incorrect sequence continue to migrate in ITP (Figure B.1, Step 3). After the target and the other analytes have been sufficiently separated, we record the fluorescence intensity of the captured target and measure the length of AR necessary to capture the target (capture length). Capture length is inversely proportional to forward (hybridization) reaction constant [3], and so provides additional information about the target-probe interaction. After this, we switch the current to a higher current value, which we refer to as "elution current" and elute the captured target. Increasing the current generates larger Joule heating, raising the temperature inside the entire capillary, and especially inside the ARs. This creates conditions favorable for target-probe melting (reverse) reaction and elutes the target. The target then migrates through the TE until it catches up with the LE-TE interface and is refocused (Step 4). We discuss the necessary spacing between the ARs to allow sufficient refocusing in SI Section B.6.4. We then repeat the hybridization step (Figure B.1, Step 3) and the elution step (Figure B.1, Step 4) for all the other ARs (Figure B.1, Step n-1, Step n).

In our method, each AR is exposed to the entire amount of target and so captures a greater amount of target than if it was exposed a fraction of the target amount. This gives our assay greater sensitivity than assays with sample splitting (e.g., traditional

microarrays). However, lack of competitive reactions with other probes during each capture may lead to lower specificity for each capture, as incorrect regions of the target may bind in small amounts to the probe. (See SI Section B.6.8 for a detailed comparison of sensitivity, specificity, precision, and diagnostic odds ratio for our assay to that for traditional parallel affinity assays.) In our assay we address this by having more stringent capture conditions that can be traditionally achieved in parallel assays. Specifically, capture and elution currents for each AR can be optimized and set independently to optimize the hybridization and elution temperature for that AR. This allows for more stringent and specific affinity reactions than where there is a single hybridization and single elution temperature for all affinity reactions (e.g., as in traditional microarrays). We discuss controlling the temperature field in the capillary and the ARs in SI Sections B.6.1 - B.6.3.

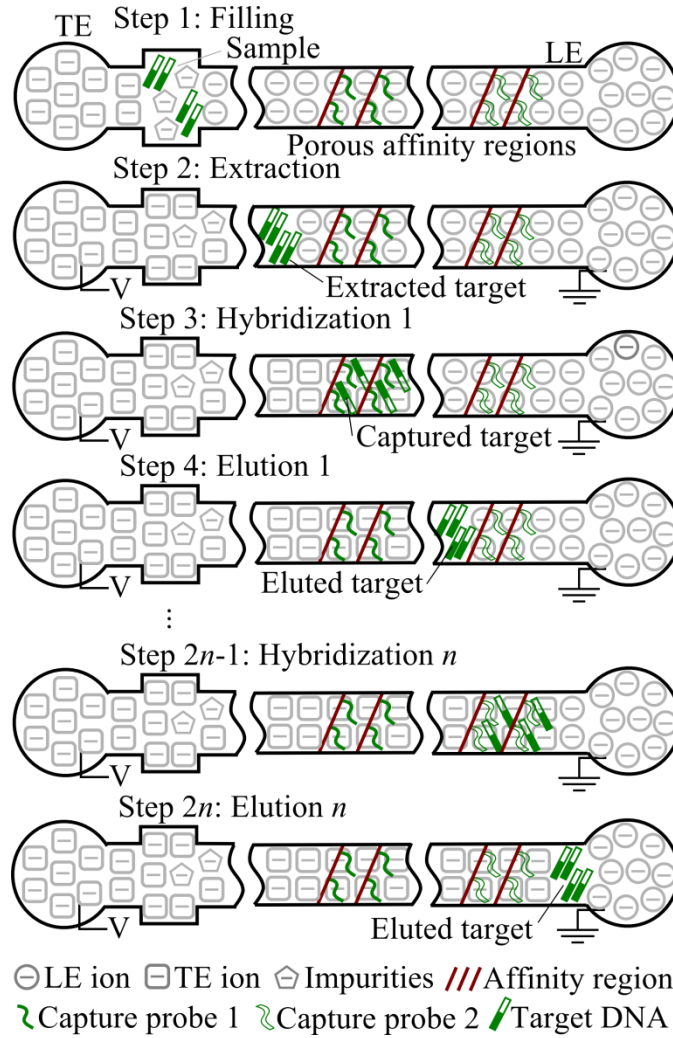


Figure B.1. Schematic illustrating our assay for sequential ITP-aided affinity chromatography with multiple porous polymer monolith affinity regions (ARs). We filled the LE reservoir and the capillary containing porous ARs with LE buffer (by applying vacuum at the TE reservoir). Then we introduce the sample into the sample reservoir and TE into the TE reservoir (Step 1). We apply an electric current (from LE to TE) and the target species are extracted and focused into a sharp ITP peak (Step 2). We lower the current value and the target migrates into the first AR and is captured by the immobilized probe (Step 3). Once the target is separated from any other species not captured by the immobilized probe, we raise the current value to increase Joule heating the electrolyte solution in the AR and elute the target. The target then catches up with the migrating LE-TE interface. (Step 4). We then repeat steps 3 and 4 $n-1$ times for the subsequent $n-1$ ARs to probe the target n times.

B.3 Materials and Methods

B.3.1 Column Fabrication

We have synthesized PPM inside 500 μm inner diameter borosilicate glass capillaries (VWR, Vasalia, CA) according to a protocol we described in detail in [8]. We briefly summarize the protocol here. We vinylized the walls of the capillaries by placing the capillaries in a solution of 30% (v/v) 3-(trimethoxysilyl)propyl methacrylate, 70% (v/v) acetone at room temperature overnight and then flushing the remaining solution with air. We then prepared a polymerization solution consisting of the photo initiator azobisisobutyronitrile (126 mM), glycidyl methacrylate (12% v/v), ethylene glycol dimethylacrylate (8% v/v), methanol (64% v/v), and hexane (16% v/v) (all from Sigma–Aldrich, St. Louis, MO). We injected a slug of this solution into the vinylized capillaries and irradiated the solution with a 12 W, ~ 405 nm peak wavelength UV lamp (Chauvet, Sunrise, FL) at 12 cm exposure distance for 2 h. After polymerization, we flushed the PPM with air to remove unreacted monomers and solvents, and dried at 20°C under vacuum for 30 min. Next, we prepared DNA immobilization solution consisting of 3X SSC buffer, 2 mM sodium deodecyl sulfate, and 250 μM 5' amine modified synthetic oligo DNA probe (from Protein and Nucleic Acid facility at Stanford University, Stanford, CA). We injected this solution into the PPM and placed the PPM containing capillaries into a water bath at 70°C for 2 h. We then flushed each capillary with 2 ml of DI water and dried at 70°C under vacuum for 1h. We thus obtained the first AR. We repeated the process with the same capillary to obtain the second AR. (See SI Section B.6.6 for details of target and probe sequences and their melting temperatures). To perform ITP-AC experiments we fixed the capillary in a custom fabricated setup containing

chambers for the LE, sample, and TE (see SI Section B.6.5 for a detailed description of the setup).

B.3.2 Imaging systems

We monitored our experiments and performed fluorescence measurements of the Cy5 labeled target with an Olympus Model IX70 inverted fluorescence microscope equipped with a 4×(NA of 0.16) objective (Olympus, Hauppauge, NY), XF110-2 filter cube (Omega Optical, Brattleboro, VT), and 627-nm red LED (ThorLabs, Newton, NJ) for illumination. We captured images with a 12-bit, 2048×2048 pixel charge coupled device (CCD) camera with 7.4 μm ×7.4 μm pixels (Photometrics CoolSNAP K4) controlled with WinView software (Roper Scientific, Trenton, NJ). We performed thermal imaging of the capillary during ITP experiments (discussed in SI Section B.6.3) using Fluke Ti10 160×120 focal plane array uncooled microbolometer with a 20 mm F# 0.8 lens (Norfolk, United Kingdom). We post-processed the images with custom in-house scripts written in MATLAB (Mathworks, Natick, MA)

B.4 Discussion

We experimentally demonstrated sequential ITP-AC by sequentially capturing and releasing Cy5 labeled 112 nt DNA target with two affinity regions. We observed and quantified the spatiotemporal behavior of sequential ITP-AC by tracking the 112 nt Cy5 labeled target while it was migrating in ITP in free solution, while it was reacting with the immobilized probe in the PPMs, and while it was eluted from the PPMs. In Figure B.2 we show a sequence of two capture and elution events for this target. We plot the area averaged

Cy5 fluorescence intensity of both ARs (left ordinate) as well as the electrical current in the channel (right ordinate) as a function of time.

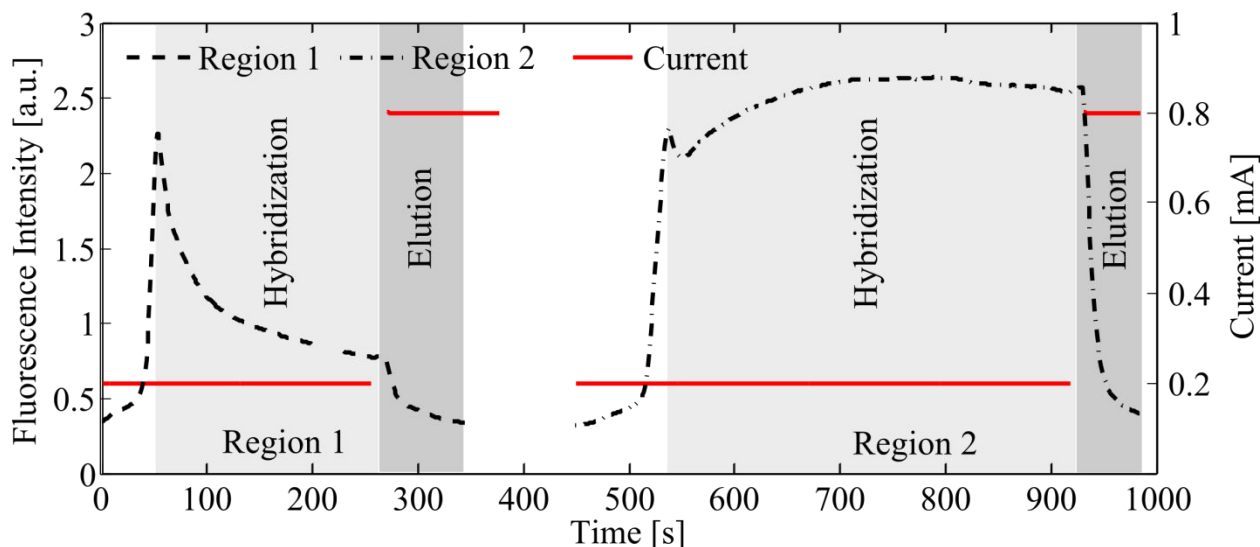


Figure B.2. Fluorescence intensity of Cy5 labeled DNA target (black dashed) and current (red solid) in ARs 1 and 2 as a function of time. The target, focused in ITP, entered the first AR under capture current of 200 μ A (generating optimal temperature for hybridization) and began to hybridize to immobilized cDNA capture probes. Once hybridization was over and non-complementary target was removed focused in ITP (see SI Figure S-5) we eluted the captured target by increasing current to 800 μ A (capture current). This current generated optimal temperature for the reverse reaction (melting) and eluting the captured DNA. This DNA migrated rapidly through the TE to catch up with the LE-TE interface and refocus. Once the DNA was refocused, we lowered the current to 200 μ A and repeated the capture and elution process at the second AR containing a different probe than AR1. Thus we interrogated two regions of the same target with two different probes.

B.4.1 Demonstration of sequential capture and release of target

In these demonstration experiments, we placed 8.3 nM Cy5 labeled 112 nt DNA target in the sample chamber and used 250 mM HCl with 500 mM Tris as the LE and 250 mM HEPES with 500 mM Tris as the TE. The 5' Cy5 labeled 112 nt DNA target was used as received (i.e., without additional sequence specific purifications). Therefore we expected some of the molecules in the target population to be of incorrect sequence or partially degraded sequence near the 3' end [196, 197]. We leveraged this effect to simulate

realistic samples where the target population contains some sequence variation (e.g., single nucleotide polymorphisms). In our experiments we first probe the region of the target closest to the 3' end (with AR 1) and then probe a region further toward the middle of the target (with AR 2). (See SI Section B.6.6 for target and probe sequences).

To start ITP, we applied a run current of 800 μA and extracted the target from the sample, focused it into a narrow Gaussian peak, and transported it in front of the first AR. We then lowered the current to a capture current of 200 μA , began recording Cy5 fluorescence shown in Figure B.2, and allowed the target to migrate into the first AR. During approximately the first 50 s shown in Figure B.2 the target begins to enter the first AR. During this time the fluorescence peaks, which corresponds to the highest amount of target that the leading edge of the AR sees. This fluorescence level corresponds to the concentration of the total amount of target. The fluorescence signal then decreases as some of the target DNA sequences do not bind to the PPM and continue to migrate in ITP (see Figure B.7 of SI Section B.6.7). This occurs because now the TE washes over the AR, ensuring high selectivity for the affinity reaction. The fluorescence signal in the region spanned by the capture length decreases, indicating that only about 30% of the total amount of target was captured by this AR. The rest of the target continues to migrate in ITP and migrates out of the AR.

Next, we elute the target by switching the current from 200 μA to 800 μA (elution current). This increases the temperature in the TE (which now covers the capture zone) from roughly 27°C to 50°C (measured thermographically in a separate experiment, see SI Section B.6.3) in about 24 s. This increase in temperature causes melting of the target-probe and elution of the target from the AR. We estimated the time constant for elution by

fitting an exponential decay function to the fluorescence intensity data (from 270 s to 350 s) in Figure B.2 via a non-linear least squares fit. We estimate that time constant for this elution was 15 s ($R^2 = 0.97$). The advection time scale for elution was 1 s (based on calculated velocity of DNA in TE and measured capture length). This suggests that this elution was dominated by the reverse reaction rate rather than the advection rate. We note that the elution was practically complete as the fluorescence signal after the elution returned to the pre-capture levels to within 5%.

As we continued to elute the target, the target caught up with the LE-TE interface and refocused. We discuss the distance necessary to refocus the target and the necessary spacing between the leading edges of the ARs in SI Section B.6.4. For our system and a ITP-AC resolution of 4 this distance is 10 mm. (We define resolution in the usual way, as the separation distance between the mean of two distributions of separated species divided by the sum of two times the standard deviation of each distribution [113]; see Shkolnikov et al. [3] for a discussion on the resolution in ITP-AC). Correspondingly, we made the distance between the leading edges of AR 1 and 2 in our system to be 10 mm. In the experiment shown in Figure B.2, this "catch up" phase lasted from 100 s (from 350 s to 450 s).

As the target neared the second AR we repeated the capture-elute cycle. We lowered the current from 800 μA (elution current) to 200 μA (capture current). During the first 100 s (from approximately 450 s to 550 s) the target entered the second AR and began to become captured. During this time the fluorescence signal peaked again and then briefly decreased. We attribute this brief decrease to a small portion of the target (15% - see SI Section B.6.7) not being captured by the AR and continuing to migrate focused in ITP.

After this the fluorescence signal continued to increase and then remained roughly constant. We attribute this small increase in signal to some of the target that did not completely catch up with the LE-TE interface in the catch up phase. Once all of the target reached the AR 2 and hybridized to the AR 2 probes the fluorescence signal remained constant. We estimate that over 85% of the target was captured by this AR.

Next, we again eluted the target by switching the current from 200 μA to 800 μA . We estimate that the time constant for the elution was 11 s ($R^2 = 0.99$), vs. 3 s for advection, and so once again the elution of target was dominated by the reverse reaction rate. We note that again the elution was practically complete as the fluorescence signal after the elution returned to the pre-capture levels to within 5%. Since the elution with Joule heating was practically complete, the capture-elution cycle can be repeated a large number of times without significant target loss. Therefore, a large number of probes can interrogate a single target.

We attribute the fact that the first AR captured only about 30% while the second AR captured over 85% of the target to the degradation and/or errors in the synthesis of the 112 nt target. It is well known that large (>70 nt) targets are difficult to synthesize with the correct sequence because of accumulation of synthesis error [196, 197]. Synthesis error accumulates especially strongly near the 3' end [197]. We leveraged this effect to simulate a realistic situation where only some of the analytes are captured, while the rest continue to migrate in ITP. AR 1 probes capture the region of the target nearest to the 3' end (most distant from the Cy5 dye). Therefore sequences that contain the Cy5 dye, but are partially degraded will not be captured by the AR 1. AR 2 probes capture the region of the target in the middle of the sequence (further from the 3' end, closer to the Cy5). Therefore there is

greater chance that sequences containing Cy5 when incorrectly synthesized or degraded will contain this region. Hence, AR 2 captures more of the target than AR 1.

B.4.2 Control and measurement of target hybridization rate

Rate of DNA hybridization is highly dependent on temperature; in sequential ITP-AC we are able to use current to control hybridization temperature and measure hybridization rate by measuring capture length. In both hybridization steps we used a capture current of 200 μA . This current heated the electrolyte, causing a temperature of glass wall surrounding the PPM to be roughly 26°C (thermographically measured in a separate experiment, see SI Section B.6.3); the temperature was likely a few degrees higher inside the PPM. Thus, we estimate the electrolyte temperature was roughly 30°C and 40°C below the melting point of the target-probe complex for the first and second AR respectively. Since the forward reaction rate of DNA hybridization is maximum around 20-30°C below the melting point of the hybrid [198] we expected the hybridization rate to be higher at the first AR than at the second.

B.5 Conclusion

We have developed a novel method to rapidly and sequentially probe different regions of the same nucleic acid molecule. This method preserves the molecule's integrity (i.e., does not require shearing of nucleic acids) and does not require amplification (and therefore avoids amplification bias). Our method first leverages ITP to concentrate target nucleic acids and migrate them through porous polymer monolith functionalized with complementary DNA probes. Our method then uses Joule heating associated with the ionic current in ITP to dissociate the captured nucleic acid target. Thirdly, our method leverages

ITP again to reconcentrate the dissociated target and react it with the next probe, repeating the process.

We compared our method's sensitivity, specificity, precision, and diagnostic odds ratio to traditional parallel affinity assays (e.g., genotyping microarrays). We analyzed important design parameters such as channel material, geometry, AR spacing and choice of capture, and elution conditions on our method's performance and provide recommendations for these parameters. We implemented our method inside a capillary with two PPM AR and investigated system performance using epifluorescence and thermographic measurements. Lastly, we have demonstrated our method by sequentially probing two regions of a synthetic, 112 nt Cy5 labeled DNA.

B.6 Supplementary Information

We here present additional information on the following topics: (1) Timescale of temperature transients during switching from capture to elution; (2) Approximate radial temperature distribution in the capillary; (3) Capillary surface temperature measurements; (4) Optimal distance between affinity regions; (5) Image of custom built capillary setup with two affinity regions; (6) Target, probes, and melting points; (7) Spatiotemporal behavior of target during capture and elution; (8) Performance metrics of serial-recycling and traditional parallel affinity assays.

B.6.1 Timescale of temperature transients during switching from capture to elution

Here we find the time scale for the transient cooling and heating of the TE during switching of the current from capture current to elution current and back to capture current.

Previously steady state temperature distributions in isotachophoresis were studied by Janak et al. [199, 200]; unsteady temperature distributions were studied Coxon and Binder [201]. We here present a simplified analysis of transient temperature distributions (including the effect of porous media) and provide a scaling pertinent to our experiments. We consider a region of the capillary that contains the TE far from the LE-TE interface and assume $\partial T/\partial z = 0$ and $\partial T/\partial \varphi = 0$ where T is temperature, z is the axial coordinate and φ is the azimuthal coordinate. Thus we write the unsteady heat equation as

$$\frac{\partial T}{\partial t} = \frac{1}{r} \frac{\partial}{\partial r} \left(\alpha r \frac{\partial T}{\partial r} \right) + \Phi, \quad (\text{B.1})$$

$$\alpha = \begin{cases} \alpha_i & r < r_i \\ \alpha_o & r_i < r < r_o \end{cases} \quad (\text{B.2})$$

$$\Phi = \begin{cases} \frac{1}{\rho c_p} \frac{j^2}{\sigma} \phi & r < r_i \\ 0 & r_i < r < r_o \end{cases} \quad (\text{B.3})$$

where r is the radial coordinate, α is the thermal diffusivity and Φ is the heat generation rate; r_i and r_o are the inner and outer radii of the capillary respectively; α_i and α_o are the thermal diffusivity of the PPM filled with TE and the glass capillary wall respectively; ρc_p is the product of the density and specific heat of PPM filled with TE; σ is the electrical conductivity of the electrolyte, j is the current density inside the PPM and ϕ is the PPM void fraction. Note j is equal to the current through the capillary divided by the product of the capillary cross-sectional area and void fraction.

At the outer surface of the capillary we have a convection boundary condition:

$$\frac{\partial T}{\partial r} + \frac{h}{k_o}(T - T_{amb}) = 0 \quad \text{at } r = r_o, \quad (\text{B.4})$$

and at the center of the capillary we have a condition that the temperature must be bounded, hence

$$\frac{\partial T}{\partial r} = 0 \quad \text{at } r = 0. \quad (\text{B.5})$$

Initially, either (a) the capillary is uniformly at ambient temperature or has a profile set by the steady state of the (b) capture or (c) elution condition. Hence,

$$T = f(r) \quad \text{at } t = 0. \quad (\text{B.6})$$

To simplify the solution and to reduce the number of parameters we non-dimensionalize the variables as follows

$$\begin{aligned} T^* &= (T - T_{amb}) / (T_0 - T_{amb}), \\ r^* &= r / r_o, \\ t^* &= t \alpha_o / r_o^2 \\ \alpha^* &= \alpha / \alpha_o. \end{aligned} \quad (\text{B.7})$$

where T_0 is anticipated surface temperature of the capillary (i.e. at $r = r_o$). Based on our experimental observations of surface temperature at various experimentally attainable current densities in our system we set $T_0 - T_{amb} = \theta_0 = 20$ K. We rewrite the governing equations and the boundary conditions using non-dimensional variables:

$$\frac{\partial T^*}{\partial t^*} = \frac{1}{r^*} \frac{\partial}{\partial r^*} \left(\alpha^* r^* \frac{\partial T^*}{\partial r^*} \right) + \Phi^*, \quad (\text{B.8})$$

$$\alpha^* = \begin{cases} A_i & r^* < R_i \\ 1 & R_i < r^* < 1 \end{cases} \quad (\text{B.9})$$

$$\Phi^* = \begin{cases} \Omega & r^* < R_i \\ 0 & R_i < r^* < 1 \end{cases} \quad (\text{B.10})$$

and define three parameters

$$\Omega = \frac{r_o^2}{\theta_o \alpha_o} \frac{1}{\rho c_p} \frac{j^2}{\sigma} \phi, \quad (\text{B.11})$$

$$R_i = r_i / r_o, \quad (\text{B.12})$$

$$A_i = \alpha_i / \alpha_o. \quad (\text{B.13})$$

Next we non-dimensionalize the initial and boundary conditions:

$$T^* = f^*(r^*) \quad \text{at } t^* = 0, \quad (\text{B.14})$$

$$\frac{\partial T^*}{\partial r^*} = 0 \quad \text{at } r^* = 0, \quad (\text{B.15})$$

$$\frac{\partial T^*}{\partial r^*} + Bi T^* = 0 \quad \text{at } r^* = 1, \quad (\text{B.16})$$

where we define the Biot number as usual

$$Bi = h r_o / k_o. \quad (\text{B.17})$$

We use the correlation from Churchill and Chu [202] for a horizontal cylinder with natural convection (external flow) for our Nusselt number:

$$Nu = \frac{1}{2} \left(0.6 + \frac{0.387 Ra^{1/6}}{\left(1 + (0.559/Pr)^{9/16} \right)^{8/27}} \right)^2, \quad (B.18)$$

where Pr is the Prandtl number, defined in the usual way as $Pr = \nu/\alpha_a$, where ν and α_a are the kinematic viscosity and thermal diffusivity of air; Ra is the Rayleigh number also defined in the usual way as

$$Ra = 8r_0^3 \frac{g\beta}{\nu\alpha_a} (T_0 - T_{amb}), \quad (B.19)$$

where g is the gravitation acceleration, and β is the thermal expansion coefficient. We summarize these parameters and their nominal values (pertinent to the experiments discussed in the main text) in Table B.1.

To obtain a scaling the time scale for the transient cooling and heating of the TE we simplify (B.8) further, assuming a constant thermal diffusivity for the entire capillary (i.e., for $0 < r^* < 1$) approximated as the cross sectional area weighted mean thermal diffusivity:

$$\alpha_m^* = R_i^2 (A_i - 1) + 1 \quad (B.20)$$

$$\frac{\partial T^*}{\partial t^*} = \alpha_m^* \frac{1}{r^*} \frac{\partial}{\partial r} \left(r^* \frac{\partial T^*}{\partial r^*} \right) + \Phi^*. \quad (B.21)$$

Equation (B.21) with initial and boundary conditions (B.14) - (B.16) has the following solution [203]:

$$T^* = \int_0^1 f^*(\xi) G(r^*, \xi, t^*) d\xi + \int_0^{t^*} \int_0^1 \Phi^*(\xi) G(r^*, \xi, t^* - \psi) d\xi d\psi, \quad (B.22)$$

where

$$G(r^*, \xi, t^*) = 2 \sum_{n=1}^{\infty} \frac{\mu_n^2 \xi}{(Bi^2 + \mu_n^2) J_0^2(\mu_n)} J_0(\mu_n r^*) J_0(\mu_n \xi) \exp(-\alpha_m^* \mu_n^2 t^*), \quad (\text{B.23})$$

where μ_n are the positive roots of the transcendental equation

$$\mu J_1(\mu) - Bi J_0(\mu) = 0. \quad (\text{B.24})$$

To obtain a scaling for cooling or heating time scale, we use only the first term in the sum in equation (B.23) and therefore obtain

$$\begin{aligned} T^* &\approx \int_0^1 f^*(\xi) G_1^\dagger(r^*, \xi) \exp[-\alpha_m^* \mu_1^2 t^*] d\xi \\ &+ \int_0^1 \Phi^*(\xi) G_1^\dagger(r^*, \xi) d\xi \int_0^{t^*} \exp(-\alpha_m^* \mu_1^2 (t^* - \psi)) d\psi, \end{aligned} \quad (\text{B.25})$$

where

$$G_1^\dagger(r^*, \xi) = \frac{2\mu_1^2 \xi}{(Bi^2 + \mu_1^2) J_0^2(\mu_1)} J_0(\mu_1 r^*) J_0(\mu_1 \xi). \quad (\text{B.26})$$

We evaluate the integral with respect to ψ in the second term and combine like terms to obtain

$$\begin{aligned} T^* &\approx \left(\exp[-t^*/\tau^*] \right) \int_0^1 (f^*(\xi) - \tau^* \Phi^*(\xi)) G_1^\dagger(r^*, \xi) d\xi \\ &+ \tau^* \int_0^1 \Phi^*(\xi) G_1^\dagger(r^*, \xi) d\xi, \end{aligned} \quad (\text{B.27})$$

where we define a non-dimensional time constant

$$\tau^* = \frac{1}{\alpha_m^* \mu_1^2}. \quad (\text{B.28})$$

We observe that the first term in equation (B.27) decays exponentially with the time constant τ^* and therefore τ^* represents the time scale of the transient heating or cooling. The second term in equation (B.27) represents the steady state temperature. We discuss the steady state temperature distribution in more detail in SI Section B.6.2.

Next we numerically solve the transcendental equation (B.24) for its first root μ_1 . We plot the solution as μ_1^2 as a function of Bi in Figure B.3. We observe that for $Bi < 1$, $\mu_1^2 \approx 1.8Bi$ to within 10%, and for $Bi > 50$ $\mu_1^2 \approx 5.8$ to within 10%. We combine this result with (B.20) to obtain

$$\begin{aligned} \tau^* &= \frac{1}{1.8Bi \left(R_i^2 (A_i - 1) + 1 \right)} & Bi < 1 \\ \tau^* &= \frac{1}{5.8 \left(R_i^2 (A_i - 1) + 1 \right)} & Bi > 50. \end{aligned} \quad (\text{B.29})$$

Next we convert the dimensionless τ^* to a dimensional time scale τ that represents the time scale of the transient heating or cooling.

$$\begin{aligned} \tau &= \frac{r_o^2}{\alpha_o} \frac{1}{1.8Bi \left(R_i^2 (A_i - 1) + 1 \right)} & Bi < 1 \\ \tau &= \frac{r_o^2}{\alpha_o} \frac{1}{5.8 \left(R_i^2 (A_i - 1) + 1 \right)} & Bi > 50 \end{aligned} \quad (\text{B.30})$$

or written in another way

$$\begin{aligned}
\tau &= \frac{r_o^5 k_o}{1.8h(r_i^2(\alpha_i - \alpha_o) + r_o^2 \alpha_o)} & Bi < 1 \\
\tau &= \frac{r_o^4}{5.8(r_i^2(\alpha_i - \alpha_o) + r_o^2 \alpha_o)} & Bi > 50.
\end{aligned} \tag{B.31}$$

We observe that the time scale of the transient is independent of heat generation parameter Ω , and independent of Bi for $Bi > 50$. The time scale of the transient can be decreased (and hence decreasing the time for the assay) by increasing R_i , A_i , α_o and by decreasing r_o ; when $Bi < 1$, increasing Bi also decreases τ . For our experiments described in the main text, we estimate τ to be 24 s.

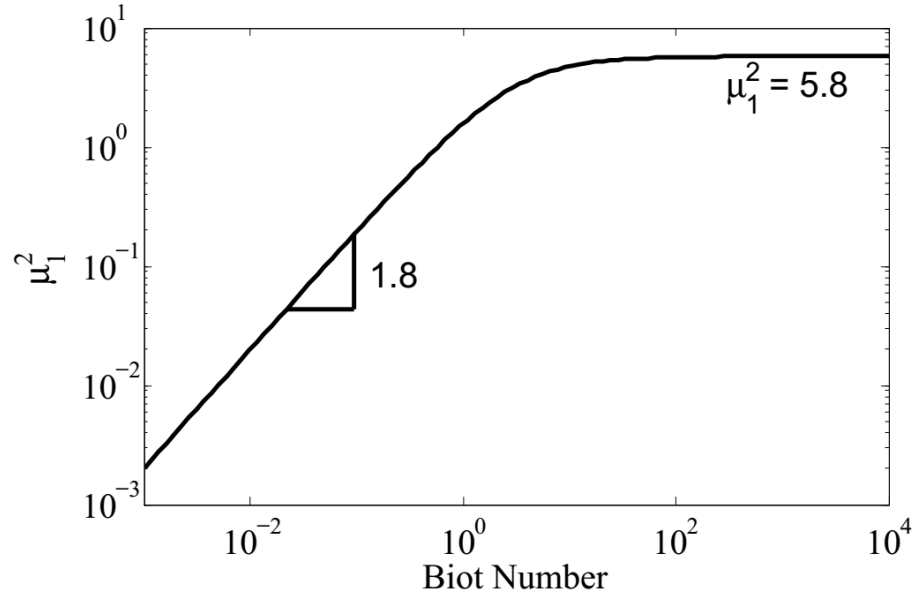


Figure B.3. Solution to the transcendental equation (B.24) as a function of Biot number. For $Bi < 1$, we approximate $\mu_1^2 \approx 1.8Bi$, which is accurate to within 10%; for $Bi > 50$ we approximate $\mu_1^2 \approx 5.8$ which is also accurate to within 10%.

Table B.1. Summary of dimensional and dimensionless parameters and their nominal values

Parameter	Value	Units	Description	Ref.
r_o	500E-6	m	Outer radius of the capillary	
r_i	250E-6	m	Inner radius of the capillary	
ϕ	0.8		Void fraction of PPM	[8]
$\rho_{electrolyte}$	992	kg/m ³	Density of electrolyte solution (assumed that of water) at 313 K	[110]
ρ_{PPM}	1180	kg/m ³	Density of PPM solid phase (assumed that of PMMA)	[204]
ρ	1030	kg/m ³	Effective density of PPM and electrolyte solution	
$c_{p-electrolyte}$	4.179E3	J/(kg K)	Specific heat of electrolyte (assumed that of water at 313 K).	[110]
c_{p-PPM}	1.47E3	J/(kg K)	Specific heat of PPM solid phase (assumed that of PMMA)	[204]
c_p	3.64E3	J/(kg K)	Effective specific heat of PPM and electrolyte solution	
$\alpha_{electrolyte}$	1.52E-7	m ² /s	Thermal diffusivity of electrolyte	[110]
α_{PPM}	1.1E-7	m ² /s	Thermal diffusivity of the PPM solid phase	[204]
α_i	1.44E-7	m ² /s	Effective thermal diffusivity of PPM and electrolyte solution	
α_a	2.39E-5	m ² /s	Thermal diffusivity of air at 313 K	[205]
α_o	6.82E-7	m ² /s	Thermal diffusivity of capillary wall (glass)	[206]
k_a	0.0271	W/(m K)	Thermal conductivity of air at 313 K	[205]
k_o	1.14	W/(m K)	Thermal conductivity of capillary wall (glass)	[206]
β	3.20E-3	1/K	Thermal expansion coefficient of air at 313 K	[205]
ν	1.70E-5	m ² /s	Kinematic viscosity of air at 313 K	[205]
T_{amb}	293	K	Ambient air temperature	
T_0	313	K	Temperature (expected) at $r = r_o$.	
θ_0	20	K	$T_0 - T_{amb}$	
c_{HEPES}	135	mM	Concentration of HEPES in adjusted TE	[207]
c_{Tris}	385	mM	Concentration of Tris in adjusted TE	[207]
σ	0.43	S/m	Electrical conductivity of adjusted TE	[207]
j	1270	A/m ²	Current density in PPM during capture	
	5090	A/m ²	Current density in PPM during elution	
Pr	0.711		Prandtl number of air, 313 K	[205]
Ra	1.55		Rayleigh number with $2r_o$ as length scale (as defined in (B.19))	
Nu	0.447		Nusselt number with r_o as length scale	
Bi	0.0106		Biot number with r_o as length scale	
A_i	0.211		Scaled effective thermal diffusivity of	
R_i	0.5		Scaled inner radius of the capillary	
Ω	0.0147		Dimensionless heat generation during capture	
	0.2360		Dimensionless heat generation during elution	

B.6.2 Approximate radial temperature distribution in the capillary

Here we explore the mean temperature and temperature difference between the capillary center and inner wall once steady state is reached, using the solution for radial temperature distribution obtained in SI Section B.6.1. We write this solution here again for convenience:

$$T^*(r^*, t^*) \approx \left(\exp[-t^*/\tau^*] \right) \int_0^1 \left(f^*(\xi) - \tau^* \Phi^*(\xi) \right) G_1^\dagger(r^*, \xi) d\xi + \tau^* \int_0^1 \Phi^*(\xi) G_1^\dagger(r^*, \xi) d\xi. \quad (\text{B.32})$$

Once steady state is reached, the first term on the right hand side in (B.32) goes to zero and only the second term remains:

$$T_{ss}^*(r^*) \approx \tau^* \int_0^1 \Phi^*(\xi) G_1^\dagger(r^*, \xi) d\xi. \quad (\text{B.33})$$

We combine (B.28), (B.26), and (B.10) with (B.33) and obtain

$$T_{ss}^*(r^*) \approx \frac{2\Omega J_0(\mu_1 r^*)}{\alpha_m^*(Bi^2 + \mu_1^2) J_0^2(\mu_1)} \int_0^{R_i} \xi J_0(\mu_1 \xi) d\xi. \quad (\text{B.34})$$

Next, we evaluate the integral in (B.34), substitute in (B.20) and obtain

$$T_{ss}^*(r^*) \approx \frac{2\Omega R_i J_1(\mu_1 R_i)}{(R_i^2 (A_i - 1) + 1) \mu_1 (Bi^2 + \mu_1^2) J_0^2(\mu_1)} J_0(\mu_1 r^*). \quad (\text{B.35})$$

We note that the dimensionless steady state temperature T_{ss}^* is directly proportional to Ω .

We explore the mean T_{ss}^* and the difference between T_{ss}^* at the centerline and at the inner wall (which we define as ΔT_{ss}^*) for Bi , A_i , and R_i relevant to the experimental device

described in the main text. We vary Bi between 0.001 and 0.1, A_i between 0.1 (thermal diffusivity of wall is dominant) and 2 (thermal diffusivity of PPM and electrolyte is dominant), and R_i between 0.05 (thick wall) and 0.95 (thin wall). See Table B.1 for nominal values of these parameters. We observe that for this range of Bi , A_i , and R_i , $(T_{ss} * Bi)/\Omega$ and $\Delta T_{ss} */ \Omega$ are roughly independent of Bi to within $< 7\%$ error over 3 orders of magnitude of $(T_{ss} * Bi)/\Omega$ and to within $< 5\%$ error for 6 orders of magnitude of $\Delta T_{ss} */ \Omega$. We plot mean $(T_{ss} * Bi)/\Omega$ and $\Delta T_{ss} */ \Omega$ as a function of A_i , and R_i in Figure B.4.

For a given Bi and Ω , the mean dimensionless temperature increases monotonically with decreasing wall thickness (increasing R_i). This is due to having a larger portion of the capillary dedicated to heat generation (occurring in the electrolyte solution) rather than passive conduction (occurring in the wall). For a given Bi and Ω , the mean dimensionless temperature also increases monotonically as the wall conduction becomes more dominant (decreasing A_i). This effect is strongest when the wall is thin and the electrolyte occupies larger portion of the capillary. This is due to having the thermal diffusivity of the electrolyte and PPM be low, therefore trapping the heat inside the PPM and electrolyte and so causing temperature there to be higher. The effect is strengthened when a larger portion of the capillary is dedicated to heat generation.

For a given Ω , the dimensionless temperature difference between the capillary center and the inner wall increases monotonically with increasing R_i . This is due to the increasing distance between the center and the inner wall and to having a larger portion of the capillary dedicated to heat generation. For a given Ω , the dimensionless temperature difference between the capillary center and the inner wall increases monotonically as the wall conduction becomes more dominant (decreasing A_i). This is due to having the thermal

diffusivity of the electrolyte and PPM be low, therefore trapping the heat inside the PPM and the electrolyte (trapping heat closer to the center) while the higher thermal diffusivity of the wall causes temperature at the inner surface of the wall to be lower.

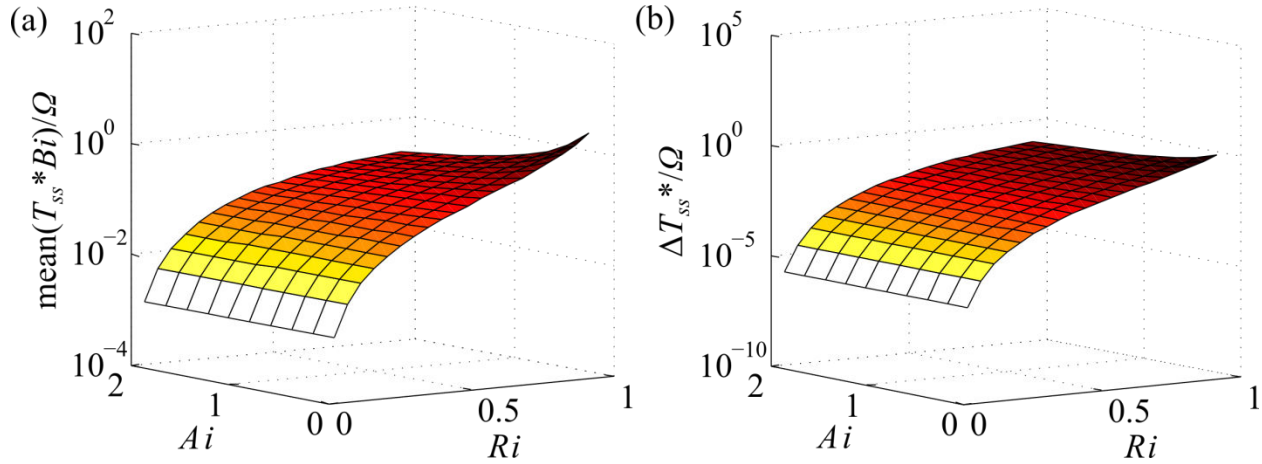


Figure B.4. Mean $(T_{ss} * Bi) / \Omega$ (a) and $\Delta T_{ss} * / \Omega$ (b) inside the capillary as a function of scaled internal thermal diffusivity, A_i (from 0.1 to 2), scaled inner capillary radius, R_i (from 0.05 to 0.95). Both $(T_{ss} * Bi) / \Omega$ and $\Delta T_{ss} * / \Omega$ increase with increasing R_i (and so increasing portion of capillary generating heat) and decreasing A_i (electrolyte and PPM trapping heat inside the capillary more effectively). Mean $(T_{ss} * Bi) / \Omega$ (a) and $\Delta T_{ss} * / \Omega$ (b) inside the capillary as a function of scaled internal thermal diffusivity, A_i (from 0.1 to 2), scaled inner capillary radius, R_i (from 0.05 to 0.95). Both $(T_{ss} * Bi) / \Omega$ and $\Delta T_{ss} * / \Omega$ increase with increasing R_i (and so increasing portion of capillary generating heat) and decreasing A_i (electrolyte and PPM trapping heat inside the capillary more effectively).

B.6.3 Capillary surface temperature measurements

Here we describe and discuss thermographic measurements of capillary surface temperature during capture and elution conditions. In these experiments, we filled the LE well, the capillary and PPM with LE (250 mM HCl, 500 mM Tris), and filled the TE well with TE (250 mM HEPES, 500 Tris) and applied a current of either 200 μ A (capture condition) or 800 μ A (elution condition). We monitored the surface temperature of the capillary in the vicinity of the PPM with a Fluke Ti10 uncooled microbolometer (160×120 array, 20 mm F# 0.8 lens). We plot radially averaged temperature as a function of capillary

axial coordinate and time in Figure B.5a and b for capture and elution conditions respectively.

We observe that the temperature in the TE is always greater than that in the LE. This is expected because LE conductivity is always higher than that of the TE. Mean temperature in the capillary scales proportionally with dimensionless heat generation parameter Ω , which in turn scales inversely with electrical conductivity of solution (see SI Sections B.6.1 and B.6.2). Since the affinity reaction occurs at the interface of LE and TE, the reaction temperature is roughly the average of the LE and TE temperatures. This makes the wash when the TE sweeps over the capture region more stringent as the TE temperature is higher than the reaction temperature, and therefore closer to the melting temperature of the affinity complex.

For the elution condition, the temperature adjacent to the porous affinity region is higher than that in free solution. We attribute this to the lower thermal diffusivity of the PPM solid than that of the electrolyte, making this region more insulative. Furthermore, the current through the free solution and the affinity region is the same (due to current continuity), while the resistance of the affinity region is higher (due to lower cross sectional area available to the electrolyte). Therefore, the heat generation inside the affinity region is higher than that in the free solution. Both of these factors contribute to the higher temperatures in the PPM compared to free solution. This effect becomes more prominent at higher heat generation rates.

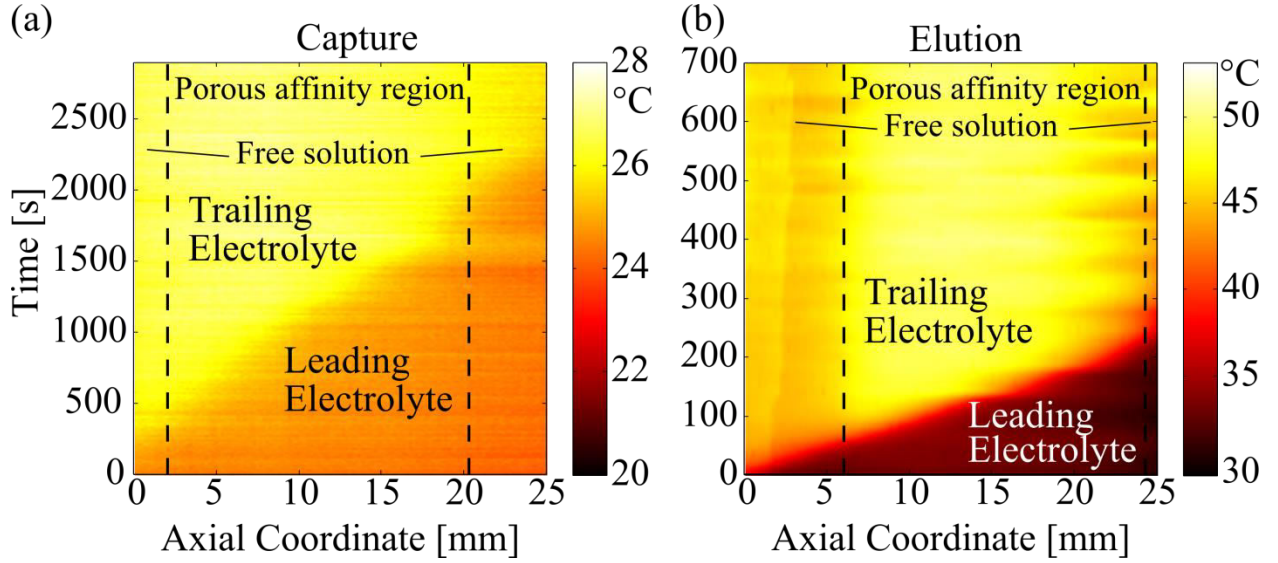


Figure B.5. Spatiotemporal plots showing radially averaged temperature in the TE and LE and in free solution and inside the porous affinity region under capture (a) and elution (b) conditions. We show the affinity region (18.3 mm long) bounded inside the black dashed lines. The temperature of the TE is higher than that of the LE, due to lower conductivity of the TE resulting in higher heat generation inside the TE (see SI Section B.6.2). For example, during capture, mean temperature in the TE was approximately 27°C, while that in the LE was 24°C. For the elution condition, the temperature adjacent to the porous affinity region is observably higher than that in free solution. (TE, free solution 45°C vs. TE, PPM 50°C; LE, free solution 33°C vs. LE, PPM 34°C). We attribute this to the relatively poor thermal diffusivity of the PPM solid compared to the electrolyte, thus trapping heat inside the porous affinity region (see Table B.1), as well as higher heat generation inside the PPM vs. free solution. This effect is more prominent at higher heat generation rates, hence a more noticeable temperature difference between free solution and PPM for the elution condition.

B.6.4 Optimal distance between affinity regions

Here we derive the relation for the recommended spacing of the affinity regions.

We begin with the distance necessary to separate the bound analyte from those continuing to travel in ITP. (see Figure B.7). If the affinity capture is done at optimal capture velocity (u_{95} , see Shkolnikov et al. [3]) this length is

$$l_0 \approx R_{ITP-AC} \sqrt{\frac{0.95}{0.05} \left(\frac{\mu_{L \text{ in LE}} \mu_{T \text{ in TE}}}{\mu_{L \text{ in LE}} - \mu_{T \text{ in TE}}} \right) \frac{k_B T}{e} \frac{p_z^*}{k_1 N}}, \quad (\text{B.36})$$

where k_B is the Boltzmann's constant, T is the absolute temperature, e is the electron charge, $\mu_{L \text{ in LE}}$ and $\mu_{T \text{ in TE}}$ are the mobilities of the LE ion in the LE and the TE ion in the TE respectively, p_z^* is the capture length (physical length to capture >95% of the target) normalized by advection-reaction length scale $u/(k_I N)$, where u is the advection velocity, k_I is the forward reaction rate constant, and N is the initial probe concentration. R_{ITP-AC} is the desired resolution for the separation. For more details see Shkolnikov et al. [3]. At the end of the affinity separation, the target is concentrated and bound to the leading edge of the PPM and other analytes are a distance l_0 downstream. During the elution the target has to catch up to the other analytes moving at ITP velocity. Hence, at the time where the target catches up with the rest of the analytes, t_c , it traverses a length

$$l_c = u_{t \text{ in TE}} (t_c - \tau_{el}), \quad (\text{B.37})$$

where $u_{t \text{ in TE}}$ is the velocity of the target in TE, and τ_{el} is the time constant of elution (see discussion section of the main text). We assume that during this elution time τ_{el} that the target is roughly immobile. During t_c , the LE-TE interface traverses a length

$$l_c = u_{ITP} t_c + l_0. \quad (\text{B.38})$$

We further assume that the temperature of the TE inside the PPM affinity region is uniform, and hence the reaction conditions are roughly uniform inside the PPM, and so all of the captured target has roughly the same elution time. See SI Section B.6.3 for radial temperature distribution inside the PPM and ways to make this temperature more uniform. Next, we assume that the affinity regions are within the same contiguous PPM and that neither the analytes focused in ITP nor the target go through an area change in the channel

(i.e, there is no change in current density). Hence, $u_{t \text{ in TE}} = \mu_{t \text{ in TE}} E_{TE}$ and $u_{ITP} = \mu_{T \text{ in TE}} E_{TE}$ where E_{TE} is the electric field in the TE (assumed to be uniform) and $\mu_{t \text{ in TE}}$ is the mobility of the target in the TE. Combining this with equations (B.37) and (B.38), we obtain

$$l_c = \frac{\mu_{t \text{ in TE}} (l_0 + u_{ITP} \tau_{el})}{\mu_{t \text{ in TE}} - \mu_{T \text{ in TE}}} \quad (\text{B.39})$$

Next, we combine (B.39) and (B.36) and that $p_z^* = 2.8$ when the affinity region is not saturated (most common operating condition) [3] and obtain

$$l_c \approx R_{ITP-AC} \frac{\mu_{t \text{ in TE}}}{\mu_{t \text{ in TE}} - \mu_{T \text{ in TE}}} \sqrt{\frac{0.95}{0.05} \left(\frac{\mu_{L \text{ in LE}} \mu_{T \text{ in TE}}}{\mu_{L \text{ in LE}} - \mu_{T \text{ in TE}}} \right) \frac{k_B T}{e} \frac{2.8}{k_1 N}} + \frac{\mu_{t \text{ in TE}} u_{ITP} \tau_{el}}{\mu_{t \text{ in TE}} - \mu_{T \text{ in TE}}}. \quad (\text{B.40})$$

The first term on the right in (B.40) is associated with the time to separate the target from the background species focused in ITP. The second term on the right in (B.40) is associated with the time scale of elution of the target. This result suggests that to decrease l_c one should choose a probe with a high forward reaction constant, k_l , to the target, have a large probe concentration, and choose a lower mobility TE. Furthermore, if this length is dominated by the elution time, one should elute at a lower ITP velocity.

For our experimental conditions $\mu_{L \text{ in LE}} \approx -60 \times 10^{-9} \text{ m}^2 \text{V}^{-1} \text{s}^{-1}$, $\mu_{T \text{ in TE}} \approx -13 \times 10^{-9} \text{ m}^2 \text{V}^{-1} \text{s}^{-1}$, $\mu_{t \text{ in TE}} \approx -25 \times 10^{-9} \text{ m}^2 \text{V}^{-1} \text{s}^{-1}$, $k_l = 10^3 \text{ M}^{-1} \text{s}^{-1}$, $N \approx 30 \text{ } \mu\text{M}$ [8], $\sigma_{TE} = 0.43 \text{ S/m}$, $j = 5090 \text{ A/m}^2$, $\tau_{el} \approx 10 \text{ s}$. We chose R_{ITP-AC} of 4, for sufficient separation between the target and background. We estimate that for our experiments, first term on the right in (B.40) is equal to 7 mm and the second term is equal to 3 mm. Therefore, the time to separate the target from the background species dominates the l_c . We recommend that the spacing

between the leading edges of affinity regions to be roughly equal to l_c . In our experiments we made the distance between the leading edges of the affinity regions in our device to be 10 mm.

B.6.5 Image of custom built capillary setup with two affinity regions

We performed ITP-AC experiments in a custom built capillary setup (shown in Figure B.6), which interfaced LE, sample, and TE reservoirs to the capillary with multiple PPMs. The block containing the sample and TE reservoirs was fabricated via stereolithography (FineLine Prototyping, Raleigh, NC) from WaterShed XC 11122 and fitted with 1/4-28 female threads to mate to 1/4-28 nut and ferrule from IDEX Health & Science (Oak Harbor, WA). The LE reservoir consisted of a IDEX Health & Science 90 degree bend fitting (female to female threads). The volumes of TE, sample, and LE reservoirs were 200 μ l, 25 μ l, and 200 μ l respectively. The capillary outer diameter was 1 mm. Custom machined acrylic brackets and platform served to secure reservoirs and electrodes in place during experiments. We aimed to keep the area around the capillary free from obstruction as to not impede natural convective cooling of the capillary.

The 500 μ m inner diameter capillary had 2 5-6 mm long GMA-EDMA PPM structures polymerized inside of it. The PPMs were covalently attached to the capillary wall. We functionalized the surface of each the PPM with DNA probe complimentary to different regions of the target. (See Materials and Methods section of the main text and SI Section B.6.6 for more information on the probes and target). To perform sequential ITP-AC, we applied current to the capillary using platinum electrodes dipped into LE and TE reservoirs.

B.6.6 Synthetic DNA oligo sequences used

Here we report properties of DNA oligo probes and target used in our experiments. We calculated ΔG , T_m , and sequence secondary structure and hybrid structure using mFold (State University of New York at Albany) [153] at the conditions indicated. While the solution composition is not the same as that used in our ITP-AC experiments, the solution ionic strength is matched as closely as possible.

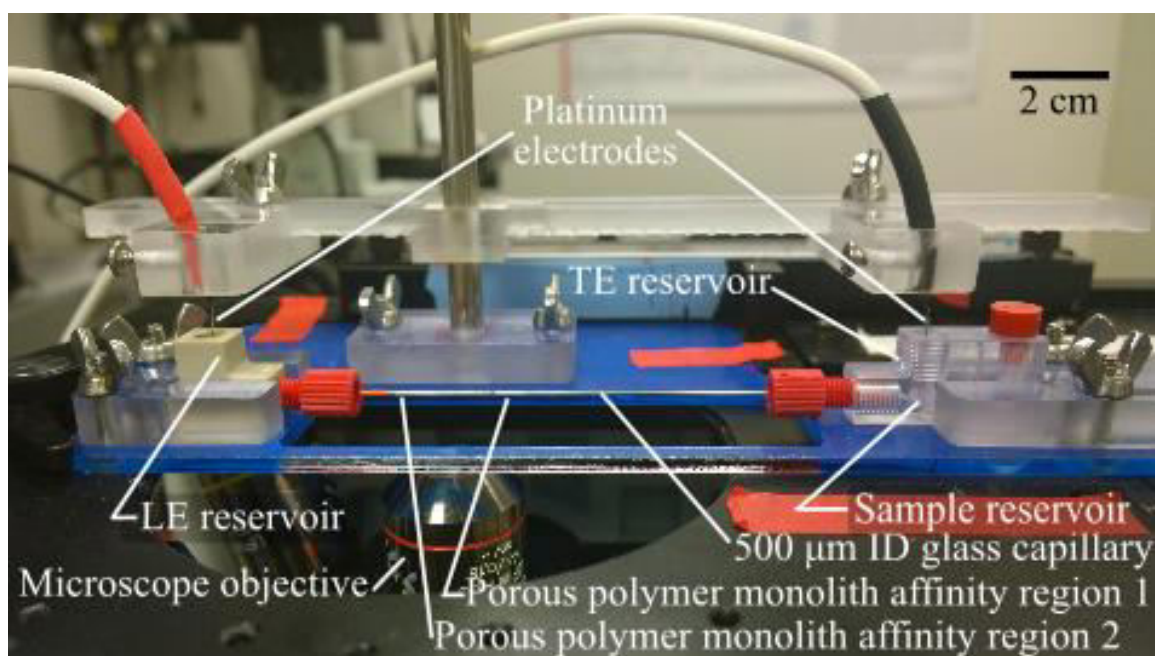


Figure B.6. Image of custom-built capillary setup consisting of LE reservoir, 500 μm inner diameter borosilicate glass capillary with two GMA-EDMA PPM for the two ARs, and a block containing sample reservoir and TE reservoir. Platinum electrodes were dipped into the LE and TE reservoirs to apply current through the capillary.

Target sequence:

Sequence: 5'- CCT CTA TTG TTG GAT CAT ATT CGT CCA CAA AAT GAT TCT GAA
TTA GCT GTA TCG TCA AGG CAC TCT TGC CTA CGC CAC CAG CTC
CAA CTA CCA CAA *GTT TAT ATT CAG TCA T* -3'

Regions: *italics* - probe 1, underline - probe 2.

Modification: 5' Cy5

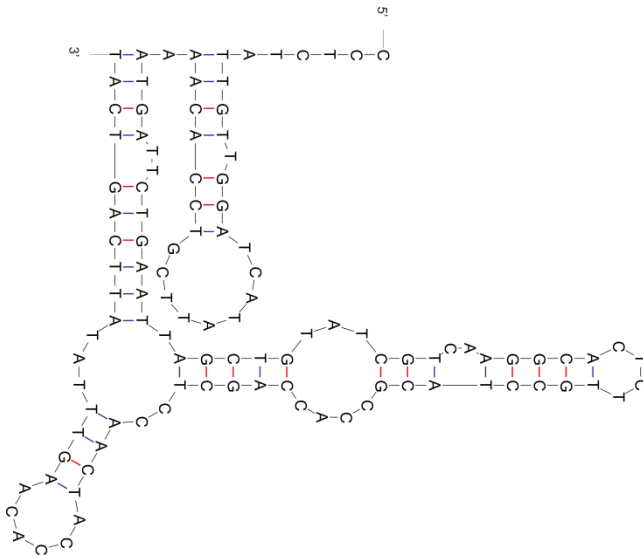
ΔG_{self}
(kcal/mol)

-16.7

$T_{m self}$ (°C)

42.7

Secondary
structure



ΔG_{probe1}
(kcal/mol)

-38.1

$T_{m Probe1}$ (°C)

59.3

ΔG_{probe2}
(kcal/mol)

-42.3

$T_{m Probe2}$ (°C)

68.5

Calculation
conditions

Temperature (°C)
20

Na⁺ concentration (M)
0.2

Mg²⁺ concentration (M)
0

Probe 1 sequence:

Sequence: 5'- ATGACTGAATATAAACTTGTGGTAGTTGG -3'

Modification: 5' C12-amine

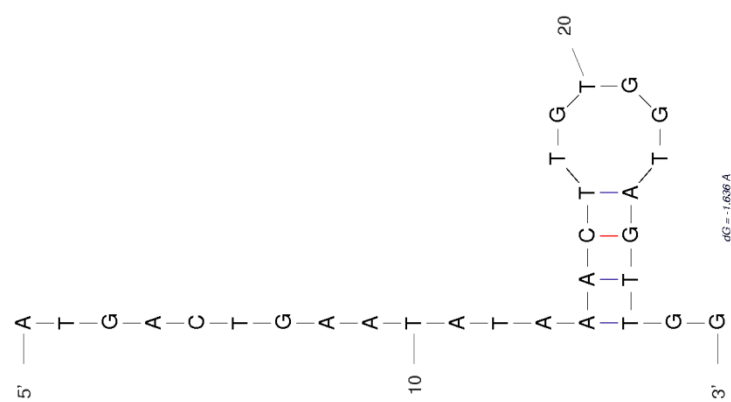
ΔG_{self}
(kcal/mol)

-1.6

$T_{m self}$ (°C)

40.0

Secondary structure



Calculation conditions	Temperature (°C)	Na ⁺ (M)	concentration	Mg ²⁺ concentration (M)
	20	0.2		0

Probe 2 sequence:

Sequence: 5'- TGGTAGTTGGAGCTGGTGGCGTAGGC -3'

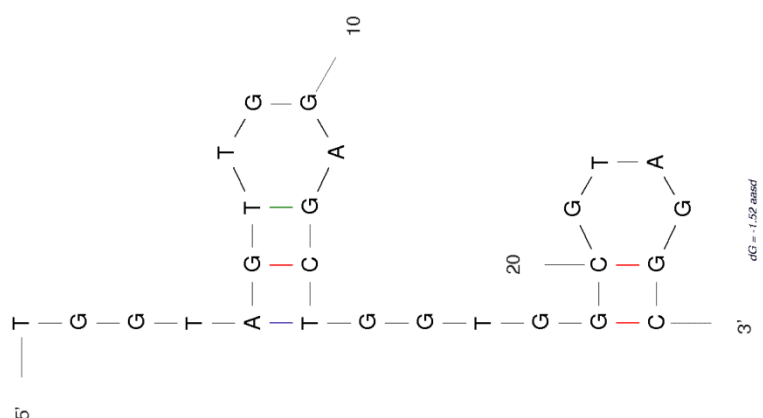
Modification: 5' C12-amine

ΔG_{self} -1.5

(kcal/mol)

$T_{m self}$ (°C) 32.2

Secondary structure



Calculation conditions	Temperature (°C)	Na ⁺ concentration (M)	Mg ²⁺ concentration (M)
	20	0.2	0

B.6.7 Spatiotemporal behavior of target during capture and elution

Here we provide some additional information regarding the experiments described in the discussion section of the main text. In those experiments we extracted 112 nt Cy5 labeled target from 25% sucrose solution placed in the sample chamber using 250 mM HCl with 500 mM Tris as the LE and 250 mM HEPES with 500 mM Tris as the TE. We captured the target twice, using two affinity regions in series. We used capture current of 200 μA and elution current of 800 μA for both affinity regions. In Figure B.7 we show a spatiotemporal plots of the target reacting with the immobilized probe in the PPM affinity regions 1 and 2. We plot the cross-sectional area averaged Cy5 fluorescence intensity as a function of distance along the axial coordinate of the capillary and time. The origin of the axial coordinate corresponds with the leading edge of the PPM. Figure B.7a shows that as the target enters the AR1 with capture current of 200 μA , about 30% of the target is immediately captured and persists on the affinity region. The rest continues to migrate focused in ITP. The capture length is roughly 0.3 mm, corresponding to a forward rate constant of $5 \times 10^3 \text{ M}^{-1} \text{ s}^{-1}$ ($u = 18 \text{ }\mu\text{m/s}$, $N = 30 \text{ }\mu\text{M}$) [3]. Once we switch the current from capture current to elution current of 800 μA at 270 s, the target begins to quickly elute. Over 95% of the target is eluted. The target then catches up with the portion of the target that was not captured (not shown). Figure B.7b shows the refocused target entering AR 2 again with a capture current of 200 μA . This AR captures roughly 85% of the target and the rest of the target continues to migrate focused in ITP. The capture length is roughly 1 mm, corresponding to a forward rate constant of $1 \times 10^3 \text{ M}^{-1} \text{ s}^{-1}$ ($u = 12 \text{ }\mu\text{m/s}$, $N = 30 \text{ }\mu\text{M}$) [3]. Once we switch the current from capture current to elution current of 800 μA again, at 490 s, the target begins to quickly elute and over 95% of the target is again eluted.

We estimate the advection time scale for elution as the time the target has to traverse the capture length at the velocity of the target in the TE. We estimate the velocity of DNA in our TE during elution to be 300 $\mu\text{m/s}$ ($\mu_{DNA \text{ in TE}} = -25 \times 10^{-9} \text{ m}^2 \text{ V}^{-1} \text{ s}^{-1}$, $\sigma_{TE} = 0.43 \text{ S/m}$). Therefore the advection timescale of elution is 1 s and 3 s for AR1 and AR2 respectively. We compare this timescale to the timescale for TE temperature to reach steady state (24 s, see SI Section B.6.3) and the observed timescale of elution (15 s and 11 s for AR1 and AR2 respectively, see Discussion section of main text). We hence note that in our

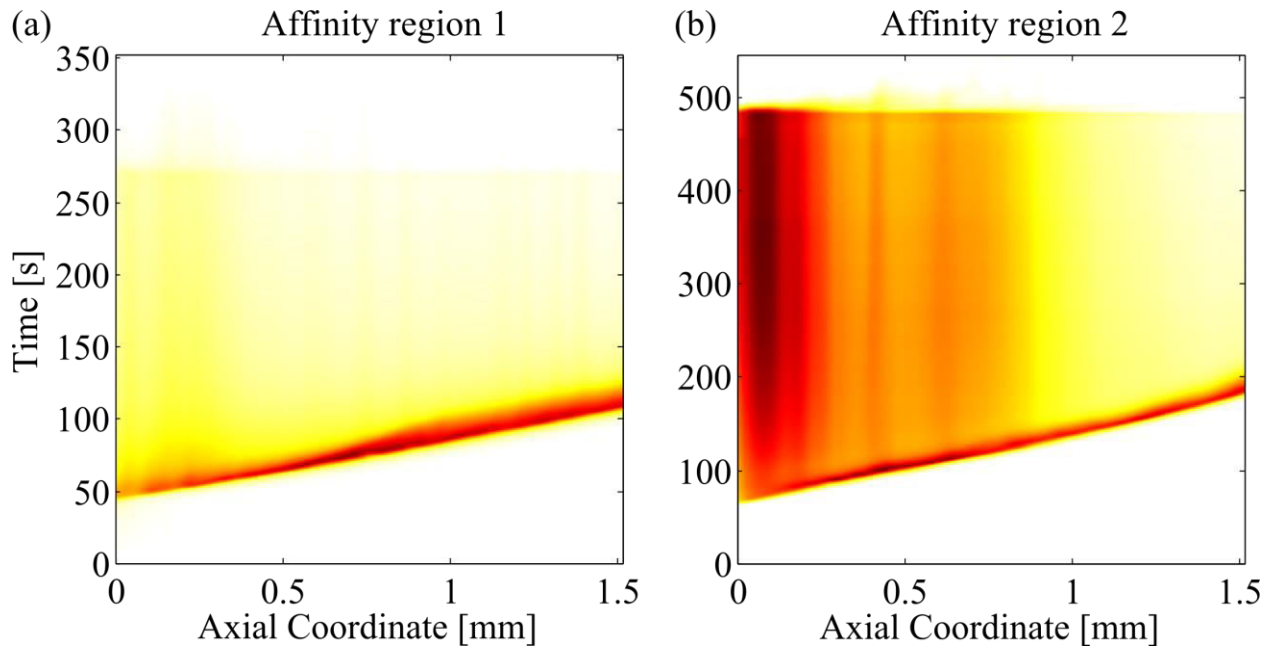


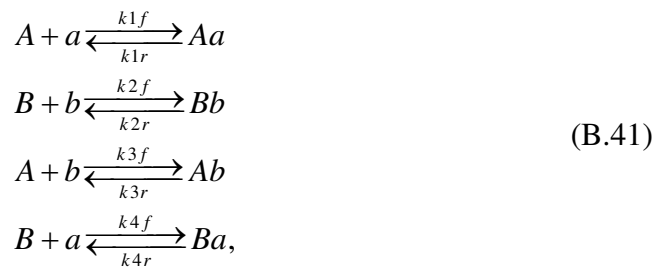
Figure B.7. Spatiotemporal plots showing Cy5 labeled target capture and elution inside affinity regions 1 and 2 (origin of axial coordinate is the leading edge of the affinity region). Intensity is proportional to the concentration of Cy5 labeled target. The target focused in ITP under capture current (200 μA) enters the AR, and a large portion of the target complementary to the immobilized affinity probe is captured and becomes immobile ($\sim 30\%$ for AR1, 85% for AR2). The rest of the target continues to migrate focused in ITP. This cleanly separates the target components, with a resolution increasing linearly with time [3]. We then elute the captured portion of the target (at 270 s for AR1, 490 s AR2) by increasing the current to an elution current of 800 μA . Upon application of higher current the temperature inside the column increases (see SI Sections SI 3-5) beyond the melting temperature of the target-probe hybrid, melting off the target. The observed target fluorescence intensity near the leading edge quickly decreases (time constant: 15 s for AR1, 11 s for AR2, see Figure B.2, main text) and over 95% of the target is eluted. The target then quickly migrates through the TE and catches up with the LE-TE interface, ready to repeat the capture and elution processes.

experiments the time scale of elution is governed by temperature change and/or reaction and not by target advection.

B.6.8 Performance metrics of serial-recycling and traditional parallel

affinity assays

Here we compare key assay performance metrics including sensitivity, false positive rate, specificity, precision, and diagnostic odds ratio for traditional parallel affinity assay (e.g., microarrays) and our serial affinity assay with analyte recycling. For the purposes of this simple comparison we analyze affinity reactions of only two species A and B and their corresponding affinity probes a and b. We assume that the reactions between the analytes themselves are negligible and the analytes only react with the probe ligands. For the purposes of a simple comparison, we also assume that the reactions are carried out to equilibrium in a well mixed reactor. For the parallel reactions case we have the following reactions:



where k_f indicates a forward reaction constant, k_r indicates a reverse reaction constant and the number in the subscript of reaction constant corresponds to the reaction number. We model this system of reactions as a second order system of reversible reactions:

$$\begin{aligned}
\frac{dc_{Aa}}{dt} &= k_{1f}c_Ac_a - k_{1r}c_{Aa} \\
\frac{dc_{Bb}}{dt} &= k_{1f}c_Bc_b - k_{1r}c_{Bb} \\
\frac{dc_{Ab}}{dt} &= k_{1f}c_Ac_b - k_{1r}c_{Ab} \\
\frac{dc_{Ba}}{dt} &= k_{1f}c_Bc_a - k_{1r}c_{Ba},
\end{aligned} \tag{B.42}$$

with the initial condition that at $t = 0$, $c_A = c_{A0}$, $c_B = c_{B0}$, $c_a = c_{a0}$, $c_b = c_{b0}$. At equilibrium time derivatives of concentrations in (B.42) are equal to zero. Furthermore, we consider a case where the probes are in excess, i.e., where probes cannot be saturated, causing unreliable measurements. Therefore, we assume that the concentration of probe at equilibrium is approximately the same as initially. Therefore at equilibrium

$$\begin{aligned}
0 &= k_{1f}c_Ac_{a0} - k_{1r}c_{Aa} \\
0 &= k_{1f}c_Bc_{b0} - k_{1r}c_{Bb} \\
0 &= k_{1f}c_Ac_{b0} - k_{1r}c_{Ab} \\
0 &= k_{1f}c_Bc_{a0} - k_{1r}c_{Ba}.
\end{aligned} \tag{B.43}$$

Furthermore, we obtain the following auxiliary equations from conservation of species:

$$\begin{aligned}
c_{A0} &= c_A + c_{Aa} + c_{Ab} \\
c_{B0} &= c_B + c_{Ba} + c_{Bb}.
\end{aligned} \tag{B.44}$$

We solve the system of algebraic equations (B.43) and (B.44) and obtain that at equilibrium

$$\begin{aligned}
c_{Aa} &= \frac{c_{A0}c_{a0}k_1}{c_{a0}k_1 + c_{b0}k_3 + 1} \\
c_{Bb} &= \frac{c_{B0}c_{b0}k_2}{c_{a0}k_4 + c_{b0}k_2 + 1} \\
c_{Ab} &= \frac{c_{A0}c_{b0}k_3}{c_{a0}k_1 + c_{b0}k_3 + 1} \\
c_{Ba} &= \frac{c_{B0}c_{a0}k_4}{c_{a0}k_4 + c_{b0}k_2 + 1},
\end{aligned} \tag{B.45}$$

where k are the association constants associated with the reaction numbered in the subscript. Next, we define for probe region a true positives (TP), false positives (FP), false negatives (FN) and true negatives (TN) in the usual way [208] as

$$\begin{aligned}
TP &= c_{Aa} \\
FP &= c_{Ba} \\
FN &= c_{A0} - c_{Aa} \\
TN &= c_{B0} - c_{Ba}.
\end{aligned} \tag{B.46}$$

We calculate the sensitivity or true positive rate (TPR), false positive rate (FPR), specificity or true negative rate (TNR), precision or positive predictive value (PPV), and the diagnostic odds ratio (DOR) [208]:

$$TPR = \frac{c_{a0}k_1}{c_{a0}k_1 + c_{b0}k_3 + 1}, \tag{B.47}$$

$$FPR = \frac{c_{a0}k_4}{c_{a0}k_4 + c_{b0}k_2 + 1}, \tag{B.48}$$

$$TNR = \frac{c_{b0}k_2 + 1}{c_{a0}k_4 + c_{b0}k_2 + 1}, \tag{B.49}$$

$$PPV = \frac{c_{A0}k_1(c_{a0}k_4 + c_{b0}k_2 + 1)}{c_{A0}k_1 + c_{B0}k_4 + c_{A0}c_{a0}k_1k_4 + c_{A0}c_{b0}k_1k_2 + c_{B0}c_{a0}k_1k_4 + c_{B0}c_{b0}k_3k_4},$$

(B.50)

$$DOR = \frac{k_1(k_2 + 1/c_{b0})}{k_4(k_3 + 1/c_{b0})}. \quad (B.51)$$

Next, we make the assumption that all the probes in the array initially are at the same concentration (i.e., $c_{a0} = c_{b0}$) and simplify equations (B.47) through (B.51)

$$TPR = \frac{k_1}{k_1 + k_3 + 1/c_{a0}} \quad (B.52)$$

$$FPR = \frac{k_4}{k_4 + k_2 + 1/c_{a0}}. \quad (B.53)$$

$$TNR = \frac{k_2 + 1/c_{a0}}{k_4 + k_2 + 1/c_{a0}} \quad (B.54)$$

$$PPV = \frac{c_{A0}k_1(k_4 + k_2 + 1/c_{a0})}{(c_{A0}/c_{a0})k_1 + (c_{B0}/c_{a0})k_4 + c_{A0}(k_1k_4 + k_1k_2) + c_{B0}(k_1k_4 + k_3k_4)} \quad (B.55)$$

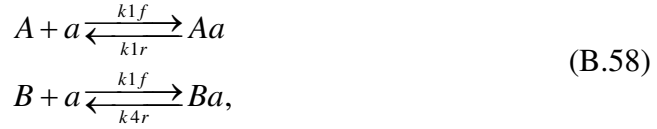
$$DOR = \frac{k_1(k_2 + 1/c_{a0})}{k_4(k_3 + 1/c_{a0})}. \quad (B.56)$$

We can combine (B.52) and (B.53) and also obtain that

$$TPR = \frac{k_1}{k_1 - k_2 + k_3 - k_4 + k_4/FPR}. \quad (B.57)$$

Next we perform similar analysis with the serial affinity reactions with analyte recycling.

For the serial reactions case, we have the following reactions at the affinity region a



and then later at the affinity region b



However, due to the recycling of analytes, in both regions the initial condition (corresponding to the target entering the region) is $c_A = c_{A0}$, $c_B = c_{B0}$, $c_a = c_{a0}$, $c_b = c_{b0}$.

Therefore, for region a, at equilibrium, with probes in excess the reactions equations simplify to

$$\begin{aligned}
0 &= k_{1f}c_Ac_{a0} - k_{1r}c_{Aa} \\
0 &= k_{4f}c_Bc_{a0} - k_{4r}c_{Ba}.
\end{aligned}
\tag{B.60}$$

For region a, the conservation of species requires that

$$\begin{aligned}
c_{A0} &= c_A + c_{Aa} \\
c_{B0} &= c_B + c_{Ba}.
\end{aligned}
\tag{B.61}$$

Solving equations (B.60) and (B.61) we obtain that at equilibrium

$$\begin{aligned}
c_{Aa} &= \frac{c_{A0}c_{a0}k_1}{c_{a0}k_1 + 1} \\
c_{Ba} &= \frac{c_{B0}c_{a0}k_4}{c_{a0}k_4 + 1}.
\end{aligned}
\tag{B.62}$$

We again calculate the TPR, FPR, TNR, PPV, and the DOR:

$$TPR = \frac{c_{a0}k_1}{c_{a0}k_1 + 1}, \quad (B.63)$$

$$FPR = \frac{c_{a0}k_4}{c_{a0}k_4 + 1}, \quad (B.64)$$

$$TNR = \frac{1}{c_{a0}k_4 + 1}, \quad (B.65)$$

$$PPV = \frac{c_{A0}k_1(c_{a0}k_4 + 1)}{c_{A0}k_1 + c_{B0}k_4 + c_{A0}c_{a0}k_1k_4 + c_{B0}c_{a0}k_1k_4}, \quad (B.66)$$

$$DOR = k_1/k_4. \quad (B.67)$$

We can combine (B.63) and (B.64) and also obtain

$$TPR = \frac{k_1}{k_1 - k_4 + k_4/FPR}. \quad (B.68)$$

We observe the sensitivity or TPR for our serial case is higher than that for the parallel case due to absence of reactions with competing probes in the serial case. However, the FPR for the serial case is also higher than that for the parallel case, again due to the absence of reactions with competing probes in the serial case. Comparing TPR for a given FPR (as in the receiver operating characteristic (ROC) curve), we assume reactions with the correct probe have approximately the same association constants (i.e., $k_1 \approx k_2$) and reactions with the incorrect probe also have approximately same association constants (i.e., $k_3 \approx k_4$). In this case, the TPR for a given FPR is higher in the parallel case. However, if the reactions with the correct probe have widely differing association constants (e.g., $k_1 \gg k_2$) and reactions with the incorrect probe also have widely differing association

constants (e.g., $k_3 \ll k_4$) then TPR for a given FPR for both serial and parallel cases is approximately the same. Therefore, the ROC for the parallel case is either the same or slightly better than for the serial case.

To compare the specificity or TNR we note that typically $k_2 \gg 1/c_{a0}$ (e.g., $k_2 = 10^9 \text{ M}^{-1}$ *versus* $1/c_{a0} = 10^5 \text{ M}^{-1}$ [8]) and assume that $k_4 \approx 1/c_{a0}$. In this case, the TPR for the parallel case is higher than that for the serial case, due to the presence of reactions with competing probes in the parallel case.

To compare precision, or PPV we assume the initial concentrations of the targets are approximately the same (i.e., $c_{A0} \approx c_{B0}$), $k_2 \gg 1/c_{a0}$, and $k_4 \approx 1/c_{a0}$. In this case, the PPV for the parallel case is higher than that for the serial case, again due to the presence of reactions with competing probes in the parallel case.

To compare DOR, we again assume $k_2 \gg 1/c_{a0}$, but also assume $k_3 \gg 1/c_{a0}$. In this case for the parallel case the DOR scales as the product of the ratios of association constants for the correct probe to incorrect target. While for the serial case, DOR scales as just the ratio of association constants for the correct probe to incorrect target for the particular probe. Therefore, the DOR is higher for the parallel case.

We observe that the sensitivity of serial reactions is higher than parallel reactions. However, the absence of competing reactions in the serial case leads to lower ROC, specificity, precision, and DOR for the serial case compared to the parallel case, when the reaction association constants are the same for both cases. Nevertheless, while our serial reaction case with recycling offers precise temperature control for each reaction, the traditional parallel case does not. Therefore, in the serial case, association constants can be

more precisely tuned to maximize the ratio of affinity constants for the correct probe to incorrect target. By increasing this ratio, serial reactions with recycling may achieve comparable or better ROC, specificity, precision, and DOR than the parallel case, while at the same time, having significantly higher sensitivity.

C. Practical guidelines for PPM synthesis and functionalization

In this appendix, we specifically provide practical guidelines for synthesis and functionalization of PPMs used in Chapters 3, 4 and Appendix A and B. We also provide tips useful to synthesis of PPM used in Chapter 2 in Sections C.2 and C.5 of this appendix.

C.1 Materials

Table C.1. Materials for PPM synthesis and functionalization

Material	Product number	Vendor
Glycidyl methacrylate (100 g)	151238	Sigma-Aldrich
Hydroxyethyl methacrylate (100 ml)	477028	Sigma-Aldrich
Ethylene glycol dimethylacrylate (100 ml)	335681	Sigma-Aldrich
n-Hexane (1 L)	39199	Alfa Aesar
Methanol (4 L)	34860	Sigma-Aldrich
Azobisisobutyronitrile (25 g)	441090	Sigma-Aldrich
Inhibitor removal media (250 g)	311332	Sigma-Aldrich
Pasteur pipette, 5.75 in	14673-010	VWR
Cotton sponge	442308	Fisher Scientific
3-(trimethoxysilyl)propyl methacrylate (100 ml)	440159	Sigma-Aldrich
Acetone (4 L)	179124	Sigma-Aldrich
Glass capillaries (250)	53432-728	VWR
Polyethylene tubing (1 pack)	427-425	Intreamedic / BD
Sodium dodecyl sulfate (25 g)	436143	Sigma-Aldrich
SSC Buffer 20x (500 ml)	AM9770	Life Technologies
DNA oligos (40 ng)	-	IDTdna
NMR disposable tubes (25 tubes)	K8971930000	Fisher Scientific
Sodium hydrosulfide (100 g)	161527	Sigma-Aldrich
Sodium phosphate dibasic (100 g)	S9390	Sigma-Aldrich
Phosphoric acid (100 g)	P5811	Sigma-Aldrich
Sulfuric acid (500 ml)	320501	Sigma-Aldrich
N-gamma-maleimidobutyl-oxysuccinimide	22309	ThermoFisher
Dimethylformamide (250 ml)	D4551	Sigma-Aldrich
Absolute ethanol (500 ml)	E7023	Sigma-Aldrich
Phosphate buffered saline tablets (100 tabs)	P4417	Sigma-Aldrich
Streptavidin (1 mg)	S0677	Sigma-Aldrich
Biotin (5-fluorescein) conjugate (1 mg)	53608	Sigma-Aldrich

C.2 Preparation of polymerization solution

1. Obtain monomer, crosslinker (crosslinking monomer), porogen solvents and initiator. We obtained all materials from Sigma-Aldrich, unless we specified otherwise (see **Table C.1**).
2. Remove polymerization inhibitors from the monomers. Monomers arrive from the manufacturer with polymerization inhibitors to prevent spontaneous polymerization and prolong monomer shelf life. We performed this by passing the monomer solutions through a packed column of inhibitor removal media, at a flow rate of roughly 0.1 ml/min. Inhibitor removal media (Sigma Aldrich product number: 311332 – CAS# 9003-70-7) consists of 0.5-1 mm white spherical beads. We prepared the inhibitor removal column and purified the monomers as follows:
 - a. We obtained a borosilicate glass Pasteur pipette 5.75 in size, standard tip (VWR 14673-010).
 - b. We stuffed a 5 x 5 mm square of cotton sponge (Kendall All Purpose Sponges 9092, 4 ply, Tyco Healthcare Group, Princeton, New Jersey, USA) into the neck of the pipette to serve as a frit to catch the inhibitor removal beads (see Figure C.1, Step 1).
 - c. We then filled the pipette 3/4 of the length of the main body with inhibitor removal beads. Note that these beads easily acquire static charge, which may make the filling difficult (Figure C.1, Step 2).
 - d. We then stuffed a 5 x 5 mm square of cotton sponge on top of the packed beads, to ensure that the beads stay packed (Figure C.1, Step 2).

- e. We applied liquid monomers to the space above the packed beads (Figure C.1, Step 3). We then would place a pipette bulb on the pipette and apply gentle pressure to ensure a roughly 0.1 ml/min flow rate of monomer liquid through the column (Figure C.1, Step 4).
 - f. We collected the purified monomer liquid into 20 ml glass scintillation vials (Figure C.1, Step 4).
 - g. We stored the purified monomers at -20°C.
3. Mix together appropriate volumes of room temperature porogen solvents. The solvents should be at room temperature to ensure that a consistent mass of solvents are mixed together each time.
 4. Then, mix together appropriate volumes of room temperature monomers.
 5. Weigh appropriate amount of initiator and then add to this vial appropriate amount of the porogen mixture, followed by an appropriate amount of monomer mixture. Note that the surface tension of typical porogen solvents and monomers is lower than that of water, therefore pipetting these liquids may be difficult. Extra care should be taken to pipette these consistently.
 6. Perform polymerization with the polymerization solution. Note, for consistent results polymerization solution should be at room temperature when starting the polymerization. As described in the main text of this thesis, temperature has a strong effect on initiator decomposition rate and thermodynamic properties of the porogen solvents and monomers, and hence a strong effect on the properties of the resulting monolith. Store the polymerization solution.
 7. The polymerization solution can be stored at -20°C in the dark for up to 3 months.

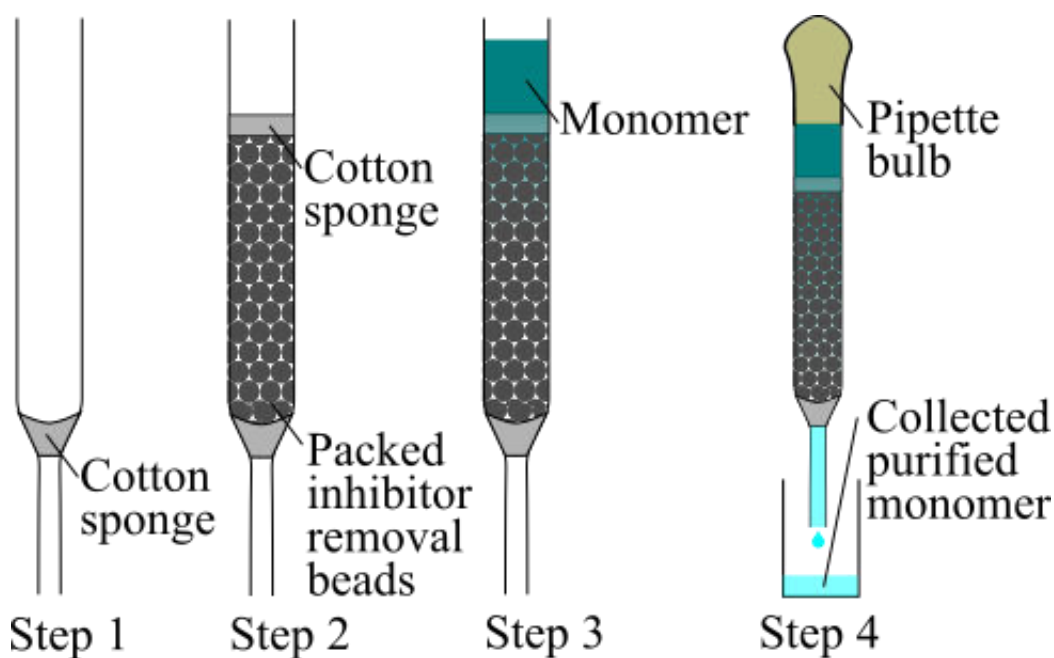


Figure C.1. Schematic showing preparation of the inhibitor removal column and purification of monomers. Step 1: Pack a small piece of a cotton sponge into the neck of a 5.75 in Pasteur pipette. Step 2: Fill the three-fourths of the pipette body with inhibitor removal beads and place a small piece of a cotton sponge on top of the beads. Step 3: Apply monomer solution to the column. Step 4: Use a pipette bulb to apply gentle pressure and flow the monomer solution through the column.

C.3 Vinylizing glass surfaces

We vinylized glass surfaces to ensure that the PPM formed inside a channel firmly, covalently adhered to the glass wall, thus avoiding channeling near the wall. To vinylize glass surfaces:

1. Prepare a solution of 30% (v/v) 3-(trimethoxysilyl)propyl methacrylate (TSPM, CAS No. 2530-85-0), 70% (v/v) acetone. TSPM is air-sensitive and so we recommend transferring TSPM using the cannula transfer method:
 - a. Place a cannula (or a thin hollow metal tube) between the septum of the TSPM bottle and the septum of a flask with dry acetone. TSPM bottle is

sold with a septum. We recommend dipping the end of the cannula into the acetone on the acetone flask end, and into the TSPM on the TSPM end.

- b. Place a pressure relief syringe with a needle into the septum of the acetone flask.
 - c. Place a needle leading to a pressurized dry nitrogen line into the TSPM septum.
 - d. Carefully turn on the nitrogen pressure, observing the pressure relief syringe on the acetone flask. The gas volume change in the syringe corresponds to the volume of added TSPM.
 - e. Once the desired volume of TSPM flowed into the acetone flask, turn off the nitrogen pressure. Remove the cannula from both septa, and then remove the pressure relief syringe and the nitrogen line from the acetone flask and TSPM bottle respectively.
 - f. The TSPM – acetone solution can be stored for at least a 1 yr at -20°C.
2. To vinylize a glass surface, place the surface into the TSPM – acetone solution for 24 hr at room temperature.
 3. Prior to performing polymerization in the glass vessel, flush the glass surface with air.

C.4 Custom-built UV polymerization setup

We performed UV polymerization in a custom-built UV polymerization setup (Figure C.2). The setup consisted of a 12 W, ~405 nm peak wavelength UV LED panel, a timer, a stage for the capillaries, and a polished aluminum plate (mirror). UV LED panel was a Chauvet LED Shadow Three-Channel DMX-512 LED UV Blacklight, (Chauvet,

Sunrise, FL). We found this LED panel superior to fluorescent tube type UV sources typically found in commercial UV chambers. Unlike fluorescent tube sources this LED panel did not flicker, and provided spatially uniform, steady (less than 5% variation in UV light intensity) for over 2 hr. Based on this experience, we strongly recommend UV LED illumination over fluorescent tube illumination for PPM synthesis, as UV flux strongly controls nucleation rate during polymerization (as described in the main text of this thesis) and has a strong effect on monolith properties. Furthermore, this UV panel allowed for direct and computer control of its light intensity, allowing for varying UV flux during polymerization, an area for potential future investigation. We controlled the timing of the UV LED panel with a Tork 454D timer (Tork, Mount Vernon, NY) using the countdown mode.

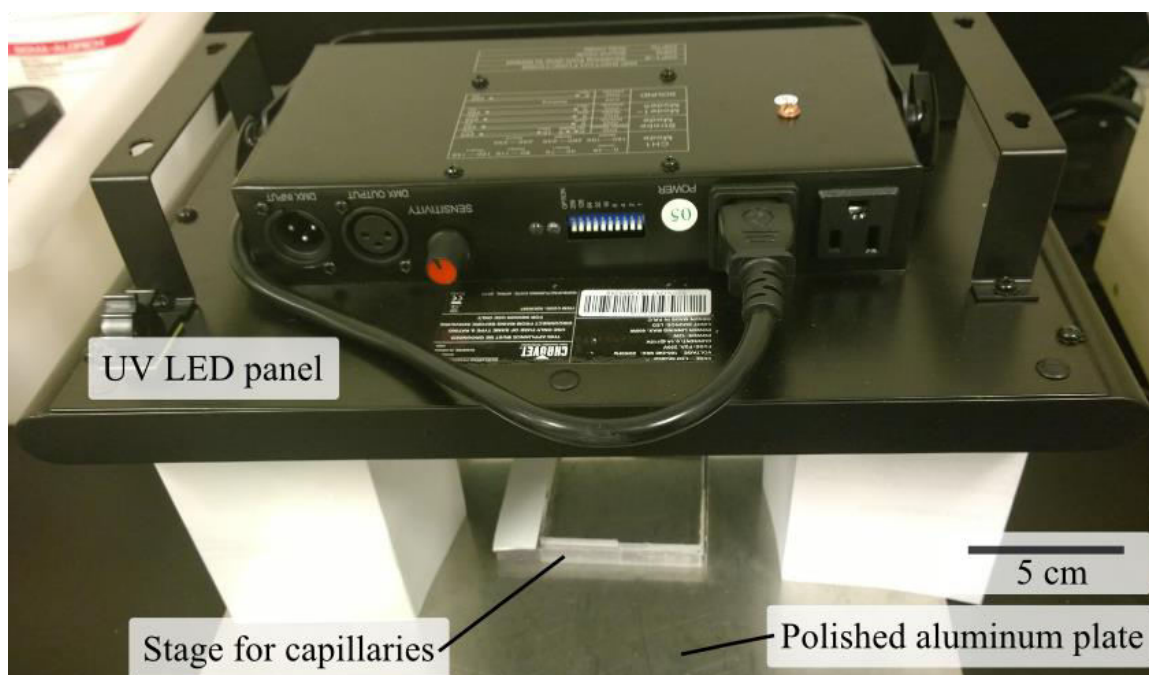


Figure C.2. Custom built UV polymerization setup. The setup consisted of a UV LED panel controlled by a timer (not shown), panel supports, an aluminum plate mirror, a polycarbonate stage for capillaries, and a cardboard enclosure (not shown). To perform UV polymerization, we placed capillaries on the stage, covered the UV LED panel with the enclosure, and turned on the timer to turn on the UV LED. The timer automatically turned off the UV LED once polymerization time was reached.

During polymerization, we placed capillaries on a stage 12 cm bellow the UV LED panel and 1 cm above a polished aluminum plate. The axes of the capillaries were orthogonal to the direction of the UV flux. The polished aluminum plate reflected some of the UV flux, so that the bottom of the solution received some UV flux despite being shadowed by the polymerized solution above it.

C.5 UV polymerization of PPM in capillaries

1. Place a slug of room temperature polymerization solution into vinalyzed capillaries.
2. Seal the capillaries at both ends with polyethylene caps. We made the polyethylene caps by heat-sealing the tubing (Intreamedic 427-425, 0.86 mm i.d., 1.52 mm o.d.) at one end. This is to ensure that the slug of polymerization mixture does not move during the polymerization, and to limit gas exchange between the capillary and the atmosphere. This is important, as oxygen tends to inhibit the free radical polymerization reaction.
3. Place the capillaries in UV chamber for the appropriate amount of time. If desired, electrical tape can be used to mask off areas where polymerization is not to occur.
4. When polymerization is complete, flush out the remaining porogen solvents with air.
5. Dry the PPM in under laboratory vacuum (~27.5 in Hg bellow atmospheric pressure) for 30 min at room temperature. The absolute pressure inside the vacuum chamber should be roughly 2.4 in Hg or 8 kPa. The vapor pressure at 22°C is roughly 13 kPa for methanol and 17 kPa for hexane [94], and so laboratory vacuum is sufficient to remove any remaining porogen solvents used for our PPM synthesis.

6. Dried PPM can be stored at room temperature until further use. If the PPMs are to be functionalized with DNA, we recommend functionalizing PPMs within 24 hr to minimize hydrolysis of surface epoxide groups from atmospheric moisture.

C.6 Functionalization of GMA-co-EDMA PPM with DNA

1. Fill the dried PPM with DNA functionalization solution. For experiments described in the main text of this thesis, our functionalization solution consisted of 3X SSC buffer (450 mM sodium chloride, 45 mM trisodium citrate), 2 mM SDS and 250 μ M 5' C12 amine modified synthetic oligo DNA. We strongly recommend requesting HPLC purified oligos from the manufacturer to reduce the amount of incompletely synthesised or degraded oligos immobilized. However, HPLC purification is ofcourse not sequence specific, and so some of the oligos with sequence errors are expected.
2. Place the capillary with the PPM inside a thin glass tube and seal it at both ends. Place this in a temperature regulated hot water bath for the appropriate amount of time. For consistent results, it is important that the tube containing the PPM have low thermal inertia so that the PPM reaches the bath temperature quickly. We found that polyethelyne sealed standard NMR tubes work well for this purpose.
3. Remove capillary with the PPM from the hot water bath. Flush the remaining functionalization solution with DI water. We found four our capillaries a flow rate 0.2 ml/min for 10 min worked well. The water flow rate for the flush should be low to allow any remaining components of the solution to diffuse out of the globules into the pore space and so be flushed out.
4. Flush the remaining DI water from the PPM with air.

5. Dry the PPM the vacuum oven at 70°C for 1 hr under laboratory vacuum (absolute pressure of roughly 8 kPa). Vapor pressure of water at 70°C is roughly 31 kPa [94], and so this should remove any remaining water. Drying functionalized PPM is important, as this prevents hydrolytic damage to the immobilized oligos.
6. Dried PPM can be stored at room temperature in the laboratory without significant degradation for over 1 yr.

C.7 Functionalization of GMA-co-EDMA PPM with Streptavidin

Here we describe a protocol for immobilization of streptavidin that we adapted from a similar protocols by Preinerstorfer et al. [209] and Liu et al. [210] for generating thiol-modified PPM and antibody-modified PPM respectively. This protocol can also be used for functionalizing GMA-co-EDMA PPM with other proteins. This protocol may also be used to produce thiol-modified PPM (stopping after step 5).

1. Prepare a fresh solution of 2 M sodium hydrosulfide pH 8 by dissolving solid sodium hydrosulfide in 20% (v/v) methanol, 80% (v/v) 0.1 M sodium phosphate dibasic. Adjust the solution pH using 2 M phosphoric acid. The solution pH must be between 7.5 and 8.3. We strongly recommend preparing this solution less than 30 min before injecting it into a PPM.
2. Inject 2 M sodium hydrosulfide solution into a dry PPM and allow to react at room temperature for 2 hr.
3. Flush the resulting PPM with deionized water at a flow rate of 0.2 ml/min, for >300 column volumes.

4. Fill the PPM with 0.5 M sulfuric acid and allow to react at 65°C for 18 hr.
5. Flush the resulting PPM with deionized water and then with ethanol at a flow rate of 0.2 ml/min, for >300 column volumes (each flush). This results in a thiol-modified PPM.
6. Prepare a 3 mM N-gamma-maleimidobutyl-oxysuccinimide ester (GMBS) solution in 1% DMF, 99% absolute ethanol. For example, dissolve 4.2 mg of GMBS powder in 50 μ l dimethylformamide to which then add 4950 μ l of ethanol (200 proof)
7. Inject GMBS solution into PPM and allow to react for 1 hr at room temperature.
8. Flush the resulting PPM with 1x phosphate buffered saline (PBS) at a flow rate of 0.2 ml/min, for >300 column volumes.
9. Prepare 0.5 mg/ml of streptavidin in 1x PBS and allow to react at room temperature for 48 hr.
10. Flush the resulting PPM with 1x phosphate buffered saline (PBS) at a flow rate of 0.2 ml/min, for >300 column volumes.
11. Store the resulting PPM at 4°C.
12. Quantify the streptavidin immobilization. Note that this quantitation is destructive, i.e., the PPM after quantitation cannot be used for biotinylated molecule capture.
 - a. Prepare 1 mg/ml biotin (5-fluorescein) conjugate solution.
 - b. Inject biotin (5-fluorescein) solution into streptavidin functionalized PPM and allow to react for 5 hr at room temperature.
 - c. Flush the resulting PPM with deionized water at a flow rate of 0.2 ml/min, for >300 column volumes.

- d. Measure PPM fluorescence using, for example, fluorescence microscopy.

We expect streptavidin density of order 10 μM on the PPM.

References

1. Viklund, C., et al., "Molded" Macroporous Poly(glycidyl methacrylate-co-trimethylolpropane trimethacrylate) Materials with Fine Controlled Porous Properties: Preparation of Monoliths Using Photoinitiated Polymerization. *Chem. Mater.*, 1997. **9**: p. 463-471.
2. Yu, C., et al., *Preparation of monolithic polymers with controlled porous properties for microfluidic chip applications using photoinitiated free-radical polymerization*. *Journal of Polymer Science Part A: Polymer Chemistry*, 2002. **40**(6): p. 755-769.
3. Shkolnikov, V. and J.G. Santiago, *Coupling Isotachophoresis with Affinity Chromatography for Rapid, Selective Purification with High Column Utilization Part 1: Theory*. *Analytical Chemistry*, 2014. **86**(13): p. 6220-6228.
4. Eeltink, S., et al., *Controlling the surface chemistry and chromatographic properties of methacrylate-ester-based monolithic capillary columns via photografting*. *J. Sep. Sci.*, 2007. **30**: p. 407-413.
5. Sackmann, E.K., A.L. Fulton, and D.J. Beebe, *The present and future role of microfluidics in biomedical research*. *Nature*, 2014. **507**(7491): p. 181-189.
6. Arora, A., et al., *Latest developments in micro total analysis systems*. *Analytical chemistry*, 2010. **82**(12): p. 4830-4847.
7. Ríos, Á. and M. Zougagh, *Sample preparation for micro total analytical systems (μ -TASs)*. *TrAC Trends in Analytical Chemistry*, 2013. **43**: p. 174-188.
8. Shkolnikov, V. and J.G. Santiago, *Coupling Isotachophoresis with Affinity Chromatography for Rapid, Selective Purification with High Column Utilization Part 2: Experimental Study*. *Analytical Chemistry*, 2014. **86**(13): p. 6229-6236.
9. Garcia-Schwarz, G., et al., *On-chip isotachophoresis for separation of ions and purification of nucleic acids*. *Journal of visualized experiments : JoVE*, 2012. **61**: p. e3890.
10. Bocek, P., *Analytical Isotachophoresis*. 1987, Cambridge: VCH.
11. Everaerts, F.M., J.L. Beckers, and T.P.E.M. Verheggen, *Isotachophoresis: Theory, Instrumentation, and Applications*. 1976, Amsterdam, New York: Elsevier.
12. Gebauer, P. and P. Boček, *Recent progress in capillary isotachophoresis*. *Electrophoresis*, 2000. **21**(18): p. 3898-3904.
13. Gebauer, P. and P. Boček, *Recent progress in capillary isotachophoresis*. *Electrophoresis*, 2002. **23**(22-23): p. 3858-3864.
14. Gebauer, P., Z. Malá, and P. Boček, *Recent progress in capillary ITP*. *Electrophoresis*, 2007. **28**(1-2): p. 26-32.
15. Gebauer, P., Z. Malá, and P. Boček, *Recent progress in analytical capillary isotachophoresis*. *Electrophoresis*, 2011. **32**(1): p. 83-89.
16. Malá, Z., P. Gebauer, and P. Boček, *Recent progress in analytical capillary isotachophoresis*. *Electrophoresis*, 2013. **34**(1): p. 19-28.
17. Bahga, S.S. and J.G. Santiago, *Coupling isotachophoresis and capillary electrophoresis: a review and comparison of methods*. *Analyst*, 2013. **138**(3): p. 735-754.
18. Bercovici, M., et al., *Rapid hybridization of nucleic acids using isotachophoresis*. *Proceedings of the National Academy of Sciences*, 2012. **109**(28): p. 11127-11132.

19. Persat, A. and J.G. Santiago, *MicroRNA profiling by simultaneous selective isotachophoresis and hybridization with molecular beacons*. Analytical Chemistry, 2011. **83**(6): p. 2310-2316.
20. Garcia-Schwarz, G. and J.G. Santiago, *Rapid High-Specificity microRNA Detection Using a Two-stage Isotachophoresis Assay*. Angewandte Chemie, 2013. **125**(44): p. 11748-11751.
21. Han, C.M., E. Katilius, and J.G. Santiago, *Increasing Hybridization Rate and Sensitivity of DNA Microarrays Using Isotachophoresis*. Lab on a Chip, 2014. **14**: p. 2958-2967.
22. Shkolnikov, V., S.S. Bahga, and J.G. Santiago, *Desalination and hydrogen, chlorine, and sodium hydroxide production via electrophoretic ion exchange and precipitation*. Physical Chemistry Chemical Physics, 2012. **14**: p. 11534–11545.
23. Shintaku, H., et al., *Increasing Hybridization Rate and Sensitivity of Bead-Based Assays Using Isotachophoresis*. Angewandte Chemie International Edition, 2014. **53** p. 13813 –13816.
24. Kundu, P.K. and I.M. Cohen, *Fluid Mechanics*. 3rd ed. 2004, Amsterdam: Elsevier.
25. MacInnes, D.A. and L.G. Longworth, *Transference Numbers by the Method of Moving Boundaries*. Chemical Reviews, 1932. **9**(2): p. 171-230.
26. Garcia-Schwarz, G., et al., *Sample dispersion in isotachophoresis*. Journal of Fluid Mechanics, 2011. **679**: p. 455-475.
27. Khurana, T.K. and J.G. Santiago, *Sample zone dynamics in peak mode isotachophoresis*. Analytical Chemistry, 2008. **80**(16): p. 6300-6307.
28. Jung, B., R. Bharadwaj, and J.G. Santiago, *On-chip millionfold sample stacking using transient isotachophoresis*. Analytical Chemistry, 2006. **78**(7): p. 2319-2327.
29. Tennikova, T.B., F. Svec, and B.G. Belenkii, *High-performance membrane chromatography. A novel method of protein separation*. J. Liq. Chromatogr., 1990. **13**: p. 63-70.
30. Nischang, I., O. Bruegemann, and F. Svec, *Advances in the preparation of porous polymer monoliths in capillaries and microfluidic chips with focus on morphological aspects*. Anal. Bioanal. Chem, 2010. **397**: p. 953-960.
31. Viklund, C., et al., *Monolithic, "Molded", Porous Materials with High Flow Characteristics for Separations, Catalysis, or Solid-Phase Chemistry: Control of Porous Properties during Polymerization*. Chem. Mater., 1996. **8**: p. 744-750.
32. Svec, F., J. Germain, and J. Frechet, *Nanoporous polymers for hydrogen storage*. Small, 2009. **5**: p. 1098-1111.
33. Zeng, S., et al., *Electroosmotic flow pumps with polymer frits*. Sens. Actuators B, 2002. **82**: p. 209-212.
34. Strickland, D.G. and J.G. Santiago, *In situ-polymerized wicks for passive water management in proton exchange membrane fuel cells*. J. Power Sources, 2010. **195**: p. 1667-1675.
35. Shkolnikov, V., et al., *Design and fabrication of porous polymer wick structures*. Sensors and Actuators B: Chemical, 2010. **150**(2): p. 556-563.
36. Xie, S., et al., *Porous Polymer Monoliths: An Alternative to Classical Beads* *Modern Advances in Chromatography*, R. Freitag, Editor. 2002, Springer Berlin / Heidelberg. p. 87-125.

37. Geiser, L., et al., *Stability and repeatability of capillary columns based on porous monoliths of poly(butyl methacrylate-co-ethylene dimethacrylate)*. Journal of Chromatography A, 2007. **1140**(1-2): p. 140-146.
38. Svec, F. and J.M.J. Frechet, *Temperature, a Simple and Efficient Tool for the Control of Pore Size Distribution in Macroporous Polymers*. Macromolecules, 1995. **28**: p. 7580-7582.
39. Svec, F. and J.M.J. Frechet, *Kinetic Control of Pore Formation in Macroporous Polymers. Formation of "Molded" Porous Materials with High Flow Characteristics for Separation or Catalysis*. Chem. Mater., 1995. **7**: p. 707-715.
40. Svec, F., *Porous polymer monoliths: Amazingly wide variety of techniques enabling their preparation*. Journal of Chromatography A, 2010. **1217**: p. 902-924.
41. He, M., et al., *Confinement effects on the morphology of photopatterned porous polymer monoliths for capillary and microchip electrophoresis of proteins*. Electrophoresis, 2008. **29**(14): p. 2980-2986.
42. Danquah, M.K. and G.M. Forde, *Preparation of macroporous methacrylate monolithic material with convective flow properties for bioseparation: Investigating the kinetics of pore formation and hydrodynamic performance*. Chemical Engineering Journal, 2008. **140**: p. 593-599.
43. Huo, Y., P.J. Schoenmakers, and W.T. Kok, *Efficiency of methacrylate monolithic columns in reversed-phase liquid chromatographic separations*. Journal of Chromatography A, 2007. **1175**(1): p. 81-88.
44. Dong, X., et al., *Capillary electrochromatography with zwitterionic stationary phase on the lysine-bonded poly(glycidyl methacrylate-co-ethylene dimethacrylate) monolithic capillary column*. Electrophoresis, 2006. **27**(12): p. 2518-2525.
45. Zhong, H. and Z. El Rassi, *Neutral polar methacrylate-based monoliths for normal phase nano-LC and CEC of polar species including N-glycans*. Journal of Separation Science, 2009. **32**(1): p. 10-20.
46. Hilder, E.F., F. Svec, and J.M.J. Fréchet, *Development and application of polymeric monolithic stationary phases for capillary electrochromatography*. Journal of Chromatography A, 2004. **1044**(1-2): p. 3-22.
47. Yu, S., et al., *Development of Porous Polymer Monolith by Photoinitiated Polymerization*. Journal of Applied Polymer Science, 2011. **120**: p. 3190-3195.
48. Brandrup, J., et al., *Polymer Handbook (4th Edition)*. John Wiley & Sons.
49. Lee, D., F. Svec, and J.M.J. Fréchet, *Photopolymerized monolithic capillary columns for rapid micro high-performance liquid chromatographic separation of proteins*. Journal of Chromatography A, 2004. **1051**(1-2): p. 53-60.
50. Buszewski, B. and M. Szumski, *Study of Bed Homogeneity of Methacrylate-Based Monolithic Columns for Micro-HPLC and CEC*. Chromatographia, 2004. **60**(0): p. S261-S267.
51. Peters, E.C., et al., *Molded Rigid Polymer Monoliths as Separation Media for Capillary Electrochromatography. 1. Fine Control of Porous Properties and Surface Chemistry*. Analytical Chemistry, 1998. **70**(11): p. 2288-2295.
52. Eeltink, S., et al., *Optimization of the porous structure and polarity of polymethacrylate-based monolithic capillary columns for the LC-MS separation of enzymatic digests*. Journal of Separation Science, 2007. **30**(17): p. 2814-2820.

53. Mair, D.A., et al., *Use of photopatterned porous polymer monoliths as passive micromixers to enhance mixing efficiency for on-chip labeling reactions*. Lab Chip, 2009. **9**: p. 877-883.
54. Peters, E.C., et al., *Molded Rigid Polymer Monoliths as Separation Media for Capillary Electrochromatography*. Analytical Chemistry, 1997. **69**(17): p. 3646-3649.
55. Jiang, T., et al., *Preparation and characterization of monolithic polymer columns for capillary electrochromatography*. Journal of Chromatography A, 2001. **923**(1-2): p. 215-227.
56. Buszewski, B., M. Szumski, and S. Sus, *Methacrylate-based monolithic columns for micro-HPLC and CEC*. LC-GC Europe, 2002. **15**(12): p. 792-798.
57. Eeltink, S., et al., *Tailoring the Morphology of Methacrylate Ester-Based Monoliths for Optimum Efficiency in Liquid Chromatography*. Analytical Chemistry, 2005. **77**(22): p. 7342-7347.
58. Ueki, Y., et al., *Preparation of low flow-resistant methacrylate-based monolithic stationary phases of different hydrophobicity and the application to rapid reversed-phase liquid chromatographic separation of alkylbenzenes at high flow rate and elevated temperature*. Journal of Chromatography A, 2006. **1106**(1-2): p. 106-111.
59. Le Gac, S., et al., *Monoliths for microfluidic devices in proteomics*. Journal of Chromatography B, 2004. **808**(1): p. 3-14.
60. Ro, K.W., et al., *Capillary high-performance liquid chromatography–electrospray ionization mass spectrometry using monolithic columns and carbon fiber electrospray ionization emitters*. Journal of Chromatography A, 2004. **1047**(1): p. 49-57.
61. Dong, J., et al., *Capillary electrochromatography with a neutral monolithic column for classification of analytes and determination of basic drugs in human serum*. Electrophoresis, 2005. **26**(18): p. 3452-3459.
62. Jiang, Z., et al., *Hydrophilic Interaction Chromatography Using Methacrylate-Based Monolithic Capillary Column for the Separation of Polar Analytes*. Analytical Chemistry, 2006. **79**(3): p. 1243-1250.
63. Yu, C., F. Svec, and J.M.J. Fréchet, *Towards stationary phases for chromatography on a microchip: Molded porous polymer monoliths prepared in capillaries by photoinitiated in situ polymerization as separation media for electrochromatography*. Electrophoresis, 2000. **21**(1): p. 120-127.
64. Pucci, V., et al., *Monolithic columns with a gradient of functionalities prepared via photoinitiated grafting for separations using capillary electrochromatography*. Journal of Separation Science, 2004. **27**(10-11): p. 779-788.
65. Pruim, P., et al., *Methacrylate monolithic capillary columns for gradient peptide separations*. Journal of Chromatography A, 2008. **1208**(1-2): p. 109-115.
66. Gu, B., Y. Li, and M.L. Lee, *Polymer Monoliths with Low Hydrophobicity for Strong Cation-Exchange Capillary Liquid Chromatography of Peptides and Proteins*. Analytical Chemistry, 2007. **79**(15): p. 5848-5855.
67. Peters, E.C., F. Svec, and J.M.J. Fréchet, *Preparation of Large-Diameter “Molded” Porous Polymer Monoliths and the Control of Pore Structure Homogeneity*. Chemistry of Materials, 1997. **9**(8): p. 1898-1902.

68. Svec, F., *Porous polymer monoliths: Amazingly wide variety of techniques enabling their preparation*. Journal of Chromatography A, 2010. **1217**(6): p. 902-924.
69. Danquah, M.K. and G.M. Forde, *Towards the design of a scalable and commercially viable technique for plasmid purification using a methacrylate monolithic stationary phase*. Journal of Chemical Technology and Biotechnology, 2007. **82**(8): p. 752-757.
70. Danquah, M.K., J. Ho, and G.M. Forde, *Performance of R-N (R')-R'' functionalised poly (glycidyl methacrylate-co-ethylene glycol dimethacrylate) monolithic sorbent for plasmid DNA adsorption*. Journal of Separation Science, 2007. **30**(17): p. 2843-2850.
71. Lendero, N., et al., *Simple method for determining the amount of ion-exchange groups on chromatographic supports*. Journal of Chromatography A, 2005. **1065**(1): p. 29-38.
72. Svec, F. and J.M. Frechet, *Modified poly (glycidyl methacrylate-co-ethylene dimethacrylate) continuous rod columns for preparative-scale ion-exchange chromatography of proteins*. Journal of Chromatography A, 1995. **702**(1): p. 89-95.
73. Bruchet, A., et al., *Synthesis and characterization of ammonium functionalized porous poly (glycidyl methacrylate-co-ethylene dimethacrylate) monoliths for microscale analysis and its application to DNA purification*. Journal of biomedical nanotechnology, 2011. **7**(3): p. 415-425.
74. Ueki, Y., et al., *Preparation and application of methacrylate-based cation-exchange monolithic columns for capillary ion chromatography*. Analytical Chemistry, 2004. **76**(23): p. 7007-7012.
75. Yang, B., et al., *Tailoring elution of tetraalkylammonium ions. Ideal electrostatic selectivity elution order on a polymeric ion exchanger*. Analytical Chemistry, 2007. **79**(2): p. 769-772.
76. Paul, S. and B. Rånby, *Methyl methacrylate (MMA)-glycidyl methacrylate (GMA) copolymers. A novel method to introduce sulfonic acid groups on the polymeric chains*. Macromolecules, 1976. **9**(2): p. 337-340.
77. Yang, G., et al., *On-line simultaneous removal of human serum albumin and enrichment of doxazosin using a weak cation-exchange monolithic column*. Journal of Chromatography A, 2006. **1129**(2): p. 231-235.
78. Wei, Y., et al., *Preparation of a monolithic column for weak cation exchange chromatography and its application in the separation of biopolymers*. Journal of Separation Science, 2006. **29**(1): p. 5-13.
79. Wei, X., et al., *On-line solid-phase extraction with a monolithic weak cation-exchange column and simultaneous screening of α 1-adrenergic receptor antagonists in human plasma*. Journal of Separation Science, 2007. **30**(17): p. 2851-2857.
80. Sethi, D., et al., *Chemical strategies for immobilization of oligonucleotides*. Biotechnology journal, 2009. **4**(11): p. 1513-1529.
81. Sinitsyna, E.S., et al., *Macroporous methacrylate-based monoliths as platforms for DNA microarrays*. Talanta, 2012. **93**: p. 139-146.

82. Satterfield, B.C., et al., *Microfluidic purification and preconcentration of mRNA by flow-through polymeric monolith*. Analytical chemistry, 2007. **79**(16): p. 6230-6235.
83. West, J.A. and B.C. Satterfield, *Fabrication of porous polymer monoliths in microfluidic chips for selective nucleic acid concentration and purification*, in *Microchip-Based Assay Systems*. 2007, Springer. p. 9-21.
84. Kasper, C., et al., *Fast isolation of protein receptors from streptococci G by means of macroporous affinity discs*. Journal of Chromatography A, 1998. **798**(1): p. 65-72.
85. Křivenková, J., Z. Bilková, and F. Foret, *Characterization of a monolithic immobilized trypsin microreactor with on-line coupling to ESI-MS*. Journal of Separation Science, 2005. **28**(14): p. 1675-1684.
86. Vlach, E.G., et al., *Monolithic peptidyl sorbents for comparison of affinity properties of plasminogen activators*. Journal of Chromatography B, 2004. **810**(1): p. 15-23.
87. Hagedorn, J., et al., *High performance flow injection analysis of recombinant protein G*. Journal of Biotechnology, 1999. **69**(1): p. 1-7.
88. Ponomareva, E., et al., *Monolithic bioreactors: Effect of chymotrypsin immobilization on its biocatalytic properties*. Journal of Chromatography B, 2010. **878**(5): p. 567-574.
89. Hahn, R., et al., *Affinity monoliths generated by in situ polymerization of the ligand*. Analytical Chemistry, 2001. **73**(21): p. 5126-5132.
90. Platonova, G.A., et al., *Quantitative fast fractionation of a pool of polyclonal antibodies by immunoaffinity membrane chromatography*. Journal of Chromatography A, 1999. **852**(1): p. 129-140.
91. Monzo, A., T. Rejtar, and A. Guttman, *Optimization of poly (GMA-co-EDMA) Monolithic Support for Trypsin Nanoreactor Fabrication*. Journal of Chromatographic Science, 2009. **47**(6): p. 467-472.
92. Kalashnikova, I., N. Ivanova, and T. Tennikova, *Macroporous monolithic layers as efficient 3-D microarrays for quantitative detection of virus-like particles*. Analytical Chemistry, 2007. **79**(14): p. 5173-5180.
93. Benčina, K., et al., *Enzyme immobilization on epoxy-and 1, 1'-carbonyldiimidazole-activated methacrylate-based monoliths*. Journal of Separation Science, 2004. **27**(10-11): p. 811-818.
94. *Handbook of Chemistry & Physics*. 92nd ed. 2011, Boca Raton, FL: CRC Press.
95. Ehlers, J.-E., et al., *Theoretical study on mechanisms of the epoxy-amine curing reaction*. Macromolecules, 2007. **40**(12): p. 4370-4377.
96. Štrancar, A., et al., *Application of compact porous disks for fast separations of biopolymers and in-process control in biotechnology*. Analytical Chemistry, 1996. **68**(19): p. 3483-3488.
97. Yu, C., et al., *Preparation of monolithic polymers with controlled porous properties for microfluidic chip applications using photoinitiated free-radical polymerization*. Journal of Polymer Science: Part A Polymer Chemistry, 2002. **40**(6): p. 755-769.
98. Chanda, M., *Introduction to polymer science and chemistry: a problem solving approach*. 2006, Boca Raton: CRC Press.

99. Hage, D.S., ed. *Handbook of Affinity Chromatography*. 2nd ed. 2006, CRC Press: Boca Raton.
100. Hage, D.S., *Affinity chromatography: a review of clinical applications*. Clinical Chemistry, 1999. **45**(5): p. 593-615.
101. Mallik, R. and D.S. Hage, *Affinity monolith chromatography*. Journal of Separation Science, 2006. **29**(12): p. 1686-1704.
102. Pfaunmiller, E.L., et al., *Affinity monolith chromatography: a review of principles and recent analytical applications*. Analytical and Bioanalytical Chemistry, 2013. **405**(7): p. 2133-2145.
103. Levenspiel, O., *Chemical Reaction Engineering* 3rd ed. 1999, New York: John Wiley & Sons.
104. Rogacs, A., L.A. Marshall, and J.G. Santiago, *Purification of Nucleic Acids using Isotachophoresis* Journal of Chromatography A, 2014. **1335**: p. 105-120.
105. Garcia-Schwarz, G. and J.G. Santiago, *Integration of on-chip isotachophoresis and functionalized hydrogels for enhanced-sensitivity nucleic acid detection*. Analytical Chemistry, 2012. **84**(15): p. 6366-6369.
106. Garcia-Schwarz, G. and J.G. Santiago, *Rapid High-Specificity microRNA Detection Using a Two-stage Isotachophoresis Assay*. Angewandte Chemie, 2013. **125**(44): p. 11748-11751.
107. Karsenty, M., S. Rubin, and M. Bercovici, *Acceleration of surface-based hybridization reactions using isotachophoretic focusing*. Analytical Chemistry, 2014.
108. Shim, J., P. Dutta, and C.F. Ivory, *Finite-volume methods for isotachophoretic separation in microchannels*. Numerical Heat Transfer, Part A: Applications, 2007. **52**(5): p. 441-461.
109. Dullien, F.A.L., *Porous Media: Fluid Transport and Pore Structure*. 2nd ed. 1991, New York: Academic Press.
110. Incropera, F.P. and D.P. DeWitt, *Fundamentals of Heat and Mass Transfer*. 1996, New York: John Wiley & Sons.
111. Stellwagen, E. and N.C. Stellwagen, *Determining the electrophoretic mobility and translational diffusion coefficients of DNA molecules in free solution*. Electrophoresis, 2002. **23**(16): p. 2794-2803.
112. Thomas, H.C., *Heterogeneous ion exchange in a flowing system*. Journal of the American Chemical Society, 1944. **66**(10): p. 1664-1666.
113. Giddings, J.C., *Generation of variance, "theoretical plates," resolution, and peak capacity in electrophoresis and sedimentation*. Separation Science and Technology, 1969. **4**(3): p. 181-189.
114. Landers, J.P., *Handbook of capillary electrophoresis*. 1997: CRC press.
115. Wolfram|Alpha. *Inverse Laplace Transform*. 2013 [cited 2013; Available from: <http://www.wolframalpha.com/input/?i=inverse+Laplace+transform+exp%28-b%2Fs%29>].
116. Konstantinov, B.P. and O.V. Oshurkova, *Instrument for analyzing electrolyte solutions by ionic mobilities*. Soviet physics - technical physics, 1966. **11**(5): p. 693-704.
117. Yao, S. and J.G. Santiago, *Porous glass electroosmotic pumps: theory*. Journal of Colloid and Interface Science, 2003. **268**(1): p. 133-142.

118. Herr, A., et al., *Electroosmotic capillary flow with nonuniform zeta potential*. Analytical Chemistry, 2000. **72**(5): p. 1053-1057.
119. Saffman, P., *Dispersion due to molecular diffusion and macroscopic mixing in flow through a network of capillaries*. Journal of Fluid Mechanics, 1960. **7**(02): p. 194-208.
120. Perfect, E. and M.C. Sukop, *Models relating solute dispersion to pore space geometry in saturated media: A review*. Sssa special publication, 2001. **56**: p. 77-146.
121. Abelev, G., et al., *Analysis of epitope specificity of monoclonal antibodies by counterflow isotachopheresis on nitrocellulose membranes*. Bulletin of Experimental Biology and Medicine, 1988. **106**(5): p. 1600-1604.
122. Abelev, G., et al., *Performance of multistep immunochemical reactions by counterflow isotachopheresis on nitrocellulose membranes—II. Epitope analysis of monoclonal antibodies*. Molecular Immunology, 1989. **26**(1): p. 49-52.
123. Abelev, G. and E. Karamova, *Performance of multistep immunochemical reactions by counterflow isotachopheresis on nitrocellulose membranes—I. Immunoblotting*. Molecular Immunology, 1989. **26**(1): p. 41-47.
124. Abelev, G. and É. Karamova, *Counterflow immunoblotting*. Bulletin of Experimental Biology and Medicine, 1988. **105**(5): p. 748-751.
125. Schranz, D., et al., *Counterflow affinity isotachopheresis on cellulose acetate membranes*. Electrophoresis, 1991. **12**(6): p. 414-419.
126. Abelev, G.I. and E.R. Karamova, *Tumor-Marker Detection by Isotachopheresis in Porous Membranes*, in *Serological Cancer Markers*. 1992, Springer. p. 453-471.
127. Abelev, G., et al., *Determination of DNA-binding proteins by countercurrent isotachopheresis on nitrocellulose membranes. I. Antibodies to DNA and its adducts*. Molekuliarnaia Biologiya, 1994. **28**(4): p. 768.
128. Pushpendra, S., P. Arvind, and B. Anil, *Nucleic Acids as Therapeutics*, in *Nucleic Acids Sequences to Molecular Medicine*. 2012, Springer. p. 19-45.
129. Haasnoot, J. and B. Berkhout, *Nucleic acids-based therapeutics in the battle against pathogenic viruses*, in *Antiviral Strategies*. 2009, Springer. p. 243-263.
130. Opalinska, J.B. and A.M. Gewirtz, *Nucleic-acid therapeutics: basic principles and recent applications*. Nature Reviews Drug Discovery, 2002. **1**(7): p. 503-514.
131. Schwarzenbach, H., D.S. Hoon, and K. Pantel, *Cell-free nucleic acids as biomarkers in cancer patients*. Nature Reviews Cancer, 2011. **11**(6): p. 426-437.
132. Wilson, I.G., *Inhibition and facilitation of nucleic acid amplification*. Applied and Environmental Microbiology, 1997. **63**(10): p. 3741.
133. Boom, R., et al., *Rapid and simple method for purification of nucleic acids*. Journal of Clinical Microbiology, 1990. **28**(3): p. 495-503.
134. Bodi, K., et al., *Comparison of Commercially Available Target Enrichment Methods for Next-Generation Sequencing*. Journal of biomolecular techniques: JBT, 2013. **24**(2): p. 73.
135. Mamanova, L., et al., *Target-enrichment strategies for next-generation sequencing*. Nature Methods, 2010. **7**(2): p. 111-118.
136. Ma, J., et al., *Monolith-based immobilized enzyme reactors: Recent developments and applications for proteome analysis*. Journal of Separation Science, 2007. **30**(17): p. 3050-3059.

137. Shkolnikov, V., et al., *Design and fabrication of porous polymer wick structures*. Sensors and Actuators B-Chemical, 2010. **150**(2): p. 556-563.
138. Shkolnikov, V. and J.G. Santiago, *A method for non-invasive full-field imaging and quantification of chemical species*. Lab on a Chip, 2013. **13**(8): p. 1632-1643.
139. Persat, A., L.A. Marshall, and J.G. Santiago, *Purification of nucleic acids from whole blood using isotachophoresis*. Analytical Chemistry, 2009. **81**(22): p. 9507-9511.
140. Edman, C.F., et al., *Electric field directed nucleic acid hybridization on microchips*. Nucleic Acids Research, 1997. **25**(24): p. 4907-4914.
141. Wetmur, J.G., *Hybridization and renaturation kinetics of nucleic acids*. Annual Review of Biophysics and Bioengineering, 1976. **5**(1): p. 337-361.
142. Gao, Y., L.K. Wolf, and R.M. Georgiadis, *Secondary structure effects on DNA hybridization kinetics: a solution versus surface comparison*. Nucleic Acids Research, 2006. **34**(11): p. 3370-3377.
143. Bhattacharyya, S., et al., *Sample dispersion in isotachophoresis with Poiseuille counterflow*. Physics of Fluids, 2013. **25**: p. 022001.
144. Peterson, A.W., R.J. Heaton, and R.M. Georgiadis, *The effect of surface probe density on DNA hybridization*. Nucleic Acids Research, 2001. **29**(24): p. 5163-5168.
145. Boček, P., et al., *Analytical isotachophoresis: The concept of the separation capacity*. Journal of Chromatography A, 1978. **160**(1): p. 1-9.
146. Marshall, L.A., *Designing automated systems for sample preparation of nucleic acids using isotachophoresis*, ed. G.G. Fuller, et al. 2013.
147. Persat, A., M.E. Suss, and J.G. Santiago, *Basic principles of electrolyte chemistry for microfluidic electrokinetics. Part II: Coupling between ion mobility, electrolysis, and acid–base equilibria*. Lab on a Chip, 2009. **9**(17): p. 2454-2469.
148. Bercovici, M., S.K. Lele, and J.G. Santiago, *Open source simulation tool for electrophoretic stacking, focusing, and separation*. Journal of Chromatography A, 2009. **1216**(6): p. 1008-1018.
149. Stellwagen, N.C., C. Gelfi, and P.G. Righetti, *The free solution mobility of DNA*. Biopolymers, 1997. **42**(6): p. 687-703.
150. Polyanskiy, M.N. *Refractive Index Database*. 2008 [cited 2013; Available from: <http://refractiveindex.info>].
151. Thomas, S.W., G.D. Joly, and T.M. Swager, *Chemical sensors based on amplifying fluorescent conjugated polymers*. Chemical Reviews, 2007. **107**(4): p. 1339-1386.
152. Lakowicz, J.R., *Principles of Fluorescence Spectroscopy*. 3 ed. 2006, New York: Springer
153. Markham, N.R., et al. *The UNAFold Web Server*. 1995 [cited 2013; Available from: <http://mfold.rna.albany.edu/>].
154. Erickson, D., D. Li, and U.J. Krull, *Modeling of DNA hybridization kinetics for spatially resolved biochips*. Analytical Biochemistry, 2003. **317**(2): p. 186-200.
155. Levicky, R. and A. Horgan, *Physicochemical perspectives on DNA microarray and biosensor technologies*. Trends in Biotechnology, 2005. **23**(3): p. 143-149.
156. Stevens, P.W., M.R. Henry, and D.M. Kelso, *DNA hybridization on microparticles: determining capture-probe density and equilibrium dissociation constants*. Nucleic Acids Research, 1999. **27**(7): p. 1719-1727.

157. Okahata, Y., et al., *Kinetic measurements of DNA hybridization on an oligonucleotide-immobilized 27-MHz quartz crystal microbalance*. Analytical Chemistry, 1998. **70**(7): p. 1288-1296.
158. Rohr, T., et al., *Porous polymer monoliths: simple and efficient mixers prepared by direct polymerization in the channels of microfluidic chips*. Electrophoresis, 2001. **22**(18): p. 3959.
159. Yu, C., et al., *Monolithic porous polymer for on-chip solid-phase extraction and preconcentration prepared by photoinitiated in situ polymerization within a microfluidic device*. Analytical Chemistry, 2001. **73**(21): p. 5088-5096.
160. Podgornik, A., et al., *Large-scale methacrylate monolithic columns: design and properties*. Journal of Biochemical and Biophysical Methods, 2004. **60**(3): p. 179-189.
161. Hruška, V. and B. Gaš, *Kohlrausch regulating function and other conservation laws in electrophoresis*. Electrophoresis, 2007. **28**(1-2): p. 3-14.
162. Kirby, B.J. and E.F. Hasselbrink, *Zeta potential of microfluidic substrates: 1. Theory, experimental techniques, and effects on separations*. Electrophoresis, 2004. **25**(2): p. 187-202.
163. Špringer, T., et al., *Shielding effect of monovalent and divalent cations on solid-phase DNA hybridization: surface plasmon resonance biosensor study*. Nucleic Acids Research, 2010. **38**(20): p. 7343-7351.
164. Mani, A., T.A. Zangle, and J.G. Santiago, *On the Propagation of Concentration Polarization from Microchannel– Nanochannel Interfaces Part I: Analytical Model and Characteristic Analysis*. Langmuir, 2009. **25**(6): p. 3898-3908.
165. Zangle, T.A., A. Mani, and J.G. Santiago, *On the Propagation of Concentration Polarization from Microchannel– Nanochannel Interfaces Part II: Numerical and Experimental Study*. Langmuir, 2009. **25**(6): p. 3909-3916.
166. Waki, H. and Y. Tokunaga, *Donnan Exclusion–Ion Exclusion Chromatography*. Journal of Liquid Chromatography, 1982. **5**(s1): p. 105-119.
167. Waki, H. and Y. Tokunaga, *Donnan exclusion chromatography: 1. Theory and application to the separation of phosphorus oxoanions or metal cations*. Journal of Chromatography A, 1980. **201**: p. 259-264.
168. Kirby, B.J. and E.F. Hasselbrink, *Zeta potential of microfluidic substrates: 2. Data for polymers*. Electrophoresis, 2004. **25**(2): p. 203-213.
169. Costanzo, L.S., *Physiology*. 4th ed. 2009: Saunders.
170. Hirokawa, T., et al., *Table of isotachophoretic indices: I. Simulated qualitative and quantitative indices of 287 anionic substances in the range ph 3–10*. Journal of Chromatography A, 1983. **271**(2): p. D1-D106.
171. Völkel, A.R. and J. Noolandi, *Electrophoresis between sieving and reptation: An investigation of the role of shape fluctuations in electrophoresis*. Electrophoresis, 1995. **16**(1): p. 2086-2093.
172. Smith, D.E., T.T. Perkins, and S. Chu, *Dynamical scaling of DNA diffusion coefficients*. Macromolecules, 1996. **29**(4): p. 1372-1373.
173. Tyn, M.T. and T.W. Gusek, *Prediction of diffusion coefficients of proteins*. Biotechnology and Bioengineering, 1990. **35**(4): p. 327-338.

174. Abcam. *KD value: A quantitative measurement of antibody affinity*. 2014 [cited 2014 May 22, 2014]; Available from: <http://www.abcam.com/index.html?pageconfig=resource&rid=15749>.
175. Lollo, B., F. Steele, and L. Gold, *Beyond antibodies: new affinity reagents to unlock the proteome*. Proteomics, 2014.
176. Hirokawa, T. and Y. Kiso, *Preparative procedures in isotachopheresis*. Journal of Chromatography A, 1994. **658**: p. 343-354.
177. Delgado, A., et al., *Measurement and interpretation of electrokinetic phenomena (IUPAC technical report)*. Pure and Applied Chemistry, 2005. **77**(10): p. 1753-1805.
178. Shkolnikov, V. and J.G. Santiago, *Fast, Specific, and Efficient Affinity Purification of Target DNA from Whole Human Blood by Combining Isotachopheresis and Affinity Chromatography*, in *Eighteenth International Conference on Miniaturized Systems for Chemistry and Life Sciences (μ TAS)*. 2014: San Antonio, TX, USA.
179. Richardson, A.J., et al., *Blood storage at 4° C—factors involved in DNA yield and quality*. Journal of Laboratory and Clinical Medicine, 2006. **147**(6): p. 290-294.
180. McLoughlin, K.S., *Microarrays for pathogen detection and analysis*. Briefings in functional genomics, 2011. **10**(6): p. 342-353.
181. Wang, D., et al., *Microarray-based detection and genotyping of viral pathogens*. Proceedings of the National Academy of Sciences, 2002. **99**(24): p. 15687-15692.
182. Malanoski, A.P., et al., *Automated identification of multiple micro-organisms from resequencing DNA microarrays*. Nucleic Acids Research, 2006. **34**(18): p. 5300-5311.
183. Belosludtsev, Y.Y., et al., *Organism identification using a genome sequence-independent universal microarray probe set*. Biotechniques, 2004. **37**(4): p. 654-660.
184. Quan, P.-L., et al., *Detection of respiratory viruses and subtype identification of influenza A viruses by GreeneChipResp oligonucleotide microarray*. Journal of Clinical Microbiology, 2007. **45**(8): p. 2359-2364.
185. Jaing, C., et al., *A functional gene array for detection of bacterial virulence elements*. PLoS One, 2008. **3**(5): p. e2163.
186. Dutt, A. and R. Beroukhim, *Single nucleotide polymorphism array analysis of cancer*. Current Opinion in Oncology, 2007. **19**(1): p. 43-49.
187. Fan, J.-B., et al., *Parallel genotyping of human SNPs using generic high-density oligonucleotide tag arrays*. Genome Research, 2000. **10**(6): p. 853-860.
188. Manolio, T.A., et al., *Finding the missing heritability of complex diseases*. Nature, 2009. **461**(7265): p. 747-753.
189. Mirzabekov, A.D., *DNA sequencing by hybridization—a megasequencing method and a diagnostic tool?* Trends in Biotechnology, 1994. **12**(1): p. 27-32.
190. Drmanac, R., et al., *Sequencing by hybridization*. Automated DNA Sequencing and Analysis, MD Adams, C. Fields, and JC Venter, eds., Academic Press, Harcourt Brace & Company, London, 1994. **4**: p. 29-36.
191. Hegde, P., et al., *A concise guide to cDNA microarray analysis*. Biotechniques, 2000. **29**(3): p. 548-563.
192. Cheung, V.G., et al., *Making and reading microarrays*. Nature Genetics, 1999. **21**: p. 15-19.

193. Bhanot, G., et al., *The importance of thermodynamic equilibrium for high throughput gene expression arrays*. Biophysical Journal, 2003. **84**(1): p. 124-135.
194. Sartor, M., et al., *Microarray results improve significantly as hybridization approaches equilibrium*. Biotechniques, 2004. **36**(5): p. 790-796.
195. Shintaku, H., et al., *Increasing Hybridization Rate and Sensitivity of Bead-Based Assays Using Isotachophoresis*. Angewandte Chemie International Edition, 2014: p. n/a-n/a.
196. Hecker, K.H. and R. Rill, *Error analysis of chemically synthesized polynucleotides*. Biotechniques, 1998. **24**(2): p. 256-260.
197. *Chemical Synthesis and Purification of Oligonucleotides*. 2011, Integrated DNA Technologies.
198. Wetmur, J.G. and N. Davidson, *Kinetics of renaturation of DNA*. Journal of Molecular Biology, 1968. **31**(3): p. 349-370.
199. Boček, P., et al., *Stationary mean temperatures and radial temperature profiles in capillary isotachophoresis*. Collection of Czechoslovak Chemical Communications, 1977. **42**(12): p. 3382-3387.
200. Ryšlavý, Z., et al., *Effects of joule heat on the steady-state temperature profiles and the mean values of temperature in isotachophoresis*. Journal of Chromatography A, 1977. **144**(1): p. 17-25.
201. Coxon, M. and M. Binder, *Radial temperature distribution in isotachophoresis columns of circular cross-section*. Journal of Chromatography A, 1974. **101**(1): p. 1-16.
202. Churchill, S.W. and H.H. Chu, *Correlating equations for laminar and turbulent free convection from a horizontal cylinder*. International Journal of Heat and Mass Transfer, 1975. **18**(9): p. 1049-1053.
203. Carslaw, H.S. and J.C. Jaeger, *Conduction of Heat in Solids*. 1984, Oxford: Clarendon Press.
204. MatWeb. *Hippe PMMA*. 2014 [cited 2014; Available from: <http://www.matweb.com/search/DataSheet.aspx?MatGUID=6204fda867fe4d53a05de303286762f3>].
205. TheEngineeringToolBox. *Air Properties: Temperature, density, specific heat, thermal conductivity, expansion coefficient, kinematic viscosity and Prandtl's number for temperatures ranging -150 - 400 C*. 2014 [cited 2014; Available from: http://www.engineeringtoolbox.com/air-properties-d_156.html].
206. CambridgeGlassblowing. *Glass Properties: Borosilicate Glass*. 2014 [cited 2014; Available from: <http://www.camglassblowing.co.uk/gproperties.htm>].
207. Bahga, S.S., M. Bercovici, and J.G. Santiago, *Robust and high-resolution simulations of nonlinear electrokinetic processes in variable cross-section channels*. Electrophoresis, 2012. **33**(19-20): p. 3036-3051.
208. Fawcett, T., *An introduction to ROC analysis*. Pattern Recognition Letters, 2006. **27**(8): p. 861-874.
209. Preinerstorfer, B., et al., *Development of reactive thiol-modified monolithic capillaries and in-column surface functionalization by radical addition of a chromatographic ligand for capillary electrochromatography*. Journal of Chromatography A, 2004. **1044**(1): p. 187-199.

210. Liu, J., et al., *Flow-through immunosensors using antibody-immobilized polymer monoliths*. *Biosensors and Bioelectronics*, 2010. **26**(1): p. 182-188.